

ADAPTIVE IMMUNITY AND THE TUMOR IMMUNE MICROENVIRONMENT

Christof C. Smith

A dissertation submitted to the faculty at the University of North Carolina at Chapel Hill
in partial fulfillment of the requirements for the degree of Doctorate of Philosophy in the
Department of Microbiology & Immunology in the UNC School of Medicine

Chapel Hill
2019

Approved by:

Edward Miao

Glenn Matsushima

Jonathan Serody

Yisong Wan

Andrew Wang

© 2019
Christof C. Smith
ALL RIGHTS RESERVED

ABSTRACT

Christof C. Smith: Role of the adaptive immune system in the tumor immune
microenvironment
(Under the direction of Jonathan S. Serody)

The adaptive immune system is essential for production of anti-tumor immune responses, with the majority of current immunotherapeutics designed to modulate the interaction between adaptive immunity and tumor cells within the tumor-immune microenvironment. This dissertation addresses three translational goals regarding our understanding and modulation of anti-tumor adaptive immunity: 1) Improvement of understanding for existing immunotherapies such as checkpoint inhibitor therapy (Chapter 2.1); 2) Improvement of efficacy for novel immunotherapeutics currently in development including tumor neoantigen vaccines (Chapter 4); and 3) Development of next-generation immunotherapies through identification of novel anti-tumor vaccine targets (Chapter 3), as well as development of diagnostic tools including biomarkers of immunotherapy response (Chapter 3) and immune-imaging modalities (Chapter 2.1).

To my loving wife and supportive parents

TABLE OF CONTENTS

LIST OF FIGURES.....	ix
LIST OF TABLES.....	xi
CHAPTER 1: General introduction to tumor immunology.....	1
1.1 Introduction to the immune system	1
1.2 The tumor immune microenvironment.....	2
1.3 Development of immunotherapies for cancer treatment.....	4
1.4 Molecular characterization of the tumor	6
1.5 Classical and non-classical tumor-specific antigens	8
1.6 Human endogenous retroviral derived cancer antigens	12
1.7 Computational prediction of tumor-specific antigens.....	15
1.8 Clinical translation of non-classical tumor-specific antigens.....	18
1.9 Therapeutic platforms for tumor antigen vaccination.....	22
1.10 Concluding remarks and contributions of this work.....	24
CHAPTER 2: Design and study of subtype-specific murine tumor models	26
2.1 Development of subtype specific mouse models of bladder cancer.....	26
2.1.1 Introduction	26
2.1.2 Materials and Methods	28

2.1.3 Results.....	37
2.1.4 Discussion	58
2.2 Immuno-PET imaging of tumor-infiltrating lymphocytes using Zirconium-89 radiolabeled anti-CD3 antibody in immune-competent mice bearing syngeneic tumors.	63
2.2.1 Introduction	63
2.2.2 Results.....	66
2.2.3 Discussion	79
2.2.4 Materials and methods	82
CHAPTER 3: Role of human endogenous retroviruses in the tumor immune microenvironment.....	88
3.1 Introduction	88
3.2 Results	90
3.3 Discussion.....	111
3.4 Methods	120
CHAPTER 4: Design and delivering of neoantigen-based therapeutic vaccines	126
4.1 Machine learning model for prediction of neoantigen immunogenicity	126
4.1.1 Introduction	126
4.1.2 Results and Discussion	128
4.1.3 Materials and methods	143
4.2 Neoantigen-delivering nanoparticles for therapeutic tumor vaccines	144
4.2.1 Introduction	144
4.2.2 Results and Discussion	146
4.2.3 Materials and methods	151

CHAPTER 5: Future Directions and Conclusion	154
APPENDIX 1: RNA-seq Analysis of the Tumor Microenvironment.....	160
APPENDIX 2: The Cancer Genome Atlas comprehensive molecular characterization of renal cell carcinoma	196
APPENDIX 3: Molecular and clinical characterization of a claudin-low subtype of gastric cancer.	197
APPENDIX 4: Endogenous retrovirus expression is associated with response to immune checkpoint blockade in clear cell renal cell carcinoma.	198
APPENDIX 5: Dual immunotherapy nanoparticle improves T-cell activation and cancer immunotherapy.	199
APPENDIX 6: CD30-Redirected Chimeric Antigen Receptor T Cells Target CD30+ and CD30- Embryonal Carcinoma via Antigen-dependent and Fas/FasL Interactions.	200
ENDNOTES	201
REFERENCES.....	204

LIST OF FIGURES

Figure 1.1: Summary of tumor-specific antigen production in the tumor cell.....	10
Figure 1.2: Summary of tumor-specific antigens	17
Figure 1.3: Average tumor specific antigen counts by cancer type.	21
Figure 1.4: Number of unique tumor specific antigens by cancer type.....	22
Figure 2.1: Inactivation of Pten and Trp53 in Upk3a-expressing cells results in high-grade muscle-invasive bladder tumors.....	39
Figure 2.2: Representative histology of UPPL tumors.....	41
Figure 2.3: BBN and UPPL tumors recapitulate the human basal and luminal molecular subtypes of bladder cancer.	43
Figure 2.4: Immune characterization of UPPL1541 and BBN963 subtype-specific bladder models.	48
Figure 2.5: Anti–PD-1 treatment of BBN963 and UPPL1541 cell line–derived tumors.	52
Figure 2.6: Description and immune characterization of BBN963 mixed-response phenotype.	54
Figure 2.7: Neoantigen prediction and validation in BBN963, UPPL1541, and MB49.....	57
Figure 2.8. Scatter dot plots from the ex-vivo biodistribution study of 89Zr-DFO-anti-CD3, 89Zr-DFO-IgG2b, and 89Zr-DFO-IgG in untreated C57BL/6J mice.....	68
Figure 2.9. Micro-PET/CT images of 89Zr-DFO-anti-CD3 in C57BL/6J mice 72h post-injection (coronal view).	70
Figure 2.10: Scatter plots from the ex-vivo biodistribution study of 89Zr-DFO-anti-CD3 in C57BL/6J mice bearing BBN975 tumors.....	72
Figure 2.11: Effects of DFO-anti-CD3 and unconjugated anti-CD3 treatment on total lymphocyte numbers and viability in the spleen of C57BL/6J mice.....	74
Figure 2.12: Representative gating (left) and immunological effects (right) of DFO-anti-CD3 on CD8+ T-cell phenotype distribution.	75

Figure 2.13: Representative gating (left) and immunological effects (right) of DFO-anti-CD3 on CD4 ⁺ T-cell phenotype distribution.	78
Figure 3.1: Human endogenous retrovirus expression and association in TCGA pan-cancer dataset.	92
Figure 3.2: Mechanism of hERV-mediated RIG-I-like pathway signaling in ccRCC.	97
Figure 3.3: hERVs associated with expression of BCR clonotypes are negatively prognostic in ccRCC.	100
Figure 3.4: Immune-related hERV signatures are prognostic for patient overall survival.	103
Figure 3.5: hERVs demonstrate evidence of targetable epitope expression in ccRCC.	106
Figure 3.6: hERV 4700 epitope-derived HLA-A*02:01 tetramers identify the presence of gag- and pol-specific T cells in ccRCC.	110
Figure 4.1: Summary of tumor antigen prediction and identification of peptide-intrinsic features.	129
Figure 4.2: Linear regression analysis between peptide-intrinsic features and tumor antigen immunogenicity.	131
Figure 4.3: Performance and validation of gradient boosting model approach for predicting neoantigen/mHA immunogenicity.	136
Figure 4.4: Luciferase imaging of luc-P815 tumor burden in DBA/2 recipients.	139
Figure 4.5: Correlative analysis of predicted neoantigen immunogenicity in TCGA human dataset.	141
Figure 4.6: IFN- γ ELISpot in a co-culture assay of neoantigen-experiences T cells and B16F10 tumor cell.	147
Figure 4.7: Tumor growth curves for B16F10 bearing mice treated with neoantigen delivering nanoparticles or free neoantigenic peptide.	149
Figure 4.8: Experimental timeline for ndNP treatment study.	149
Figure 4.9: Heatmap of Luminex cytokine z-scores measured in day 10 plasma levels from animals in Fig. 2 treatment study.	150

LIST OF TABLES

Table 1.1: Advantages and disadvantages of targeting tumor specific antigen classes, and relevant cancers.	11
Table 1.2: Tools for prediction of non-classical tumor-specific antigens.....	16
Table 2.1. Results from the ex-vivo biodistribution of 89Zr-DFO-anti-CD3, 89Zr-DFO-IgG2b, and 89Zr-DFO-IgG in C57BL/6J mice (n = 6 per group).	69
Table 2.2. Results from the ex-vivo biodistribution studies of 89Zr-DFO-anti-CD3 and 89Zr-DFO-IgG2b in C57BL/6J mice bearing BBN975 tumors (n = 6 per group).	73
Table 2.3. Effects of DFO-anti-CD3 and unconjugated anti-CD3 treatment on frequency of total, naïve, memory, central memory, and effector memory CD8+ T-cells in the spleen of C57BL/6J mice are shown.	76
Table 2.4. Effects of DFO-anti-CD3 and unconjugated anti-CD3 treatment on frequency of total, naïve, memory, central memory, and effector memory CD4+ T-cells in the spleen of C57BL/6J mice.	79
Table 4.1: Characterization of neoantigen-delivering nanoparticle formulations and controls.	148

CHAPTER 1: General introduction to tumor immunology

1.1 Introduction to the immune system

The immune system is the body's host defense composed of barrier structures (e.g. skin, mucosal barrier), cells (leukocytes), and soluble factors (e.g. cytokines, chemokines, complement proteins, immunoglobulins) which work in a concerted effort to recognize and respond to foreign entities. Classically, immunity is divided into the innate and adaptive arms of the immune system. The former is an evolutionarily older defense system whose major functions include recruitment of immune cells through release of cytokines and chemokines, activation of the complement cascade, removal of foreign targets or debris through phagocytosis, and activation of the adaptive immune system through antigen presentation. While an innate immune response can react rapidly against a broad set of targets, there is low target specificity with little evidence currently of immunological memory. In contrast, the adaptive immune system is composed of T and B lymphocytes (including B-cell generated antibodies) that develop in response to specific immunological antigens. Development of a primary adaptive immune response takes 7-10 days in humans and mice, with formation of immunological memory allowing for a faster and more robust secondary response against the same antigen (i.e. immunological memory). Adaptive immunity targets include antigens derived from pathogens (e.g. viruses and bacteria) and tumor-derived antigens. The last of these listed targets underscores the capacity for adaptive

immunity to promote anti-cancer immunological responses, which has laid the foundation for development of cancer immunotherapies within the past century.

1.2 The tumor immune microenvironment

The interaction between cancer and the immune system is dictated by the ability of the immune system to recognize non-self-antigens that arise during tumorigenesis. Recognition of tumor antigens and inflammatory signals can promote infiltration of immune cells, including sentinel antigen presenting cells (APC; e.g. dendritic cells [DC], macrophages/monocytes), neutrophils, natural killer [NK] cells, and T/B lymphocytes). In addition to infiltration, anti-tumor immune responses also necessitate an inflamed state, allowing for lymphocytes to carry out effector function. This combination of infiltration and inflammation has led to classification of tumors into several states: 1) Infiltrated-excluded “cold” tumors (characterized by exclusion of lymphocytes from the tumor core), 2) Infiltrated-inflamed “hot” tumors (characterized by infiltration of the tumor core by lymphocytes, with high expression of programmed cell death protein 1 [PD-1] and its corresponding ligands [PD-L1/PD-L2]), and 3) infiltrated tumors with inclusion of tertiary lymphoid structures (characterized by formation of lymphoid structures within the tumor secondary to enhanced inflammation, often associated with positive prognosis)¹.

T cells are widely recognized as the most important immune cell population for performing anti-tumor immunity, including direct anti-tumor cytotoxicity in the case of CD8⁺ T cells and generation of pro-inflammatory cytokines and chemokines in the case of CD4⁺ T cells. The T-cell receptor (TCR) is typically comprised of variable alpha and beta chains (with gamma and delta chains expressed on a minority of alternative T cells). Each beta chain undergoes somatic V(D)J recombination in the thymus to form a

unique variable region (comprised of a recombinant V [variable], D [diversity], and J [joining] region), while alpha chains undergo VJ recombination without an intervening D region. Pairing of recombined alpha and beta chains allows for specificity of binding to a particular antigen bound to a major histocompatibility complex (MHC) complex. Subsequently to formation of the TCR, thymic deletion occurs to TCRs incapable of binding to any antigen/MHC (positive selection) as well as those which bind too strongly to self-antigens (negative selection). T cell recognition of tumor antigens occurs through TCR engagement with tumor-specific antigenic peptides presented on MHC, either on the surface of antigen presenting cells during T cell activation or directly on the tumor cell during T cell effector function. CD8⁺ T cells bind to class I MHC, while CD4⁺ bind to class II MHC, with CD8 and CD4 acting as TCR co-receptors that enhance binding affinity of the TCR to the MHC.

Activation of T cells requires three distinct signals. Signal 1 is the binding of the TCR to an antigen/MHC complex, which begins intracellular signaling cascades to promote T cell activation through key transcriptional pathways (MAPK, NF- κ B, NFAT). However, proper activation of these pathways additionally requires Signal 2, which is signaling through a T cell co-stimulatory molecule. The best characterized of these co-stimulatory molecules is CD28, which interacts with CD80 and CD86 on the surface of antigen presenting cells, resulting in completion of the intracellular signals necessary for proliferation, differentiation, and survival of the T cell. Activation of the TCR without concurrent co-stimulation may result in T cell anergy, deletion, or immune tolerance. Lastly, Signal 3 occurs through T cell recognition of pro-inflammatory cytokines (e.g.

type I interferon [IFN], IL-12 for activation of CD8⁺ T cells), which are necessary for continued survival, proliferation, and memory-formation of Signal 1/2 activated T cells.

Subsequently to activation, T cells upregulate checkpoint molecules which can act as a “break” to downregulate effector function. The expression of the checkpoint molecules on tumor infiltrating T lymphocytes is a major indicator for inflammatory status. Perhaps the best characterized and biologically important of these markers is PD-1, a surface receptor expressed on multiple immune populations whose function is most clearly elucidated in T cells, where upregulation occurs secondary to T-cell receptor (TCR) signaling. Subsequent binding of PD-1 to its ligands PD-L1 and PD-L2 results in downregulation of T cell effector function. This occurs through the PD-1 intracellular immunoreceptor tyrosine-based inhibitory motif (ITIM), which recruits binding of SHP-2 to suppress TCR signaling through the ZAP-70 domain. Within the tumor microenvironment, where PD-L1/L2 are frequently expressed by both tumor and immune cells, PD-1 expression on T lymphocytes is associated with an exhausted immune phenotype, whereby memory and effector T cells which have recognized tumor antigens have decreased functions characterized by decreased proliferation, decreased inflammatory cytokine and IL-2 production, increased apoptosis, and upregulation of other exhaustion markers such as LAG-3, CD244, and CD160². As such, therapeutic antibodies that act to prevent PD-1/PD-L1 interactions have become an essential aspect of cancer immunotherapy.

1.3 Development of immunotherapies for cancer treatment

In addition to PD-1, cytotoxic T-lymphocyte-associated protein 4 (CTLA-4) is another key checkpoint protein of T cell function. Unlike PD-1, CTLA-4 is an early

“break” for T cell function, competing against the binding of T cell protein CD28 (a co-stimulatory receptor for T cell activation) to its ligands CD80/86 (expressed on activated APCs). As such, CTLA-4 is not frequently used as a marker for T cell exhaustion but can be similarly targeted as PD-1 to prevent immune checkpoint regulation. PD-1 and CTLA-4 were first characterized in the early 1990’s, primarily by Drs. James Allison and Tasuku Honjo, respectively. Since initial studies demonstrating the effects of these two checkpoint molecules, therapeutics aimed to block their pathways (known as checkpoint inhibitor therapies) have been developed for cancer immunotherapies. Currently, anti-PD-1 (aPD-1) and/or anti-PD-L1 therapies are standard of care for a wide variety of cancer types, including melanoma, urothelial cancer, non-small cell lung cancer, renal cell carcinoma, Hodgkin lymphoma, gastric cancer, colorectal cancer, hepatocellular carcinoma, Merkel cell carcinoma, and all cancers with high microsatellite instability (MSI)³. aPD-1 therapy has revolutionized our ability to treat these cancers, providing cure with long lasting immunological memory against tumor in a subset of patients that would have otherwise had incurable disease with conventional therapies. Despite these advances, responders to aPD-1 therapy comprise a minority of all treated patients in most tumor types. As such, a key goal in the field of immuno-oncology has been to elucidate factors which associate with checkpoint inhibitor response.

Among the set of features currently known to associate with response to immunotherapies includes tumor molecular subtyping, which (unlike conventional histological subtyping) is defined by genomic characteristics of the tumor. The first description of tumor molecular subtyping was in human breast cancers, grouped into five distinct subtypes: luminal A, luminal B, HER2 enriched, basal-like, and claudin-low⁴.

Subsequently, other cancers have been shown to contain similar molecular subtypes, including bladder cancer, which contains basal and luminal subtypes as the two major classifications⁵⁻⁷. However unlike breast cancer, a limited repertoire of *in vivo* tumor models exist in bladder cancer, with no molecular subtype specific models described until recently. Lack of animal models has encumbered capacity to study the differential effects of immunotherapies in subtype specific bladder cancers, making the development of biologically faithful murine models of bladder cancer a vital goal. In Chapter 2, we will discuss our efforts in the design of molecular subtype-specific models of basal and luminal bladder cancer, with elucidation of tumor response/nonresponse in a basal-like bladder cancer model that demonstrates a mixed response phenotype to aPD-1 therapy (Chapter 2.1). We additionally describe the use of these subtype-specific models in the design of novel immuno-based PET/CT imaging modalities to study *in vivo* T cell infiltration (Chapter 2.2).

1.4 Molecular characterization of the tumor

In an attempt to identify the mechanism behind patient responsiveness/nonresponsiveness to aPD-1 therapy, many investigators have applied next generation sequencing immunogenomic techniques (e.g. DNA/RNA-sequencing) to elucidate the molecular profiles associated with various patient outcomes. Below is a summary of several landmark papers which have applied immunogenomic techniques to examine biomarkers for aPD-1 response:

- Hugo *et al.* 2016⁸: Identification of an innately resistant tumor signature to PD-1 (termed IPRES) in melanoma, comprised of genes involved in the regulation of

mesenchymal transition, cell adhesion, extracellular matrix remodeling, angiogenesis, and wound healing.

- Riaz *et al.* 2017⁹: Study of whole exome, whole transcriptome, and TCR repertoire sequencing in aPD-1 +/- anti-CTLA-4 treated melanoma patients. In responders to therapy, neoantigen load was reduced relative to pre-treatment baseline, with evidence of clonal T cell expansion post-treatment. Responders also demonstrated higher gene levels corresponding to CD8+ T cells and NK cells, with significant decreases in macrophage signatures.
- Auslander *et al.* 2018¹⁰: Study of melanoma and neuroblastoma patient sample derived RNA-seq data to build an immuno-predictive score (IMPRES) based upon pairwise ratios of immune checkpoint related genes. This study outperformed several previous papers, including the Hugo *et al.* IPRES signature.
- Smith *et al.* 2018¹¹ and Panda *et al.* 2018¹²: We have identified that the expression of several specific human endogenous retroviruses in pre-treatment nephrectomy samples from clear cell renal cell carcinoma patients is associated with subsequent responsiveness to aPD-1 therapy. These studies are covered in Chapter 3 and Appendix IV, respectively.

From these above studies, it is clear that the use of immunogenomic techniques to probe the tumor immune microenvironment can provide molecular signatures predictive for patient responsiveness to aPD-1 therapy. Summary of methods for RNA-sequencing characterization of the tumor microenvironment is covered in Appendix I. Common themes among these above studies show that responsiveness to aPD1 therapy necessitates 1) infiltration of effector and pro-inflammatory immune cells

(memory T cells, B cells, M1 polarized macrophages, activated DCs), 2) exclusion of immunosuppressive populations (regulatory T cells [T_{regs}], myeloid derived suppresser cells [MDSC], M2 polarized macrophages), 3) evidence of TCR clonal expansion, and 4) presence and presentation of targetable tumor antigens. This set of features underscores the importance of generating T cell responses against tumor-specific antigens (TSA) in order for patients to generate robust tumor immunity. With evidence that responsiveness to aPD-1 therapy is largely dependent upon T cell activation against TSAs, it has become widely hypothesized that vaccine therapies against TSAs could be an effective strategy to generate or boost existing anti-tumor immunity.

1.5 Classical and non-classical tumor-specific antigens

The role of tumor specific antigens (TSA) as targets of anti-cancer immunity has been well recognized throughout the past century, with studies of TSA-based vaccines becoming more prevalent this past decade^{13–15}. *Neoantigens* are variant peptides derived from proteins encoded by genetic variations present in the tumor but not normal DNA, presented by MHC molecules, and recognized by T cells. The most commonly studied class of neoantigens are those derived from single nucleotide variations (SNV), which cause non-synonymous changes in a protein that subsequently may trigger antigen-specific T-cell responses against the tumor. These conventional neoantigens have the distinct advantage over other classes of tumor antigens (e.g. tumor associated self-antigens and cancer/testis antigens) in having no expression in normal tissues. As a result, T cells with specificity for these neoantigens can escape thymic negative selection, leading to generation of a TSA-specific T-cell repertoire.

Despite advantages of SNV-neoantigens, their applicability as vaccine targets may be limited to cancers with high mutational burden. While metastatic melanoma (which contains the highest SNV burden of any cancer) has been the primary focus of current neoantigen clinical studies, other cancers with lower mutation rates may contain a limited repertoire of potential targets. As such, SNV-neoantigen vaccine development may be hindered in these cancers.

In response, many investigators including our group have begun to evaluate non-classical TSAs – here defined as high-specificity tumor antigens arising from non-SNV genomic sources. Genomic analysis of tumor-antigen burden has demonstrated expression of various classes of TSAs are not always co-correlated, suggesting non-classical TSAs may be targetable in certain cancers despite low SNV-neoantigen burden. This is exemplified by clear cell renal cell carcinoma (ccRCC), a checkpoint inhibitor sensitive cancer which contains a low SNV burden but high expression of frameshift-neoantigens¹⁶ and tumor-specific endogenous retroviral antigens¹¹. Additionally, leukemia and sarcoma (which contain among the lowest SNV burden of any cancers) express shared gene fusion mutations and splice variant transcripts, both of which can produce neoantigens. Among non-classical TSAs include those generated from 1) mutational frameshifts, 2) splice variants, 3) gene fusions, 4) viral antigens, 5) endogenous retroviral antigens, and other less well characterized classes such as HLA-somatic mutation derived antigens, minor histocompatibility mismatch antigens, and retrotransposons (**Figure 1.1, Table 1.1**).

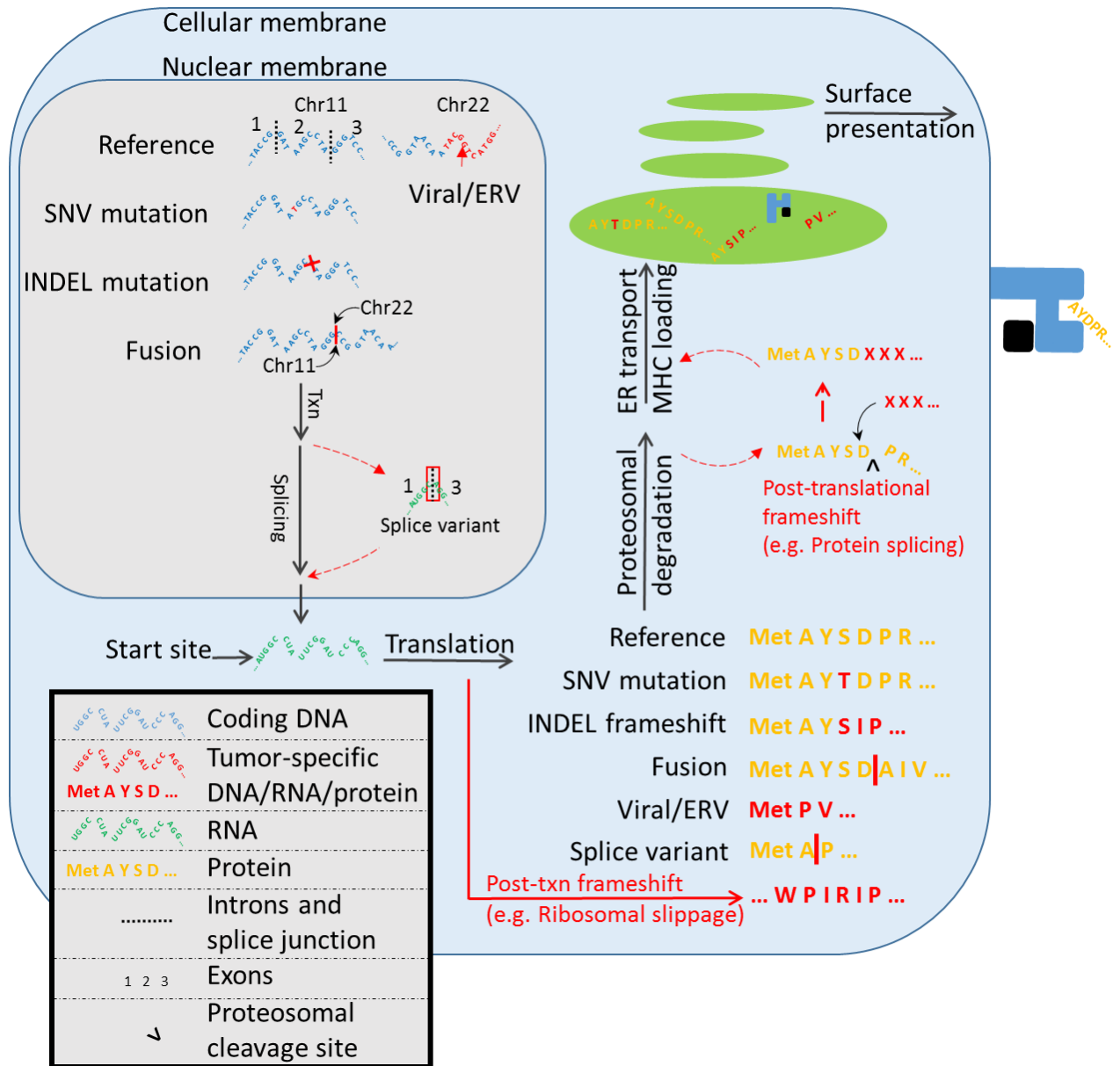


Figure 1.1: Summary of tumor-specific antigen production in the tumor cell.

Antigen class	Advantages	Disadvantages	Relevant Cancers
SNV neoantigens	<ul style="list-style-type: none"> • Well studied • Simple prediction • Relatively high burden 	<ul style="list-style-type: none"> • Similar to self-antigen • Rarely shared between patients 	<ul style="list-style-type: none"> • Melanoma • Lung (adeno and squamous) • Bladder cancer
INDEL frameshift neoantigens	<ul style="list-style-type: none"> • Many targets per mutation • More dissimilar from self-antigen 	<ul style="list-style-type: none"> • Relatively low burden 	<ul style="list-style-type: none"> • Microsatellite instability-high tumors • Clear cell, papillary, and chromophobe renal cell carcinomas
Splice variant neoantigens	<ul style="list-style-type: none"> • High number of predicted targets • More dissimilar from self-antigen 	<ul style="list-style-type: none"> • Fewer tools available • Not well validated <i>in vivo</i> • Current tools do not account for nonsense mediated decay 	<ul style="list-style-type: none"> • Acute myelogenous Leukemia • Chronic myelomonocytic leukemia • Chronic lymphocytic leukemia • Myelodysplastic syndrome
Fusion protein neoantigens	<ul style="list-style-type: none"> • More dissimilar from self-antigen • Shared targets between tumors • More potential targets per mutation 	<ul style="list-style-type: none"> • Relatively low burden 	<ul style="list-style-type: none"> • Acute myelogenous leukemia • Acute lymphoblastic leukemia • Chronic Myelogenous Leukemia • Sarcomas
Viral antigens	<ul style="list-style-type: none"> • Large number of targets per virus • Higher immunogenicity • Shared between patients • Can be 100% tumor specific 	<ul style="list-style-type: none"> • Limited repertoire of cancers with specific expression 	<ul style="list-style-type: none"> • Cervical cancers • Head and neck squamous cell carcinoma • Hepatocellular carcinoma • Gastric adenocarcinoma
Endogenous retroviral antigens	<ul style="list-style-type: none"> • Large number of targets per ERV • Higher immunogenicity • Shared between patients 	<ul style="list-style-type: none"> • Less well studied • Potential for off-target effects • Difficult to validate protein translation 	<ul style="list-style-type: none"> • Clear cell renal cell carcinoma • Low grade glioma • Testicular cancer

Table 1.1: Advantages and disadvantages of targeting tumor specific antigen classes, and relevant cancers.

1.6 Human endogenous retroviral derived cancer antigens

Among the classes of non-classical TSAs listed above, a major focus of the work presented here addresses the role of human endogenous retroviruses (hERVs) in modulation of the tumor immune microenvironment (**Chapter 3**). hERVs are remnants of exogenous retroviruses which incorporated into the genome throughout evolution¹⁷. hERVs impact pathogenesis and progression of cancers, including melanomas, lymphoma, leukemia, ovarian, prostate, urothelial, and renal carcinomas^{18–27}. Expression of tumor-specific/enriched hERVs partly arise through epigenetic dysregulation of the cancer genome, resulting in expression of hERV-containing genomic regions otherwise not observed under physiological conditions^{28,29}. These tumor-specific/enriched hERVs can impact both the innate and adaptive immune system through distinct mechanisms. In the innate immune system, hERVs signal through innate sensors, most commonly the RIG-I-like pathway recognition of viral double stranded RNAs^{28,29}. This results in downstream NF- κ B-mediated inflammation, with release of type I IFN which causes immune activation and increased tumor class I MHC expression. Additionally, hERV-derived protein antigens can induce B- and T-cell activation^{30–32}. As such, it is speculated that tumor-specific hERV antigens could be applied for anti-tumor adoptive cellular therapies and therapeutic vaccines.

hERV-derived therapies are particularly relevant for several cancer types. In addition to INDEL-derived neoantigens, hERVs have been proposed as key driver of anti-tumor immunity in ccRCC^{11,12}. In ccRCC, hERV expression is strongly prognostic and predictive for checkpoint inhibitor therapy response. As such, hERV-derived antigens may be a viable non-classical TSA target in ccRCC. Additionally, recent

evidence suggests a potential role for hERVs in the modulation of low grade glioma (LGG) where SNV burden is among the lowest of any cancer¹¹ and testicular cancer (particularly those with *KIT* mutations) where global DNA hypomethylation is associated with high hERV expression³³.

Several computational methods for hERV quantification currently exist, with the majority providing quantification of hERV-like or retrotransposon-like elements (partial or full-length) rather than full-length, intact hERVs at specific genomic coordinates. The most well-known tool is *RepeatMasker*, designed to identify interspersed repeats and low complexity sequences of any class, including simple and tandem repeats, segmental duplications, and interspersed repeats (including hERV-like elements, long and short interspersed nuclear elements [LINE/SINE], long terminal repeats [LTR], and other classes)³⁴. RepeatMasker used in its default state is not optimal for detection of hERVs. However, nearly all hERV-specific databases (e.g. HERVd³⁵, HESAS³⁶, EnHERV³⁷) have been subsequently generated using RepeatMasker. A more recently quantifier designed by our group aimed specifically for analysis of hERVs from RNA-seq data is *hervQuant*¹¹, which quantifies full-length, intact hERV proviral sequences. The *hervQuant* reference is derived from Vargiu *et al.* which compiled genomic coordinates for 3,173 full-length hERV proviruses³⁸. As these above methods are quantifiers of hERV/hERV-like element expression, they must be paired with downstream epitope prediction software (e.g. NetMHCpan³⁹) for hERV-antigen prediction.

Until recently, the majority of hERV-related studies have examined particular hERVs (e.g. hERV-K HML-2, CT-RCC HERV-E) in the pathology of a particular disease state (e.g. melanoma and ccRCC). A 2015 study from Rooney *et al.* provided an initial

genomic look into the interaction between hERVs and the tumor-immune microenvironment, demonstrating three of 66 hERVs (ERVH-5, ERVH48-1, ERVE-4) identified in a previous study from Mayer *et al.*⁴⁰ to have tumor specific expression and to correlate with expression of a cytotoxicity signature (GZMA and PRF1) in several cancers⁴¹. Based on this study, as well as several other translational studies showing the presence of a hERV-specific T-cell response in ccRCC^{31,42}, we (Smith *et al.*¹¹) and Panda *et al.*¹² performed comprehensive analyses into the role of hERVs in ccRCC. hervQuant analysis of TCGA pan-cancer dataset provided broad correlative descriptions for the role of hERVs upon patient outcome and immune features, demonstrating hERV expression to most strongly associate with patient clinical outcomes in ccRCC and LGG¹¹. Both studies demonstrated the association between hERV expression in pre-treatment ccRCC nephrectomy samples with subsequent response to anti-PD-1 checkpoint blockade therapy, providing evidence for hERVs as a biomarker for immunotherapy response and potentially as a direct immunological tumor-specific target.

With substantial evidence in favor of a hERV-directed tumor-specific immune response, several studies have described the translational application of tumor-specific hERV targets. A 2016 study from Cherkasova *et al.* identified a CD8⁺ T cell (CTL) clone from a patient with regressing ccRCC and found the clone to have tumor-specific cytotoxicity against tumor cells *in vitro*³¹. The CTL recognized an antigen from a specific hERV CT-RCC HERV-E – which coincidentally was the same as one of the tumor-specific hERVs (ERVE-4) described by Rooney *et al.* and was also identified during our screen of differentially expressed hERVs in ccRCC (hERV 2256). This

particular CTL clone is being studied in clinical trials for adoptive T-cell therapy in metastatic ccRCC (NCT03354390). Our analysis additionally identified a second hERV (hERV 4700) with preferential expression in ccRCC compared to normal tissues, evidence of translation, and presence of tumor infiltrating CTLs specific for *gag* and *pol* derived antigens of the virus¹¹. Notably, this provided the first description of a broad genomic screening method for tumor-specific hERV antigens.

1.7 Computational prediction of tumor-specific antigens

Recent advancements in DNA and RNA sequencing have allowed for development of genomic and computational methods of TSA prediction (**Table 1.2**). Methods for generating TSA therapies generally rely on a conserved set of steps: 1) Variant calling, 2) HLA-typing, 3) peptide enumeration, 4) HLA binding prediction, and 5) therapy generation (**Figure 1.2**). Variant calling is the identification of genomic regions with high tumor specificity. In the case of SNV, INDEL, and gene fusions neoantigens, variants are derived from mutations within the tumor exome. Alternatively, viral and endogenous retroviral (ERV) antigens are derived from RNA expression data, selected for viruses/ERVs with higher expression in the tumor compared to matched normal tissues. Splice variant neoantigens can be identified through a variety of techniques, discussed later in detail. Subsequently, tumor HLA type is derived using an HLA caller (e.g. POLYSOLVER⁴³, OptiType⁴⁴, PHLAT⁴⁵, HLAScan⁴⁶, HLAProfiler⁴⁷), which relies on DNA and/or RNA sequencing data, depending upon the software. Peptide enumeration is then performed, whereby variant genomic regions are translated into peptide sequences, with translation-incompatible sequences removed (e.g. nonsense mutations, low RNA coverage). HLA binding prediction is next performed using

prediction software (e.g. NetMHCpan³⁹), with binding typically accepted in the literature as ≤ 500 nM^{15,48,49}. Lastly, predicted TSAs are used to generate a therapeutic product, either as a vaccine (i.e. DNA/RNA, peptide, or dendritic cell vaccine) or a cellular therapy product (i.e. adoptive T cell therapy). Below, we will discuss the relevant biology for each non-classical TSA class, with detailed descriptions of available tools.

	SNV	INDEL	Splice variant	Fusion	Viral	hERV
INTEGRATE-neo				Only calls MHC I		
pVACtools	pVAC-Seq: missense SNV	pVAC-Seq		pVACfuse: Works downstream of INTEGRATE-neo calls		
Neopepsee	Missense; MHC I only	MHC I only				
MuPeXI	Missense	Yes				
TSNAD	Missense/nonsense	Yes				
NeoantigenR			MHC I only			
NeoepitopePred	Missense; MHC I only			MHC I only		
Epidisco	Missense/nonsense; MHC I only	Yes; MHC I only	Yes; Only RNA-seq based; MHC I only			
Antigen.garnish	Missense	Yes				
Neoepiscope	Missense/nonsense	Yes				
Virdetect					Quantifier only	
PathSeq					Quantifier only	
BioBloom Tools					Quantifier only	
RepeatMasker						Quantifier only; not hERV specific
hervQuant						Quantifier only

Table 1.2: Tools for prediction of non-classical tumor-specific antigens.

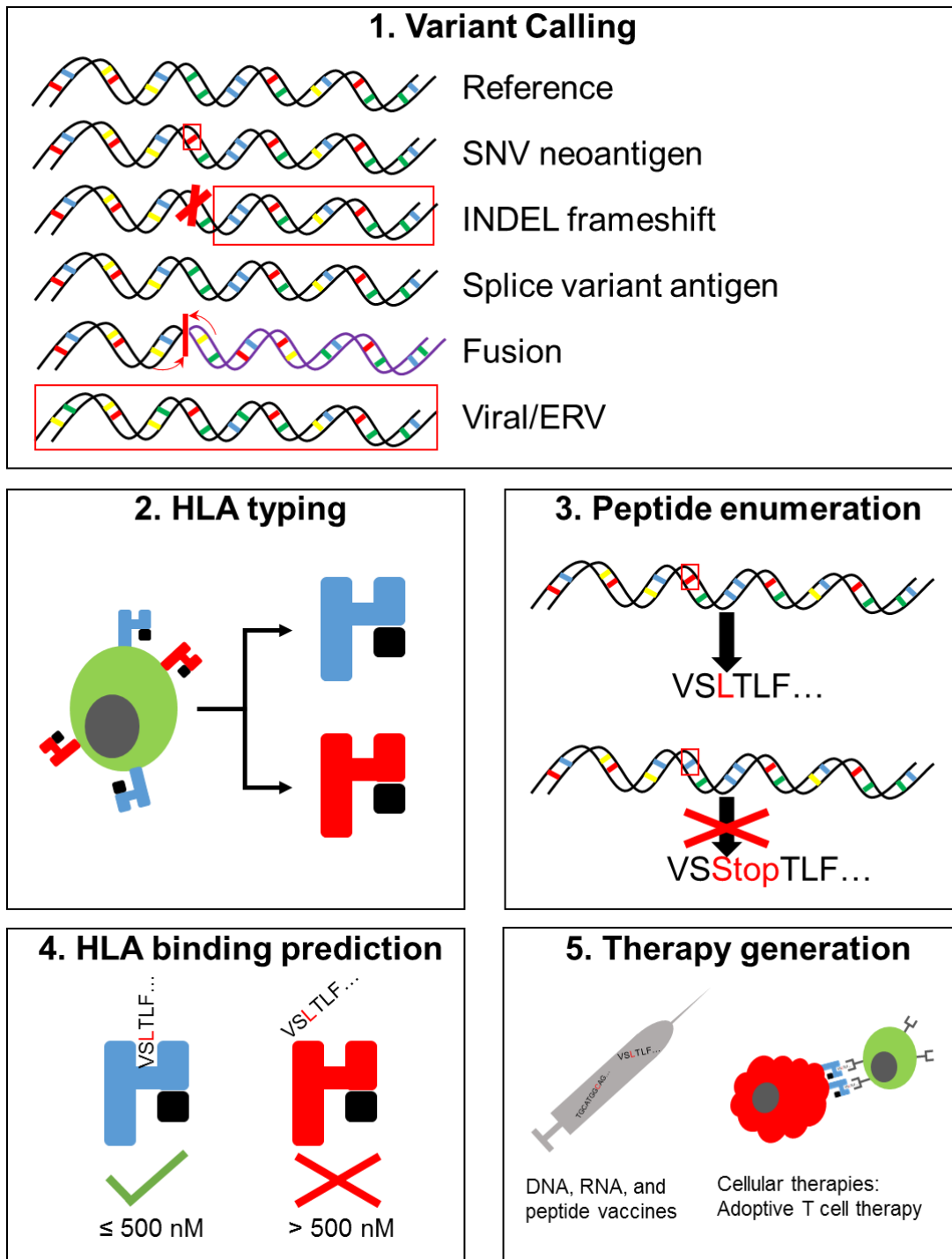


Figure 1.2: Summary of tumor-specific antigens

1.8 Clinical translation of non-classical tumor-specific antigens

Recent studies (including several from our group) have provided estimates for antigenic burden of each TSA class among TCGA pan-cancer data, which we have compiled here (**Figure 1.3, 1.4**)^{11,50–53}.

In addition to the clinical applicability of hERVs in ccRCC and LGG, testicular cancer (TGCT) contained substantially greater burden of hERV-derived TSAs than any other cancer type. This is in agreement with previous findings that TGCT was among the cancer types with the greatest hERV expression due to widespread hypomethylation^{11,33}.

Viral antigen burden was highest in cervical (CESC; HPV) and hepatocellular (LIHC; HBV) cancers, but also observed in subsets of head/neck squamous cell (HNSC; HPV) and stomach adenocarcinoma (STAD; EBV) tumors. Associated with these findings, therapeutic cancer vaccines are currently in development for HPV-driven cervical cancer (VGX-3100⁵⁴), as well as EBV-driven nasopharyngeal cancers and NK/T-cell lymphomas (MVA-EL⁵⁵ and CMD-003⁵⁶). Currently, no HBV therapeutic vaccines have demonstrated convincing therapeutic efficacy.

INDEL- and SNV-neoantigen counts derived from a recent TCGA pan-cancer analysis demonstrated significant co-correlation among all cancer types (coefficient: 0.81, $p < 0.0001$)⁵⁰. In agreement with Turajilic *et al.*, notable outliers were clear cell and papillary RCC, where the INDEL-to-SNV ratio was significantly higher than other cancer types (KIRC: 0.85 and KIRP: 0.90; all others: 0.43 – 0.72). In addition, colon adenocarcinoma (COAD) demonstrated a distinct population of INDEL-high tumors, corresponding to those cancers with high microsatellite instability (MSI-H). MSI-H is

characterized by impaired DNA mismatch repair pathways, contain significantly greater INDEL burden compared to non-MSI-H tumors^{57,58}. These data suggest that in RCC, MSI-H tumors, and cancer types known to have high SNV-burden, INDEL-derived neoantigens should also be considered for vaccine selection.

Mean burden of fusion-derived neoantigens per sample was highest in sarcomas (SARC: 1.1, UCS: 0.78), with carcinoma fusion burden highest in breast and prostate cancer (BRCA: 0.70, PRAD: 0.58). SARC, BRCA, and PRAD all fall within the lower half of SNV-neoantigen number among all cancer types, making fusion-derived neoantigens another potential avenue for vaccine development. While gene fusion data was not available for acute myeloid leukemia (LAML), gene fusion neoantigens have been a focus of study in leukemia (particularly AML, acute lymphocytic leukemia [ALL], and chronic myelogenous leukemia [CML]⁵⁹).

Splice variant neoantigens demonstrated similar burden to INDEL-neoantigens, with significant co-correlation with INDEL- and SNV-neoantigen burden. A notably outlier is thyroid cancer (THCA), where average number of splice variant neoantigens per sample is higher than SNV-neoantigens. Mutations in spliceosome proteins (e.g. SF3B1, SRSF2, U2AF1/2) are common in myelodysplastic syndrome, acute myelogenous leukemia (AML), chronic myelomonocytic leukemia (CMML), and chronic lymphocytic leukemia (CLL)^{60–64}, resulting in the hypothesis that spliceosome mutations may cause expression of splice variant mRNA, leading to translation of neoantigens^{65–67}. As splice variant neoantigens have greater potential for dissimilarity from reference compared to SNV-neoantigens, this TSA class should be pursued for vaccine development.

Conventional SNV-neoantigens remain the most well studied class of TSA, with distinct advantages of ease of prediction, prevalence in a wide cohort of patients, and promising pre-clinical therapeutic evidence. While SNV-neoantigens will continue to be a driving force for therapeutic vaccine development in the coming years, many groups have broadened the search for other non-classical TSAs derived from self and non-self-antigens. While certain non-classical TSAs have been studied for decades (e.g. fusion proteins), the advent of powerful computational methods for patient-specific prediction of TSAs has expanded the breadth of targets available for clinical application. Unlike SNV-neoantigens, which are largely patient specific in expression, many non-classical TSAs are shared among the population (e.g. viral, hERV, gene fusions), making them ideal for off-the-shelf therapies. Additionally, many of these peptide sequences are entirely dissimilar from germline (e.g. frameshifts, viral, hERV), allowing for potentially greater immunogenicity than SNV-neoantigens. Thus, non-classical TSAs should play a major role in the future of cancer immunotherapy.

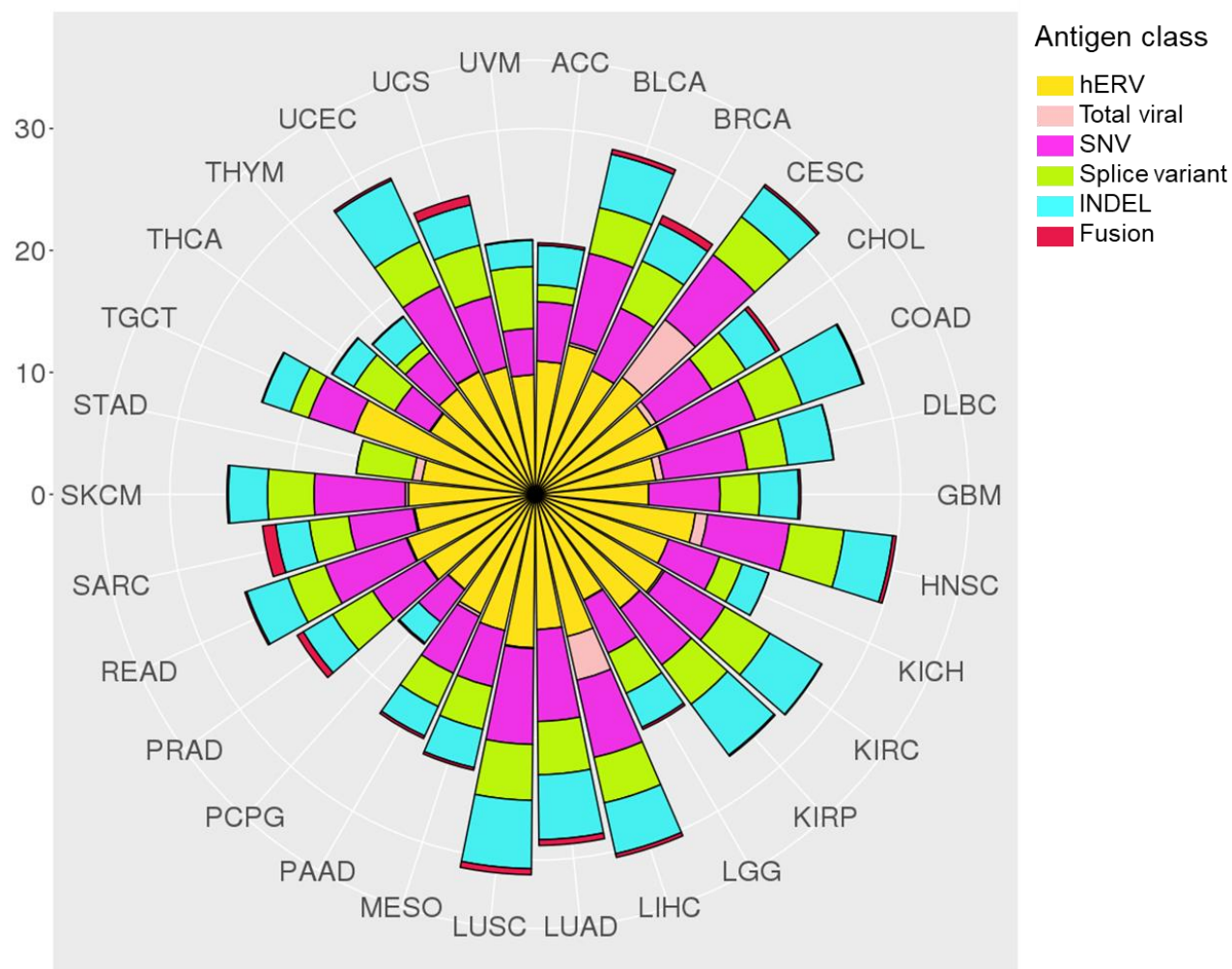


Figure 1.3: Average tumor specific antigen counts by cancer type. Plots represent number of unique identified epitopes by TCGA cancer type. SNV and INDEL epitopes are derived from Thorsson et al. (Immunity, 2018). Fusion epitopes are derived from Gao et al. (Cell Reports, 2018). Splice variant epitopes are derived from Jayasinghe et al. (Cell Reports, 2018). Viral epitopes are derived from Selitsky et al. (mSystems, 2018). hERV epitopes are derived from Smith et al. (JCI, 2018). All TSA classes represent the average number of predicted class I HLA binders (8-11mers, <500 nM) predicted from NetMHCPan. STAD INDEL and SNV calls were absent from Thorsson et al. ESCA, LAML, and OV were omitted from all reports.

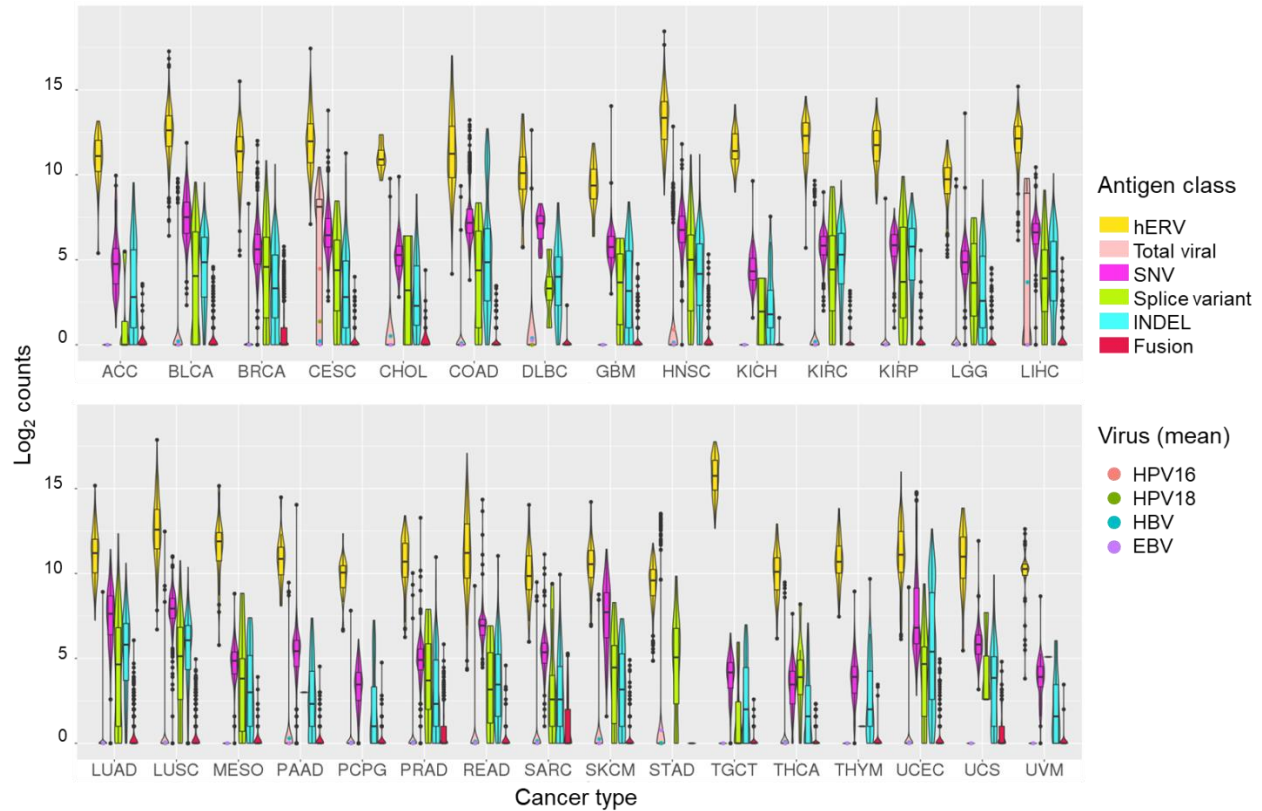


Figure 1.4: Number of unique tumor specific antigens by cancer type. Plots represent number of unique identified epitopes by TCGA cancer type. SNV and INDEL epitopes are derived from Thorsson et al. (Immunity, 2018). Fusion epitopes are derived from Gao et al. (Cell Reports, 2018). Splice variant epitopes are derived from Jayasinghe et al. (Cell Reports, 2018). Viral epitopes are derived from Selitsky et al. (mSystems, 2018). hERV epitopes are derived from Smith et al. (JCI, 2018). All TSA classes represent number of predicted class I HLA binders (8-11mers, <500 nM) predicted from NetMHCPan. STAD INDEL and SNV calls were absent from Thorsson et al. ESCA, LAML, and OV were omitted from all reports.

1.9 Therapeutic platforms for tumor antigen vaccination

The efficacy of a therapeutic vaccine is greatly affected by the delivery vehicle. The most common vaccine strategy is combination of free-peptide with an immune adjuvant, delivered as a subcutaneous/intradermal injection. However, free-peptide vaccines with adjuvant have limited efficacy, due to inadequate immune stimulation and rapid degradation of the peptide by peptidases in the body⁶⁸. To address these

concerns, nanoparticle-based vaccine platforms have been proposed as an alternative vehicle strategy for tumor antigen vaccines.

Nanotherapeutics encompasses a class of delivery vehicles, including nanoparticles, liposomes, dendrimers, and nano-discs. While nanotherapeutic delivery vehicles have been widely studied for vaccine platforms throughout the last several decades, neoantigen-based nano-vaccine platforms have arisen within the last several years^{68,69}. The first description of a nanotherapeutic neoantigen vaccination platform was from Kreiter *et al.*, where mRNAs encoding for neoantigen epitope sequences were encompassed within a liposomal delivery system to generate tumor-specific T cell responses in several murine tumor models⁷⁰. Built off of a previous report from Castle *et al.*⁷¹, the research group led by Ugur Sahin and Ozlem Tureci demonstrated the efficacy of these neoantigen epitope encoding mRNAs to be derived from simultaneous activation of intra-cytoplasmic TLR7 (providing a DC activation and maturation signal) and mRNA translation within sentinel dendritic cells (DCs), which subsequently present these neoantigen epitopes alongside co-stimulatory receptor signaling ligands to activation neoantigen-specific T cells (primarily CD4 T cells) that induced anti-tumor response^{14,72}.

Since this initial description, several other groups have provided peptide-based nanotherapeutic approaches for tumor therapeutic vaccination. Relying upon previously published neoantigen sequences, Kuai *et al.* designed a high density lipoprotein based nanodisc platform loaded with neoantigen peptides, importantly capable of cross-presentation to induce a CD8 T cell response to a higher degree than demonstrated by Kreiter *et al.*^{73,74}. Additionally, a paper from Min *et al.* demonstrated the ability to

generate poly(lactic-co-glycolic acid (PLGA)-based antigen-capturing nanoparticles to improve the abscopal effect after B16F10 tumor irradiation⁷⁵. Among the antigens captured by the particles included several that were derived from proteins which contained neoantigenic epitopes, suggesting neoantigenic priming may be a potential mechanism behind the efficacy of this platform. Following these approaches, our work presented in Chapter 4.2 focuses on the design of a PLGA-based neoantigen peptide delivery platform.

1.10 Concluding remarks and contributions of this work

The studies presented in this document provide a multidisciplinary approach to address key understudied aspects of immuno-oncology, including aims to better understand the mechanism of currently immunotherapies, and to discover and develop the next generation of immunotherapeutics to further advance our ability to cure cancers. The work presented here was made possible through many collaborative efforts. Additionally, Dr. Benjamin Vincent provided co-mentorship for all projects described in this dissertation. Chapter 2.1 was performed in collaboration with the lab of William Kim. Chapter 2.2 was performed in collaboration with the lab of Matthew Parrott. Chapter 3 was performed in collaboration with the lab of W. Kymrin Rathmell and Sara Selitsky of the Lineberger Bioinformatics Group. Chapter 4.2 was performed in collaboration with the lab of Andrew Wang.

Appendices to this dissertation include a summary of RNA-seq methods (Appendix I), molecular characterization of human ccRCC (Appendix II) and gastric (Appendix III) cancers, complimentary analyses of hERVs in ccRCC (Appendix IV), design of nanoparticle strategies for immunotherapy delivery (Appendix V), and study of CD30-directed chimeric antigen receptor (CAR) cellular therapies (Appendix VI). My role all projects presented in this dissertation are provided in the Endnotes chapter.

CHAPTER 2: Design and study of subtype-specific murine tumor models

2.1 Development of subtype specific mouse models of bladder cancer.

2.1.1 Introduction

In the United States, bladder cancer is the fifth most common malignancy with approximately 79,000 new cases and nearly 17,000 deaths expected in 2017⁷⁶. Bladder cancer is comprised of both low-grade and high-grade tumors. Although low-grade tumors are almost uniformly noninvasive (Ta), high-grade tumors can become muscle-invasive and metastatic.

Multiple studies have now identified distinct RNA expression subtypes within both low- and high-grade bladder cancer^{5-7,77-82}. Building upon the work of Hoglund and colleagues⁷⁷, we along with others have recently described distinct subtypes of high-grade muscle-invasive urothelial carcinoma, which we have termed luminal-like and basal-like, that have gene expression patterns that appear to be consistent with differentiation states of normal urothelium and reflect gene expression patterns and biology between breast and bladder cancer^{5-7,83}.

Cisplatin-based chemotherapy has been the only FDA-approved therapy to treat advanced bladder cancer for over two decades until the recent approval of immune checkpoint antibodies targeting the PD-1/PD-L1 axis. PD-1 axis blockade induces a response in approximately 20% to 30% of patients with advanced urothelial carcinoma, with the premise that activation of immune checkpoint pathways result in active

immunosuppression^{84–89}. Response to PD-1 axis inhibition in urothelial bladder cancer has been associated with a number of intrinsic tumor features such as tumor mutational burden and tumor molecular subtype, as well as tumor microenvironment features such as the presence of PD-L1–expressing tumor-infiltrating immune cells, CD8+ cytotoxic T cells in the tumor, and expression of effector T-cell genes by gene expression profiling⁸⁵.

Multiple immunocompetent mouse models of bladder cancer currently exist including the carcinogen-induced models: MB49 (DMBA-derived cell line) and BBN [N-butyl-N-(4-hydroxybutyl)nitrosamine]^{90,91} as well as numerous autochthonous, genetically engineered murine (GEM) models⁹², some of which progress to muscle-invasive bladder cancer and metastasis^{93–96}.

We report here the generation of a novel GEM model of high-grade, muscle-invasive bladder cancer that faithfully recapitulates the luminal molecular subtype of bladder cancer: Upk3a-CreERT2; Trp53L/L; PtenL/L; Rosa26LSL-Luc (UPPL) mice. This model is characterized by papillary histology and decreased levels of immune infiltration relative to basal tumors derived from BBN-treated animals, a pattern that is similar to human disease^{7,77,83}. We have generated cell line adoptive transfer models for luminal-like UPPL tumors as well as for basal tumors derived from BBN-treated animals. Cell line–derived tumors from the UPPL model maintain luminal-like characteristics, such as high expression of Pparg and Gata3 gene signatures. Moreover, gene expression profiles from BBN and UPPL models more closely map to human bladder cancer and to normal murine urothelial cells than the commonly used MB49 model, which appears to more closely resemble fibroblasts. As models of bladder cancer

biology in immunocompetent mice, these models can be used to interrogate subtype-specific responses to immune checkpoint inhibition and other immunotherapy strategies in vivo.

2.1.2 Materials and Methods

Mouse models and establishment of mouse bladder cancer cell lines

All animal studies were reviewed and approved by The University of North Carolina at Chapel Hill Institutional Animal Care and Use Committee. For the BBN carcinogen-induced mouse bladder cancer model, C57BL/6 mice (Charles River Laboratories) were continuously exposed to 0.05% N-butyl-N-(4-hydroxybutyl) nitrosamine (BBN) in drinking water. Trp53 and Pten conditional knockout mice were obtained from The Jackson Laboratory (STOCK: 008462) and Terry Van Dyke (National Cancer Institute, Bethesda, MD; ref. 25)⁹⁷, respectively, and crossed with Upk3a-CreERT2 allele (The Jackson Laboratory STOCK: 015855) and the Rosa26LSL-Luciferase allele (The Jackson Laboratory, STOCK: 005125; UPPL model) or crossed with Krt5-CreERT2 allele (a gift from Brigid Hogan, Duke University, Durham, NC) and Rosa26LSL-tdTomato (The Jackson Laboratory, STOCK: 007914; KPPT model). In order to induce Cre recombination in the bladder of UPPL or KPPT mice, 5 mg of tamoxifen was given orally by gavage in both the UPPL and KPPT model. In the KPPT model, transurethral injection of 4-hydroxy-tamoxifen was also performed. Tumor development was regularly monitored by bladder ultrasonography.

Mice were sacrificed for the humane endpoints as follows. For the autochthonous mouse models, mice were sacrificed for weight loss more than 10% of the initial weight

or tumor size diameter of >7 mm as evaluated by bladder ultrasound. In our studies, all mice were sacrificed because of tumor size. The endpoint for allograft models was tumor volume >500 mm³, skin ulcer formation, or weight loss greater than 20% body weight.

Generation of UPPL1541 and BBN963 cell lines

Once the bladder tumors became >7 mm in diameter, they were harvested for pathologic evaluation, in vitro analysis, and for establishing cell lines. Tumors were dissociated and digested with collagenase and dispase (Roche). The dissociated tumor cells were resuspended in growth media and plated to a plastic plate as described previously⁹⁸. Cell lines were passaged more than 10 times before use. Mycoplasma testing was performed monthly while cells were in culture.

MB49 cell lines were obtained from Molly Ingersol (Institut Pasteur, Paris, France). Mycoplasma testing was performed monthly while cells were in culture.

RNA/DNA extraction, library prep, and RNA sequencing or whole-exome sequencing

RNA was extracted from the primary tumors and the established cell lines using an RNeasy Kit (QIAGEN), and DNA was extracted from primary tumors, established cell lines, and tail clippings using a DNeasy Kit (Qiagen). Whole-exome and transcriptome library preparation was performed using Agilent SureSelect XT All Exon and Illumina TruSeq Stranded mRNA Library Preparation Kits, respectively. Libraries were sequenced via 2 × 100 runs on an Illumina HiSeq 2500 at the UNC High Throughput Sequencing Facility.

RNA sequencing analysis

Sequence reads were aligned to the murine genome (mm9), and gene expression was generated as reads per kilobase of exon model per million mapped reads per gene by using MapSplice and upper quartile normalized via RSEM (University of Kentucky Bioinformatics Labs, Lexington, KY; ref. 27)⁹⁹.

RNA sequencing (RNA-seq) data were normalized for variations in read counts, log2 transformed, and median centered before analysis. When combining datasets, we adjusted for batch effects using the surrogate variable analysis R package (version 3.12.0; R Foundation). Subtype calls were made using the BASE47 classification algorithm based on the median-centered expression of *Mus musculus* homologs of genes found in the classifier⁷. Clustering was done using average linkage clustering with a centered correlation similarity metric. Immune gene signature scores were derived as described previously⁸³.

Gene data were grouped into immune gene signatures, which were murine orthologs of signatures previously identified through unsupervised clustering and gene expression profiling of sorted immune cells^{83,100,101}. Gene data were matched to predefined immune gene signature clusters via Entrez IDs. Each gene signature was calculated as the average value of all genes included in the signature. Differential expression for each gene signature was analyzed between tumor models and treatment groups via ANOVA (one-way ANOVA), adjusted for multiple testing using an FDR of 0.05. To determine the prognostic value of each immune gene signature, linear univariate correlation modeling was used with signature/clinical variable as a continuous

variable compared with tumor size. Heat map of the log10 transformed P value of gene signature correlations was displayed with color gradient calculated via:

$$-(\log_{10}(p - value) - \log_{10}(0.05)) \cdot \text{sign of coefficient}$$

Gata3 and Pparg gene signatures

The PPAR γ gene signature was derived by determining the genes that are significantly upregulated (samr package FDR < 0.05) in UMUC9 cells treated with rosiglitazone, a PPAR γ agonist in the GSE47993 dataset⁸³. The GATA3 gene signature was pulled from the BIOCARTEA curated gene signature set in MSigDB. Gene expression data have been deposited GSE112973.

PvClust

The significance of clustering nodes was determined using the pvclust R package (version 2.0-0, R Foundation; ref. 30)¹⁰². Significance of all nodes was calculated with a correlation distance metric and average linkage clustering.

qPCR normalization for TCR/BCR repertoire profiling

Tumor RNA concentrations were determined using a Qubit RNA BR Assay Kit, 1:200 in dilution buffer. Using a Qiagen Quantitect Reverse Transcription Kit, cDNA was synthesized from 50 ng to 1 μ g starting total RNA. RNA derived from column-purified T/B cells was included as a positive control, and DI H₂O was included as a negative control. The reaction was carried out according to the manufacturer's instructions, using a Veriti thermocycler (Applied Biosystems).

Quantitative PCR was performed in triplicate with 0.5 $\mu\text{mol/L}$ of each forward and reverse primers, 0.1 $\mu\text{mol/L}$ TaqMan probe [T-cell receptor (TCR): FAM reporter with TAMRA quencher; B-cell receptor (BCR): VIC reporter with TAMRA quencher], cDNA (2.5 μL), and Bio-Rad SsoAdvanced Universal Probe Supermix (2 \times) and DI H₂O for a final volume of 10 μL per well. Cycling conditions for TCR and BCR were both set for 45 cycles of recommended TaqMan conditions for the QuantStudio 6 Flex system.

Purified T/B-cell cDNA was used for positive control and calibration curve, and the template-free cDNA synthesis reaction was used for negative control. The calibration curve was determined using C_t values from purified T/B-cell cDNA, 10-fold serially diluted in nuclease-free water ranging from 1:0 (cDNA: H₂O, v/v) to 1:1 $\times 10^{12}$. For both T- and B-cell calibration curves, C_t values were detectable as dilute as 1:1 $\times 10^5$, with a coefficient of determination of >0.99 for the linear fit of $\log_{10}(\text{dilution})$ versus C_t . Each sample's C_t value was read out as the ratio of T- or B-cell cDNA to total cDNA.

5' RACE amplification of TCR/BCR sequences

Based on qPCR results, all tumor samples were normalized by T- or B-cell RNA starting template. Using a Clontech SMARTer RACE 5'/3' Kit, cDNA was generated using the manufacturer's protocol. cDNA was diluted with tricine/EDTA buffer, and 5' RACE was carried out using the manufacturer's protocol with 0.5 $\mu\text{mol/L}$ custom barcoded gene-specific reverse primer, using a Veriti thermocycler (Applied Biosystems Veriti 96-well) with the following cycling conditions:

30 cycles:

- 94°C, 30 seconds

- 68°C, 30 seconds
- 72°C, 3 minutes

5' RACE products were pooled, and clean-up/concentration were performed using a Zymogen Genomic DNA Clean & Concentrator. Pools of samples were eluted in 32 μ L of nuclease-free water heated to 70°C. DNA concentration was measured using a Qubit DNA HS Assay Kit. Purity (A260/280nm and A260/230nm ratios) was determined using a ND-1000 spectrophotometer. Pooled DNA (1–5 μ L) was visualized in a 1.5% agarose gel to confirm the presence of proper band sizes (TCR and BCR: 400–500 bp).

TCR/BCR repertoire profiling

For TCR/BCR repertoire studies, pooled TCR or BCR amplicons were size selected using a Sage Science Pippin Prep 1.5% agarose cassette (HTC1510). Bands were size selected at 450 to 650 bp. After size selection, samples were analyzed using either Agilent 2100 Bioanalyzer or Tapestation to ensure purity. Illumina MiSeq library preparation was performed using a KAPA Biosystems DNA Preparation Kit. Libraries were run at 6 pmol/L on an Illumina MiSeq using a 600-cycle kit (2 \times 300 paired-end), with 15% PhiX spike-in.

Mouse allograft model and treatment by anti-PD-1 antibody

BBN963 and UPPL1541 cell lines were injected subcutaneously in C57BL/6J mice at 1×10^7 and 1×10^6 cells, respectively. Once tumors reached 200 mm³ in tumor volume, treatment either by anti-PD-1 antibody (clone RMP1-14, Millipore) or isotype control IgG (Sigma) by intraperitoneal injection was started. The treatment was

administered once a week at a dose of 10 mg/kg. The tumor size was measured by caliper weekly or twice weekly.

Flow cytometry

For tissue dissociation, tissues were homogenized in cold media using the GentleMACs Dissociator, and the samples were passed through a 70 μ m cell strainer using a 5-mL syringe plunger. The samples were centrifuged for 7 minutes at 290 RCF, 4°C, decanting the supernatant. The remaining pellet was resuspended into 1 mL of ACK lysis buffer (150 mmol/L NH₄Cl, 10 mmol/L, KHCO₃, 0.1 nmol/L Na₂EDTA in DPBS, pH 7.3) for 2 minutes at room temperature before quenching with 10 mL of cold media. The samples were centrifuged for 7 minutes at 290 RCF, 4°C, resuspended in 10 mL of cold media, and passed through a 40 μ m cell strainer. Cell counting was performed by running a diluted aliquot of sample on a MACSQuant flow cytometer, counting lymphocytes as gated by forward scatter area versus side scatter area.

Samples were washed and resuspended in cold DPBS, normalized by count, and transferred onto a 96-well V-bottom plate at 2.5×10^6 lymphocytes per well. Cells were resuspended in FVS700 viability stain (BD, 1:1,000 dilution in 100 μ L DPBS) for 40 minutes on ice. Wells not receiving viability staining were resuspended in DPBS. Cells were washed twice in staining buffer (0.02% NaN₃, 2% BSA in DPBS), resuspended in 50 μ L Fc block (1:50 dilution in staining buffer), and incubated on ice for 15 minutes. Antibody master mix was added to samples at 50 μ L per sample with final antibody concentrations as indicated in Supplementary Table S1 (all mAbs from BD Biosciences). Please see Supplementary Table S1 for list of antibodies.

Cells were incubated on ice in the dark for 45 minutes and washed twice with staining buffer. Cells were fixed in 2% paraformaldehyde overnight. The following morning, a minimum of 100,000 events were collected for each sample on a BD LSRIFortessa flow cytometer. FlowJo flow software Version 10 (Treestar) was used for analyses. Fluorescence Minus One controls were used to guide gating strategies.

Analysis and statistics

All flow cytometry, TCR/BCR sharing, and Shannon entropy statistics were calculated with Mann–Whitney U test.

For TCR/BCR amplicon sequencing analyses, raw .fastq files were demultiplexed by barcode sequences of the gene-specific primers. Sorted R1 and R2 files were respectively merged. Sequencing quality was confirmed through the FastQC quality control tool. TCR and BCR amplicon data were analyzed via IMGT/HighV-QUEST. Data were converted into standard in-lab format, and downstream analysis was performed with custom scripts as well as the tcR R package.

Neoantigen prediction

C57BL/6 mice were given a single subcutaneous flank injection of BBN963, UPPL1541, or MB49 cells. Tumor growth was monitored until tumors reached 100 mm³, at which point mice were humanely sacrificed with CO₂ asphyxiation followed by cervical dislocation. Tumors were dissected for downstream DNA/RNA extraction as described above. Matched normal DNA was extracted from tail-clippings or liver from the mouse in which the cell lines were respectively derived. Library prep and sequencing were performed as described above. Bioinformatics prediction of

neoantigens was performed as described previously⁸³. Predicted neoantigens were filtered on expression in all replicates with >5× read support.

Vaccine/ELISPOT assay for neoantigen immunogenicity

Predicted neoantigen peptides were synthesized by New England Peptide, using custom peptide array technology. C57BL/6 mice were vaccinated with predicted neoantigen peptides, given as a subcutaneous injection of a pool of 8 equimolar peptides (5 nmol total peptide) and 50 µg poly(I:C) in PBS. A second identical injection was repeated 6 to 7 days after primary injection. Mice were humanely sacrificed with CO₂ asphyxiation followed by cervical dislocation 5 to 6 days after second injection. Spleens were harvested and prepared into a red blood cell lysed, single-cell suspension. Splenocytes were plated in triplicate at 5×10^5 cells per 100 µL media onto an IFN-γ capture antibody-coated ELISPOT plate (BD Biosciences) for 48 hours, along with 1 nmol of a single peptide against which the respective mouse was vaccinated. IFN-γ expression was compared with splenocytes incubated with vehicle control.

Neoantigen-enriched T-cell coculture

C57BL/6 mice were vaccinated with either a pool of the top 8 predicted BBN963 neoantigens or irrelevant peptide (SIINFEKL) control, with a second identical booster given 7 days after primary vaccine. One week after secondary vaccination, spleens were harvested and prepared into a red blood cell lysed, single-cell suspension. T cells were isolated using Miltenyi murine Pan T Cell Isolation Kit II. Using previously described methods¹⁰³, T cells were expanded in the presence of bone marrow–derived dendritic cells pulsed with a single peptide against which the derivative mouse was

vaccinated against. Seven days following ex vivo expansion, 1×10^5 T cells were cocultured 10:1 with BBN963 cells onto an IFN- γ capture ELISPOT plate for 72 hours. Controls included T cell only, BBN963 only, and media only negative controls, as well as antigen-enriched T cells cocultured with respective peptide-pulsed UPPL1541 cells as positive control. Signal intensity was read out using an ELISPOT plate reader. T-cell/BBN963 coculture spot counts were subtracted from their respective T-cell only control, and then taken as a percentage of the counts from their respective peptide-pulsed target positive controls.

Supplemental material

All supplemental figures and tables cited in Chapter 2.1 are listed according to the original published manuscript, which can be found at <http://cancerres.aacrjournals.org/content/78/14/3954.figures-only>.

2.1.3 Results

Inactivation of Pten and Trp53 in Uroplakin3a-expressing cells results in muscle-invasive, high-grade urothelial carcinoma

Our previously published studies describing luminal-like and basal-like molecular subtypes of bladder cancer demonstrated that these subtypes reflect the gene expression patterns of the differentiation states of the normal urothelium⁷. Basal-like bladder tumors harbor gene expression patterns most similar to basal and intermediate cell layers of the bladder, whereas luminal tumors harbor gene expression patterns most similar to umbrella cells^{5,7}. To determine whether different cells of origin account for the differential gene expression patterns between basal-like and luminal-like high-

grade, muscle-invasive bladder cancer, we conditionally inactivated Pten and Trp53 in Keratin5 (K5) or Uroplakin3a (Upk3a)-expressing basal/intermediate and umbrella/intermediate cell layers, respectively, using previously reported K5-CreERT2¹⁰⁴ and Upk3a-CreERT2 (The Jackson Laboratory) transgenic mice. Dual inactivation of Pten and Trp53 by surgical injection of adenoviral cre into the bladder has been previously shown to induce bladder cancer in mice⁹⁶. Using standard animal husbandry, we generated cohorts of Upk3a-CreERT2; Trp53L/L; Pte/L/L; Rosa26LSL-Luc mice (hereafter termed “UPPL”) as well as K5-CreERT2; Trp53L/L; PtenL/L; Rosa26LSL-tdTomato mice (hereafter called “KPPT”) that were backcrossed 10 times to a C57BL/6 background. Both UPPL and KPPT mice were gavaged with tamoxifen every other day for 3 doses starting at 6 to 8 weeks of age to induce CreERT2 activity. Serial in vivo luminescence (for UPPL mice) and ultrasound of the bladder were used to monitor for tumor development and growth. UPPL mice demonstrated gradually increasing luminescence signal over time in the region of the bladder (**Figure 2.1A,B**). In addition, by ultrasound, papillary-appearing tumors began to be apparent at a median of 58 weeks (**Figure 2.1 C,D**).

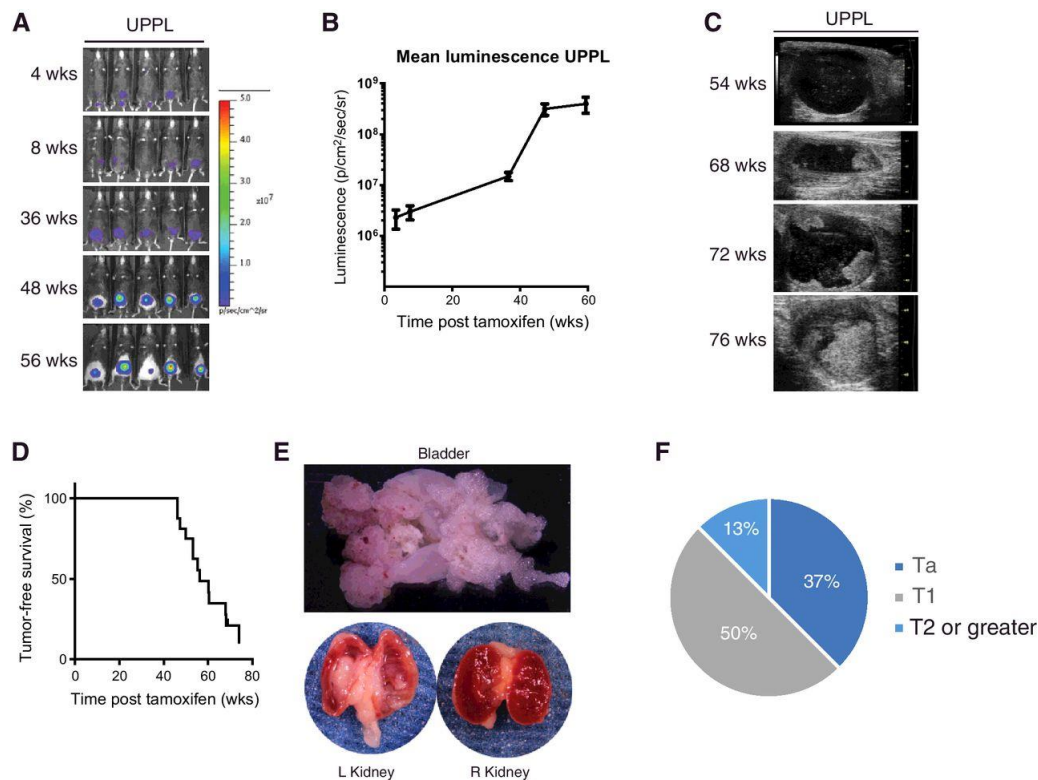


Figure 2.1: Inactivation of Pten and Trp53 in Upk3a-expressing cells results in high-grade muscle-invasive bladder tumors. (A) Bioluminescent images of UPPL mice at indicated time points. (B) Quantification of luminescence over the region of the bladder. (C) Ultrasound images of bladder tumor formation. (D) Tumor-free survival as detected by ultrasound. (E) Gross images of the kidneys and bladder from a tumor-bearing UPPL mouse. (F) Tumor stage assessed histologically based on human TNM staging.

In contrast, KPPT mice administered tamoxifen by gavage died rapidly of epithelial hyperplasia of the snout, paws, and papillary skin lesions (Supplementary Fig. S1A–S1C). This likely represents the inactivation of Pten and Trp53 (and pursuant epithelial overgrowth) in K5-expressing basal cells in multiple organs including the epidermis, trachea, and gastrointestinal tract. In an attempt to activate K5-CreERT2 solely in the K5-expressing basal cells of the bladder, we administered 4-hydroxytamoxifen (4-OHT) intravesically at various concentrations (2,000 and 200 nmol/L). Mice injected with intravesical 4-OHT at 2,000 nmol/L exhibited a similar but

attenuated phenotype to KPPT mice that had been gavaged with tamoxifen (Supplementary Fig. S1B and S1C) and had a shortened survival. In contrast, KPPT mice injected with intravesical 4-OHT at 200 nmol/L had an extended survival but did not develop bladder tumors despite Cre-mediated recombination as evidenced by increased tdTomato signal over the region of the bladder by IVIS imaging (Supplementary Fig. S1D). Moreover, histologic examination of the bladders of mice injected with intravesical 4-OHT at 2,000 or 200 nmol/L showed no significant histologic changes of the urothelium (Supplementary Fig. S1E).

Approximately 95% of UPPL mice developed tumors within 77 weeks (**Figure 2.1D**). Grossly, bladder tumors in UPPL mice appeared to be papillary in nature (**Figure 2.1E**), which is a feature documented to be enriched in the luminal-like molecular subtype^{5,6}. Histologically, the UPPL tumors were characterized as high grade by an expert genitourinary pathologist (S.E. Wobker) and were found to be of varying tumor stage (**Figure 2.1F**) as well as rarely metastatic (**Figure 2.2A**). UPPL tumors also had microscopic papillary features (**Figure 2.2B-D**) and some had prominent squamous differentiation (**Figure 2.2D,E**). In addition, UPPL tumors were noted to have different depths of invasion into the bladder wall including both lamina propria invasion (**Figure 2.1F, 2.2F**) and muscularis propria invasion (**Figure 2.2G**). In keeping with the known field defect of urothelial tumors in human disease, tumors were also noted to form in the renal pelvis and ureters of about a third of mice (**Figure 2.1E, 2.2A,H,I**). Finally, rare macroscopic metastases were seen (**Figure 2.2A,J,K**).

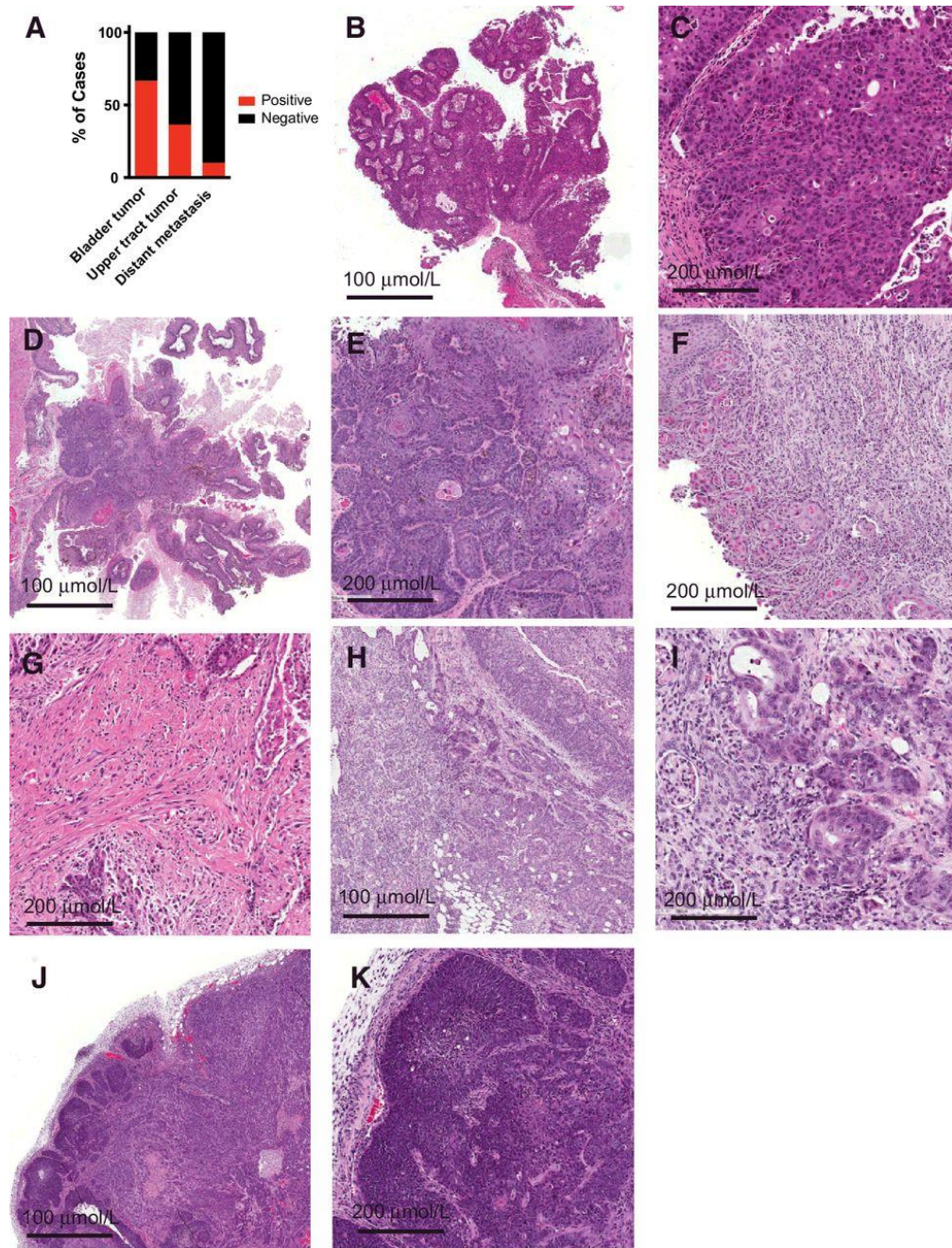


Figure 2.2: Representative histology of UPPL tumors. (A) Bar graph indicating the percentage of UPPL mice that developed bladder tumors, upper tract tumors, and distant metastases at the time of sacrifice. (B) Low-power view of papillary-appearing UPPL tumor. (C) High-power view of papillary UPPL tumor. (D) Low-power view of papillary tumor with squamous histology. (E) High-power view of squamous histology. (F) UPPL tumor showing lamina propria invasion. (G) UPPL tumor with muscularis propria invasion. (H) Upper tract tumor demonstrating invasion into the renal parenchyma. (I) High-power view of urothelial tumor invading renal parenchyma. (J) Cervical lymph node metastases. (K) High-power view of cervical lymph node metastases.

BBN and UPPL models are basal- and luminal-like models, respectively, of human bladder cancer

Bladder tumors induced by the carcinogen N-Butyl-N-(4-hydroxybutyl) (BBN) have been previously documented to harbor a number of histologic features (e.g., squamous differentiation, Supplementary Fig. S2A–S2D) and gene expression patterns known to be found in basal-like bladder tumors⁷⁹. We therefore established 11 independent BBN-induced bladder tumors by continuously administering 0.05% BBN in drinking water as described previously⁹¹. Given the papillary nature of UPPL tumors, we hypothesized that they correspond to a luminal-like molecular subtype. We therefore performed global transcriptome profiling of 9 UPPL and 11 BBN mouse tumors using RNA-seq. We first performed molecular subtype classification using our previously published BASE47 (bladder cancer analysis of subtypes by gene expression; ref. 3)⁷ subtype classifier and found that 8 of the 9 UPPL tumors had high correlation to the luminal centroid of gene expression (**Figure 2.3A**). To further validate our observation, we coclustered the UPPL and BBN murine tumors with human tumors from the The Cancer Genome Atlas (TCGA; n = 408) using genes with corresponding homologs across the species and found that the majority of UPPL and BBN tumors coclustered with human luminal-like tumors and basal-like tumors, respectively (**Figure 2.3B**).

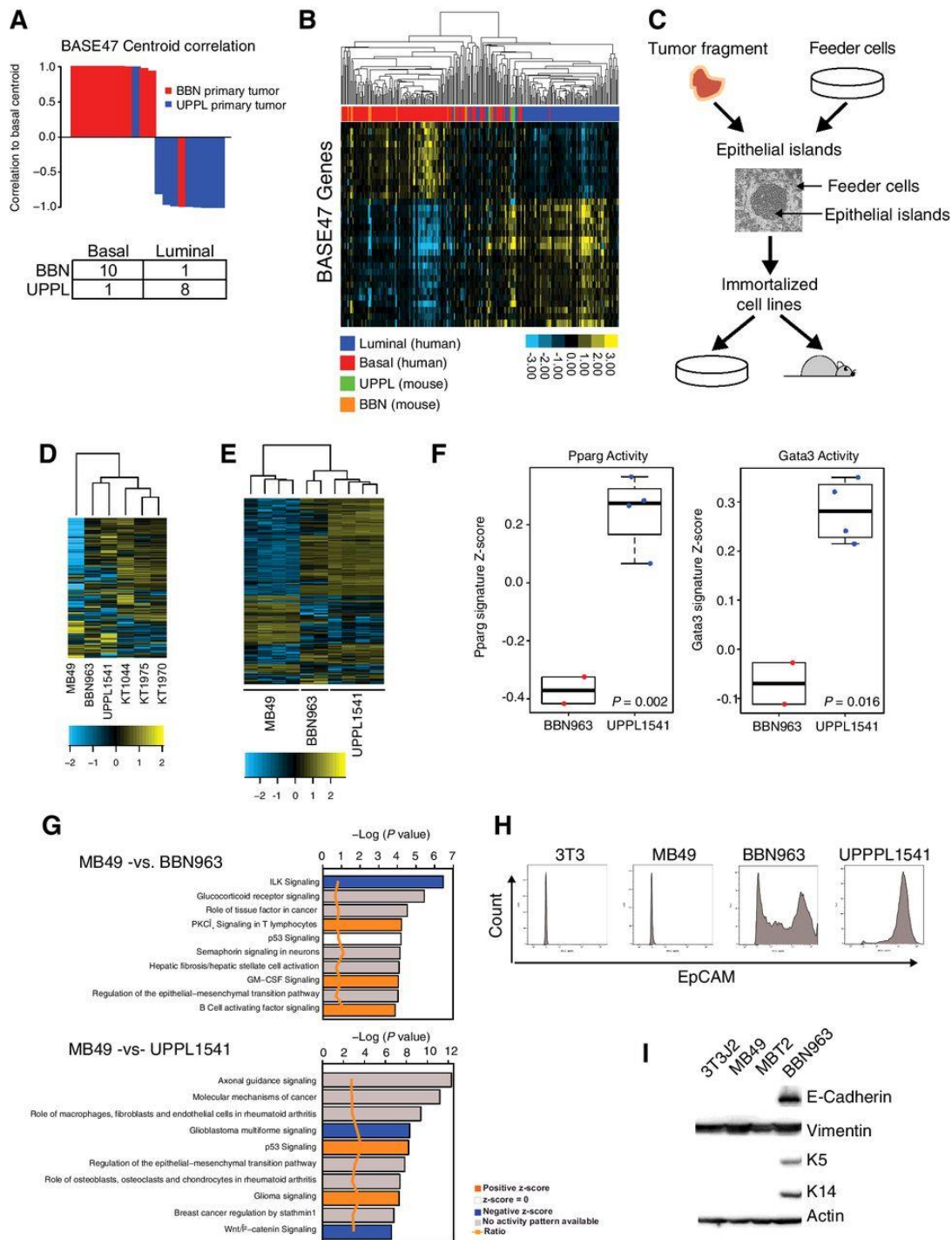


Figure 2.3: BBN and UPPL tumors recapitulate the human basal and luminal molecular subtypes of bladder cancer. (A) Waterfall plot of the correlation to the basal centroid for BBN and UPPL primary tumors, with an accompanying confusion matrix indicating the subtype calls. (B) Unsupervised clustering heatmap of BBN and UPPL primary tumor samples with the TCGA BLCA dataset across genes in the BASE47 classifier. (C) Representative flowchart of the workflow to transition a primary tumor extracted from a mouse model to a cell line and a cell line-derived tumor. (D) Unsupervised clustering

heatmap of MB49, BBN963, UPPL1541, and normal urothelium (KT) cell lines across the top 10% most differentially expressed genes across the samples. (E) Unsupervised clustering heatmap of MB49, BBN963, and UPPL1541 cell line–derived tumors across the top 10% most differentially expressed genes across the samples. (F) Box plots of Pparg and Gata3 gene signature scores from RNA-seq data of BBN963 and UPPL1541 cell line–derived tumors. (G) IPA analysis plots showing activated pathways in MB49 cell line–derived tumors relative to BBN963 and UPPL1541 cell line–derived tumors. (H) Flow cytometry plot for EpCAM expression in 3T3, MB49, UPPL1541, and BBN963 cell lines. (I) Western blot of whole-cell lysates from 3T3, MB49, MBT2, and BBN963 cell lines blotted for the indicated antibodies.

Currently, very few cell lines exist for modeling bladder cancer in immunocompetent mice; therefore, we set out to generate additional cell lines that could be utilized in future studies. In particular, MB49 cells have long been the workhorse of syngeneic bladder cancer cell lines⁹⁰ for studies requiring an immunocompetent host. Given the long latency of tumor formation in the UPPL model, we established tumor cell lines from both UPPL and BBN tumors using the conditional reprogramming of cells (CRC) method described previously⁹⁸. Specifically, transplantable cell lines were established from BBN (BBN963) and UPPL (UPPL1541) tumors (**Figure 2.3C**) and have been confirmed to grow in C57BL/6 mice. In parallel, using the CRC method, we generated three primary cell lines derived from normal mouse urothelium of tamoxifen-treated K5-CreERT2; Rosa26LSL-tdTomato mice, hereafter called KT mice (KT1044, KT1975, and KT1970) as a normal reference for comparison. Interestingly, the vast majority of epithelial cells that grew in vitro from CRC culture of KT mouse bladders expressed tdTomato, suggesting they at some point had expressed K5 (Supplementary Fig. S3).

To assess the similarities between our newly generated models and MB49 cells, we performed whole-transcriptome profiling on the BBN963 and UPPL1541 cell lines, MB49 cells, 3T3 cells, and three primary mouse urothelial cell lines (KT1044, KT1975,

and KT1970). Unsupervised hierarchical clustering of the cell lines on differentially regulated genes across samples (Supplementary Table S2) demonstrated that MB49 cells had transcriptome profiles that differed significantly from the other cell lines (**Figure 2.3D**) when tested by multiscale bootstrap resampling ($P = 0.0$, Supplementary Fig. S4A), whereas BBN963 and UPPL1541 cells had transcriptome profiles that more closely resembled normal urothelial (KT) cells. To ensure that we had not tainted our MB49 cells, we obtained MB49 cells from an independent source (Phil Abbosh, Fox Chase Cancer Center, Philadelphia, PA) and performed transcriptome profiling. We found that the transcript level (across all genes) is highly correlated when comparing “UNC MB49” with “FCCC MB49” ($R = 0.94$ respectively, Supplementary Fig. S4B), suggesting our MB49 cells were genuine. Intriguingly, hierarchical clustering of MB49 cells with 3T3 cells, our three primary mouse urothelial cell lines, BBN963 cells, and UPPL1541 cells demonstrated that the MB49 cells coclustered with 3T3 cells (Supplementary Fig. S4C) significantly by PVClust (Supplementary Fig. S4D). To examine the RNA expression profiles of these cell lines in the context of the tumor microenvironment, we generated RNA expression data on cell line–derived tumors from MB49, BBN963, and UPPL1541 cells. Clustering of these cell line–derived tumors using differentially regulated genes (Supplementary Table S3) again demonstrated that MB49 tumors have significantly divergent transcriptome profiles when tested by multiscale bootstrap resampling ($P = 0.0$, Supplementary Fig. S5A) and demonstrate that this finding is not merely an artifact of cell culture (**Figure 2.3E**). Finally, reassuringly, Pparg and Gata3 gene signatures were upregulated in UPPL1541 tumors relative to BBN963

tumors (**Figure 2.3F**), demonstrating that cell line–derived UPPL1541 tumors maintain molecular features of a luminal-like molecular subtype.

We next performed Ingenuity Pathway Analysis comparing MB49, UPPL1541, and BBN963 cell line–derived tumors. General pathways related to cancer were enriched in BBN963 tumors relative to UPPL1541 tumors (Supplementary Fig. S5B). In contrast, pathways related to fibrosis and epithelial-to-mesenchymal transition (EMT) appeared to be highly upregulated in MB49 cell line–derived tumors compared with either the BBN963 or UPPL1541 tumors (**Figure 2.3G**). Based on these observations, we examined the expression of a set of epithelial markers in the mouse bladder cell lines. Assessment of EpCAM by flow cytometry demonstrated that a significant proportion of BBN963 and UPPL1541 cells expressed cell surface EpCAM while MB49 cells had little to no EpCAM expression, similar to the mouse fibroblast line 3T3 (**Figure 2.3H**). In keeping with this finding, we also noted that MB49 cells did not express K5 or K14 in immunoblots of whole-cell lysates (**Figure 2.3I**), implying that MB49 cells have lost characteristic urothelial cytokeratin expression patterns potentially from undergoing EMT. Furthermore, we noted that MB49 cell line–derived tumors had relatively high and low expression of vimentin and Cdh1 (E-cadherin), respectively, consistent with MB49 cells being more mesenchymal than BBN963 and UPPL1541 cell line–derived tumors (**Figure 2.3I**; Supplementary Fig. S6). In aggregate, these findings suggest that MB49 cells and tumors more closely resemble fibroblasts than urothelial cells and highlight the potential benefit of our models.

BBN963 tumors demonstrate evidence of an antigen-driven T-cell response

Human basal-like and luminal-like bladder cancers demonstrate different patterns of immune infiltration and are also correlated with differential response to checkpoint inhibitor therapy^{83,85}, suggesting subtype-specific differences in the tumor-immune microenvironment. Immune gene signature expression derived from previously published studies were compared among 11 BBN and 9 UPPL models^{83,100,101,105}. Consistent with immune gene signature patterns observed in human tumors, BBN (basal-like) tumors demonstrated greater overall expression of immune gene signatures (**Figure 2.4A**; Supplementary Fig. S7A) than did UPPL (luminal-like) tumors, including those for T cells, B cells, dendritic cells, other innate immune cells, and immunosuppression⁸³.

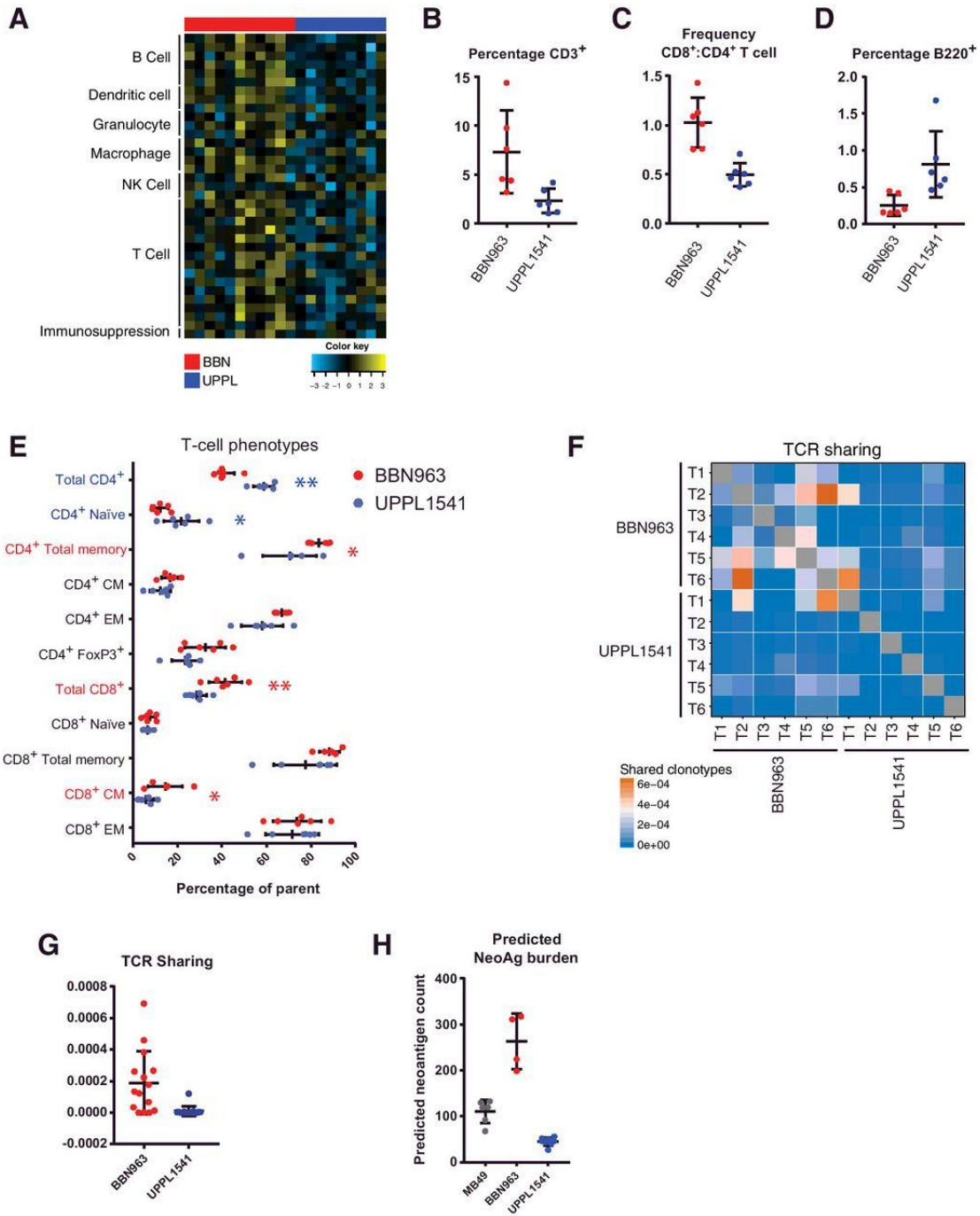


Figure 2.4: Immune characterization of UPPL1541 and BBN963 subtype-specific bladder models. (A) Immune gene signature expression across 9 UPPL and 11 BBN primary tumors. (B) Flow cytometric characterization of tumor-infiltrating T cells (CD3⁺) in cell line-derived (allograft) BBN963 and UPPL1541 tumors. Each datapoint represents an independent mouse. (C) Frequency of CD8⁺ to CD4⁺ T cells in cell line-derived BBN963 and UPPL1541 tumors. (D) Flow cytometric characterization of tumor-infiltrating B cells (B220⁺) in cell line-derived BBN963 and UPPL1541 tumors. (E) T-cell phenotypic subpopulations in cell line-derived BBN963 and UPPL1541 tumors, with significantly

increased phenotypes highlighted with respective colors (Mann–Whitney U test, *, $P < 0.05$; **, $P < 0.001$). (F and G), Heatmap (F) and respective quantification (G) of T-cell receptor clonotype sharing within cell line–derived BBN963 and UPPL1541 tumors, derived from whole-tumor RNA-based T-cell receptor amplicon sequencing. H) Predicted neoantigen burden (class I and II, >500 nmol/L predicted binding affinity) in MB49, BBN963, and UPPL1541 cell line–derived tumors.

To further explain the observed immunologic differences between BBN and UPPL tumors, we performed flow cytometric analysis in cell line–derived BBN963 and UPPL1541 tumors. Comparing the frequency of tumor infiltrating lymphocytes (TIL) by flow cytometry from BBN963 and UPPL1541 tumors, we observed significantly greater frequencies of CD3+ T cells (**Figure 2.4B**), as well as increased ratio of CD8+ cytotoxic T cells to CD4+ helper T cells (**Figure 2.4C**) in BBN963. Somewhat surprisingly, the proportion of B cells was higher in UPPL tumors; however, the overall proportion of B cells in the lymphocytic infiltrate was low (**Figure 2.4D**). To further characterize the phenotype of the tumor-infiltrating T cells, expressions of CD44 and CD62L were used to identify naïve (CD44–, CD62L+), central memory (CM; CD44+, CD62L+), and effector memory (EM; CD44+, CD62L–) populations. Among CD4+ T cells, UPPL1541 tumors were enriched for naïve T cells, whereas the frequency of the total memory pool (CD44+) was significantly greater in BBN963 tumors (**Figure 2.4E**). Moreover, EM and CM frequencies both trended higher in BBN963. Among CD8+ T cells, the CM frequency was significantly greater in BBN963. In addition, CD4+ FoxP3+ regulatory T cells trended toward higher frequency in BBN963. Thus, memory subpopulations of both CD8+ and CD4+ T cells had increased frequencies in the BBN tumors, suggesting the presence of an antigen driven T-cell response in BBN963.

Analyzing BBN963 and UPPL1541 cell line–derived tumors by TCR repertoire profiling, BBN963 tumors demonstrated a higher degree of clonotype sharing between

animals (**Figure 2.4F,G**), suggesting that there may be greater convergent repertoire selection in BBN tumor-infiltrating T cells in the context of an antigen-driven response. To examine whether the increased immune infiltration and TCR repertoire sharing seen in BBN tumors were associated with the number of targetable tumor antigens, we performed neoantigen prediction on BBN963 and UPPL1541 cells and not unexpectedly observed significantly higher neoantigen burden in BBN963 compared with UPPL1541 (**Figure 2.4H**; Supplementary Tables S4 and S5). This, in combination with the increased TCR repertoire sharing, further supports the hypothesis that the immune infiltration seen in BBN tumors is driven by an antigen-specific immune response.

To investigate the functional significance of immune infiltrating T-cell subpopulations, we performed univariable linear regression with frequency of T-cell phenotypic subpopulations as a continuous predictor variable and tumor mass as the response variable in untreated mice. In BBN963, the frequency of total and naïve CD8+ T cells was positively associated with tumor mass, and the frequency of CD4+ memory, CD4+ CM, total CD8+ memory, and CD8+ EM T cells were all inversely correlated with tumor mass (Supplementary Fig. S7B). In UPPL1541, no features were positively associated with tumor mass, whereas CD8+ total memory and specifically CD8+ CM T cells were both weakly inversely correlated with tumor mass. These associations are suggestive of tumor-infiltrating memory T cells being functional and capable of antitumor activity in both BBN and UPPL, with greater functional significance in BBN963.

BBN963 tumors stratify by response to PD-1 axis inhibition

The relative overexpression of immune gene signatures and evidence of an antigen driven T-cell response in BBN963 cell line–derived tumors are suggestive of possible greater responsiveness to immune checkpoint inhibitor therapy in BBN963. Accordingly, we observed dramatic decreases in mean tumor volume in BBN963 following anti–PD-1 therapy, while UPPL1541 tumors demonstrated only modest control of tumor growth (**Figure 2.5A,B**). Despite the mean tumor size being substantially controlled in BBN963 following anti–PD-1 therapy, the growth pattern of individual tumors demonstrated a mixed-response pattern (**Figure 2.5C**). There was heterogeneity of anti–PD-1 response in UPPL1541 tumors as well (**Figure 2.5D**). The difference in responsiveness between BBN963 and UPPL1541 tumors did not appear to be secondary to differential expression of PD-L1 as both BBN963 and UPPL1541 cell lines upregulated PD-L1 expression when exposed to IFN- γ (**Figure 2.5E**).

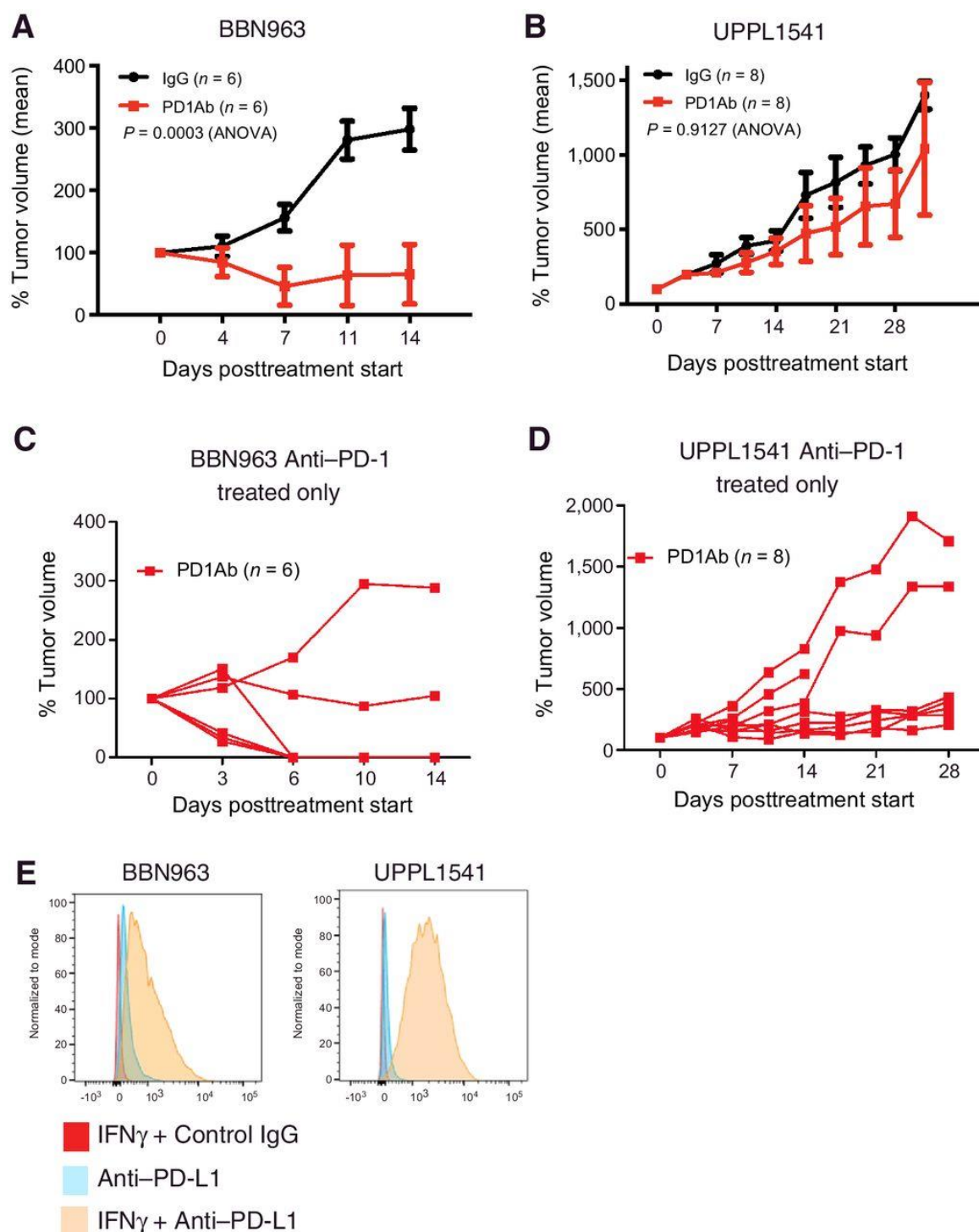


Figure 2.5: Anti-PD-1 treatment of BBN963 and UPPL1541 cell line-derived tumors. (A) Mean tumor volume of C57BL/6 mice bearing BBN963 tumors treated with either control IgG or anti-PD-1 antibody. Anti-PD-1 treatment was begun when tumors reached 200 mm³. (B) Mean tumor volume of C57BL/6 mice bearing UPPL1541 tumors treated with either control IgG or anti-PD-1 antibody. Anti-PD-1 treatment was begun when tumors

reached 200 mm³. (C) Tumor volume of individual mice from A. (D) Tumor volume of individual mice from B. (E) BBN963 and UPPL1541 cells were treated with IFN- γ , and flow cytometry was used to detect cell surface PD-L1 expression.

In order to elucidate the immune correlates of these two phenotypes in response to anti-PD-1 therapy, we repeated anti-PD-1 antibody treatments (**Figure 2.6A**) and analyzed the TIL populations among anti-PD-1 responder and nonresponder BBN963 tumors once response class could be determined on day +14 following tumor inoculation. Surprisingly, no significant changes were observed in the overall T- and B-cell infiltration frequencies by flow cytometry in responders versus nonresponders (**Figure 2.6B**). In addition, phenotyping of tumor-infiltrating T cells demonstrated only significantly greater frequencies of total CD4⁺ among nonresponders, with subtle, nonsignificant variations among other T-cell phenotypic subpopulations (**Figure 2.6C**). Despite these minimal differences, comparison of subpopulation ratios demonstrated an overall significant increase in the frequency of total memory-to-regulatory T cells as well as significantly higher ratios of CD8⁺ to CD4⁺ T cells in responders (**Figure 2.6D**). To further examine the role of TILs among responder and nonresponder tumors, we calculated immune gene signatures derived from total tumor RNA-seq and independently correlated these signatures to tumor mass. Although nonresponders only demonstrated modest inverse correlation between a single CD8⁺ T-cell immune signature and tumor mass, responder tumor mass was inversely correlated with multiple immune cell signatures, most significantly with cytotoxic T-cell and CD8⁺ T-cell signatures (**Figure 2.6E**). These data in aggregate demonstrate the potential importance of the balance of effector to suppressor T-cell subpopulations, rather than just absolute numbers, in mediating an antitumor response in responding BBN963 tumors.

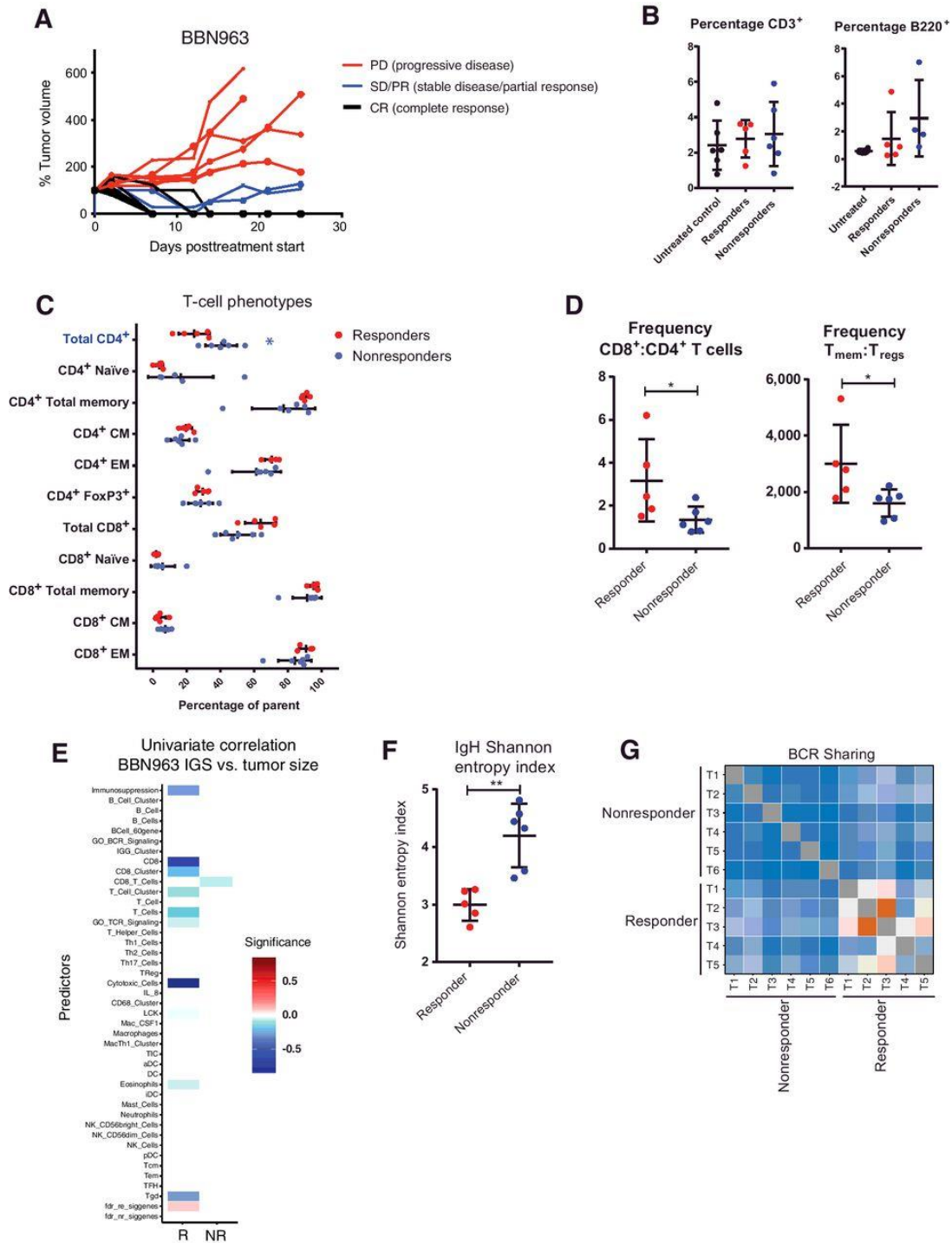


Figure 2.6: Description and immune characterization of BBN963 mixed-response phenotype. (A) Tumor growth curves of anti-PD-1 treated, cell line-derived BBN963 tumors, showing responders (black) and nonresponders (red) to therapy. (B) Flow characterization of tumor-infiltrating T cells (CD3⁺) and B cells (B220⁺) in untreated (black), responder (red), and nonresponder (blue) BBN963 tumors. (C) T-cell phenotypic subpopulations in cell line-derived BBN963 and UPPL1541 tumors, with significantly

increased phenotypes highlighted with respective colors (Mann–Whitney U test, *, $P < 0.05$). (D) Frequency of memory to regulatory T cells (CD3+CD44+: CD3+CD4+FoxP3+) and CD8+ to CD4+ T cells in responder versus nonresponder BBN963 tumors. (E) Univariable correlation of tumor size to immune gene signature expression in responder (left) and nonresponder (right) BBN963 tumors. Shannon entropy index (F) and receptor clonotype sharing (G) of tumor-infiltrating B-cell receptor heavy chain expression in responder and nonresponder BBN963 tumors.

To address the role of clonality of the tumor-infiltrating lymphocytes in controlling tumor growth in anti–PD-1 responsive BBN963 tumors, we performed TCR and BCR repertoire profiling of responder and nonresponder whole tumor RNA. We observed a modest, nonsignificant increase in TCR clonotype sharing (Supplementary Fig. S8A and S8B) and no differences in Shannon entropy (Supplementary Fig. S8C) between responder and nonresponder tumors. In contrast, BCR profiling demonstrated significantly lower Shannon entropy indices (**Figure 2.6F**) and significantly greater clonotype sharing among responders (**Figure 2.6G**), suggesting a potentially important role for B-cell clonal shift in mediating response in the BBN963 model.

BBN963 and UPPL1541 models express targetable, immunogenic neoantigens

With the recent interest in neoantigens as biomarkers of immunotherapy response and therapeutic targets for personalized immunotherapy, we sought to identify and validate neoantigen targets in our subtype-specific bladder models. Using previously described methods⁸³, neoantigens were predicted in BBN963, MB49, and UPPL1541 cell line–derived tumors (**Figure 2.7A**), selecting for predicted class I and II binders by NetMHCpan and NetMHCIIpan (affinity < 500 nmol/L). Using 5x RNA-seq coverage and expression in all replicates as cutoffs, we observed BBN963 to have the greatest number of class I (48) and class II (18) predicted neoantigens, followed by MB49 (I: 29; II: 8), and lastly by UPPL1541 (I: 2; II: 5). To validate the immunogenic

potential of these predicted neoantigens, we synthesized 96 of 110 predicted neoantigens and performed vaccination/ELISPOT analyses to identify the ability of each peptide to induce an IFN- γ response in T cells stimulated by neoantigen peptide-pulsed dendritic cells. Mice were vaccinated with a pool of eight random, equimolar peptides, and splenocytes derived from vaccinated mice were subsequently pulsed with one of the eight peptides on an IFN- γ capture ELISPOT plate (**Figure 2.7B,C**). Based on the number of spots induced by each peptide, we observed MB49 to contain the most highly immunogenic class I and II peptides, holding eight of the top 10 neoantigens by IFN- γ response. This is followed by BBN963, and lastly by UPPL1541, which contained only one peptide within the top 15. Class I and II neoantigens were equally represented among the top binders, with four and six of 10 top neoantigens predicted as class II and class I, respectively. Finally, to test the potential for these peptides to generate neoantigen-enriched T-cell populations, we performed two rounds of vaccination in wild-type C57BL/6 mice using the top eight BBN963 neoantigens, followed by ex vivo stimulation using one of the respective peptides. Coculture of these neoantigen-enriched T cells with BBN963 tumor cells demonstrated an IFN- γ response over that of irrelevant peptide control in five of eight peptides, emphasizing the potential of these peptides for use in neoantigen-based BBN963 treatment models (**Figure 2.7D**).

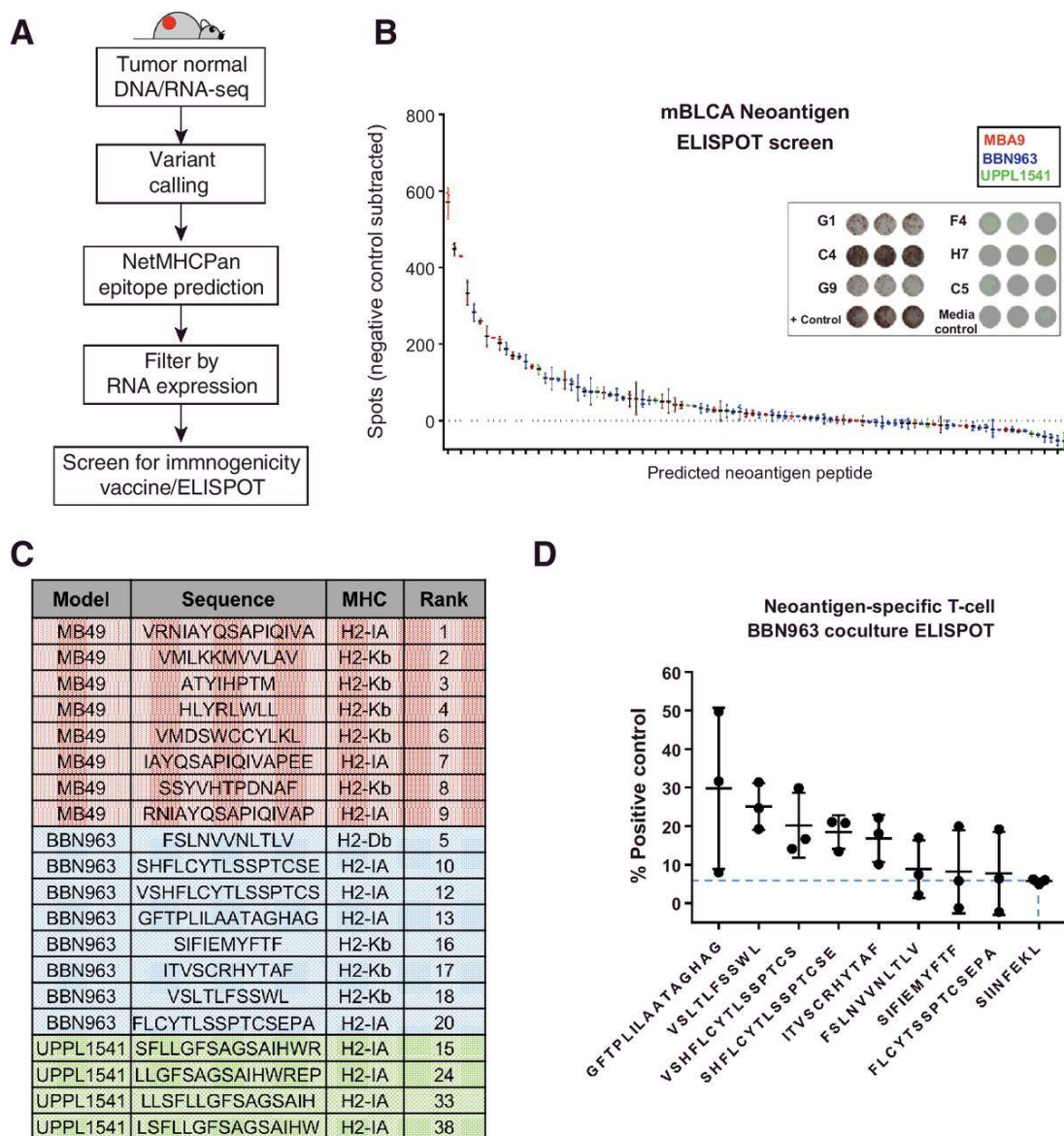


Figure 2.7: Neoantigen prediction and validation in BBN963, UPPL1541, and MB49. (A) Schema for neoantigen prediction workflow, using tumor DNA, tumor RNA, and matched normal DNA to call mutations via UNSeqr, epitope prediction to identify predicted class I and II binders, and vaccine/ELISPOT validation. (B) Summary of vaccine/ELISPOT results in MB49, BBN963, and UPPL1541, with background subtracted counts ranked by number of spots and representative figures of highly immunogenic wells (G1, C4, G9), weakly immunogenic wells (F4, H7, C5), and controls. (C) Summary of top eight predicted neoantigens in MB49 (red), BBN963 (blue), and top four predicted neoantigens in UPPL1541 (green), including sequence, predicted MHC class, and rank among all screened peptides within all three models. (D) IFN- γ ELISPOT results of BBN963 neoantigen-enriched T cells cocultured with BBN963 tumors, as a percentage peptide-pulsed target positive control. Blue dashed line marks IFN- γ intensity of irrelevant peptide (SIINFEKL) enriched T cells cocultured with BBN963.

2.1.4 Discussion

We describe here the first molecular subtype-specific murine model of luminal-like bladder cancer. The BBN model was derived from carcinogen-treated mice that develop spontaneous bladder tumors and exhibit a basal phenotype as previously described by others⁷⁹. We extend these findings by demonstrating that the BBN model also has an immune infiltration pattern that is consistent with that of human basal tumors⁸³. The UPPL model was derived from mice with directed knockout of Trp53 and Pten in the urothelial umbrella cells under the control of the Uroplakin-3a promoter. UPPL tumors have papillary histology, decreased immune infiltration, and decreased response to PD-1 inhibition relative to BBN tumors. Characterized by gene expression profiling, these models reflect human bladder cancer and normal urothelium more closely than does the commonly used MB49 model, which appears to more closely resemble fibroblasts. These results imply the BBN and UPPL models will prove to be valuable resources in studying bladder cancer in immunocompetent animals, and they will be a unique resource with which to study molecular subtype-specific biology and treatment effects.

Although dual inactivation of Trp53 and Pten in Upk3a-expressing cells led to robust bladder tumor formation, inactivation of these same genes in K5-expressing cells did not result in any apparent neoplasia or preneoplastic changes. Although we had set out with the goal of answering whether inactivation of Trp53 and Pten in K5-expressing basal and intermediate urothelial cells was permissive for tumorigenesis, we are hesitant to conclude too much from our negative findings given the significant technical differences between how Trp53 and Pten were inactivated in Upk3a-expressing cells

(systemic tamoxifen by gavage) and K5-expressing cells (local 4-OHT administration into the bladder). Nonetheless, at face value, our results suggest that dual inactivation of Trp53 and Pten are sufficient to initiate bladder tumors in Upk3a-expressing but not K5-expressing urothelium.

The immune microenvironments of the mouse models also reflect patterns seen in human disease, with increased overall immune infiltration seen in the BBN basal-like model⁸³. In parallel with the active immune response, BBN tumors showed increased expression of genes associated with immunosuppression, which is presumably an adaptive response to suppress and/or evade antitumor immunity. In the BBN (basal-like) model, we noted increased memory polarization, which is complimented by significantly higher expression of EM T-cell immune gene signatures in human basal versus luminal tumors among TCGA BLCA samples (Supplementary Fig. S9). These patterns mirror those observed in our prior study of human bladder cancer⁸³ and imply that tumor immunobiology and mechanisms of resistance to immunotherapy may differ by tumor molecular subtype. Importantly, there were a number of aspects noted in the described mouse models that have not been as yet examined in human tumors. In the BBN (basal-like) model, we noted increased T-cell clonotype sharing, suggesting the presence of an active antigen-driven response in these tumors. In contrast, UPPL (luminal-like) tumors showed decreased overall immune infiltration along with an increased frequency of naïve T cells, consistent with immune exclusion and lack of antigen experience, respectively.

Our study also highlights several limitations of the widely used MB49 murine bladder cancer model. We demonstrate that MB49 tumors show lack of characteristic

urothelial cytokeratins, lack of EpCAM expression, and a profound skewing toward having undergone epithelial-to-mesenchymal cell transition. Compared with BBN and UPPL tumors, MB49 had a wide transcriptomic distance from both normal murine urothelial cells and more closely resemble immortalized fibroblasts. These results suggest that although MB49 may be adequate (or in some cases preferred) for studying some aspects of bladder cancer biology (e.g., the post-EMT state), the models reported in our study should gain wide use in the translational bladder cancer research community, both for their subtype specificity and increased fidelity to human bladder cancer gene expression profiles.

Although recent work highlights the mutational faithfulness of the BBN model to human bladder cancer¹⁰⁶ one limitation of the UPPL1541 and BBN963 models is the lack of driver mutations that are also known drivers in human basal-like and luminal-like bladder tumors. Major bladder cancer driver mutations such as MLL, FGFR3, and ARID1A are not mutated in either model, and suspected driver mutations in our BBN963 line such as TCF4, FGFR2, and ITK are not seen at high frequencies in human disease (Supplementary Fig. S10). This limitation is not unique to our models, as it is also a feature of MB49. As RNA transcription is downstream of genetic events such as mutations and gene fusions and upstream of protein translation, we feel the transcriptomic fidelity of our models to human bladder cancer is evidence that these models can be used to faithfully study bladder cancer biology in general and subtype-specific biology in particular. As both BBN and UPPL tumors exist as transplantable cell lines syngeneic with the C57BL/6 background and are able to grow both subcutaneously and orthotopically in the bladder, genetic manipulation strategies such

as CRISPR/Cas9 may be used to manipulate these tumors should researchers desire to study effects of specific mutations in the context of subtype-specific tumors. A second limitation of the UPPL model, especially for tumor immunology studies, is accounting for the potential effect of PTEN inactivation on the immune microenvironment. PTEN has been found to promote nuclear import of the transcription factor Interferon Regulatory Factor 3 (IRF3), thereby positively regulating type I IFN induction¹⁰⁷. PTEN loss has also been associated with impaired T-cell tumor ingress and T-cell mediated cytotoxicity in a preclinical model of melanoma where human tumor cell lines engineered with PTEN silenced and to express the murine MHC class I molecule H-2D^b were injected into immunocompromised mice followed by transfer of murine antigen-specific T cells and antigen-presenting cells 7 days later¹⁰⁸. Thus, it is possible that the UPPL model may be skewed toward an immune evaded or suppressed phenotype due to PTEN loss.

In the ImVigor 210 study, Rosenberg and colleagues showed that a subset of luminal tumors were more likely to respond to PD-1 axis inhibition using an anti-PD-L1 antibody⁸⁵. We report here that response to monotherapy using an mAb against PD-1 was effective in the BBN but not the UPPL model. This represents a potential discrepancy between our murine models and their homonymous human subtypes; however, that conclusion is tempered by two considerations: (i) Our group's luminal versus basal predictor is different from that used by the ImVigor investigators, and unfortunately despite publication the ImVigor RNA-seq data have yet to be made public, and (ii) the subset of luminal tumors more likely to respond was also more heavily immune infiltrated and skewed toward effector T-cell expression, which may have

marked them as basal by our classifier and/or represent a subset of luminal tumors not modeled by UPPL.

The BBN model exhibited a mixed response to anti-PD-1 therapy, which allowed us to evaluate differences in the tumor immune microenvironment between responders and nonresponders. Responsive tumors showed higher degrees of CD8⁺-to-CD4⁺ T-cell infiltration and memory-to-regulatory polarization of the tumor-infiltrating T cells. The former finding is consistent with prior results in human bladder cancer⁸⁵, whereas the latter is to our knowledge the first report of memory T-cell polarization associating with response to immune checkpoint inhibition in bladder cancer. This is consistent with the hypothesis that tumor clearance is augmented by generation of T-cell memory.

Although multiple T-cell immune gene signatures were strongly correlated with tumor mass in responders, we observed an overall lack of TCR clonotype sharing increase in tumor-infiltrating T cells in responders compared with nonresponders. In addition, significant changes to the B-cell clonotype sharing and diversity were observed, suggesting B cells may play an important role in the response to checkpoint inhibitor therapy. Presumably, this pattern of TCR and BCR expression could be explained by several hypotheses: (i) that effector T-cell clones capable of promoting antitumor immunity are only present in responders but their frequencies are too low to result in discriminating differences in global T-cell diversity changes, or (ii) that effector T-cell clones capable of promoting antitumor immunity are present in both responders and nonresponders, but the presence of specific B-cell clones is necessary to mediate their function. Ongoing studies are evaluating pretreatment tumor features and on-treatment features measurable from the peripheral blood that associate with eventual response to

therapy, as well as to test novel combinations of immunotherapy agents. Thus, this model provides a novel mixed-response platform to study efficacy and mechanisms of immunotherapy in bladder cancer.

2.2 Immuno-PET imaging of tumor-infiltrating lymphocytes using Zirconium-89 radiolabeled anti-CD3 antibody in immune-competent mice bearing syngeneic tumors.

2.2.1 Introduction

Successful clinical trials using blocking antibodies to the T-cell co-inhibitory receptors CTLA-4 and PD-1 have driven the recent emergence of interest in cancer immunotherapy, leading to accelerated approval timelines for several immunotherapeutic agents across multiple tumor indications^{85,109–114}. However, the magnitude of interaction between the immune system and tumors varies greatly both within and across tumor types, resulting in differences in the response to checkpoint immunotherapy. Many of these alterations depend on the presence of impaired tumor antigen-specific effector T cells, which have been positively associated with treatment efficacy^{115,116}. Thus, one hypothesis has been that the presence of T cells within the tumor microenvironment is critical to the success of checkpoint immunotherapy.

The ability to monitor T cells within the tumor microenvironment and the immune response over the course of therapy may allow for early determination of the treatment efficacy^{117,118}. Flow cytometry, quantitative polymerase chain reaction, V β spectratyping, high-throughput sequencing, and immunohistochemistry are among the techniques that have provided useful information about antitumor T-cell immunity. These procedures require biopsies to evaluate the tumor immune microenvironment,

greatly limiting the ability to monitor intratumoral T-cell accumulation in vivo or in real time. With the expanding implementation of immunotherapies, tools to monitor immune cell activity become increasingly crucial for guiding clinical decision-making and elucidating treatment options. Additionally, immune cell monitoring can be applied to chimeric antigen receptor (CAR) T cell based therapies, which have demonstrated clinical efficacy in human B cell cancers, providing a measure of both patient and donor T cell location and activity¹¹⁸. Non-invasive imaging of T cells and tumor-infiltrating lymphocytes will be an attractive means of detecting T cell infiltration and tracking the response to therapy¹¹⁹. Non-invasive monitoring could therefore change how therapies are applied and assessed, to the benefit of patients¹¹⁹.

Positron emission tomography (PET) and single-photon emission computed tomography (SPECT) have been successfully used to obtain clinical images of immune cell populations^{117,120}. Other techniques such as ex vivo cell labeling and radiolabeled metabolic probes have also been used to non-invasively image lymphocytes. However, these approaches are not specific for T cells, have toxic effects, or simply fail to detect lymphocytes infiltrating within the tumor¹²¹. Immuno-PET is an emerging technique that combines the specificity of monoclonal antibodies (mAb) with the high sensitivity and quantitative potential of PET to non-invasively identify disease, stage, and response to therapy. Immuno-PET targeting of lymphocytes can provide spatial and temporal information that is currently unavailable using the standard techniques¹²¹. Antibodies with high affinity and specificity can be conjugated to radionuclides, and PET imaging can be used to non-invasively monitor and quantify mAb distribution in real time¹²². Zirconium-89 (89Zr) is a positron emitting radionuclide that has been recently approved

for immuno-PET clinical studies due to its physical and biological characteristics¹²³. In addition, ⁸⁹Zr is a residualizing isotope, which prevents the isotope from leaving the target after internalization of labeled antibody¹²⁴. Thus, ⁸⁹Zr-immuno-PET is a powerful tool to study antigen-antibody interactions.

Recent reports have demonstrated that antibody fragments radiolabeled with ⁶⁴Cu can non-invasively detect CD8+ cytotoxic T lymphocytes in mice using immuno-PET¹²⁵. In a similar fashion, zirconium-89 radiolabeled cys-diabodies were successfully used to non-invasively detect CD4+ T-cell repopulation in wild-type mice and a model of immune reconstitution following hematopoietic stem cell transplantation¹²¹. Furthermore, ⁸⁹Zr radiolabeled cys-diabody detected increased CD8+ tumor-infiltrating lymphocytes in an animal model of colon carcinoma¹²⁶. This work demonstrated that immuno-PET targeting of CD4 and CD8 has the potential to non-invasively detect helper/regulatory and cytotoxic T-cell populations in vivo.

One limitation of the use of antibodies specific for CD4 and/or CD8 for imaging is the limited information obtained regarding the breadth of the T cell response. A more inclusive cell surface protein expressed by T cells is the pan T-cell marker CD3, which is found at all stages of T-cell development. The specificity of the CD3 antigen for T-cell lineage cells and its presence at all stages of T-cell development make CD3 a rational candidate for detecting pan-T-cell populations in vivo.

Antibodies specific for CD3 can have substantial effects on the function of CD4+ and CD8+ T cells in vivo, including induced T cell activation and expansion^{127–129}. Furthermore, administration of high dose anti-CD3 mAb can preferentially deplete T

cells in vivo^{116,129}. Therefore, while anti-CD3 mAb can be used to tag T cells, its effects in vivo are variable and depend on dosage, isotype, surface antigen density on target T cells, and antigen internalization/modulation of the target cell population^{127–132}.

Previously, zirconium-89 labeled anti-CD3 indicated a strong correlation between anti-CTLA-4–treated mice and tumor volume¹³³. However, the immunological effects of radiolabeled anti-CD3 mAb at the doses used for PET imaging are still unknown. It is therefore important to elucidate the immunomodulatory effects of this novel compound to determine if it has the potential to polarize T cells toward an activated and potentially anti-tumor phenotype when used as a component of immuno-PET imaging.

We hypothesized that ⁸⁹Zr radiolabeled anti-CD3 mAb has potential for immuno-PET detection of tumor-infiltrating T lymphocytes in mice bearing syngeneic tumors without changing overall lymphocyte numbers or viability.

2.2.2 Results

⁸⁹Zr-DFO-anti-CD3 reagent generation and evaluation

Full details of DFO-conjugation, radiolabeling and subsequent chemical analysis can be found in the supplementary information (S1 File). Briefly, the conjugation reaction between murine anti-CD3 mAb and DFO yielded 1.1 chelating group per protein molecule based on MALDI-TOF mass spectrometry ($[m/z \text{ (DFO-anti-CD3)} - m/z \text{ (anti-CD3)}] / M.W \text{ (DFO)} = 148438 - 147606 / 752 = 1.1$). The DFO-anti-CD3 was isolated and purified with chemical purity higher than 98%. Non-reduced SDS-PAGE for both DFO-anti-CD3 conjugate and unmodified anti-CD3 showed similar bands with apparent molecular weights of ~150kDa. Furthermore, reduced SDS-PAGE showed a modest

change in apparent molecular weight between the heavy chains of the DFO-anti-CD3 conjugate and unmodified anti-CD3. This further confirmed the low degree of DFO conjugation to anti-CD3 determined by MALDI-TOF-MS. The ^{89}Zr -DFO-mAb conjugates were isolated using size exclusion chromatography (SEC) with radiolabeling yields > 85% and specific activities >185 MBq/mg (>5 mCi/mg). Following SEC purification, the radiochemical purity of ^{89}Zr -DFO-anti-CD3 was higher than 97%. SE-HPLC chromatograms, MALDI-TOF MS spectrums and SDS-PAGE can be seen in supplementary info (S1, S2 and S3 Figs). To ensure the stability of our antibody conjugate in mouse serum, we performed an in vitro 72h serum stability assay. The radiochemical purity of ^{89}Zr -DFO-CD3 remained higher than 98% at 72h post-incubation in C57BL/6 mouse serum. This corresponds with the lower uptake of ^{89}Zr -DFO-CD3 in bone seen in the $\mu\text{PET/CT}$ and ex-vivo biodistribution studies (S4 Fig). To demonstrate that labeling of antiCD3 did not alter the biological activity of the protein, a saturation binding assay was performed, resulting in a binding affinity of ^{89}Zr -DFO-antiCD3 of 14.17 ± 3.75 nM and saturation plateau, indicating fully preserved immunoreactivity (S5 Fig).

Biodistribution of ^{89}Zr -DFO-anti-CD3, ^{89}Zr -DFO-IgG2b, and ^{89}Zr -DFO-IgG in healthy C57BL/6J mice

In order to evaluate in vivo targeting of ^{89}Zr -DFO-anti-CD3, a biodistribution study was performed on 6 healthy C57BL/6J mice. Mice were intravenously injected via tail vein with 825.1 ± 14.8 kBq (22.3 ± 0.4 μCi , ~ 4 μg , 100 μL) of ^{89}Zr -DFO-anti-CD3, or ^{89}Zr -DFO-IgG2b or ^{89}Zr -DFO-IgG as isotype and non-isotype specific matched heavy-chain controls, respectively. IgG2b (BE0090), an isotype control for the anti-CD3

(BE0002), was also radiolabeled with ^{89}Zr and evaluated in vivo to ensure that the Fc region was not responsible for uptake in target organs. The biodistribution of generic ^{89}Zr -IgG in C57BL/6J was likewise performed in order to determine nonspecific binding from organs involved with antibody clearance and elimination. T cells reside in the spleen, lymph nodes, thymus, and bone marrow; therefore those organs were harvested and measured for radioactivity¹³⁴. The liver and blood were additionally harvested to monitor antibody clearance through the hepatobiliary pathway. Finally, the contrast ratio of tissue to blood was evaluated to determine in vivo imaging potential. Biodistribution results are shown in **Figure 2.8** and **Table 2.1**. ^{89}Zr -DFO-anti-CD3 showed the highest uptake in the spleen followed by the axillary lymph nodes (ALN) at 72h post-injection. Very low concentrations of ^{89}Zr -DFO-anti-CD3 were measured in the blood and bone marrow at 72h post-injection.

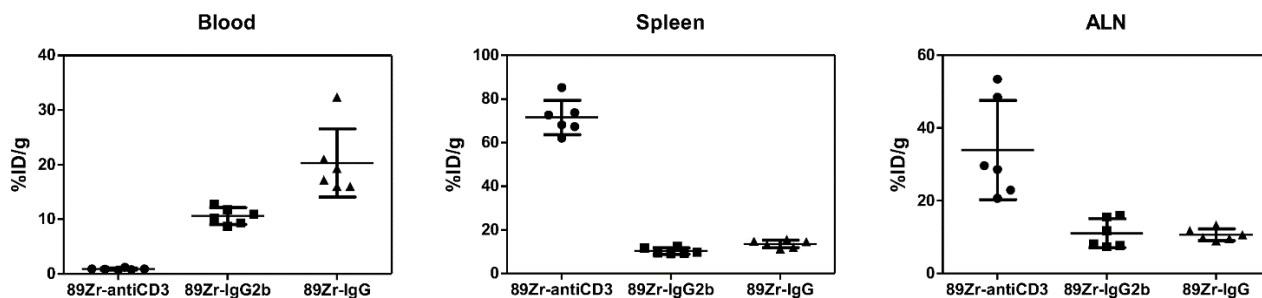


Figure 2.8. Scatter dot plots from the ex-vivo biodistribution study of ^{89}Zr -DFO-anti-CD3, ^{89}Zr -DFO-IgG2b, and ^{89}Zr -DFO-IgG in untreated C57BL/6J mice. Each dot represents a unique mouse. Six mice ($n = 6$) were analyzed in each of the 3 groups for a total of 18 mice. Horizontal lines represent mean \pm standard deviation. All tissue uptake data were normalized by the weight of the tissue being measured. All measurements were taken at 72 hours after injection of antibody. P-values were calculated in Table 2.1 using randomization permutation tests.

	% Injected dose/ gram of tissue (%ID/g)							
	⁸⁹ Zr-DFO-anti-CD3		⁸⁹ Zr-DFO-IgG2b		⁸⁹ Zr-DFO-IgG		Kruskal-Wallis test	
	Mean	SD	Mean	SD	Mean	SD	P value	
Blood	0.90%	0.17%	10.61%	1.52%	20.31%	6.23%	0.0005	***
Liver	9.42%	0.81%	16.38%	3.71%	16.86%	4.77%	0.0062	**
Spleen	71.50%	7.91%	10.27%	1.47%	13.56%	1.72%	0.0009	***
ALN	33.96%	13.67%	11.09%	3.98%	10.68%	1.60%	0.0033	**
Thymus	11.99%	3.34%	7.12%	1.46%	16.16%	9.26%	0.025	*
Bone	0.69%	0.28%	8.95%	2.19%	0.63%	0.62%	0.0034	*
	Tissue to blood ratios							
	⁸⁹ Zr-DFO-anti-CD3		⁸⁹ Zr-DFO-IgG2b		⁸⁹ Zr-DFO-IgG		Kruskal-Wallis test	
	Mean	SD	Mean	SD	Mean	SD	P value	
Liver	10.8	2.16	1.61	0.59	0.9	0.3	0.0008	***
Spleen	82.59	21.59	0.97	0.08	0.7	0.13	0.0005	***
ALN	37.69	12.66	1.02	0.24	0.57	0.19	0.0008	***
Thymus	14.14	6.12	0.68	0.15	0.86	0.61	0.0033	**
Bone	0.76	0.31	0.86	0.27	0.03	0.03	0.0034	**

All measurements were taken at 72 hours after injection of antibody. P-values were calculated using randomization permutation tests. For pairwise comparisons

* p<0.05

** p<0.01

*** p<0.001.

Table 2.1. Results from the ex-vivo biodistribution of ⁸⁹Zr-DFO-anti-CD3, ⁸⁹Zr-DFO-IgG2b, and ⁸⁹Zr-DFO-IgG in C57BL/6J mice (n = 6 per group).

To evaluate whether the uptake in target organs may be due to the interaction between ⁸⁹Zr-DFO-anti-CD3 and T-cells, the biodistributions of both isotype control (⁸⁹Zr-DFO-IgG2b) and IgG control (⁸⁹Zr-DFO-IgG) were also tested in healthy C57BL/6J mice (n = 6 per group). At 72h post injection, the blood concentration of ⁸⁹Zr-DFO-anti-CD3 was minimal (0.9% ID/g) when compared to ⁸⁹Zr-DFO-IgG2b (10.61%) and ⁸⁹Zr-DFO-IgG (20.31%) controls. Indicating rapid clearance and/or uptake of ⁸⁹Zr-DFO-anti-CD3 (**Figure 2.8, Table 2.1**). Moreover, localization of ⁸⁹Zr-DFO-anti-CD3 to T cell rich organ like spleen, and lymph nodes showed significantly higher accumulation than the controls. Finally, liver uptake for ⁸⁹Zr-DFO-anti-CD3 was significantly lower than ⁸⁹Zr-DFO-IgG2b and ⁸⁹Zr-DFO-IgG. Whole counts of the thymus did not show large statistical differences, however, when the thymus to blood ratio was considered; the ⁸⁹Zr-DFO-anti-CD3 was statically higher than either of the two controls. High axillary lymph node (ALN) to blood, spleen to blood and thymus to blood ratios

observed for ^{89}Zr -DFO-anti-CD3 confirmed high accumulation in tissue known to have high T cell counts.

PET/CT studies of ^{89}Zr -DFO-anti-CD3 in healthy C57BL/6J mice

Following the promising results from the biodistribution study, a microPET/CT study was performed on six healthy C57BL/6J mice ($n = 6$) to evaluate immuno-PET imaging potential of T cells with ^{89}Zr -DFO-anti-CD3. Healthy C57BL/6J mice were intravenously injected via tail vein with 5.6 ± 0.2 MBq (153.4 ± 4.1 μCi , $\sim 25\mu\text{g}$, $100\mu\text{L}$) of ^{89}Zr -DFO-anti-CD3. High-contrast images were obtained at 72h post-injection (**Figure 2.9A**), where spleen, lymph nodes, and thymus were clearly visualized with low background.

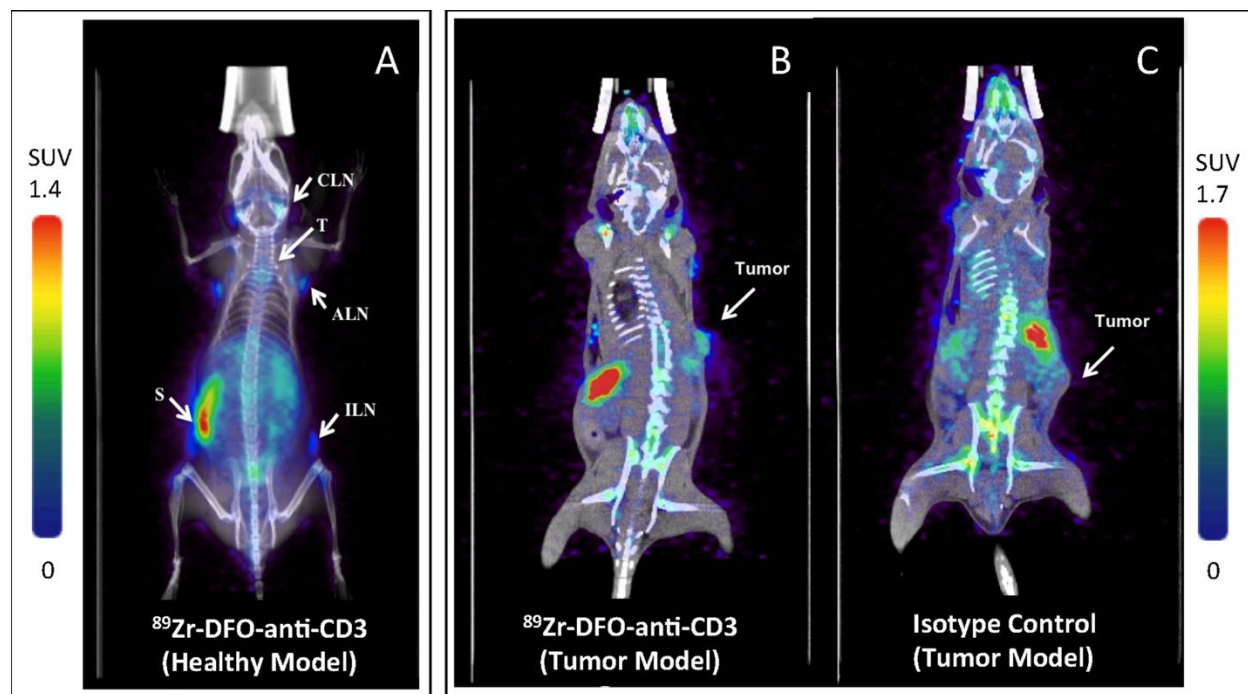


Figure 2.9. Micro-PET/CT images of ^{89}Zr -DFO-anti-CD3 in C57BL/6J mice 72h post-injection (coronal view). (A) Maximum intensity projection of ^{89}Zr -DFO-anti-CD3 injected into a healthy, immune-competent mouse. The radiolabeled antibody accumulated in the following lymphoid organs: cervical lymph nodes (CLN), thymus (T), axillary lymph nodes (ALN), inguinal lymph nodes (ILN) and spleen (S). (B) Micro-

PET/CT (coronal slice) of ^{89}Zr -DFO-anti-CD3 in C57BL/6J mice bearing BBN975 tumors and (C) a coronal slice of isotype control ^{89}Zr -DFO-IgG2b in C57BL/6J mice bearing BBN975 tumors. Six mice ($n = 6$) in each of the 3 groups were imaged using PET/CT. SUV color bar on the left-hand side of the figure corresponds with subfigure A; SUV color bar on the right-hand side of the figure corresponds to subfigures B and C. Additional scans can be seen in the supplementary information.

PET/CT and ex-vivo biodistribution studies of ^{89}Zr -DFO-anti-CD3 and ^{89}Zr -DFO-IgG2b in C57BL/6J mice bearing syngeneic tumors

Next, we tested the ability of ^{89}Zr -DFO-anti-CD3 to image tumor infiltrating T cells found in C57BL/6J mice bearing BBN975 syngeneic tumors. We compared ^{89}Zr -DFO-anti-CD3 versus the isotype control ^{89}Zr -DFO-IgG2b using 6 mice for each group (2 groups, $n = 6$). Each group of C57BL/6J mice bearing BBN975 tumors were intravenously injected with 6.0 ± 0.1 MBq (162.5 ± 1.8 μCi , $\sim 25\mu\text{g}$, 100 μL) of ^{89}Zr -DFO-anti-CD3 or ^{89}Zr -DFO-IgG2b. Immuno-PET scans of ^{89}Zr -DFO-anti-CD3 showed high uptake in spleen, lymph nodes, and tumor (**Figure 2.9B**). Conversely, the isotype control (^{89}Zr -DFO-IgG2b) did not show tumor uptake in microPET/CT scans (**Figure 2.9C**). The isotype control also showed higher background than that for ^{89}Zr -DFO-anti-CD3 due to large amount of antibody-conjugate that remained in circulation.

To further validate the microPET/CT scans, an ex-vivo biodistribution study of ^{89}Zr -DFO-anti-CD3 and ^{89}Zr -DFO-IgG2b in C57BL/6J mice bearing BBN975 syngeneic tumors were performed immediately following each PET scan (**Figure 2.10**). The results are summarized in **Figure 2.10** and **Table 2.2**. Similar to the healthy-mouse study, the ^{89}Zr -DFO-anti-CD3 had a significantly lower concentration in blood than the isotype control (^{89}Zr -DFO-IgG2b). Also, ^{89}Zr -DFO-anti-CD3 showed higher uptake in spleen, ALN, and thymus when compared against the uptake for ^{89}Zr -DFO-IgG2b.

Liver uptake was significantly higher for ^{89}Zr -DFO-IgG2b than for ^{89}Zr -DFO-anti-CD3.

Although there was a not statistical difference in tumor uptake between ^{89}Zr -DFO-IgG2b and ^{89}Zr -DFO-anti-CD3, the tumor-to-blood ratio of ^{89}Zr -DFO-anti-CD3 was 11.5-fold higher than that for ^{89}Zr -DFO-IgG2b.

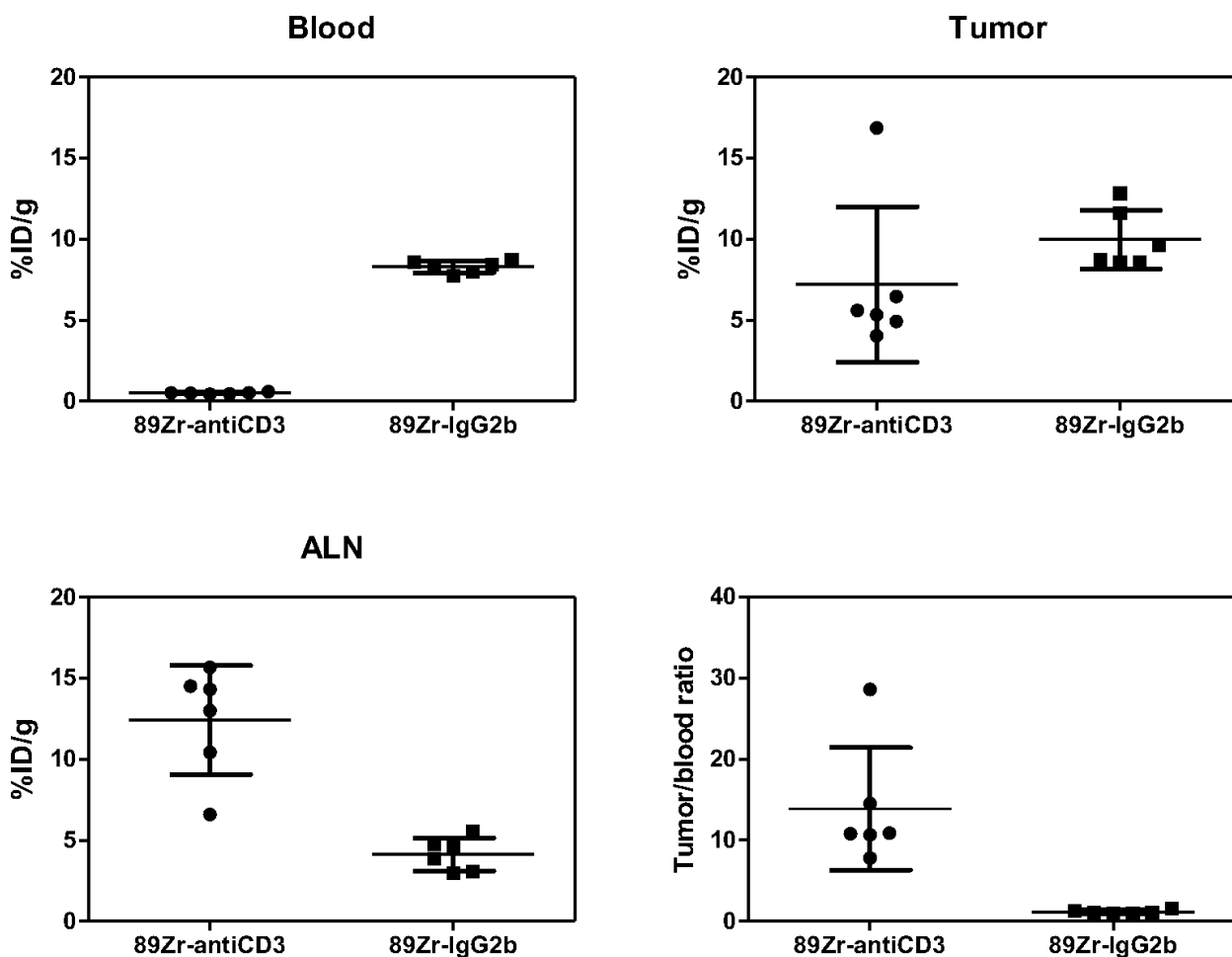


Figure 2.10: Scatter plots from the ex-vivo biodistribution study of ^{89}Zr -DFO-anti-CD3 in C57BL/6J mice bearing BBN975 tumors. Each dot represents a unique mouse. Six mice ($n = 6$) were analyzed in each of the 2 groups for a total of 12 mice. Horizontal lines represent mean \pm standard deviation. All tissue uptake data were normalized by the weight of the tissue being measured. All measurements were taken at 72 hours after injection of antibody. P-values were calculated in Table 2.2 using randomization permutation tests.

	% Injected dose/ gram of tissue (%ID/g)							
	⁸⁹ Zr-DFO-anti-CD3		⁸⁹ Zr-DFO-IgG2b		T-test		Mann Whitney Test	
	Mean	SD	Mean	SD				
Tumor	7.20%	4.79%	9.99%	1.81%	2.13E-01	ns	0.0649	ns
Blood	0.50%	0.05%	8.31%	0.37%	2.11E-13	***	0.005	**
Liver	13.96%	2.45%	23.87%	3.59%	2.33E-04	***	0.0022	**
Spleen	51.22%	9.39%	11.98%	0.69%	1.31E-06	***	0.0022	**
ALN	12.42%	3.36%	4.14%	1.01%	1.77E-04	***	0.0022	**
Thymus	10.12%	1.70%	5.39%	0.71%	9.00E-05	***	0.0022	**
Bone	1.66%	0.39%	2.47%	0.86%	6.18E-02	ns	0.026	*
	Tissue to blood ratios							
	⁸⁹ Zr-DFO-anti-CD3		⁸⁹ Zr-DFO-IgG2b		T-test		Mann Whitney Test	
	Mean	SD	Mean	SD				
Tumor	13.9	7.5	1.2	0.23	2.00E-03	***	0.0022	**
Liver	28.1	5.98	2.88	0.49	1.23E-06	***	0.0022	**
Spleen	103.4	25.89	1.44	0.06	2.21E-06	***	0.0022	**
ALN	25.3	8.17	0.5	0.13	2.23E-05	***	0.0022	**
Thymus	20.49	5.11	0.65	0.07	2.50E-06	***	0.0022	**
Bone	3.36	0.92	0.3	0.11	1.12E-05	***	0.0022	**

All measurements were taken at 72 hours after injection of antibody. P-values were calculated using randomization permutation tests. For pairwise comparisons

* p<0.05

** p<0.01

*** p<0.001.

Table 2.2. Results from the ex-vivo biodistribution studies of ⁸⁹Zr-DFO-anti-CD3 and ⁸⁹Zr-DFO-IgG2b in C57BL/6J mice bearing BBN975 tumors (n = 6 per group).

Immunological effects of DFO-anti-CD3 in C57BL/6J mice

To assess the immunological effects of antibodies used in the context of T-cell imaging, flow cytometric analysis of splenocytes from mice dosed with 25 µg of DFO-anti-CD3, 25 µg of native anti-CD3, or PBS control was performed. Administration of antibody showed no significant differences in lymphocyte count or viability compared to PBS control (**Figure 2.11**). These metrics demonstrate that this dose of DFO-anti-CD3 does not result in net-depletion of the splenic pan-lymphocyte population, of which T cells are a major component. To ensure free DFO did not significantly influence the T cell population within our studies, we performed a control experiment comparing T cell phenotypic subpopulation frequencies in free DFO versus PBS control treated animals. Free DFO was administered in equimolar amounts relative to DFO-anti-CD3 treated

animals (0.4265 nmol), with no significant changes observed in any T cell population relative to PBS control (S7 Fig).

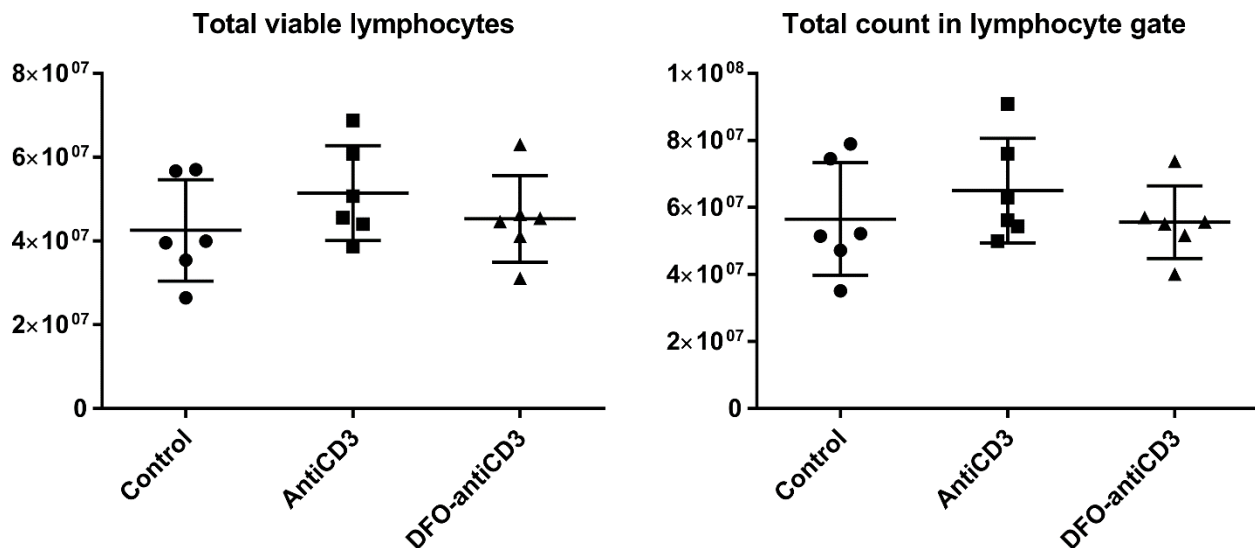


Figure 2.11: Effects of DFO-anti-CD3 and unconjugated anti-CD3 treatment on total lymphocyte numbers and viability in the spleen of C57BL/6J mice. Y-axis corresponds to absolute event counts for each respective subfigure.

DFO-anti-CD3 decreases the naïve CD8+ population and increases central/effector memory CD8+ populations

Since changes in the frequency and enumeration of peripheral lymphocytes were not observed following DFO-anti-CD3 injection, we therefore determined if the DFO-anti-CD3 altered the distribution of CD8+ and CD4+ T-cell sub-populations¹³⁵.

Specifically, naïve, total memory, central memory, and effector memory sub-populations were analyzed within the total CD8+ or CD4+ T-cell pools. The effect of DFO-anti-CD3 resulted in a modest increase in the total CD8+ T cell population compared to the PBS control (16.22% vs 13.07%, $p < 0.05$, Table 2.3, S1 Table). There was a small but significant increase in the percentage of CD8+ T cells in the DFO-anti-CD3 treated

group compared to unmodified anti-CD3 treated animals (16.22% vs 12.45%, $p < 0.05$, Figure 2.12, Table 2.3, S1 Table).

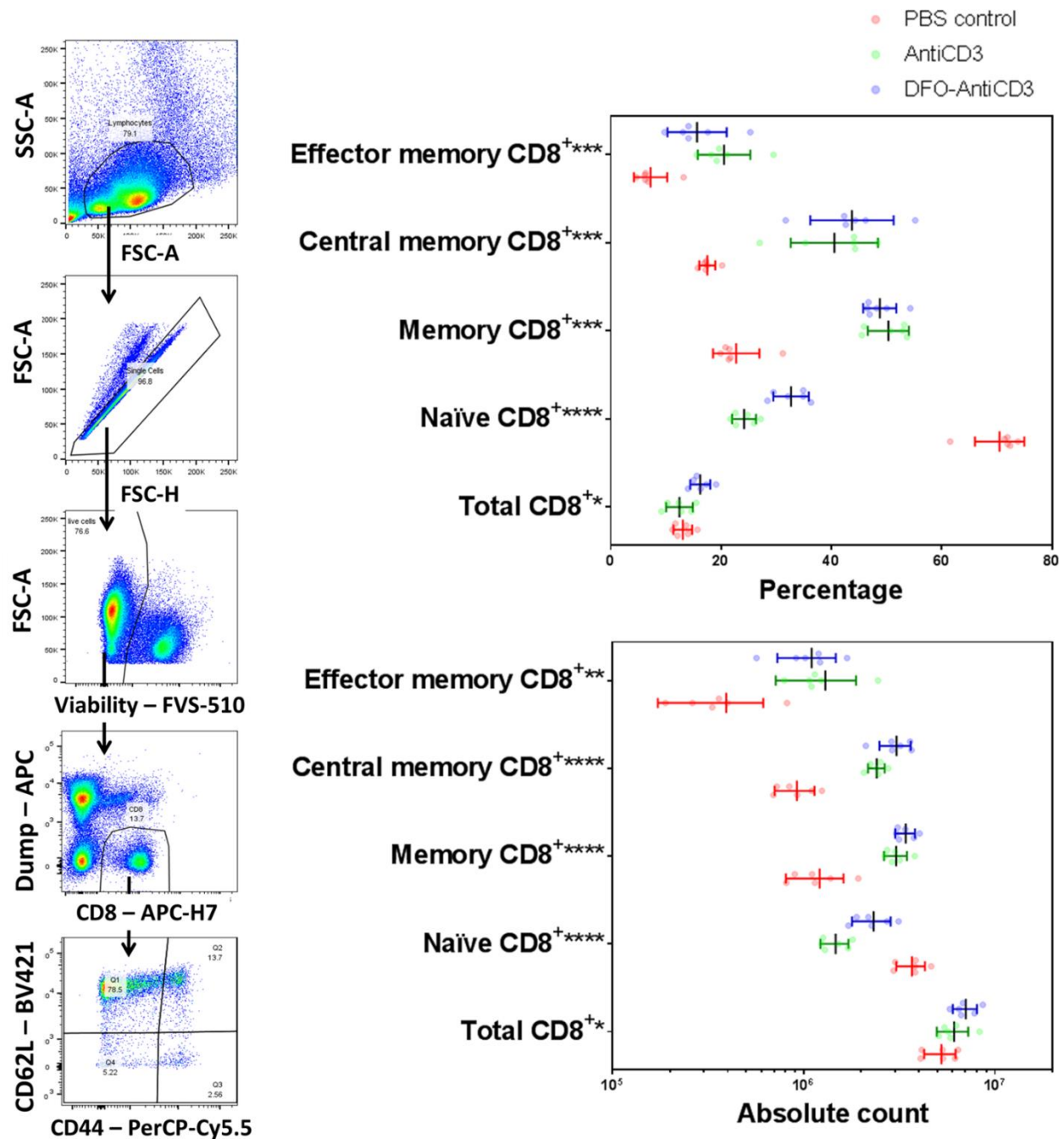


Figure 2.12: Representative gating (left) and immunological effects (right) of DFO-anti-CD3 on CD8⁺ T-cell phenotype distribution. Effects of DFO-anti-CD3 and unconjugated anti-CD3 treatment on frequency of total, naïve, memory, central memory, and effector memory CD8⁺ T-cells in the spleen of C57BL/6J mice are shown. Total CD8⁺ percentages and counts are with respect to all live singlets within the lymphocyte gate.

Naïve, memory, central memory, and effector memory CD8⁺ percentages are with respect to total CD8⁺ populations. For all samples, statistical significance was determined via Kruskal-Wallis with a significance cutoff of * ($P \leq 0.05$), ** ($P \leq 0.01$), *** ($P \leq 0.001$), or **** ($P \leq 0.0001$), with $n = 6$ in all groups. Error bars represent standard deviation from the mean.

	By Percentage (%)							
	PBS Control		Anti-CD3		DFO-Anti-CD3		Kruskal-Wallis Test	
	Mean	SD	Mean	SD	Mean	SD		
Total CD8 ⁺	13.07	1.70	12.45	2.42	16.22	1.80	0.0140	*
Naïve CD8 ⁺	70.48	4.48	24.17	2.18	32.68	3.22	<0.0001	****
Memory CD8 ⁺	22.75	4.19	50.32	3.72	48.77	3.01	0.0005	***
Central memory CD8 ⁺	17.50	1.45	40.53	7.90	43.72	7.56	0.0004	***
Effector memory CD8 ⁺	7.23	3.01	20.53	4.76	15.66	5.35	0.0002	***
	By Absolute Count (x10 ⁶)							
	PBS Control		Anti-CD3		DFO-Anti-CD3		Kruskal-Wallis Test	
	Mean	SD	Mean	SD	Mean	SD		
Total CD8 ⁺	5.24	0.98	6.10	1.14	7.03	1.02	0.0172	*
Naïve CD8 ⁺	3.68	0.63	1.47	2.45	2.32	0.53	<0.0001	****
Memory CD8 ⁺	1.21	0.40	3.04	4.17	3.41	0.40	<0.0001	****
Central memory CD8 ⁺	0.92	0.22	2.41	2.40	3.06	0.57	<0.0001	****
Effector memory CD8 ⁺	0.39	0.22	1.30	5.82	1.10	0.37	0.0018	**

For all samples, statistical significance was determined via Kruskal-Wallis with a significance cutoff of * ($P \leq 0.05$), ** ($P \leq 0.01$), *** ($P \leq 0.001$), or **** ($P \leq 0.0001$), with $n = 6$ in all groups.

Table 2.3. Effects of DFO-anti-CD3 and unconjugated anti-CD3 treatment on frequency of total, naïve, memory, central memory, and effector memory CD8⁺ T-cells in the spleen of C57BL/6J mice are shown.

When comparing population changes between the DFO-anti-CD3 treated group versus the PBS control (S1 Table), we observed a significant decrease in naïve CD8⁺ T cells both in percentage (32.68% vs 70.48%) and total count (2.32×10^6 vs 3.68×10^6). A corresponding increase in memory CD8⁺ T cells by percentage (48.77% vs 22.75%) and count (3.41×10^6 vs 1.21×10^6) was also observed. A deeper look into the central memory and the effector memory populations identified significant changes when comparing DFO-anti-CD3 treated mice against PBS treated mice. Specifically, there was a significant increase in the central memory population (43.72% vs 17.50%, $p < 0.001$) and a significant increase in the effector memory population (15.66% vs 7.23%, $p < 0.001$). All corresponding cell populations from unconjugated anti-CD3 treated

animals trended similarly to the respective cell populations in DFO-anti-CD3 treated animals.

DFO-anti-CD3 decreases total CD4+ T cells and may decrease naïve, central memory, and effector memory populations

Following interrogation of the CD8+ T-cell populations, we next looked at the effects of DFO-anti-CD3 on splenic CD4+ T cells. In contrast to the increases observed in the CD8+ T-cell population, total CD4+ T cells significantly decreased in the DFO-anti-CD3 group when compared against a PBS control (9.02% vs 21.43%, $p < 0.001$, **Table 2.4, S1 Table**). There were no significant differences in the percentages of naïve, total memory, central memory, or effector memory CD4+ T-cell sub-populations between the DFO-anti-CD3 and PBS groups (**Fig 2.13, Table 2.4, S1 Table**). However, all of these populations trended toward a decrease in absolute count for the DFO-anti-CD3 group likely due to the lower initial total CD4+ count. Changes in all CD4+ populations trended similarly between DFO-anti-CD3 and unconjugated anti-CD3 treated groups, without significant differences in frequency or count.

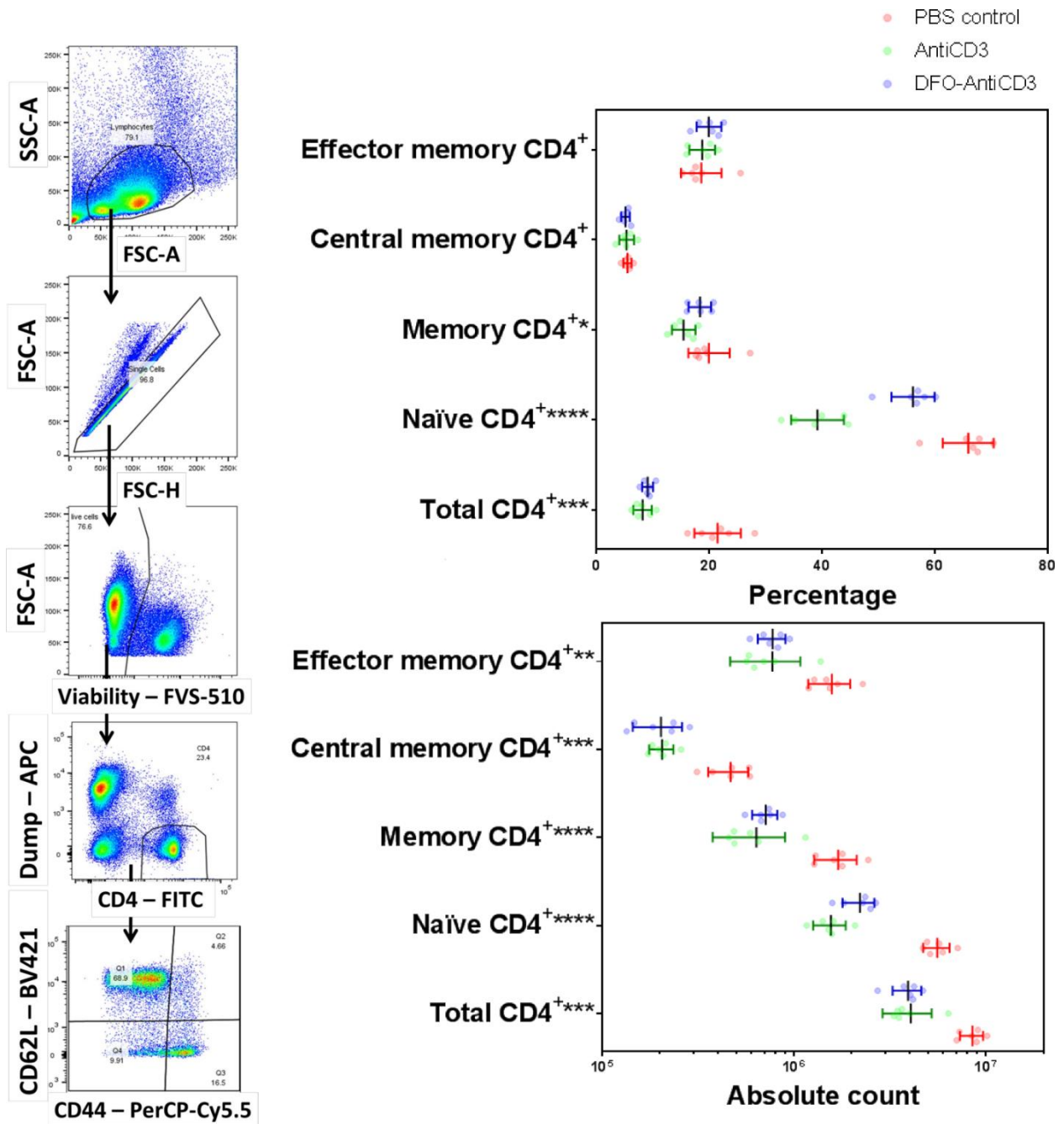


Figure 2.13: Representative gating (left) and immunological effects (right) of DFO-anti-CD3 on CD4⁺ T-cell phenotype distribution. Effects of DFO-anti-CD3 and unconjugated anti-CD3 treatment on frequency of total, naïve, memory, central memory, and effector memory CD4⁺ T-cells in the spleen of C57BL/6J mice. Total CD4⁺ percentages and counts are with respect to all live singlets within the lymphocyte gate. Naïve, memory, central memory, and effector memory CD4⁺ percentages are with respect to total CD4⁺ populations. For all samples, statistical significance was determined via Kruskal-Wallis with a significance cutoff of * ($P \leq 0.05$), ** ($P \leq 0.01$), *** ($P \leq 0.001$), or **** ($P \leq 0.0001$), with $n = 6$ in all groups. Error bars represent standard deviation from the mean.

	By Percentage (%)							
	PBS Control		Anti-CD3		DFO-Anti-CD3		Kruskal-Wallis Test	
	Mean	SD	Mean	SD	Mean	SD		
Total CD4 ⁺	21.43	4.11	8.14	1.63	9.02	0.97	0.0003	***
Naïve CD4 ⁺	65.83	4.52	39.13	4.68	56.05	3.86	<0.0001	****
Memory CD4 ⁺	19.90	3.66	15.40	2.08	18.28	2.02	0.0210	*
Central memory CD4 ⁺	5.46	0.74	5.31	1.31	5.11	0.78	0.8120	ns
Effector memory CD4 ⁺	18.53	3.59	18.70	2.28	19.88	2.20	0.4234	ns
	By Absolute Count (x10 ⁶)							
	PBS Control		Anti-CD3		DFO-Anti-CD3		Kruskal-Wallis Test	
	Mean	SD	Mean	SD	Mean	SD		
Total CD4 ⁺	8.48	1.17	4.05	1.16	3.92	0.67	0.0003	***
Naïve CD4 ⁺	5.58	0.89	1.56	0.30	2.20	0.42	<0.0001	****
Memory CD4 ⁺	1.70	0.43	0.64	0.26	0.71	0.11	<0.0001	****
Central memory CD4 ⁺	0.47	0.11	0.21	0.03	0.20	0.06	0.0006	***
Effector memory CD4 ⁺	1.57	0.39	0.77	0.31	0.78	0.13	0.0015	**

For all samples, statistical significance was determined via Kruskal-Wallis with a significance cutoff of * ($P \leq 0.05$), ** ($P \leq 0.01$), *** ($P \leq 0.001$), or **** ($P \leq 0.0001$), with $n = 6$ in all groups.

Table 2.4. Effects of DFO-anti-CD3 and unconjugated anti-CD3 treatment on frequency of total, naïve, memory, central memory, and effector memory CD4⁺ T-cells in the spleen of C57BL/6J mice.

2.2.3 Discussion

We report a non-invasive immuno-PET imaging study in which ⁸⁹Zr radiolabeled anti-CD3 antibody was used to detect T-cell distributions in healthy mice and tumor-infiltrating T lymphocytes in an immune-competent animal model bearing syngeneic tumors. Our method for targeting CD3 in vivo provides a sensitive and specific imaging technique for detecting peripheral and tumor infiltrating T lymphocytes. To the best of our knowledge, we are the first to elucidate the immunological effects of an anti-CD3 ImmunoPET-agent on systemic T cell populations. Our results demonstrate that the CD3 antigen is a rational target to non-invasively study T cell populations in vivo. Further development of ⁸⁹Zr-DFO-anti-CD3 mAb may be used to evaluate tumor-infiltrating T cells cancer patients and predict their response to therapy.

The design of an ⁸⁹Zr-anti-CD3 immunoPET-agent required the conjugation of a bifunctional chelator to the CD3 antibody¹³⁶. DFO was chosen as the bifunctional

chelator because its complex with Zr^{4+} has high chemical and biological stability¹³⁷. In addition, the radiolabeling of ^{89}Zr with DFO-conjugates takes place at room temperature, which is convenient for protein-based conjugates¹³⁸. The chemical and radiochemical properties of our conjugate were consistent with other ^{89}Zr -DFO-mAb radioimmunoconjugates previously reported^{138–140}.

The ^{89}Zr -DFO-anti-CD3 conjugate demonstrated a remarkable ability to target and detect tumor-infiltrating and peripheral T cells in an immune-competent syngeneic-tumor model. Absolute tumor signal was similar between ^{89}Zr -DFO-anti-CD3 and the isotype control, but the ^{89}Zr -DFO-anti-CD3 showed rapid clearance from the blood and yielded a tumor to blood ratio that was 11.5 times higher than the control. The combination of swift clearance and rapid protein recognition between ^{89}Zr -DFO-anti-CD3 and CD3⁺ T cells resulted in the clear visualization of tumor-infiltrating and peripheral T cells by microPET/CT.

Investigation of the immunological effects of anti-CD3 and DFO-anti-CD3 on total lymphocyte frequency, number, and viability showed modest and non-significant differences compared to the PBS control. A deeper look at the immunological effects of DFO-anti-CD3 on CD4⁺ and CD8⁺ T-cell populations noted a more dramatic difference. For CD4⁺ T cells, DFO-anti-CD3 decreased the total count and percentage of the total CD4⁺ pool. This decrease was observed across all CD4⁺ sub-populations. The implication of this could be a decrease in a CD4⁺ T-cell mediated anti-tumor response, with a potentially diminished cellular (Th1/Th17) or humoral (Th2) immune function. There could also be a potential decrease in the CD4⁺ regulatory T cell population, in turn dampening the regulation of anti-tumor effector T-cell function. Further studies are

needed to identify how DFO-anti-CD3 affects each of these subpopulations, and to determine whether the overall skew is in favor of an anti-tumor immune response.

Conversely, the immunological effects of DFO-anti-CD3 on CD8+ T-cells showed a significant increase in the total CD8+ pool. Our experiments suggest that DFO-anti-CD3 caused phenotypic skewing of CD8+ T cells from naïve into central memory (CM) and effector memory (EM) populations. Both CM and EM cells are able to recognize and target tumors for cytolysis and to yield progeny effector cells that drive a robust cytotoxic response¹¹⁵. The potential benefit of this increase in memory T cell populations is underscored by the association between tumor infiltration of memory T cells and better patient prognosis in several cancers. It is therefore possible that the systemic effects of DFO-anti-CD3 may increase activation of antigen-specific T cells, thereby increasing the number of tumor infiltrating T cell. This increase would further improve imaging capabilities and could provide secondary therapeutic effects. Further studies are needed to confirm this effect, most notably within the tumor microenvironment. Additionally, survival studies are needed to provide direct evidence that DFO-anti-CD3 treatment could have dual roles as both an imaging and therapeutic agent.

Overall, DFO-anti-CD3 demonstrated no significant change in total T cell count, but a depletion of CD4+ T cells and subsequent increase of CD8+ memory T cells. Coincidentally, a higher CD8+ to CD4+ T cell ratio has been associated with better patient prognosis in several cancers^{141–143}.

An anti-CD3 antibody was successfully radiolabeled with ^{89}Zr via DFO chelating agent. ^{89}Zr -DFO-anti-CD3 was found to specifically bind to T-cells populations in healthy mice and was able to detect tumor-infiltrating T lymphocytes in C57BL/6J mice bearing syngeneic tumors. DFO-anti-CD3 showed no change in overall T lymphocyte numbers or viability, but had diminished CD4+ T-cell counts and polarization of the CD8+ T-cell pool towards a memory phenotype. These studies showed that DFO-anti-CD3 could have beneficial immunomodulatory properties favoring a more anti-tumor phenotype. Translation of this CD3-based immunoPET-agent to the clinic could provide actionable information about the tumor immune microenvironment in cancer patients, all while avoiding unwanted and invasive medical procedures.

2.2.4 Materials and methods

Synthesis and characterization of ^{89}Zr -DFO-anti-CD3

An anti-CD3 antibody was modified with p-isothiocyanatobenzyl desferrioxamine (DFO) and radiolabeled with Zr-89 following a previously described method¹³⁸. A detailed description of the synthesis, radiolabeling and characterization of ^{89}Zr -DFO-anti-CD3 can be found in the supplementary information (S1 File).

^{89}Zr -DFO-antiCD3 in vitro binding affinity assay

Immunoreactivity of ^{89}Zr -DFO-antiCD3 was tested by binding saturation assay. C57BL/6J murine splenocytes (1.5×10^6) in microtubes were incubated with increasing concentrations of ^{89}Zr -DFO-antiCD3 (0.4–112 nM). Triplicate microtubes were used for each measuring point. After incubation, the suspension was centrifuged at 2000 x g for 5 min and the supernatant remove. This process was repeat 2 more times. The pellets

were measured for radioactivity using an automatic γ -counter. Binding affinity (K_d) was calculated GraphPad Prism software (GraphPad Software, Inc., California, USA).

Animal model

All animal studies were reviewed and approved by the University of North Carolina Animal Care and Use Committee (IUCAC). C57BL/6J mice (male, 4–6 weeks old, Charles River Laboratories) were used in all of the experiments. Syngeneic bladder tumors in C57BL/6J mice were induced using continuous exposure of 0.05% N-Butyl-N-(4-hydroxybutyl) nitrosamine (BBN) in drinking water^{144,145}. Tumor progression and size were monitored in the bladder by ultrasonography. Once the bladder tumors reached 5–10 mm in diameter, they were harvested and dissociated. Portions of the tumor were resuspended in growth media and plated to a 60mm plastic plate. By repeating passage, syngeneic bladder cancer cell lines, including BBN975, were successfully established and the expression of EpCAM was confirmed by flow cytometry. For immuno-PET and biodistribution assays, each C57BL/6J mouse was injected with 10 million BBN975 cells subcutaneously in the right flank. When tumors reached 50–100 mm³, typically 20–30 days post tumor injection, immuno-PET and biodistribution assays were performed. All animals were humanely sacrificed under CO₂ asphyxiation followed by cervical dislocation, accordingly with UNC Institutional Animal Care and Use Committee (IACUC) protocol.

Biodistribution of ⁸⁹Zr-DFO-anti-CD3, ⁸⁹Zr-DFO-IgG2b, and ⁸⁹Zr-DFO-IgG in healthy C57BL/6J mice

Three groups of healthy C57BL/6J mice ($n = 6$) were intravenously injected via tail vein with 825.1 ± 14.8 kBq (22.3 ± 0.4 μ Ci, ~ 4 μ g, 100 μ L) of ^{89}Zr -DFO-anti-CD3, ^{89}Zr -DFO-IgG2b, or ^{89}Zr -DFO-IgG. Anti-mouse CD3 mAb (BioXCell InVivoMab, clone 17A2) was chosen because of its availability and extensive references. Rat IgG 2b (clone BE0090) was purchased from BioXCell and Rat IgG (clone 02902) was purchased from Life technologies. Three days post-injection, we harvested blood, liver, spleen, axillary lymph node, thymus, and bone. The tissues were weighed and measured for radioactivity using a Capintec CRC-55tW dose calibrator and well counter. Whole tails were also measured for radioactivity to eliminate the variability of injections. Radioactivity measurements from tissues were decay-corrected back to the time of injection. The percent of injected dose per gram of tissue (%ID/g) were calculated using these decay-corrected radioactive counts.

microPET/CT studies of ^{89}Zr -DFO-anti-CD3 in healthy C57BL/6J mice

Healthy C57BL/6J mice were intravenously injected via tail vein with 5.6 ± 0.2 MBq (153.4 ± 4.1 μ Ci, ~ 25 μ g, 100 μ L) of ^{89}Zr -DFO-anti-CD3. At 72 hours post injection the mice were anesthetized with 2% Isoflurane/Oxygen and statically scanned by CT and PET for 30 min. CT imaging was performed at 40kV, 140uA, 360 projections per bed. MicroPET energy window 250–700 keV was used for the experiment. The CT and PET scans were co-registered using AMIDE imaging software.

microPET/CT and ex vivo biodistribution studies of ^{89}Zr -DFO-anti-CD3 and ^{89}Zr -DFO-IgG2 in C57BL/6J mice bearing BBN975 tumors

Two groups of C57BL/6J mice bearing BBN975 tumors (n = 6) were intravenously injected with 6.0 ± 0.1 MBq (162.5 ± 1.8 μ Ci, $\sim 25\mu$ g, 100 μ L) of ^{89}Zr -DFO-anti-CD3 or ^{89}Zr -DFO-IgG2b. At 72h post injection, the mice were anesthetized with 2% Isoflurane/Oxygen and statically scanned by CT and PET for 30 min. After PET/CT scanning, we collected blood, liver, spleen, axillary lymph node, thymus, bone, and tumor from the treated mice. All tissues were weighed, and measured for radioactivity. The percent of injected dose per gram of tissue (%ID/g) and tumor-to-non tumor tissue (T/nT) ratios were calculated. The CT and PET scans were co-registered using AMIDE imaging software.

Tissue dissociation

Spleens were homogenized using the GentleMACs Dissociator and the samples were passed through a 70 μ M cell strainer, followed by homogenization with a 5 mL syringe plunger. The samples were centrifuged for 7 minutes at 1200 RPM, 4°C, decanting the supernatant. The remaining pellet was resuspended into 1 mL of ACK lysis buffer (150 mM NH_4Cl , 10 mM, KHCO_3 , 0.1 mM Na_2EDTA in DPBS, pH 7.3) for 2 minutes at room temperature before quenching with 10 mL of cold media. The samples were centrifuged for 7 minutes at 1200 RPM, 4°C, resuspended in 10 mL of cold media, and passed through a 40 μ M cell strainer. Cell counting was performed by running a diluted aliquot of sample on a MACSQuant flow cytometer, counting lymphocytes as gated by forward scatter area versus side scatter area.

Flow cytometry

Samples were washed and resuspended in cold DPBS, normalized by count, and transferred onto a 96 well V-bottom plate at 1 million lymphocytes per well. Cells were resuspended in FVS510 viability stain (1:1000 dilution in 100 μ L DPBS) for 40 minutes on ice. Wells not receiving viability staining were resuspended in DPBS. Cells were washed twice in staining buffer (0.02% NaN₃, 2% BSA in DPBS), resuspended in 50 μ L Fc block (1:50 dilution in staining buffer), and incubated on ice for 15 minutes. Antibody master mix was added to samples at 50 μ L per sample with final antibody concentrations of: CD3e PE (1:100; 145-2C11), CD8a APC-H7 (1:100; 53–6.7), CD4 FITC (1:200; RM4-5), CD44 PerCP-Cy5.5 (1:200; IM7), CD62L BV421 (1:200; MEL-14), NK1.1 APC (1:100; PK136), CD14 APC (1:100; rmC5-3), CD19 APC (1:100; 1D3). (All mAbs from BD Biosciences). Cells were incubated on ice for 45 minutes and washed twice with staining buffer. Cells were fixed in 2% paraformaldehyde overnight. The following morning, a minimum of 100,000 events were collected for each sample on a BD LSRFortessa flow cytometer.

Flow cytometry analysis

FlowJo flow cytometry software Version 10 was used for analyses of all flow cytometric data (S8A Fig). Lymphocytes were identified on the 2-dimensional scatterplot of forward scatter (FSC)-area by side scatter (SSC)-area, followed by discrimination of singlet cells through FSC-area by FSC-height. Live cells were next identified by negative signal from viability staining. From this population of lymphocytes, T cells were identified as events which were CD19, CD14, and NK1.1 negative and either CD4 or CD8 positive. This strategy for T cell identification was used in place of CD3 staining due to significant decreases in CD3 median fluorescence intensity of anti-CD3 and

DFO-antiCD3 treated animals (S8C and S8D Fig), presumably due to competitive binding of treatment and staining antibodies. Within CD4+ and CD8+ T cell populations, cells were identified as naïve (CD44-, CD62L+), central memory (CD44+, CD62L+), or effector memory (CD44+, CD62L-) (S9 Fig).

Statistical analysis

Data are shown as mean \pm standard deviation. Differences between multiple groups were tested for significance using Kruskal-Wallis test followed by a Bonferroni corrected Mann-Whitney U-test or Dunn's multiple comparison post-test to compare differences between two groups (GraphPad, Prism 5). Non-parametric statistical analysis between two groups was performed using Mann-Whitney U-test (GraphPad, Prism 5). P values ≤ 0.05 were considered significant.

Supplemental material

All supplemental figures and tables cited in Chapter 2.2 are listed according to the original published manuscript, which can be found at <https://journals.plos.org/plosone/article?id=10.1371/journal.pone.0193832#sec023>.

CHAPTER 3: Role of human endogenous retroviruses in the tumor immune microenvironment

3.1 Introduction

Human endogenous retroviruses (hERVs) are remnants of exogenous retroviruses integrated into the primate genome over evolutionary time¹⁷. hERVs share genomic similarities to other retroviruses, including the presence of functional and remnant 5' and 3' long terminal repeats (LTRs), and gag, pro, pol, and env genes. Subsets of recently integrated hERVs still maintain limited translation under physiological and pathological conditions^{18,19,38,146,147}, including evidence for modulation of melanoma, lymphomas, leukemias, and ovarian, breast, prostate, urothelial, and renal carcinomas^{18,20–25,27,148}. Although studies have identified the role of specific hERVs in the pathogenesis and progression of these cancers, to date there have been a limited number of pan-cancer studies elucidating the landscape and impact of hERV expression. A recent study by Rooney et al. analyzed features associated with genes important for immune cytolytic activity, finding that one of these associated features was expression of a small subset of hERVs⁴¹. While this study provided evidence that hERV expression associated with an immune phenotype, the exploration of hERVs was limited by a small reference set, no reported mechanism of association or prognostic impact of hERV expression, and no confirmation of a hERV-specific immune population within any tumor type. Thus, the role of hERVs in modulating the tumor immune microenvironment remains largely unexplored, predominately due to a lack of tools for

identification of full-length, intact hERVs from sequencing data. To fully understand the role of hERVs in antitumor immunity, a more comprehensive database containing greater numbers of individual full-length hERVs is required. Understanding patterns of hERV expression will allow for greater knowledge of the impact of hERVs on tumor-immune interactions, the design of new prognostic models based on hERV signatures, and further identification of tumor-specific hERV epitopes for targeted tumor vaccinations.

Currently, a limited repertoire of tools are available for hERV quantification. There exist several databases of hERV elements, including HERVd, which contains hERV-like elements, and their genomic locations that have been used for analysis of RNA-Seq data^{35,149,150}. Additionally, there are several tools for identification of intra- and intergenic hERV-like elements³⁷, related transposable elements¹⁵¹, and interspersed repeats (RepeatMasker) among human transcripts³⁴. While these resources provide methods to quantify expression of hERV-like elements among transcripts, they do not provide quantification based on an intact, full-length hERV proviral reference. This capability to distinguish and quantify individual hERVs provides a useful tool to classify hERVs into distinct groups based on biological associations in various cancers.

Recently, Vargiu et al. compiled a database of 3,173 intact, full-length hERV sequences and developed a comprehensive method for classifying these sequences into 11 superfamilies (Supplemental Table 1)³⁸. Using this database as a reference, we designed a computational workflow for identifying the expression of specific hERVs from RNA sequencing (RNA-Seq), hervQuant, and quantified hERV expression within the Cancer Genome Atlas (TCGA) pan-cancer dataset. We assessed interactions of

specific hERVs with immune and clinical features. Among all cancer types encompassed within the pan-cancer dataset, clear cell renal cell carcinoma (ccRCC, designated by TCGA as KIRC) contained the greatest number of prognostic hERVs. Thus, we explored two mechanisms by which hERV expression may influence the tumor immune microenvironment in ccRCC: (i) activation of RIG-I-like pathway signaling and (ii) hERV epitope-triggered T and B cell activation. Using biological classes of hERV signatures derived from these two mechanisms, we further demonstrated the ability of hERV expression to predict patient survival in a multivariate regression model, independent of traditional clinical staging and molecular subtyping. Last, we used a publicly available ccRCC ribosome profiling (Ribo-Seq) dataset¹⁵² to screen for translation of tumor-specific hERV epitopes, validated their capacity to bind HLA in vitro, and demonstrated the presence of tetramer-positive epitope-specific T cells within ccRCC tumors. We found tumor-specific hERV expression to be associated with clinical response to PD-1 axis inhibition in ccRCC patients, suggesting that hERV expression may provide a biomarker for immunotherapy responsiveness and hERV viral proteins may provide targetable, tumor-specific epitopes. The information gained from hERV expression profiling gives new insight into the role of hERVs within tumor-immune microenvironment interactions and provides evidence for hERV expression-based molecular models for patient prognosis and responsiveness to immunotherapy.

3.2 Results

Expression and association of hERVs in TCGA pan-cancer.

TCGA pan-cancer hERV expression was determined using hERVQuant, described in detail in the Supplemental Notes (**Figure 3.1A** and Supplemental Figures 1 and 2).

For consistency, only samples sequenced by Illumina NextSeq at 2 × 50 bp were analyzed, resulting in complete removal of ESCA, GBM, OV, and STAD and partial removal of COAD, UCEC, and READ subtypes (see Supplemental Table 2 for tumor abbreviations). All 3,173 reference hERVs were expressed in at least one sample, encompassing all 11 superfamilies and 3 lineages (Supplemental Table 1). Relative hERV expression patterns were strikingly homogenous across all cancer types (**Figure 3.1B** and Supplemental Figure 3). Among all cancer types, TGCT demonstrated the greatest mean and median hERV expression, while LIHC, ACC, and UVM ranked last (Supplemental Figure 4). To identify similar hERV expression patterns across models, we calculated the Euclidean distance of mean hERV expression between each cancer type (**Figure 3.1B** and Supplemental Figure 5). Tumor types with lowest overall hERV expression (LIHC, ACC, UVM) were closely related by unsupervised clustering and shared very low similarity with all other tumor types. Two large clusters comprised 10 (PCPG, SKCM, CHOL, SARC, THYM, DLBC, PRAD, THCA, KICH, and LGG) and 8 (LUAD, PAAD, BLCA, CESC, MESO, UCEC, UCS, and BRCA) cancer types. While several cancer types demonstrated similar hERV expression patterns based on tissue location (UCEC and UCS, HNSC and LUSC, KIRC and KIRP, and READ and COAD), the clustering observed between various tumor types suggests that hERV expression may be conserved among cancers across a variety of tissues. Notably, two tumor types with immune-privileged tissues of origin (TGCT and UVM) demonstrated lower similarities to all other cancers. Lack of immune interactions within these native tissues may potentially result in unique hERV expression profiles in these tumors, suggesting that shared hERV expression profiles within other tumor types may be shaped by the

presence of related tumor immune responses.

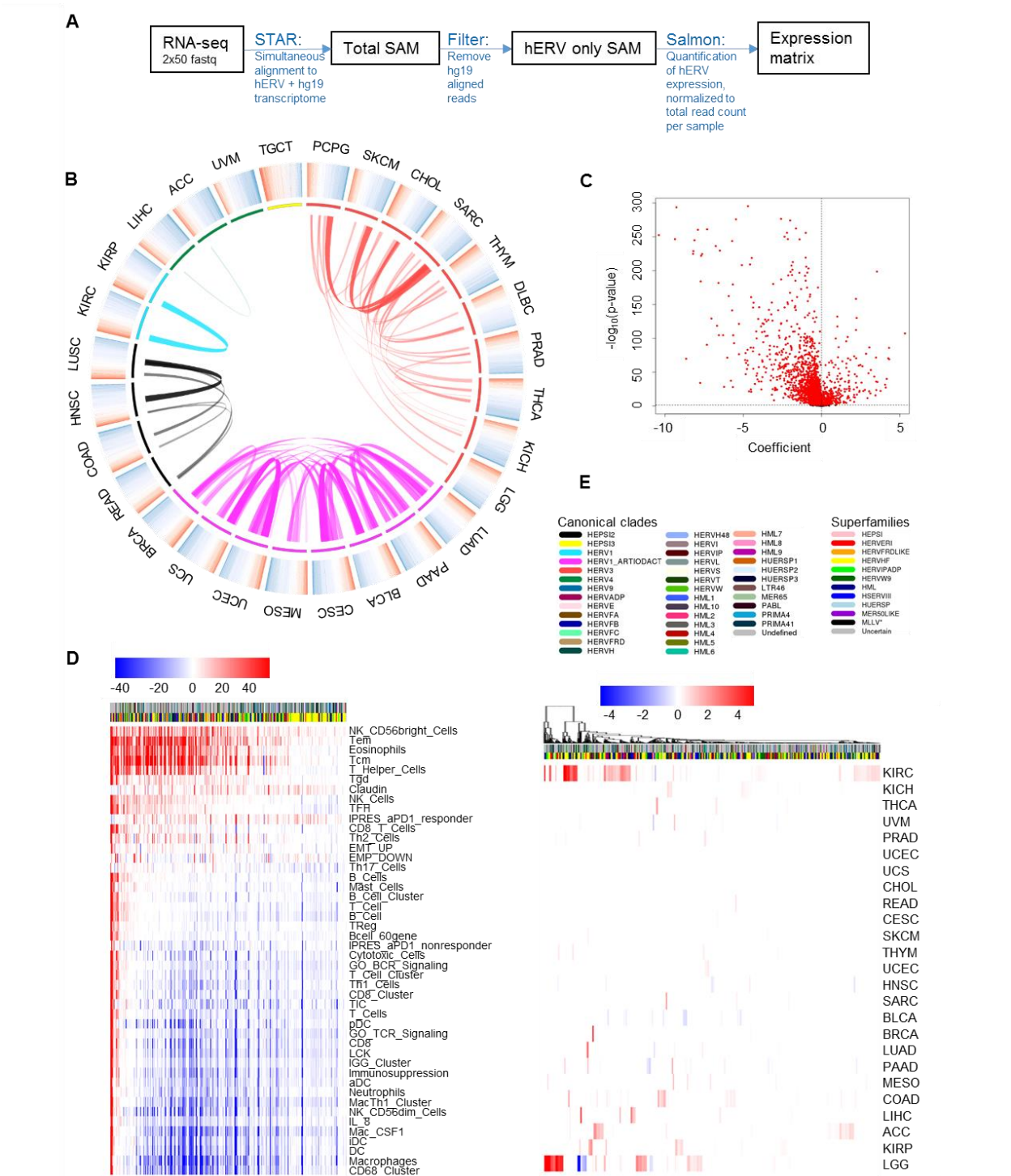


Figure 3.1: Human endogenous retrovirus expression and association in TCGA pan-cancer dataset. (A) Schematic of the hervQuant workflow. (B) hERV expression displayed by heatmaps in the outermost layer, ranked by mean expression across the pan-cancer

dataset. Tumor groups shown in the middle ring, with colors representing clusters determined from a cut-tree (height = 140) of hierarchical clustering of Euclidean distance of mean hERV expression between each cancer type. Innermost lines represent hERV expression pairwise Euclidean distance ≤ 40 between tumor types. Opacity and width of inner lines increase with greater similarity. (C) Volcano plot of association (GLM) between read-normalized hERV expression and the mean of the methylation β coefficient, with GLM coefficient along the x axis and $-\log_{10}$ FDR-corrected P value along the y axis. (D and E) Association (GLM) between read-normalized hERV expression and (D) IGS expression and (E) survival among TCGA pan-cancer dataset. FDR- (D) or Bonferroni-corrected (E) P represented by intensity of color and direction of coefficient represented by color (red, positive; blue, negative). Color bar displays hERV superfamily and canonical clade classifications. (D) Rows and columns are ordered by number of significantly positive associations. (E) Survival analysis filtered by hERVs and tumor types with at least 1 significant comparison. See Supplemental Table 2 for number of samples per TCGA cancer cohort.

Overexpression of specific hERVs within tumors has been attributed to epigenetic demethylation of genes associated with provirus expression, which can be triggered through the use of epigenetic modulatory agents^{27,28,153–156}. hERV expression was highly associated with Illumina Methylation450K-derived methylation patterns, with the majority of hERVs significantly associated with demethylation (2,639 hERVs with generalized linear model [GLM] FDR-corrected $P \leq 0.05$; 2,205 with coefficient < 0 ; 434 with coefficient > 0 ; **Figure 3.1C**).

We next examined the association between hERV expression and immune features, age, and survival among tumor types. We first performed multivariable linear regression of hERV expression by cancer type with 46 immune gene signatures (IGS) previously described in the literature^{83,100,101,157–159} (**Figure 3.1D** and Supplemental Figure 6). A small population of hERVs demonstrated near ubiquitous positive or negative association with all IGS, with the majority of hERVs showing a split association pattern. Included among IGS that demonstrated positive association with the majority of significant hERVs (GLM FDR-corrected $P < 0.05$) were those associated with immune

cells known to have antitumor effector function, including effector and central memory T cells and NK cells. Additionally, a signature of anti-PD-1 (aPD1) responsiveness (IPRES_aPD1_responder) was positively associated with hERV expression in 79.2% (1,472 of 1,858) of significantly associated hERVs, while a signature for nonresponder tumor biopsies (IPRES_aPD1_nonresponder) was negatively associated with all hERV expression in 83.0% (1,679 of 2,024) of significantly associated hERVs⁸. We next examined the association between hERV expression and age, controlling for tumor type, and observed that the majority of significantly associated hERVs demonstrated negative association between expression and patient age (GLM FDR-corrected $P < 0.05$; 150 with coefficient <0 ; 13 with coefficient >0 ; Supplemental Figure 7). To elucidate whether hERV expression associated with clinical outcome, we performed Cox's proportional hazard regression (CoxPH) for hERV expression across all cancer types. Association of survival with mean hERV expression identified 3 tumor types with prognostic mean hERV expression (KICH, COAD, and KIRC). In all 3 tumor types, mean hERV expression was negatively prognostic (Supplemental Figure 8). Additionally, we examined Kaplan-Meier survival curves for each TCGA cancer type split by upper versus lower 50th percentile mean hERV expression, and observed 5 cancer types with significant separation of survival curves (Supplemental Figure 9; BLCA, COAD, KICH, KIRC, and PCPG; log-ranked $P < 0.05$). Among these 5 cancer types, KIRC was the most associated with survival. All cancer types except BLCA demonstrated shorter survival in patients with greater mean hERV expression. To perform a more detailed analysis, we associated survival with expression of each individual hERV (**Figure 3.1E** and Supplemental Figure 10). TCGA KIRC (ccRCC), a

tumor type in which several hERVs have been shown to be actively translated^{27,31,32,42}, constituted 25.1% of all significantly prognostic hERVs, with over 1.5x more significant hERVs than the next highest cancer, LGG (KIRC: 362; LGG: 230; **Figure 3.1E**). To elucidate the immune mechanisms behind this enrichment of prognostic hERVs in ccRCC, we focused on this cancer type for the remainder of our analyses.

hERV expression in ccRCC demonstrates evidence of immune stimulation through RIG-I-like signaling.

Several groups have demonstrated that activation of select endogenous retroviral elements can trigger signaling through innate immune sensors, including double-stranded RNAs (dsRNA) that subsequently signal through cytosolic RIG-I-like receptors^{28,156}. To elucidate a more comprehensive role for hERVs in the RIG-I-like pathway in ccRCC, we studied the association between hERV expression and genes in the RIG-I-like receptor signature (Molecular Signatures Database)¹⁶⁰, observing marked separation of genes into 2 groups by hierarchical clustering (**Figure 3.2A**). We defined 2 hERV groups (1 and 2; Supplemental Table 3) based on the ratio between each hERV's mean linear regression coefficients within each gene cluster (>1 or <1) and validated their definitions using principal component analysis (**Figure 3.2B**). While both groups demonstrated significant positive association between hERV expression and genes that activate the RIG-I-like pathway, group 2 hERVs demonstrated a significant positive association with several key antagonist genes downstream of NF- κ B signaling (most notably NFKBIB), along with a significant negative association to key agonistic genes in NF- κ B signaling (e.g. TBK1, TANK, and AZI2). CoxPH of hERV expression within TCGA KIRC provided further evidence that these groups are biologically distinct, with

the majority of group 1 and 2 hERVs providing association with longer and shorter overall survival, respectively (**Figure 3.2C**). In addition, group 2 and non-prognostic group 1 hERVs (CoxPH Bonferroni-corrected $P > 0.05$) demonstrated a significant positive association with the majority of IGS (93%, 57%, and 60%, respectively), while prognostic group 1 hERVs (Bonferroni-corrected $P \leq 0.05$; majority associated with longer overall survival) largely demonstrated a negative association with IGS (33%), including those for T cells, B cells, dendritic cells, macrophages, and NK cells (**Figure 3.2D** and Supplemental Figure 11). Despite these negative association patterns with IGS observed in prognostic group 1 hERVs, TCGA KIRC samples with greater expression of these hERVs had decreased ratios of Treg to CD8+ IGS (Treg IGS divided by the mean of 3 CD8+ IGS) compared with any other hERV group, suggesting the immune infiltrate associated with prognostic group 1 hERVs was less immunosuppressive than that of non-prognostic group 1 and group 2 hERVs (Supplemental Figure 12). Additionally, prognostic group 1 hERVs demonstrated positive association with signatures for Th17 T cells, which have been associated with a more favorable prognosis in ccRCC¹⁶¹. Overall, this analysis provided the first evidence to our knowledge for biologically distinct hERV groups that differentially interact with innate immune sensing, with differential downstream prognostic and immunological effects and prognostic associations.

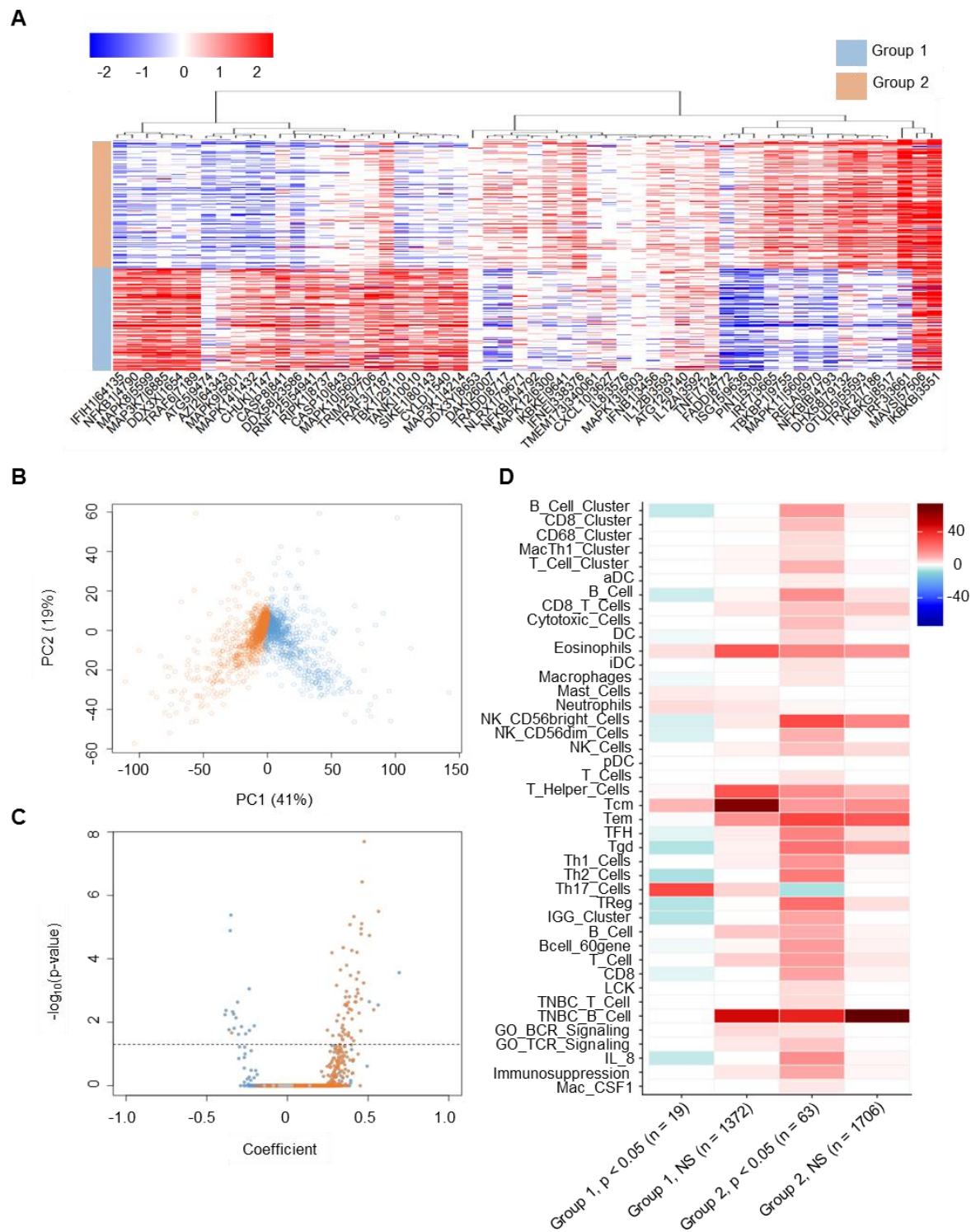


Figure 3.2: Mechanism of hERV-mediated RIG-I-like pathway signaling in ccRCC. (A) Heatmap of association (GLM) between hERV expression and RIG-I-like pathway-associated genes. FDR-corrected $-\log_{10}(\text{P value})$ represented by intensity of color, and direction of coefficient represented by color (red: positive, blue: negative). Group 1 (blue)

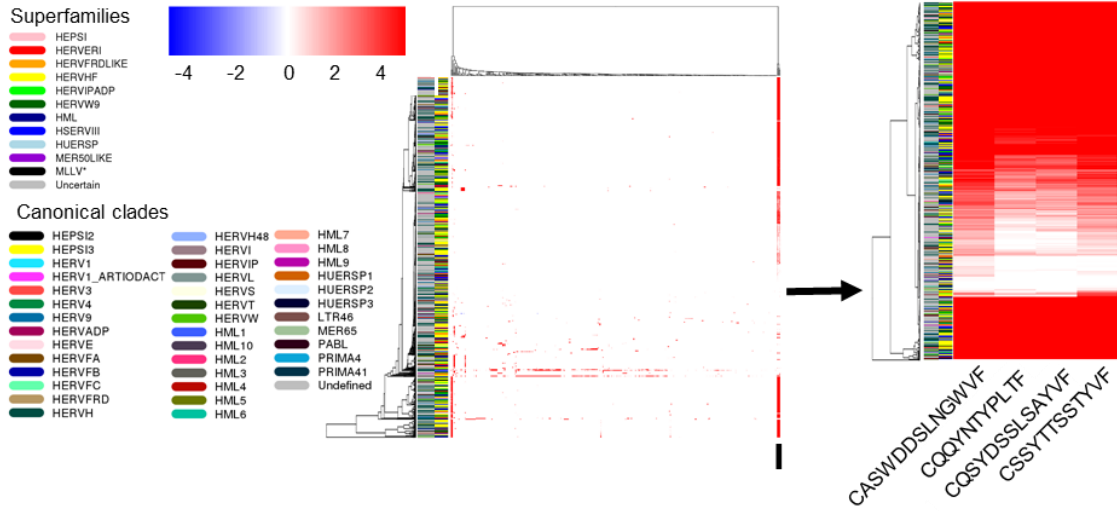
and 2 (orange) hERVs are represented by color along the left-side color bar. (B) PC1 versus PC2 from PCA of association matrix in A between hERV expression and RIG-I-like pathway-associated genes from for group 1 and 2 hERVs. Percentage of variance for principal component 1 (PC1) and PC2 is shown in parentheses along each axis. (C) Volcano plot of CoxPH analysis of UQN hERV expression as a predictor of survival, with Bonferroni-corrected $-\log_{10}(\text{P value})$ displayed as a function of hazard ratio for each hERV. Dashed horizontal line represents FDR-corrected $P = 0.05$. (B and C) Groups 1 and 2, and other hERVs defined from A (group 1: blue; group 2: orange; neither: gray). (D) Heatmap of association (GLM) between expression of IGSs with group 1 and 2 hERV signatures (average expression), split by either significant or nonsignificant association with patient prognosis. FDR-corrected P values represented by intensity of color, and direction of coefficient represented by color (red, positive; blue, negative).

hERV expression in ccRCC demonstrates evidence of B cell activation.

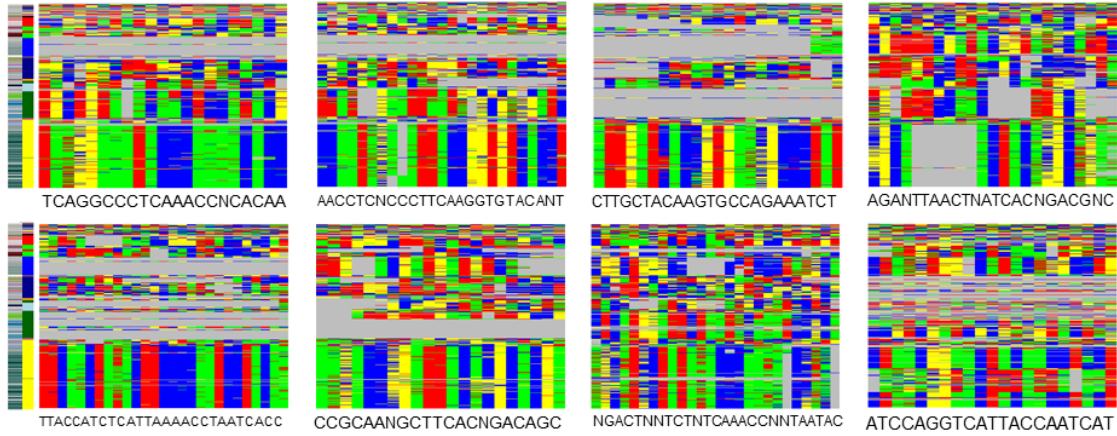
In addition to innate immune sensor signaling, hERVs can trigger antitumor immunity through tumor-specific expression of viral epitopes. In cancer patients, high antibody titers have been known to develop against hERV proteins with specificity of expression within the tumor, with little else known regarding the role of this B cell response³⁰. To determine whether hERVs show evidence of an adaptive immune response in ccRCC, we identified T/B cell clonotype repertoires in TCGA KIRC using MiXCR and filtered on T/B cell receptors (TCRs/BCRs; defined as shared CDR3 amino acid sequence) observed in $\geq 10\%$ of patients¹⁶². These filtering criteria resulted in no shared TCR clonotypes, suggesting potentially low sensitivity of detection for MiXCR-derived TCR data in RNA-Seq data. In contrast, 437 shared BCRs were identified, of which 397 were significantly associated with expression of ≥ 1 hERV (**Figure 3.3A**, left). Within this pool, 4 clones had significant positive association with the expression of 1,207 hERVs, suggesting a potential hERV epitope-driven B cell response (**Figure 3.3A**, right, and Supplemental Table 3). Differential superfamily distribution patterns were observed between BCR-associated and non-BCR-associated hERVs, suggesting certain superfamilies may have a greater propensity for triggering B cell activation

(HERVERI, HML, HSERVIII, and HERVW9; FDR-corrected χ^2 test $P \leq 0.05$; Supplemental Figure 13). Furthermore, multiple sequence alignment (Clustal Omega) of proviral sequences from these BCR-associated hERVs identified large regions of high sequence identity (Supplemental Figure 14). Filtering on sequence identity of $\geq 25\%$ of all BCR-associated hERVs with a sequence length ≥ 21 base pairs (the approximate minimal length necessary for immunoglobulin CDR3 region specificity)¹⁶³, we observed 8 regions of conserved DNA similarity (**Figure 3.3B**). NIH Retrovirus Protein BLAST (<https://www.ncbi.nlm.nih.gov/genome/viruses/retroviruses/>) of these sequences showed similarity to known hERV env genes in 8 of 8 sequences, with additional similarity to other retroviral genes in 2 of 8 sequences. While suggestive of potentially targetable antigens within the hERV env region, CoxPH demonstrated significantly higher hazard ratios among BCR-associated compared with non-BCR-associated hERVs (Welch's t test $P = 2.4 \times 10^{-3}$; **Figure 3.3C**). Differential expression analysis (DESeq2) of BCR-associated hERVs demonstrated a balanced proportion of hERVs with both higher tumor-to-matched normal and matched normal-to-tumor expression (tumor: $n = 542$; matched: $n = 72$; **Figure 3.3D**), suggesting an overall lack of tumor specificity among BCR-associated hERVs.

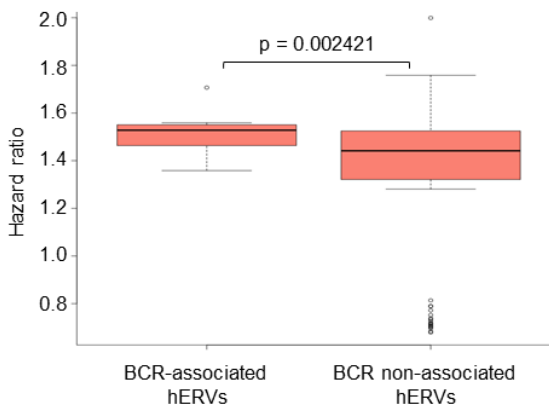
A



B



C



D

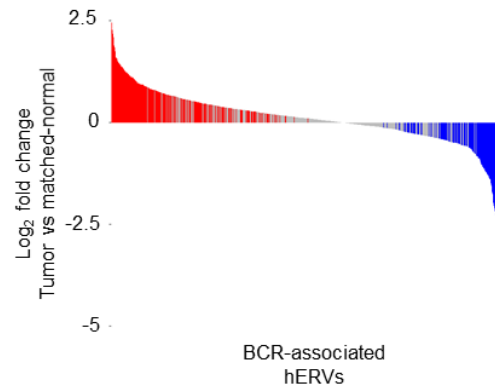


Figure 3.3: hERVs associated with expression of BCR clonotypes are negatively prognostic in ccRCC. (A) Heatmap of association (GLM) between hERV expression and expression of B cell clonotypes, displaying all TCRs and BCRs that demonstrate association (left, FDR-corrected $P \leq 0.05$) and a magnified view of the top 4 B cell clones

with highest numbers of significantly associated hERVs (right, underscored by black box to the bottom left). FDR-corrected P values represented by intensity of color and direction of coefficient represented by color (red: positive, blue: negative). (B) Multiple sequence alignment of areas of DNA identity in $\geq 25\%$ of hERVs (all hERVs significantly associated with the top 4 B cell clones) and ≥ 24 base pairs in length (minimum BCR epitope length). Base pair sequences displayed by color (A: blue; T: red; C: green; G: yellow; gap: gray) and sequence below. y axis order is conserved in all plots. (A and B) Color bars at left show superfamily and canonical clade classification. (C) Hazard ratios among all hERVs significantly associated to the top 4 B cell clones (left) or non-BCR-associated hERVs (right) within TCGA KIRC, with Welch's t test P value displayed. Data represent median (middle line), with boxes encompassing the 25th to 75th percentile, whiskers encompassing 1.5x the interquartile range from the box, and outliers shown by dots. (D) Waterfall plot displaying the log2 fold change in mean expression of hERVs associated with the top 4 B cell clones in the tumor compared with matched normal tissue. FDR-adjusted P value significance ($P \leq 0.05$) from DESeq2 analysis displayed in red (positive fold difference), blue (negative fold difference), and gray (nonsignificant).

hERV signatures of innate and adaptive immune activation provides prognostic value in ccRCC.

Currently, clinical stage is the most robust prognostic variable for ccRCC. While molecular features such as M1–M4 molecular subtyping have been shown to be potentially prognostic, no molecular markers have been widely adapted for clinical decision making in ccRCC, making identification of a robust molecular marker for prognosis an appealing goal¹⁶⁴. Throughout this study, we identified pools of hERVs with evidence of both RIG-I-like-mediated innate immune activation and inhibition, as well as B cell-mediated adaptive immunity (**Figure 3.4A,B**). To provide evidence that these classes can be used to generate a model of clinical outcome in ccRCC, we derived signatures corresponding to the mean expression of prognostic hERVs (CoxPH Bonferroni-corrected $P \leq 0.05$) within each class. According to log-rank test, Kaplan-Meier overall survival curves for patients within the upper versus lower 50th percentiles for each of the 3 signatures were significantly different (RIG-I-like upregulated [up]: $P = 4.5 \times 10^{-10}$; RIG-I-like downregulated [down]: $P = 6.3 \times 10^{-14}$; BCR-associated: $P = 1.1$

$\times 10^{-5}$; **Figure 3.4C**). Patients with both higher expression of RIG-I-like down and BCR-associated signatures had significantly shorter overall survival, while those with higher expression of the RIG-I-like up signature had longer overall survival. Recent analyses also provided metrics for disease-specific survival (DSS) and progression-free interval (PFI) in TCGA KIRC, additionally with an underpowered reporting of disease-free interval (DFI)¹⁶⁵. Of these metrics, DSS and PFI trended similarly to curves observed with overall survival, providing further evidence that these hERV signatures are specifically associated with disease burden (Supplemental Figure 15). We performed multivariable CoxPH modeling with clinical stage and with or without molecular subtype (M1–M4) and hERV signatures as predictors for patient outcome in TCGA KIRC. Comparing a full model against an all-but-one-feature model, all 3 signatures provided significant prognostic value in addition to stage and molecular subtype, with the RIG-I-like down signature contributing nearly as much prognostic power as traditional staging and each of the 3 signatures providing greater prognostic power than molecular subtyping (**Figure 3.4D** and Supplemental Table 4). To establish whether these hERV signatures were prognostic in other tumors, we performed univariable CoxPH for each signature within all TCGA cancer types (**Figure 3.4E**). Among these 3 signatures, BCR-associated hERVs were additionally prognostic in COAD and LGG, while RIG-I-like down hERVs were additionally prognostic in BLCA, COAD, KIRP, LGG, and LIHC, suggesting these additional cancer types may have hERV–immune microenvironment interactions similar to those in ccRCC. Included among these cancer types were KIRP and COAD, both of which were closely related to KIRC by hierarchical clustering of

hERV expression patterns (Supplemental Figure 5), and LGG, which contained the second greatest number of prognostic hERVs after KIRC (Figure 1E).

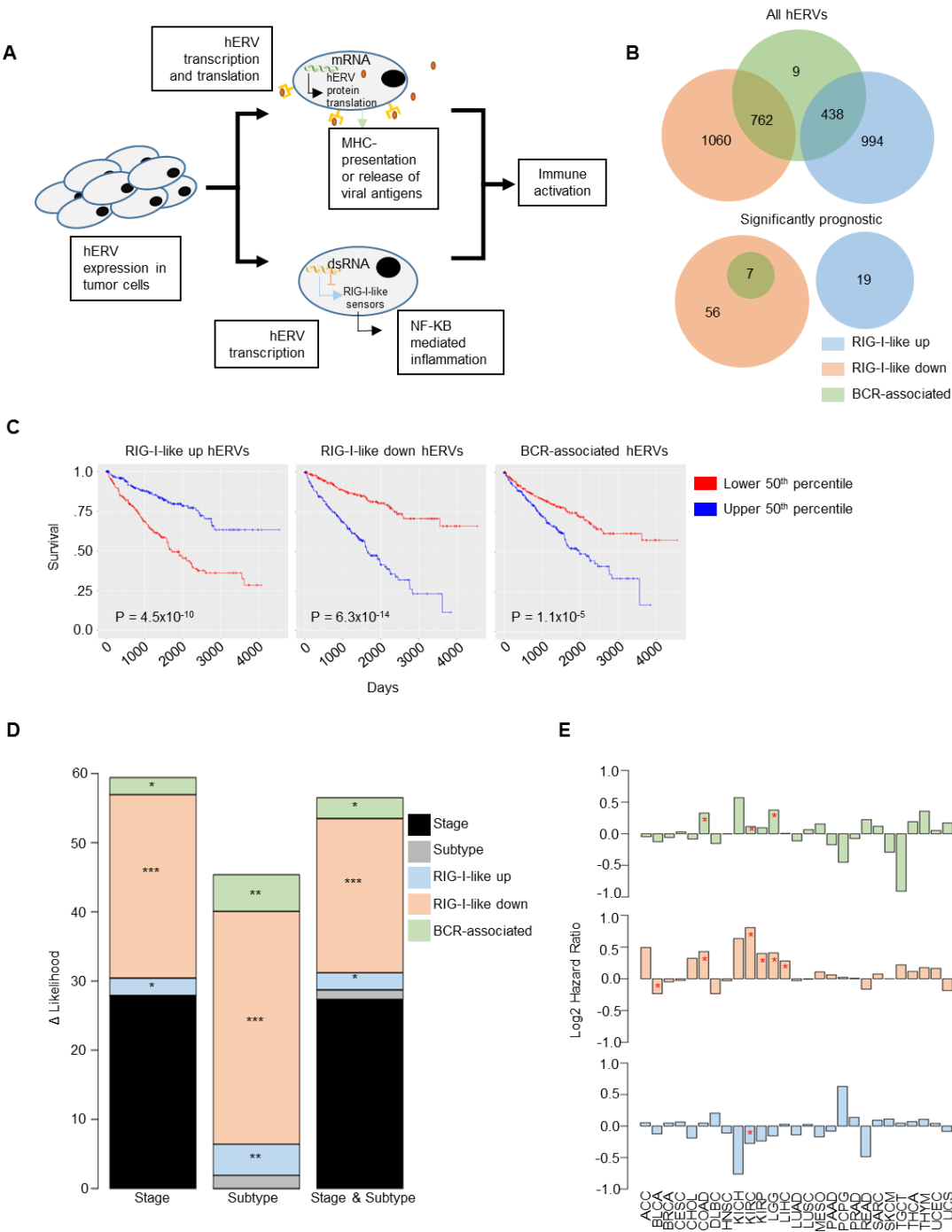


Figure 3.4: Immune-related hERV signatures are prognostic for patient overall survival. (A) Schematic summary of hERV interactions with the immune system in the context of

an anti-tumor immune response. (B) Venn diagram showing the number hERVs significantly associated (GLM, FDR-corrected $P < 0.05$) with genes corresponding to the upregulation (blue) or downregulation (orange) of the RIG-I-like pathway or positively associated (GLM, FDR corrected $P < 0.05$) with expression of B cell clones (green). (C) Kaplan-Meier survival curves for TCGA KIRC patients split by the upper (blue) and lower (red) 50th percentile of expression for each of the 3 hERV group signatures represented in A. (D) Change in multivariable CoxPH log-likelihood ratios in TCGA KIRC using clinical stage and/or M1–M4 molecular subtyping and the 3 classes of hERV groups represented in B as predictors for survival. Stacked bars show the change in likelihood ratio for each feature when removed from the full model, as well as the χ^2 test P value for each hERV group signature when removed from the full model (* $P \leq 0.05$, ** $P \leq 0.01$, *** $P \leq 0.001$). (E) Univariable CoxPH coefficients for hERV signatures as a predictor for overall survival among each cancer type. FDR-corrected P value represented by red asterisks (* $P \leq 0.05$).

hERVs demonstrate evidence of tumor-specific presentation of targetable viral epitopes.

Previous studies have identified select tumor-specific hERV epitopes in ccRCC that trigger in vitro antitumor responses with limited in vivo efficacy^{31,32,42}. Studies regarding neoantigens have suggested that a large number of potential epitopes are required for screening in order to identify a few clinically relevant peptides with significant in vivo antitumor efficacy^{15,70,166,167}. We examined hERV expression patterns between tumors and matched normal tissue within TCGA KIRC and observed that normal samples clustered together (Supplemental Figure 16). The majority of hERVs were heavily upregulated in tumor compared with matched normal samples, leading us to hypothesize that there may be many more differentially expressed and targetable hERVs within tumor than previously described. In an attempt to expand the potentially targetable hERV epitope pool in ccRCC, we first ranked hERVs based on fold change in expression between tumor and matched normal samples (Supplemental Figure 17)¹⁶⁸. Notably, CT-RCC hERV-E (HERVERI/gammaretrovirus-like, designated as hERV 2256 in the reference database, also known as ERVE-4), one of the few hERVs demonstrated to be capable of eliciting a vaccine-inducible CD8+ T cell response, ranked second highest in tumor versus normal fold change in expression^{31,32,42}. This

same hERV was previously described by Rooney et al. (ERVE-4) and was found to be significantly upregulated in ccRCC and associated with a signature of cytotoxicity⁴¹. To ensure that our analyses were consistent with these previously published findings, we performed linear regression between CT-RCC hERV-E and IGS expression including the Rooney signature for cytotoxicity (CYT), and observed a significant association between expression of this hERV and the majority of IGS in our set, including CYT (Supplemental Figure 18).

Similar to the pattern observed in CT-RCC hERV-E, hERVs that were overexpressed within tumors were ubiquitously positively associated with IGS, while those that demonstrated overexpression within matched normal tissue demonstrated a mixed association pattern (FDR-corrected $P \leq 0.05$; **Figure 3.5A**), suggesting that preferential hERV expression in the tumor may facilitate immune activation. Interestingly, none of the top 10 hERVs by tumor versus normal expression were significantly associated with TCR/BCR clonotype expression or with survival. Given that (i) these hERVs were significantly associated with immune activation and (ii) there is evidence of functional epitopes and public hERV-specific T cells in at least one of these hERVs (CT-RCC hERV-E), the inability to computationally detect TCRs/BCRs significantly associated with these hERVs suggests we lacked the sensitivity necessary to identify these hERV-specific TCR/BCR clones. This lack of detectable public adaptive immune response is also characteristic of neoantigens, which despite failing to show association with TCR/BCR expression and survival in the absence of immunotherapy in ccRCC, have been recently demonstrated to provide vaccine-induced efficacy in melanoma^{14,15}.

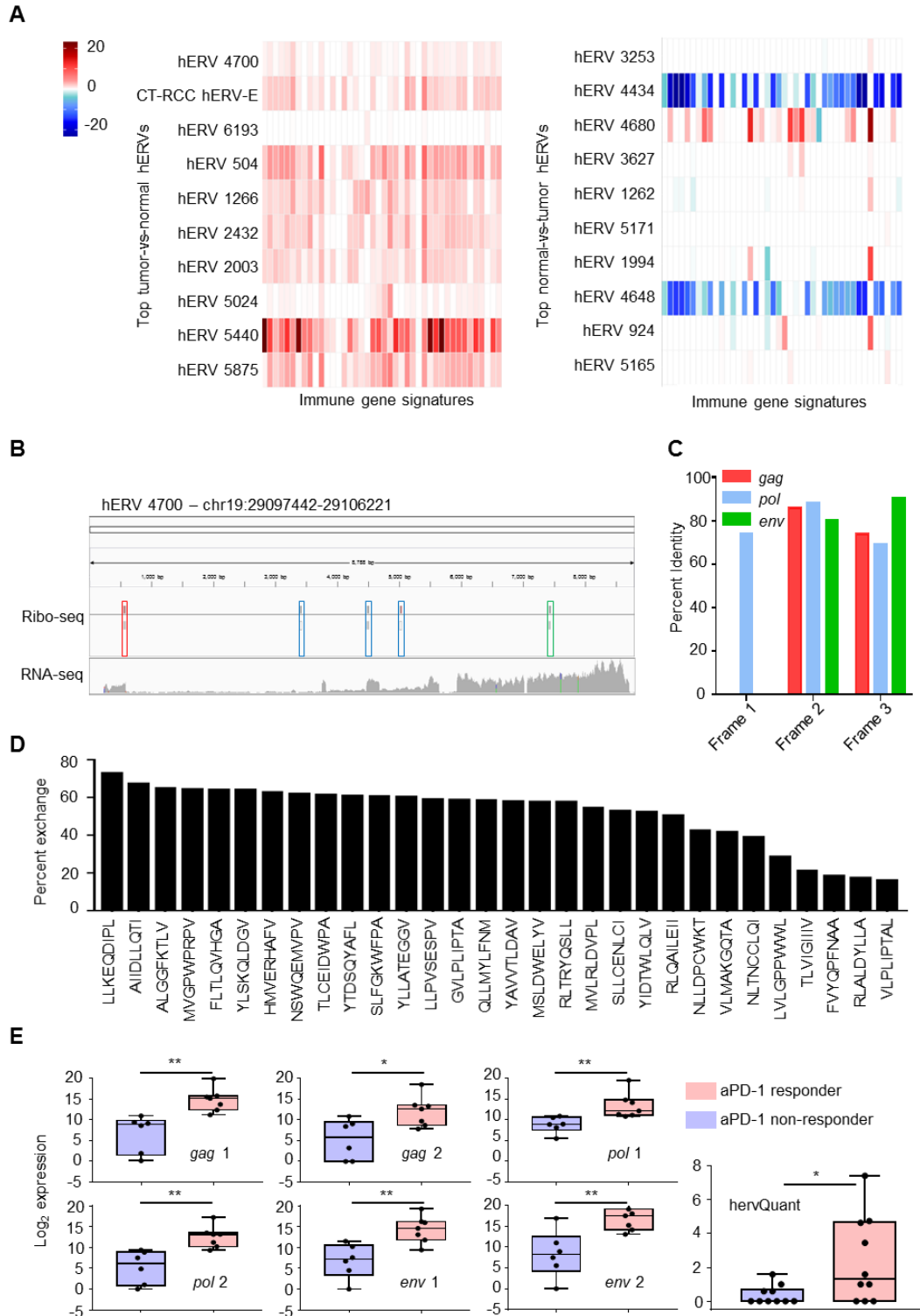


Figure 3.5: hERVs demonstrate evidence of targetable epitope expression in ccRCC. (A) Association (GLM) of the 10 most positively (left) and negatively (right) differentially expressed hERVs (TCGA KIRC tumor relative to matched normal tissue) with IGS

expression. FDR-corrected P values represented by intensity of color and direction of coefficient represented by color (red: positive, blue: negative). (B) Read coverage from ccRCC Ribo-Seq data for hERV 4700, demonstrating read coverage of coding regions for gag (red), pol (blue), and env (green) genes. (C) Percent identity between all reading frames of translated amino acid sequences from the reference gag (red), pol (blue), and env (green) sequences for hERV 4700 with known hERV proteins in the NIH retroviral protein BLAST database. (D) Exchange efficiency for HLA-A*02:01 monomer UV exchange of predicted hERV 4700 epitopes. (E) Left: RT-qPCR (responders: n = 7; nonresponders: n = 6) log₂ expression of hERV 4700 gag, pol, and, env sequences. Right: hervQuant-derived (responders: n = 10; nonresponders: n = 10) hERV 4700 expression in Nivolumab-treated (aPD1-treated) ccRCC tumor biopsies. Statistical analysis performed using Mann-Whitney U test (*P ≤ 0.05, **P ≤ 0.01, NS: P > 0.05). Data presented as values (dots) and median (middle line), with boxes encompassing the 25th to 75th percentile and whiskers encompassing minimum to maximum values.

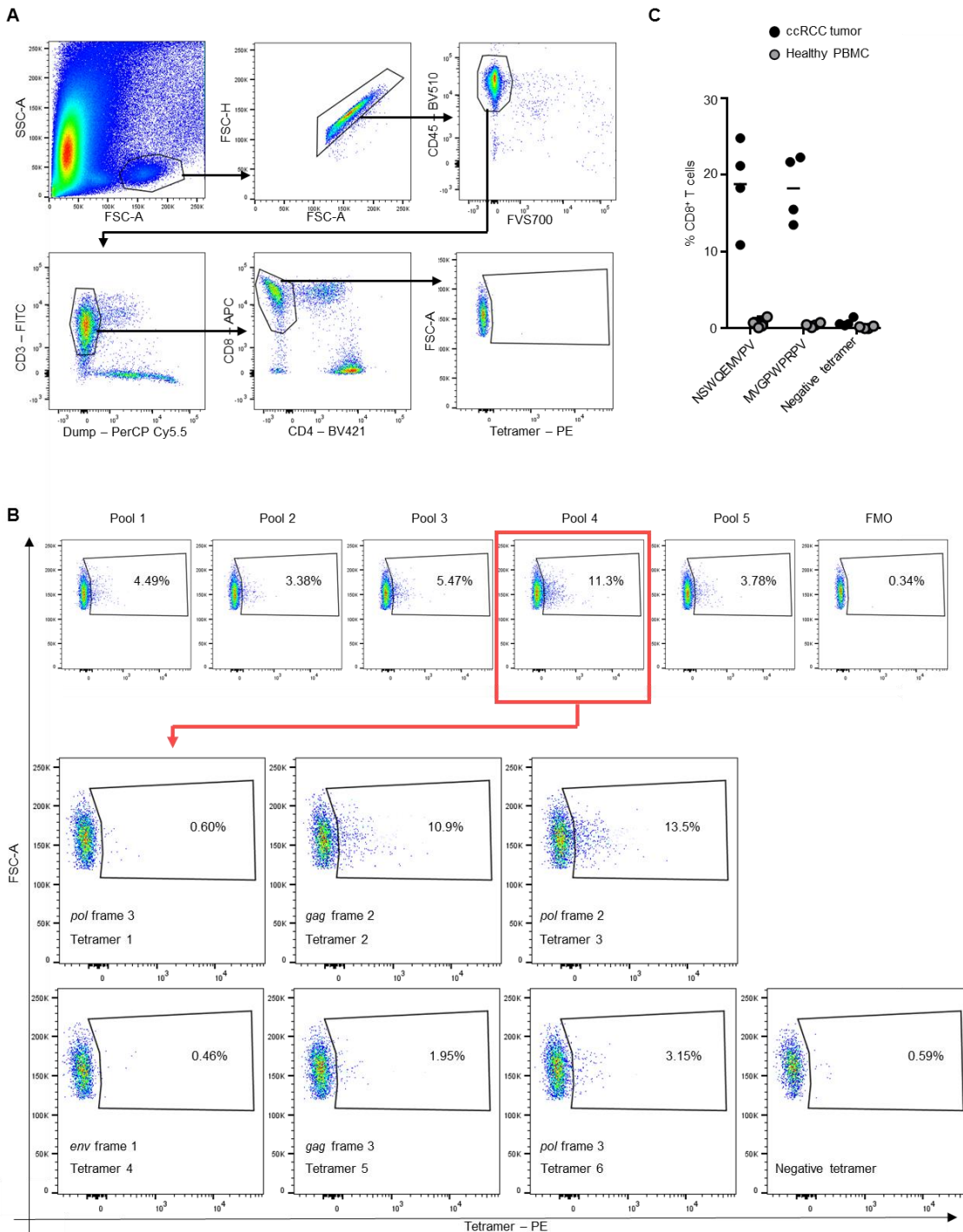
Tumor-specific transcription is necessary for epitope generation but is not sufficient without downstream translation. Since the majority of hERVs are translationally inactive, we ran hervQuant on a publicly available Ribo-Seq dataset comprising several regions from 2 ccRCC and matched normal kidney nephrectomy samples (4 regions per tumor; 2 regions per matched normal)¹⁵². To filter for hERVs with the strongest evidence of differential expression by both Ribo-Seq and RNA-Seq, we ranked hERVs by the sum of RNA-Seq and Ribo-Seq fold change in expression in tumor versus normal samples (Supplemental Figure 19). Despite evidence of translation in the literature, CT-RCC hERV-E did not demonstrate coverage by Ribo-Seq in this ccRCC dataset, suggesting the relative insensitivity of Ribo-Seq– compared with RNA-Seq–based hERV identification. However, analysis of the GWIPS database¹⁶⁹ containing aggregate data from >30 Ribo-Seq datasets provided evidence for translation of CT-RCC hERV-E in several human lymphoblastic cell lines but minimal translation in all other sets, including normal human tissues, suggesting that CT-RCC hERV-E had the capacity for translation within tumor-like tissues (Supplemental Figure 20). hERV 4700 (HERVERI/gammaretrovirus-like), which demonstrated the highest

tumor versus normal expression by RNA-Seq, was identified as the most differentially expressed hERV with greatest evidence of translation. Additionally, hERV 4700 was expressed at low levels in matched normal tissues from all other tumor subtypes (Supplemental Figure 21) and demonstrated additional evidence of translation among GWIPS tumor cell line samples (Supplemental Figure 22). Although Ribo-Seq coverage of hERV 4700 within ccRCC samples was relatively low, coverage patterns were similar to those observed by RNA-Seq (**Figure 3.5B**). Areas of coverage within the hERV 4700 proviral reference corresponded to viral gag (red), pol (blue), and env (green) genes. Protein-BLAST of these regions translated across each reading frame provided high sequence similarity with known reference hERV sequences across all 3 frames of pol and env, and frame 2 of gag (**Figure 3.5C** and Supplemental Figure 23). Using the longest sequence identified within each protein reading frame, we performed NetMHCPan4.0 epitope prediction, identifying 30 predicted HLA-A*02:01 binders (binding affinity ≤ 500 nM; Supplemental Table 5)³⁹. To ensure these predicted epitopes were hERV specific, we searched for overlap between amino acid sequences of each peptide with known human proteins in the GENCODE hg19 protein-coding transcript translated sequences, observing no overlap between epitopes and non-hERV proteins. Using an HLA-A*02:01 monomer UV exchange assay and HLA ELISA readout^{170–175}, we validated the binding of 30 of 30 predicted epitopes to HLA-A*02:01 with exchange efficiencies ranging from 16.1% to 73.1% (**Figure 3.5D**).

hERV epitopes associate with aPD1 response with evidence of epitope-specific T cells in ccRCC.

To explore whether hERV 4700 expression is predictive for patient response to aPD1 therapy, we performed quantitative real-time PCR (RT-qPCR) quantification of hERV 4700 with 2 of each gag-, pol-, and env-specific primer/probe sets on ccRCC tumor biopsy RNA in aPD1-treated patients (responders: n = 7, nonresponders: n = 6; **Figure 3.5E** and Supplemental Tables 6–8). We observed greater mean RT-qPCR signal in aPD1 responders in all primer/probe sets (Mann-Whitney U test $P < 0.05$; Supplemental Table 9), as well as hervQuant-derived hERV 4700 expression from the same set with added samples (responders: n = 10, nonresponders: n = 10; Mann-Whitney U test $P = 0.0455$), suggesting that transcription of hERV 4700 is associated with greater responsiveness to immunotherapy. Additionally, multivariable linear regression (GLM) provided perfect fit of primer/probe sets as a predictor for response. To demonstrate the presence of an anti-hERV 4700 T cell immune response in ccRCC, we performed tetramer staining of an HLA-A*02:01 ccRCC tumor sample using the 30 MHC tetramers described above (**Figure 3.6A,B**). Using a stepwise approach, we first screened the tumor using 5 pools of 6 tetramers, which demonstrated that pool 4 had the largest tetramer-positive CD8+ T cell population (11.3% tetramer-positive). Running the 6 individual tetramers, we observed tetramers 2 and 3 to have the greatest staining, which corresponded to peptides derived from frame 2 of the gag (10.9% positive) and pol (13.5%) protein regions, respectively. We validated the presence of these T cell populations in 3 additional ccRCC tumors (gag: 10.9%–24.8%; pol: 13.5%–22.3%), as well as observing staining within the range of negative control tetramers in 4 healthy donor peripheral blood mononuclear cells (PBMC) samples (gag: 0.12%–1.51%, pol: 0.13%–0.76%; **Figure 3.6C** and Supplemental Figure 24). Overall, these data validate

our epitope prediction method and provide evidence for the presence of hERV 4700-specific T cells within ccRCC.



for identification of CD8+ epitope-specific T cells in ccRCC tumor. (B) Epitope gating for 5 pools of 6 tetramers (top), as well as staining of individual tetramers from pool 4 (bottom) in ccRCC. (C) Percent tetramer-specific CD8+ T cells for epitopes identified in B (tetramer 2: NSWQEMVPV; tetramer 3: MVGPWPRPV) in ccRCC tumors (n = 4) and healthy donor PBMC samples (n = 4). Dots represent values for each sample, with bars representing the mean across each group. Negative controls for gating definitions include tetramer fluorescence-minus-one (FMO) (A) and nonspecific HLA-A*02:01-negative tetramer (B and C). Data presented in Figure 6 represent results from 4 independent experiments.

3.3 Discussion

We report here a hierarchical analysis of hERV-immune microenvironment interactions within the TCGA pan-cancer dataset, integrated with Ribo-Seq data, RNA-Seq data from immunotherapy-treated patients, and functional biological assays, to provide insight into hERV immunobiology in cancer. Our broad survey of hERV expression and association patterns provided multiple lines of evidence that hERVs shape the tumor immune microenvironment in several cancer types. Conditioning on cancer type, we observed that gene signatures of immune responsiveness (aPD1-responsive signature, effector immune cells) were positively associated with hERV expression, suggesting that hERVs may either directly interact with antitumor immunity through immune activation or provide a biomarker for an active antitumor immune response. In agreement with this view, we observed that hERVs were significantly prognostic in multiple cancer types, with the greatest enrichment of prognostic hERVs observed in ccRCC. Interestingly, BLCA was the only cancer type in which greater average hERV expression resulted in significantly longer survival times. This finding suggests potentially different hERV-mediated tumor immunobiology in BLCA and should be further explored in future studies. For IGS and CoxPH analyses, hERV expression data were normalized either (i) to total RNA-Seq read count (reads per million; RPM) to determine the impact of absolute hERV expression or (ii) to upper quartile normalization

(UQN) of hERV reads within each sample to determine the impact of relative hERV proportions (Supplemental Tables 10 and 11). IGS patterns of association were strongly conserved between hERV expression by UQN and read normalization. We observed variability in hERV association patterns with 3 CD8+ T cell signatures derived from different publications (CD8_T_Cell, CD8_Cluster, CD8)^{100,101,159}, with CD8_T_Cell showing an association pattern different from the other 2 signatures. The CD8_T_Cell signature contained a set of 8 genes that accounted for its variation from the other 2 signatures — HAUS3 (cytokinesis and mitosis), SF1 (pre-mRNA splicing), SFRS7 (pre-mRNA splicing), ZNF91 (protein coding), ZNF609 (protein coding), THUMPD1 (gene expression/rRNA processing), MYST3 (histone acetyltransferase), and CDKN2A (cell cycle regulator) — all of which are nonspecific to CD8+ T cells in function (Supplemental Figure 25). Nevertheless, we included the CD8_T_Cell signature within all analyses (including Treg-to-CD8+ ratio) because it remains a commonly used signature for CD8+ T cells within the literature.

In contrast to IGS, CoxPH analysis with UQN hERV data contained a greater number of positively prognostic hERVs compared with read-normalized data, suggesting that the proportional expression of hERVs may also influence overall survival. We additionally observed that the majority of hERVs were associated with younger patient age. Since most tumor types show an association between older age and worse outcome, and the majority of significantly prognostic hERVs were associated with worse outcome, these results suggest that the association between hERVs and patient outcome was not simply due to an association with age.

Due to the diverse tumor-immune interactions observed among different cancer types, we narrowed down further the role of hERVs upon the tumor immune microenvironment to one cancer type. We focused on ccRCC to further study the role of hERVs in shaping the tumor immune microenvironment because (i) it contained the greatest number of prognostic hERVs and (ii) hERV proteins are known to be expressed and immunogenic in ccRCC^{27,31,32,42}.

Within ccRCC, we considered the potential for hERVs to impact both arms of the immune system. The role of hERVs in triggering an innate immune response is underscored by several recent reports noting that epigenetic-modifying agents that promote greater DNA demethylation — decitabine (methyltransferase inhibitor) and abemaciclib (CDK4/6 inhibitor)^{28,156} — increased expression of retroviral elements and triggered subsequent antitumor responses through innate sensor signaling, including induction of RIG-I-like pathway detection of viral dsRNAs. While these previous reports demonstrated only the proinflammatory nature of selected hERV elements, we were surprised to find two strikingly distinct patterns of association between hERV expression in ccRCC and expression of genes associated with the RIG-I-like family. The implication of this clustering pattern (along with the significantly different patterns of association between these hERV groups with survival and IGS expression) is that hERVs may play both agonistic and antagonistic roles in innate sensor immunity. Potentially, group 2 hERVs (RIG-I-like down) may interfere with RIG-I-like signaling through a currently unknown mechanism, ultimately skewing the tumor immune microenvironment in favor of an immunosuppressive phenotype with greater Treg-to-CD8+ T cell ratios and negatively impacting patient prognosis.

Next, we studied the role of hERVs in triggering an adaptive immune response through hERV-mediated immune activation of retroviral epitope-driven T and B cell responses. MiXCR analysis of TCGA KIRC failed to identify TCR clones that were shared across at least 10% of samples, suggesting that while hERV epitopes have the capacity to trigger a T cell–driven antitumor response^{31,32,42}, we lacked the sensitivity to computationally identify public hERV-specific TCR clones. In agreement with this, comparison of MiXCR-derived TCR expression with previously described TCRs derived from amplicon-based adaptive TCR repertoire profiling in 3 TCGA KIRC samples demonstrated low total TCR counts of MiXCR data with low frequencies of overlapping clones (Supplemental Figure 26). In contrast, we observed a large pool of shared BCRs. It is important to note that BCR repertoires are likely more completely sampled from RNA-Seq data than are TCR repertoires, as we observed increased BCR sequence reads, consistent with the greater transcription of immunoglobulin mRNA from cells of the B cell lineage compared with TCR mRNA transcription from activated T cells. Thus, our study had greater power to detect BCR than TCR repertoire associations. Multiple sequence alignment of BCR-associated hERVs demonstrated clustering of proviral sequences by superfamily, suggesting that a B cell response generated against shared hERV epitopes is likely to occur within one or several closely related superfamilies. The higher hazard ratios among BCR-associated hERVs may be related to the lack of tumor specificity for these hERVs. The majority of IGS in ccRCC, including those for B cells, have been shown to be associated with worse prognosis¹⁰⁵. While the mechanism for this finding is currently undetermined, a potential contributor to this pattern may be a B cell response in which hERVs are generated in the tumor with

epitopes shared by hERVS upregulated within the surrounding normal tissues. Further investigation should be performed to study the importance of this potential anti-hERV B cell response in ccRCC.

Evidence for hERV-mediated activation of the innate and adaptive immune responses suggests that expression of these proviruses within tumors may contribute to immune editing of tumor cell populations. Highly immunogenic hERVs with the capacity to be recognized by endogenous T and B cell responses are likely cleared by the immune system or otherwise expressed under a heavily immunosuppressed microenvironment. There may also exist additional hERV epitopes that generate immune responses too weak to promote antitumor immunity. These two groups can both be potentially targeted for immune activation through the use of nonspecific (e.g., checkpoint blockade therapy, innate immune agonists) or epitope-specific (vaccination, adoptive T cell therapy) immunotherapies. Further time-course immune profiling studies should be performed to study the mechanisms of hERV-mediated immune surveillance in a developing tumor.

With evidence of hERV-mediated activation of both innate and adaptive immune responses, we sought to examine whether these responses could be used to develop a model for patient prognosis in ccRCC. Apart from molecular subtyping, no molecular markers have improved the prognostic capabilities of current clinical predictive systems in ccRCC, suggesting the potential for development of hERV-based signatures as a biomarker for survival. In attempt to identify such a prognostic biomarker, we created hERV signatures derived from our previous analysis of hERV interactions with the innate and adaptive immune response. Based on these signatures, we developed a

model that provided significantly greater prognostic power than M1–M4 molecular subtyping and levels of prognostic information similar to those of traditional clinical staging. Additionally, while these hERV signatures were derived and optimized for ccRCC, we showed 2 signatures to provide prognosis in several other tumor models related to ccRCC by hERV expression patterns, level of prognostic hERVs, and tissue of origin, implying that additional hERV signatures for patient prognosis can be independently developed for other cancer types.

Last, we sought to develop a screening method for detection of hERVs actively undergoing translation. The implication of such a tool is the potential for development of immune response biomarkers and antitumor T cell vaccine therapies, similar to those developed in neoantigen-based vaccine studies. Our analysis of tumor-specific hERVs in ccRCC identified CT-RCC hERV-E as the second highest differentially expressed hERV by RNA-Seq expression. This particular hERV has been well described in the literature as a ccRCC tumor-specific provirus with evidence of hERV-specific T cell responses^{31,32,42}. Within our Ribo-Seq analysis, we were underpowered to detect evidence of CT-RCC hERV-E translation among 2 ccRCC samples. However, our analysis of the GWIPS database provided evidence for the translation of CT-RCC hERV-E in human tumor cells but not in normal blood, fibroblasts, or muscle tissue. This conforms to the view that CT-RCC hERV-E has the capacity for translation under tumor-specific conditions and suggests that deeper Ribo-Seq coverage in ccRCC may be needed to increase the sensitivity of our computational screening to broaden the set of potentially targetable hERV epitopes. Our analysis of CT-RCC hERV-E RNA-Seq expression in TCGA KIRC data supports the previous report by Rooney et al. identifying

this hERV as being upregulated in ccRCC and associated with a gene expression index of cytotoxicity⁴¹. We observed the same significant association with their cytotoxicity signature and additionally identified a large proportion of other IGS strongly associated with its expression. Among these, the most significantly associated was the Treg signature, suggesting that expression of CT-RCC hERV-E may be also associated with immunosuppression. This strong association with immunosuppressive signatures suggests CT-RCC hERV-E may be another potential marker of response for immunotherapies such as aPD1 checkpoint blockade therapy.

RNA-Seq analysis of hERV 4700 demonstrated preferential expression within ccRCC, with modest expression in normal kidney and liver. This preferential expression underscores the potential for hERV 4700–targeted immunotherapies, with the caveat that a particularly robust anti–hERV 4700 immune response could potentially result in on-target/on-tissue and on-target/off-tissue toxicity. We provided additionally validation for the transcription of this hERV through RT-qPCR and hervQuant analysis of an aPD1-treated ccRCC dataset, and showed that expression of hERV 4700 is associated with responsiveness to immunotherapy.

Ribo-Seq screening provided evidence for translation of hERV 4700, supporting translation of epitopes that we further validated to bind MHC. Additionally, tetramer staining of predicted hERV 4700 epitopes in 4 ccRCC tumors demonstrated the presence of infiltrating T cells with receptors specific for gag- and pol-derived epitopes, supporting the idea that (i) hERV 4700 may act as a direct target in ccRCC, whereby aPD1 could trigger an antitumor response against hERV 4700–derived epitopes, and (ii) hERV 4700 expression may be a new biomarker of aPD1 responsiveness in ccRCC.

These same T cell populations were scarce to absent in healthy donor PBMCs, confirming the specificity of these T cells in ccRCC tumors. Tetramer-specific T cell frequencies were particularly high among ccRCC tumors (NSWQEMPV, 10.9%–24.8%; MVFPWPRPV, 13.5%–22.3%), suggesting that as much as 40% of tumor-infiltrating CD8⁺ T cells may be specific for these 2 hERV 4700 epitopes. We recognize that these frequencies are particularly high for a tumor-infiltrating population, and several caveats exist for our analyses. First is the potential for T cell cross-reactivity against these tetramers, as well as peptide impurities that recognize other infiltrating T cell populations. Additionally, tetramer-positive populations contained a large range of fluorescence intensities, suggesting these T cells do not necessarily comprise a single clone but likely several different clones with different TCR affinities. Future studies to characterize the TCR sequences and phenotypic characteristics of these tetramer-positive populations should be performed to further elucidate the role of these populations and determine the basis for these and other potential caveats.

In addition to hERV 4700, we observed 172 other hERVs that were differentially expressed between aPD1 responders and nonresponders by hervQuant profiling (Wilcoxon's test, $P < 0.05$), suggesting that a more comprehensive set of hERV expression signatures may exist for the development of an aPD1 response biomarker in ccRCC (Supplemental Figure 27). Of these hERVs, 6 demonstrated overlap with the RIG-I-like down signature, one with the BCR-associated signature and 34 with all prognostic hERVs, suggesting relatively low overlap between the set of predictive and prognostic hERVs. Overall, hervQuant is the first described method to our knowledge for comprehensive identification of potentially targetable hERV epitopes. Further

validation should be performed to confirm the capacity of these potential hERV epitopes as therapeutic vaccine targets and to develop a robust hERV-based biomarker for immunotherapy response in ccRCC.

In summary, we describe a computational workflow, *hervQuant*, for robust quantification of individual hERVs using RNA-Seq data. The data gained through *hervQuant* provide insights into the pan-cancer landscape of hERV expression and immune modulation. Within ccRCC, we found a distinct group of hERVs that were inversely associated with RIG-I-like signaling genes, prognosis, and IGS expression. Additionally, we examined the interaction between hERV expression in ccRCC and activation of B cell clonotypes, and demonstrated the capacity of the above-mentioned hERV classes to provide a multivariable model of patient prognosis that significantly outperforms traditional clinical staging and molecular subtype prognosis models in ccRCC. We provide evidence for a new method of hERV epitope prediction based on differential hERV expression in the tumor, Ribo-Seq screening for translation, computational epitope prediction, in vitro validation for HLA binding, and in vivo detection of epitope-specific T cells in a ccRCC tumor. Importantly, we observed that hERV sequences identified through this approach were significantly associated with aPD1 responsiveness in ccRCC tumors, supporting continued research into hERVs as biomarkers and therapeutic targets for immunotherapy. With the recent increasing interest in the role of hERVs in modulating the tumor immune microenvironment, we believe the work presented here substantially expands our understanding of hERV biology and opens the way for future development of technologies to exploit hERV biology for new therapeutic tools.

3.4 Methods

Alignment and quantification of hERV expression from RNA-Seq data.

hERV genomic coordinates were derived from a previously published study by Vargiu et al.³⁸. Full-length hERV sequences were masked for low complexity reads (9 or more repeating single nt; 7 or more repeating double nt; 4 or more repeating nt patterns of 3; 3 or more repeating nt patterns of 4; 2 or more repeating patterns of 5; 2 or more repeating nt patterns of 5) and compiled alongside human hg19 transcriptome reads into a reference file for downstream alignment. RNA-Seq FASTQ files were aligned to the hERV reference using STAR v2.5.3 (multimaps ≤ 10 , mismatch ≤ 7)¹⁷⁶. BAM output files were filtered for reads that mapped to hERV reference using SAMtools (v1.4)¹⁷⁷, then quantified using Salmon v0.8.2 (Quant mode, -1 ISF)¹⁷⁸. Raw expression matrices were either normalized to hERV counts per million total FASTQ reads and log2 transformed, or normalized to the upper quartile hERV expression value among non-zero values within each sample and log2 transformed (Supplemental Tables 12–14). Only TCGA pan-cancer samples sequenced with Illumina HiSeq 2 × 50 bp were analyzed. See the supplemental material for optimization details and input parameters.

RNA-Seq expression, IGS analysis, and survival analysis.

MapSplice-aligned, RSEM-quantified RNA-Seq expression matrices and survival data were downloaded from FireBrowse (<http://firebrowse.org/>). Expression matrices were merged between all cancer types, upper quartile normalized within each sample, and log2 transformed. IGS were derived from previously described signatures^{83,100,101,157–159}, with expression calculated as the mean expression of each

gene within the signature. TCGA LAML samples were omitted from analysis in order to prevent skewing of IGS patterns.

TCR/BCR alignment.

MiXCR (v2.1.1) was used for identification of TCR and BCR sequences with TCGA KIRC¹⁶². Following suggested run methods provided by MiXCR's documentation for RNA-Seq data (<https://mixcr.readthedocs.io/en/latest/rnaseq.html>), paired-end FASTQ files were run through alignment in RNA-Seq mode, 2 rounds of contig assembly, extension of incomplete CDR3s, assembly, and export. Data were subsequently converted into an expression matrix, dropping all clones (defined as conserved amino acid CDR3 sequence) with expression in fewer than 10% of all TCGA KIRC samples, and scaled to counts per billion total FASTQ reads.

*HLA-A*02:01 monomer UV exchange and β 2-microglobulin ELISA.*

Epitope prediction was performed with the NetMHCpan 4.0 Server interface, defining predicted HLA binders as those with binding affinity ≤ 500 nM³⁹. Predicted hERV epitopes were synthesized through New England Peptide array technology. Monomer exchange reaction was carried out using the BioLegend Flex-T HLA-A*02:01 monomer UV exchange protocol¹⁷⁴. Peptide exchange efficiency was performed using the BioLegend HLA class I ELISA protocol¹⁷⁵.

RT-qPCR validation of hERV 4700.

Expression levels of hERV 4700 were assessed by RT-qPCR in a collection of ccRCC formalin-fixed, paraffin-embedded (FFPE) archival tissue from responders (n = 7

patients; 9 samples) and nonresponders (n = 6 patients; 6 samples). RT-qPCR was performed on all available samples, with no further selection process. Total RNA isolation was performed using the RNAeasy FFPE Kit (QIAGEN). DNase treatment was performed during RNA isolation using RNase-free DNase I (QIAGEN). RNA quality and concentration were assessed using a NanoDrop ND-1000 spectrophotometer (NanoDrop Technologies).

First-strand cDNA synthesis was performed using 250 ng total RNA, random hexamers, and the SuperScript IV Reverse Transcriptase Kit (Life Technologies). RT-qPCR was performed on a CFX96 Touch Real-Time PCR Detection System (Bio-Rad) using TaqMan Universal PCR Master Mix (Applied Biosystems). RT-qPCR primer and probe sequences are shown in Supplemental Table 7. All analyses were performed in triplicate, and relative RNA levels were determined using hypoxanthine phosphoribosyltransferase 1 (HPRT1) as an endogenous internal control (Applied Biosystems, catalog 4333768). A HeLa control RNA sample was included for inter-plate calibration. hERV 4700 expression levels were calculated using the $\Delta\Delta C_t$ method. Expression levels for 2 sample pairs derived from the same patients were averaged for statistical analyses in Figure 3.5E.

Flow cytometric analysis.

Tetramer and cell surface staining was performed as described previously¹⁷⁹. Briefly, viably frozen, histologically subtyped ccRCC tumor samples were thawed and stained for HLA-A2 (BD Biosciences; clone BB7.2, allophycocyanin [APC]). Separately, samples positive for HLA-A2 were treated with 50 nM dasatinib for 30 minutes at 37°C,

then stained using approximately 10 µg/ml tetramer (phycoerythrin [PE]) or Beckman Coulter iTA_g MHC class I human–negative tetramer control on ice for 30 minutes. Cells were then washed and incubated on ice with 5 µg/ml biotin-conjugated anti-PE antibody (BioLegend; PE001) for 20 minutes, followed by 2 washes, then further incubation with 5 µg/ml streptavidin, R-PE conjugate (SAPE) for 10 minutes on ice. Cells were then washed and stained for viability using BD fixable viability dye FVS700 according to the manufacturer's directions. Last, cells were Fc blocked using mouse immunoglobulin (MilliporeSigma, catalog I5381) for 10 minutes, followed by surface staining for 20 minutes on ice with the following markers: anti-CD45 (BD Biosciences; clone HI30, BV510), anti-CD3 (BD Biosciences; clone UCHT1, FITC), anti-CD8 (Beckman Coulter; SFCI21THy2D3 [T8], APC), anti-CD4 (BD Biosciences; clone RPA-T4, BV421), anti-CD14 (BD Biosciences; clone MφP9, PerCP Cy 5.5), anti-CD19 (BD Biosciences; clone HIB19, PerCP Cy5.5), and anti-CD56 (BD Biosciences; clone BL59, PerCP Cy5.5).

A minimum of 1,000,000 events were collected for each sample on a BD LSRFortessa flow cytometer. FlowJo flow cytometry software version 10 was used for analyses of all flow cytometric data. Tumors were derived from viably frozen nephrectomy samples from UNC Chapel Hill and Vanderbilt University hospital patients with clear cell histology. Healthy donor PBMCs were screened by and purchased from Gulf Coast Regional Blood Center, Houston, Texas, USA.

Data availability.

TCGA analyses were performed on data collected and generated by the TCGA Research Network — expression matrices can be accessed at <http://firebrowse.org/>;

TCGA raw data can be accessed in the database of Genotypes and Phenotypes (dbGaP, accession phs000178). Ribo-Seq analysis was performed on data collected by Loayza-Puch et al. and can be accessed in the NCBI's Gene Expression Omnibus database (GEO GSE59821)¹⁵². hervQuant expression matrices for TCGA pan-cancer (UQN and RPM) and aPD1-treated ccRCC (raw reads) RNA-Seq datasets are available in Supplemental Tables 12–14. The GWIPS ribosomal profiling database is available at <https://gwips.ucc.ie/>. The hervQuant workflow reference and instructions are available for download at <https://unclineberger.org/vincent/resources>

Statistics.

GLM using the R “glm” package was used for all univariable regression, unless otherwise stated. Univariable and multivariable CoxPH was performed with the R “survival” package. Multiple sequence alignment was performed with Clustal Omega through the R “msa” package¹⁸⁰. Differential hERV expression was calculated using the DESeq2 R package¹⁶⁸. For all CoxPH analyses, P value correction was performed using Bonferroni's correction to maintain a conservative cutoff of significance. For all other analyses, 5% FDR multiple testing correction for P values was performed unless otherwise stated. Welch's t test was performed for statistical calculation in Figure 3.3C. Log rank test was performed for statistical calculation in Figure 3.4C, with no multiple testing correction. Multivariable CoxPH and χ^2 test were performed for statistical calculation in Figure 3.4D, with no multiple testing correction. Mann-Whitney U test was performed for statistical calculation in Figure 3.5E, with no multiple testing correction. $P < 0.05$ was considered significant for all statistical tests performed.

Study approval and sample acquisition.

The present studies in humans were reviewed and approved by the Vanderbilt University Human Research Protections Program, and the University of North Carolina at Chapel Hill IRB and the Office of Human Research Ethics (CB 7097). Subjects provided written informed consent prior to their participation in the study. Biopsy samples were collected according to a protocol approved by the Vanderbilt University IRB (no. 160979), and the UNC IRB approved the biorepository protocol (LCCC 1212). Patients were identified through an IRB-approved protocol and identified using a pharmacy-based list. Line of treatment for each patient varied. The response was first determined by chart review of clinicians' notes and then confirmed by the authors of this article based on RECISTS 1.1 imaging criteria.

Supplemental material

All supplemental figures and tables cited in Chapter 2.2 are listed according to the original published manuscript, which can be found at <https://www.jci.org/articles/view/121476#sd>.

CHAPTER 4: Design and delivering of neoantigen-based therapeutic vaccines

4.1 Machine learning model for prediction of neoantigen immunogenicity

4.1.1 Introduction

T cells are a key driver of anti-tumor immune response through recognition of antigenic tumor peptides presented on cell surface major histocompatibility complex (MHC) proteins. These peptides include *tumor neoantigens*, which are derived from mutation-containing proteins that generate novel immunogenic epitopes, as well as *minor histocompatibility antigens* (mHA), which are variants within the same MHC allele arising from single nucleotide polymorphisms, most commonly in the setting of hematopoietic stem cell transplants. Despite the ability of these antigen-based therapeutic tumor vaccines to promote tumor-specific T-cell responses in a number of pre-clinical models^{70–72}, clinical efficacy remains to be demonstrated^{14,15}.

Among significant challenges impeding clinical translation of neoantigen/mHA therapies includes the ability to select the subset of immunogenic antigens from all possible computationally-predicted neoantigens. Unlike murine pre-clinical models where *in vivo/ex vivo* methods to screen for immunogenicity exist, no such benchtop prediction method for immunogenicity is currently available in humans. As such, the development of an algorithm for predicting the immunogenicity of computationally-predicted antigens could advance clinical translation of neoantigen therapies.

While there are robust methods to predict for the binding affinity of potential peptide epitopes across multiple species^{39,181}, these methods are insufficient to determine whether an immune response will be generated against said epitope *in vivo*. In the case of neoantigens and mHA, where most predictions are based on SNV/SNP mutations, predicted binders share high sequence identity to native protein sequences. This high sequence identity results in greater potential for central tolerance compared to epitopes derived from non-self-proteins (such as viral antigens).

While a subset of predicted neoantigens/mHA are capable of promoting an effector T cell response, it isn't currently clear whether specific features of the predicted antigen sequence predicts for immunogenicity. Here, we correlate peptide-intrinsic features of predicted murine neoantigens and mHA with immune response in the vaccine setting. Using a gradient boosting method with cross-validation, we design a novel model to predict for neoantigen/mHA peptide immunogenicity based on peptide-intrinsic characteristics. We predicted for the immunogenicity of predicted neoantigens in the BBN963 basal-like bladder model and mHA in the P815 (BALB/c host, DBA/2 recipient) mastocytoma transplant model and demonstrated the capacity of epitopes with high predicted immunogenicity to control tumor growth better than those with low predicted immunogenicity and untreated control. Lastly, using our model on predicted class I neoantigens among the TCGA pan-cancer dataset, we observed high association between highly immunogenic neoantigens and MSI-high driven immune features in colon adenocarcinoma (COAD) and a strong negative association between MYC amplification and highly immunogenic neoantigen numbers in lung adenocarcinoma (LUAD) cancer types.

4.1.2 Results and Discussion

Identification, screening, and computational processing of murine neoantigens

Neoantigens and mHA were predicted in six murine tumor models (B16F10, BBN963, MB49, UPPL1541, P815, and T11) spanning the murine b and d haplotypes (**Figure 4.1A**). Neoantigen prediction was performed as previously described¹⁸². Briefly (**Figure 4.1B**), whole exome sequencing was performed on tumor and matched-normal tail or liver DNA, along with whole transcriptome sequencing of tumor RNA. Tumor mutations were called using UNCEqR¹⁸³, filtering for SNV mutations with at least 5x coverage by RNA-seq. Translated 8-11mer (class I) or 15mer (class II) peptides were derived across three open reading frames, and then predicted for MHC binding affinity using NetMHCPan3.0¹⁸⁴. Minor mismatch antigens were predicted similarly in the P815 model (derived from DBA/2 background) against the BALB/c histocompatible host. Predicted binders were filtered by binding affinity < 500nM, with top binding epitopes synthesized using New England Peptide array technology. To screen for immunogenicity, animals were vaccinated on days zero and seven with pools of eight peptides. Splenocytes from vaccinated animals were collected on day 14 and plated in triplicate onto an IFN- γ capture ELISpot alongside one antigenic peptide contained within the vaccine. Immunogenicity was defined as the average number of spots identified using an ELISpot plate reader, with no-peptide background subtracted from each epitope.

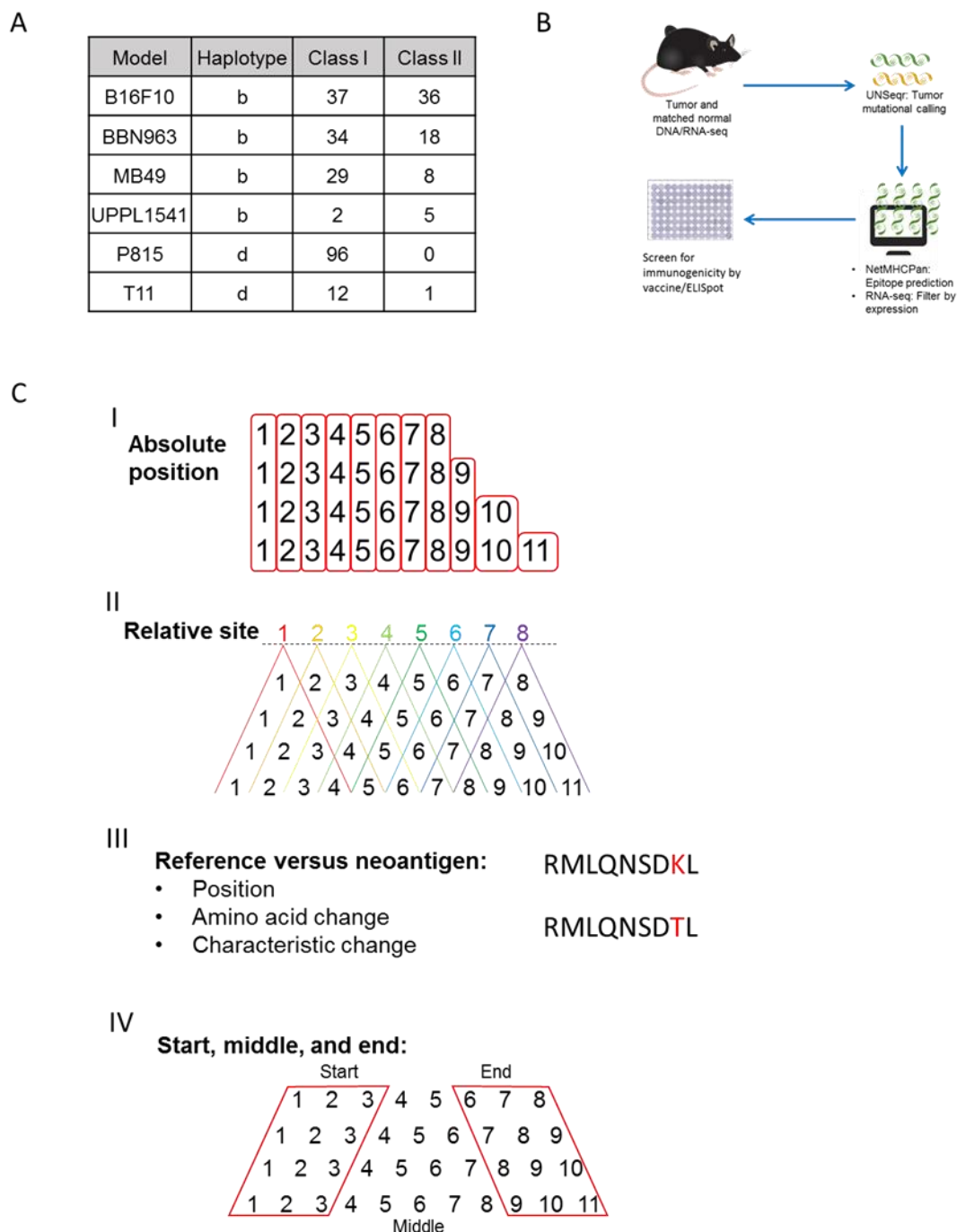


Figure 4.1: Summary of tumor antigen prediction and identification of peptide-intrinsic features. (A) Number of MHC class I and II neoantigens/mHA per tumor model contained within the study. (B) Schematic of neoantigen/mHA prediction and ELISpot validation workflow. (C) Summary of major classes of peptide-intrinsic features identified for each antigen, including amino acid sequence and characteristics at I) each absolute position, II) each relative site, III) the mutation position, and IV) the start, middle, and end of each peptide.

With the goal of identifying peptide-intrinsic features that associate with immunogenicity, we derived a set of features for each peptide, including the amino acid sequence and characteristic (via R package aaComp: Tiny, Small, Aliphatic, Aromatic, Nonpolar, Polar, Charged, Basic, and Acid) at each absolute position (**Figure 4.1C: I**), relative site (**Figure 4.1C: II**), at the site of mutation (**Figure 4.1C: III**), and at the first three, middle, or last three sequences of each peptide (**Figure 4.1C: IV**). We began our analysis by performing univariable and multivariable generalized linear model (GLM) regression between these sets of peptide-intrinsic features with immunogenicity, independently for class I and class II peptides.

Associations of immunogenicity in class I MHC epitopes

Univariable regression between intrinsic peptide features and immunogenicity in class I antigens demonstrated 38 significant features (FDR-correlated p-value < 0.05; **Figure 4.2A**). Among these features, the most strongly positively associated with immunogenicity were changes at the mutation position into a small amino acid (“Mutated_position_change_of_Small_feature”), valine at relative site 2 (“Relative_site_2_V”), and basic amino acids at the mutated position of the reference epitope (“Reference_AA_at_mutated_position_Basic”), while the most strongly negatively correlated were small amino acids at the mutated position of the reference epitope (“Reference_AA_at_mutated_position_Small”), changes in the mutated position into a basic amino acid (“Mutated_position_change_of_Basic_feature”), and polar amino acids at position 6 (“Absolute_position_6_Polar”).

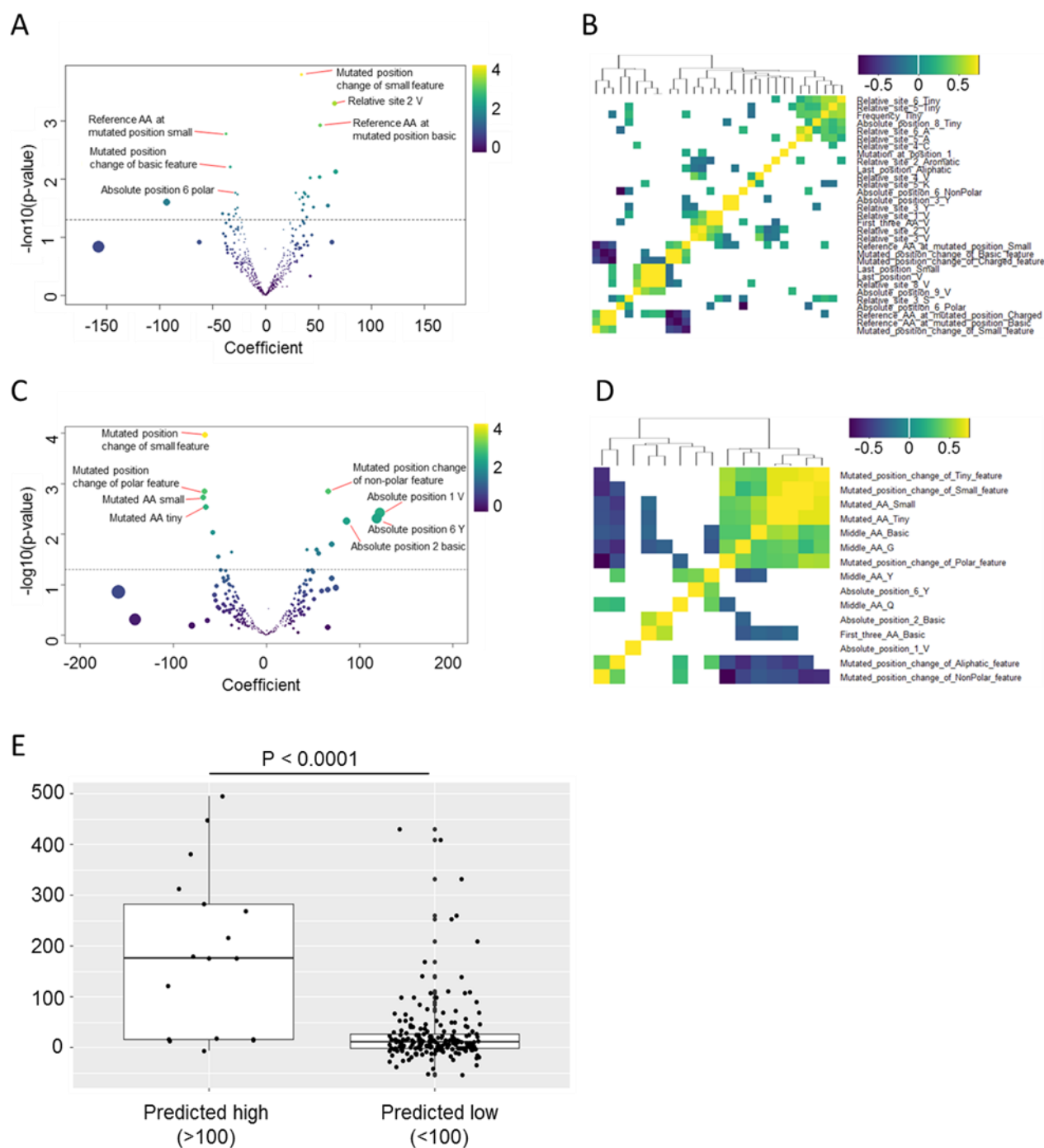


Figure 4.2: Linear regression analysis between peptide-intrinsic features and tumor antigen immunogenicity. (A and C) Volcano plot representing GLM coefficient (x-axis) and $-\log_{10}(\text{FDR p-value})$ (y-axis) for each peptide-intrinsic feature as a predictor for immunogenicity in (A) class I and (C) class II neoantigens/mHA. Dashed line represents FDR p-value = 0.05. Spot color represents $-\log_{10}(\text{p-value})$ magnitude and size represents magnitude of the coefficient. (B and D) Heatmap representing

Spearman correlation between each significantly correlated feature from (A and C) for (B) class I and (D) class II neoantigens/mHA, respectively. Significantly correlated features are shown in color, with coefficient direction and magnitude represented by color. (E) ELISpot-derived immunogenicity scores for class I neoantigens/mHA classified as predicted high (>100) or low (<100) immunogenic by multivariable GLM regression, with significant features from (A) as independent variables.

We additionally looked for co-correlation among the 38 significant features, observing relatively low numbers of significantly co-correlated features (**Figure 4.2B**). Significant features which demonstrated strong co-correlation were expectedly related, such as 1) charged or basic amino acid residues at the mutated position of the reference peptide, 2) valine or small amino acids at absolute position 11, and 3) valine or small amino acid at the last position, and valine at relative site 8. Thus, these significant peptide-intrinsic features largely provided predictive power independently of one-another, suggesting a multivariable model may outperform univariable regression. To increase confidence of our multivariable model, we performed univariable GLM with 1000-fold bootstrapping with 2/3rd resampling and kept features which were significant in >50% of iterations. Nine significant features from bootstrapping were inputted into a multivariable GLM regression model, observing significant linear fit between the actual immunogenicity and the predicted immunogenicity generated from the complete model (coefficient 0.48, $p < 0.0001$). Within the multivariable model, five significant features (“Relative_site_2_V” $p < 0.0001$; “Relative_site_5_K” $p = 0.0035$; “Last_position_V” $p = 0.0050$; “Absolute_position_3_Y” $p = 0.0045$; “Mutated_position_change_of_Small_feature” $p = 0.0087$) primarily drove the fit, with antigens classified by this model as predicted high (>100) or low (<100) immunogenicity demonstrating significant differences in actual immunogenicity scores (Wilcoxon $p < 0.0001$; **Figure 4.2E**). To ensure this model was accurately representing both H^b and

H^d haplotypes, we observed the immunogenicity for each of these five significant features split categorically by haplotype, which generally demonstrated the same pattern between both haplotypes.

Correlates of immunogenicity in class II MHC epitopes

Among class II epitopes, 15 peptide-intrinsic features were significantly correlated with immunogenicity (**Figure 4.2C**). Among the most positively associated features included changes in the mutation position into a non-polar amino acid (“Mutated_position_change_of_NonPolar_feature”), valine at position 1, tyrosine at position 6, and basic amino acid at position 2. Interestingly, the strongest negatively associated feature was changes in the mutation position into a small amino acid (“Mutated_position_change_of_Small_feature”), which was positively associated in class I epitopes. Additionally negatively associated features included changes in the mutation position into a polar amino acid (“Mutated_position_change_of_Polar_feature”), and small/tiny amino acids at the mutated site. Among significant features, four features corresponding to small or tiny amino acids at the mutational site were strongly co-correlated, with all other features demonstrating moderate to low co-correlation (**Figure 4.2D**). Multivariable GLM regression using these 15 features demonstrated significant linear fit between actual and predicted immunogenicity (coefficient 0.73, $p < 0.0001$), with two significant features “Absolute_position_1_V” and “Mutated_position_change_of_Small_feature” primarily driving the fit ($p = 0.0044$ and 0.0036 , respectively).

Multivariate models for immunogenicity prediction in class I MHC epitopes

To design a predictive model for neoantigen and mHA immunogenicity, we split our class I epitope database into an exploration (75% of epitopes, $n = 157$) and validation (25% of epitopes, $n = 53$) sets (**Figure 4.3A**). Class II modeling was not attempted, due to the low number of epitopes available within our database ($n = 68$). This lower class II epitope count is a result of i) fewer sequences with predicted binding affinity < 500 nM among class II epitopes, but additionally ii) lack of class II prediction in the P815 model. The consistently lower number of predicted class II epitopes suggests either that there are indeed fewer biologically relevant class II neoantigen/mHA compared to class I antigens, or that the binding affinity threshold should be changed for class II predictions to include those with higher predicted nM scores than the 500 nM cutoff currently implemented. Currently, no studies have examined optimal predicted binding affinity cutoffs for class I and II neoantigens, with 500 nM widely used as the cutoff for both classes.

In order to reduce noise within our model, we collapsed immunogenicity counts with absolute values less than or equal to the absolute value of the most negative count to zero. Within the exploration set, we used a 10,000-fold bootstrapping (2/3rd resampling) approach, comparing multivariable GLM, elastic net, random forest, gradient boosting, and linear and radial support vector machine methods. Input variables for each model included either all peptide-intrinsic features or a subset of features that demonstrated significant univariable correlation in $>50\%$ of 1000-fold bootstrapping iterations (2/3rd resampling) within the exploration set. Performance for each model and each set of input variables was determined by r-squared values, demonstrating that a univariable pre-filter outperformed a no-filter approach for all

tested models. Among the pre-filtered models, gradient boosting outperformed all other methods and was selected for our final model. The class I validation set was run through the final model, demonstrating significant correlation between the actual immunogenicity by ELISpot and the predicted immunogenicity by modeling ($p = 0.013$, coefficient = 0.30, **Figure 4.3B**). Among peptides with predicted immunogenicity above the 75th percentile, 5 of 17 epitopes (29.4%) were identified as true-positives (actual immunogenicity above background) while 2 of 13 epitopes (15.4%) within the bottom 25th percentile were false-positives. This high true-negative rate is particularly important in the setting of filtering for a large pool of predicted tumor antigens, as it allows for narrowing of the potential set of immunogenic peptides to pursue for vaccine studies.

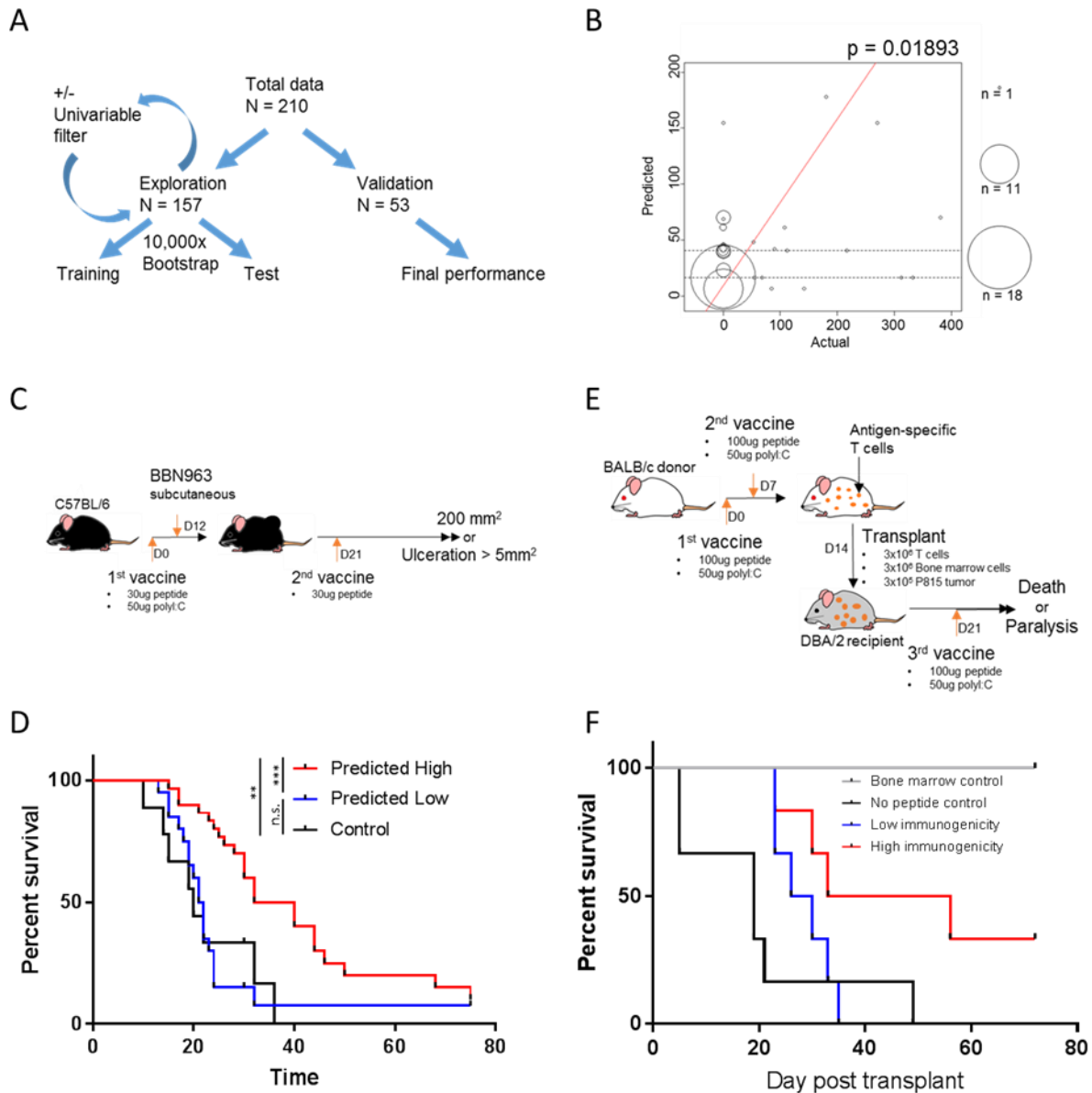


Figure 4.3: Performance and validation of gradient boosting model approach for predicting neoantigen/mHA immunogenicity. (A) Schema of cross-validation approach used for GBM model building. (B) Performance of final GBM model in validation set, showing actual (x-axis) versus predicted (y-axis) immunogenicity scores. Size of each point represents number of antigens at each coordinate. Red line represents line of best fit, with p-value of fit shown above the graph. (C and E) Schema for in vivo validation experiments, with tumor vaccine studies performed in (C) BBN963 basal-like bladder cancer and (E) P815 mastocytoma syngeneic transplant models. (D and F) Kaplan-Meier survival curves for (C and E) respectively, for animals treated with predicted high (red) or low (blue) immunogenicity antigens, no-peptide control (black),

or bone marrow only control (grey). Statistics performed with log-ranked testing (**: $p < 0.01$; ***: $p < 0.001$)

In vivo validation of class I immunogenicity prediction model

To demonstrate our final model could be used to increase the likelihood of identifying a clinically relevant, immunogenic epitope for anti-tumor vaccine response, we performed vaccine studies using two models within our validation set: BBN963 basal-like bladder model (solid tumor) and P815 mastocytoma (liquid tumor, syngeneic transplant model). BBN963 epitopes were predicted neoantigens in the C57BL/6 background, while P815 epitopes were selected for mHA in the BALB/c background against a DBA/2 host.

In BBN963, three predicted high and two predicted low immunogenicity neoantigens were identified. Animals were vaccinated with 30 μg of one of these peptides (or no-peptide control) alongside 50 μg poly(I:C) as adjuvant, challenged with tumor at 12 days after vaccination, and given a 30 μg peptide booster on day 21 after initial vaccination (**Figure 4.3C**). We observed significantly better survival among animals vaccinated with a predicted high immunogenicity peptide than predicted low immunogenicity peptide (log-rank $p < 0.001$) or no-peptide control (log-rank $p < 0.01$; **Figure 4.3D**), while predicted low immunogenicity peptide and no-peptide control groups did not demonstrate significant difference in survival.

In P815, there were a total of two predicted high and three predicted low immunogenicity graft-vs-tumor mHA. BALB/c donor animals were vaccinated with a pool of predicted high or low immunogenicity peptides (100 μg each peptide) or no-peptide control, alongside 50 μg poly(I:C) as adjuvant on days 0 and 7. DBA/2 recipient animals were irradiated (800 cGy) on day 13; transplanted with 3×10^6 BALB/c T cells,

3x10⁶ BALC/c bone marrow cells, and 3x10⁵ P815 tumor cells on day 14; and given a 3rd booster vaccine on day 21 (**Figure 4.3E**). Animals given predicted high immunogenicity T cells survived for longer than those given predicted low immunogenicity T cells, both of which survived for longer than no-peptide control T cells (**Figure 4.3F**). Additionally, we observed significantly lower tumor burden in high immunogenicity versus low immunogenicity animals by luciferase imaging by day 26 (Wilcoxon test of total luminescence $p < 0.05$; **Figure 4.4**), without significant differences in weight loss or clinical score. In summary, these experiments demonstrate the clinical relevance of our immunogenicity prediction model, with significant differences observed between predicted high and low immunogenicity epitopes. These experiments used neoantigen/mHA in both the prophylactic and therapeutic setting, rather than strictly treating animals after tumor injection. This method was selected due to the intrinsic low efficacy of free-peptide vaccines, whereby differences in therapeutic efficacy may not be observed between predicted high and low immunogenicity antigens. As such, while these experiments provide evidence for the clinical relevance of our computational model, development of more robust therapeutic vaccine platforms are necessary for improving response rates to peptide-based tumor-specific antigen vaccines.

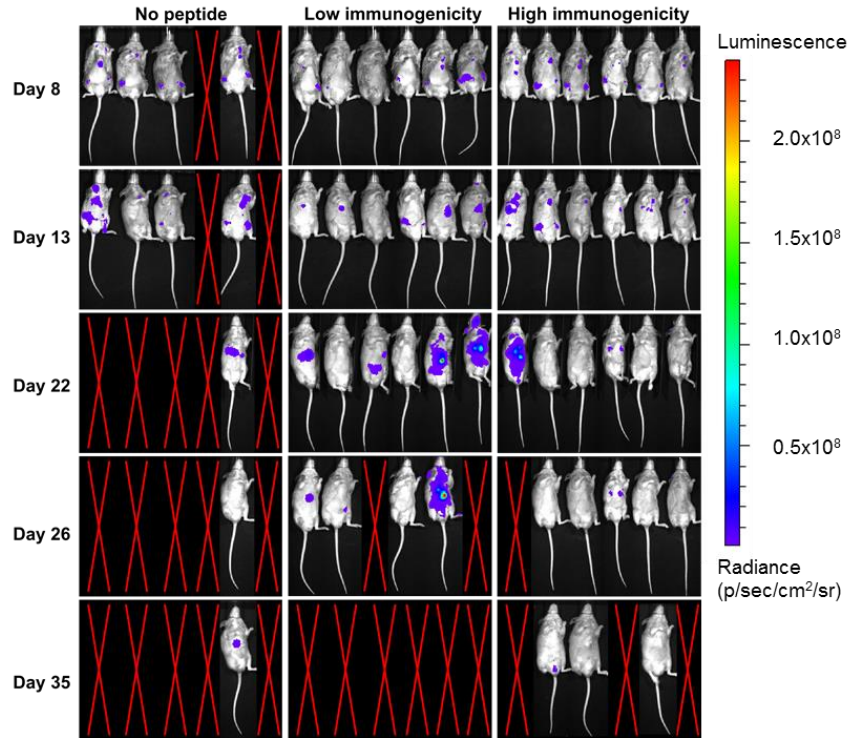


Figure 4.4: Luciferase imaging of luc-P815 tumor burden in DBA/2 recipients.

Correlates of predicted immunogenicity in human class I epitopes

While this immunogenicity prediction model was designed and validated in mouse, we hypothesized that similar rules of immunogenicity may exist among human neoantigens. To test this hypothesis, we ran predicted class I neoantigens from the Cancer Genome Atlas (TCGA) database through our final model, generating immunogenicity scores for each epitope. As expected, we observed strong correlation between the number of highly immunogenic neoantigens (HIN) identified by our model (>95th percentile) with number of total neoantigens (Pearson correlation $p < 0.0001$). From our validation experiments in BBN963 and P815 models, we observed that predicted high immunogenicity peptides had greater clinical benefit in the therapeutic

vaccine setting than predicted low immunogenicity peptides. As such, we reasoned that while HIN count and total neoantigen burden were highly co-correlated, the most highly immunogenic neoantigens were the key drivers of immunity. Thus, we performed regression studies between HIN count and immune features without controlling for total neoantigen burden.

We observed significant association between HIN count and immune gene signatures of IFN- γ , cytotoxicity, CD8 and total T cells, and B cells among the TCGA pan-cancer dataset (**Figure 4.5A**). When analyzed by tumor type, the majority of these significant associations were encompassed by the colon (COAD) and lung (LUAD) adenocarcinoma cancer types (**Figure 4.5B**). Within COAD, there was strong positive association between HIN count and T-cell and cytotoxicity signatures. To identify potential drivers of this pattern, we looked for co-expression of HIN count and MSI status, observing MSI-high COAD tumors having significantly higher HIN counts (**Figure 4.5C**), suggesting MSI may drive generation of highly immunogenic SNV neoantigens.

immunogenic neoantigens (x-axis) versus MSI score (y-axis) for TCGA COAD dataset. (D) Volcano plot representing GLM coefficient (x-axis) and $-\log_{10}(\text{FDR p-value})$ (y-axis) between numbers of highly immunogenic neoantigens and cancer driver mutations in TCGA LUAD dataset. (A and D) Dashed line represents FDR p-value = 0.05.

In contrast, LUAD largely demonstrated negative association with immune gene signatures of PD-1 responsiveness, T and B cells, and several innate immune cell signatures. We examined the association between whole-exome sequencing derived oncogene/tumor suppressor copy numbers with HIN count, which demonstrated significant negative association with the MYC gene (FDR p-value < 0.01; **Figure 4.5D**). Among MYC amplified tumors, there was significantly greater expression of genes corresponding to cell cycle gene patterns, as well as enrichment of downstream genes to the MYC pathway (gene set enrichment analysis and DAVID gene ontology analysis), suggesting MYC amplification provides a strong pro-tumorigenesis signal. Additionally, there was a decrease in sharing of MiXCR-derived T-cell receptor sequences in MYC amplified tumors, providing evidence that decreased neoantigen burden may negatively impact the anti-tumor immune response in LUAD. A potential explanation for this pattern between MYC amplification and lower HIN count is a result of decreased selective pressures for accumulation of mutations in MYC-driven LUAD cancers, where further mutations in oncogene/tumor-suppressors are not necessary for oncogenesis.

In summary, we demonstrate that peptide-intrinsic features are associated with neoantigen and mHA immunogenicity. We provide here a description of a machine learning algorithm for predicting neoantigen immunogenicity, validated with therapeutic vaccine experiments. Analysis of human cancer data reveals that the number of predicted high immunogenicity neoantigens is associated with immunological and oncogenic features of colon and lung adenocarcinomas. This model provides a proof-

of-concept for computational prediction of SNV/SNP-derived neoantigen/mHA immunogenicity, demonstrating the potential of applying such a method on human data to improve clinical selection of tumor antigen targets for therapeutic vaccine development.

4.1.3 Materials and methods

Neoantigen and mHA prediction and ELISpot immunogenicity studies

Neoantigen and mHA predictions were performed using protocol previously described in section 2.1.2: *Neoantigen prediction*. ELISpot immunogenicity studies were performed according to protocol previously described in section 2.1.2:

Vaccine/ELISPOT assay for neoantigen immunogenicity

Linear regression and computational modelling

Intrinsic peptide features were derived from custom scripts, as well as from the R package *Peptides*. Univariable and multivariable linear regression was performed with a general linear method (GLM) using the R package *glm*. Multivariable models, including the final gradient boosting model, were built from the R package *caret*, with custom scripts to perform cross-validation.

Peptide treatment studies

Biological validation treatment studies were performed as summarized in **Figure 4.3C,D**. Briefly, BBN963 treatment studies began with pre-tumor vaccination with 30 µg of a single peptide (or no-peptide control) and 50 µg poly(I:C) adjuvant, injected in 100 µL PBS intradermally in the flank of 8-10 week old female C57BL/6 mice (Charles River). Twelve days after vaccination, 1×10^7 BBN963 cells were injected in 100 µL PBS subcutaneously in the flank. On day 21, animals were given a vaccine booster with 30

µg of the initial respective peptide with no poly(I:C) adjuvant. This booster was delivered in 100 µL PBS intradermally in the skin directly adjacent to the tumor. Animals were monitored for tumor growth and survival every 2-3 days for the remainder of the study, with UNC Institutional Animal Care and Use Committee (IACUC) defined endpoints of area >200 mm² or ulceration >5 mm in the longest diameter.

For P815 treatment studies, 8-12 week old male BALB/c donors (Jackson Laboratory) were vaccinated on days 0 and 7 with 100 µg total peptide (3-4 pooled equimolar peptides, or no-peptide control) and 50 µg poly(I:C) adjuvant in 100 µL PBS intradermally in the flank. DBA/2 recipients were treated with 800 rad total body irradiation on day 13. On day 14, splenic-derived T cells and bone marrow cells were isolated from donor BALB/c animals, and recipient DBA/2 animals were given tail-vein IV injections of 3x10⁶ T cells, 3x10⁶ bone marrow cells, and 3x10⁵ P815-luciferase tumor cells (or bone-marrow only control). DBA/2 recipients were given a booster vaccine on day 21 (100 µg total peptide, 50 µg poly(I:C)), with animals monitored every 2-3 days for survival, with UNC IACUC defined endpoints of bilateral hind-limb paralysis. Luciferase imaging studies were performed on days 8, 13, 22, 26, and 35 after transplant, using an IVIS imaging system on animals given intraperitoneal luciferin.

4.2 Neoantigen-delivering nanoparticles for therapeutic tumor vaccines

4.2.1 Introduction

Tumor-specific vaccine targets are currently under development for patient-specific tumor therapies. Neoantigens are largely patient specific variant peptides that can be recognized by T cells to direct tumor killing^{185–187}, and they are an appealing target for therapeutic vaccines because neoantigen-specific T cells can escape thymic selection

and can recognize the restricted expression of neoantigens by the tumor cell^{188–192}. Despite the ability of neoantigen-based therapeutic tumor vaccines to promote tumor-specific T-cell responses in a small number of pre-clinical models, clinical efficacy remains to be demonstrated^{14,49,70–72}. A key challenge arising in the field of tumor-vaccine therapy is the development of a vaccine platform to allow for optimal immune response against the vaccine target antigens. Most neoantigen studies rely upon free-peptide vaccination, which are sub-optimally immunogenic compared to other delivery vehicles such as nanoparticle (NP)-based platforms due to factors such as exogenous proteases and poor uptake by antigen-presenting cells⁶⁸.

To address the challenges of neoantigen delivery, we have developed a NP vaccine platform for the delivery of neoantigen peptides. NPs are an effective platform for a diverse range of cancer immunotherapies⁶⁸, as exemplified by recent development of a tumor-lysate delivering NP system which significantly delayed tumor growth and increased survival in B16F10 melanoma model tumor-bearing mice⁷⁵. This NP platform was hypothesized to derive therapeutic efficacy from capture of neoantigen-containing proteins that promote anti-tumor immunity, as evident by the most efficacious NP formulation contained the highest number of captured neoantigen-containing proteins. In addition, we recently demonstrated the efficacy of a dual checkpoint inhibitor/T-cell stimulatory antibody (α PD-1/ α OX-40) delivering NP platform, which caused tumor regression and long term survival in >30% of B16F10 melanoma tumor-bearing mice when used in combination with radiation therapy, outperforming dual free-antibody (**Appendix V**)¹⁹³. This study demonstrated the effectiveness of immunotherapy co-localization – a principle which can be applied in a NP vaccine platform through co-

delivery of the antigen and an immune adjuvant. Based on these preliminary studies, we believe vaccination with a similar neoantigen-delivering NP (ndNP) platform will generate robust anti-tumor immune responses over conventional free-peptide based vaccines. In this study, we describe an ndNP platform with improved efficacy and immune activation over conventional free-peptide vaccination.

4.2.2 Results and Discussion

Neoantigen prediction and NP design

Neoantigen prediction and validation was performed in the B16F10 melanoma model, as described previously (Chapter 2.1, Materials and methods). From the total pool of ELISpot-validated neoantigen peptides, we selected the top two MHC class I and class II epitopes for treatment experiments. In addition, we also tested four neoantigens previously identified and validated by Min *et al.* using a tumor antigen capture NP approach⁷⁵. This pool of neoantigens was compared to a previously described neoantigen sequence with therapeutic efficacy in B16F10 (B16-M30: PSKPSFQEFVDWENVSPELNSTDQPFL) in a publication from Kreiter *et al.*⁷⁰. To look for evidence of neoantigen presentation on the B16F10 tumor cell, T cells were isolated from respective neoantigen vaccinated C57BL/6 mice and expanded *ex vivo* in a neoantigen-pulsed dendritic cell co-culture. These enriched neoantigen-experienced T cells were co-cultured against B16F10 cells, with anti-tumor response measured via IFN- γ capture ELISpot (**Figure 4.6**). Compared to a non-specific (SIINFEKL) T cell control, we observed IFN- γ signal above background in 7 of 9 tested neoantigen peptides, providing evidence of endogenous neoantigen presentation on the B16F10 tumor.

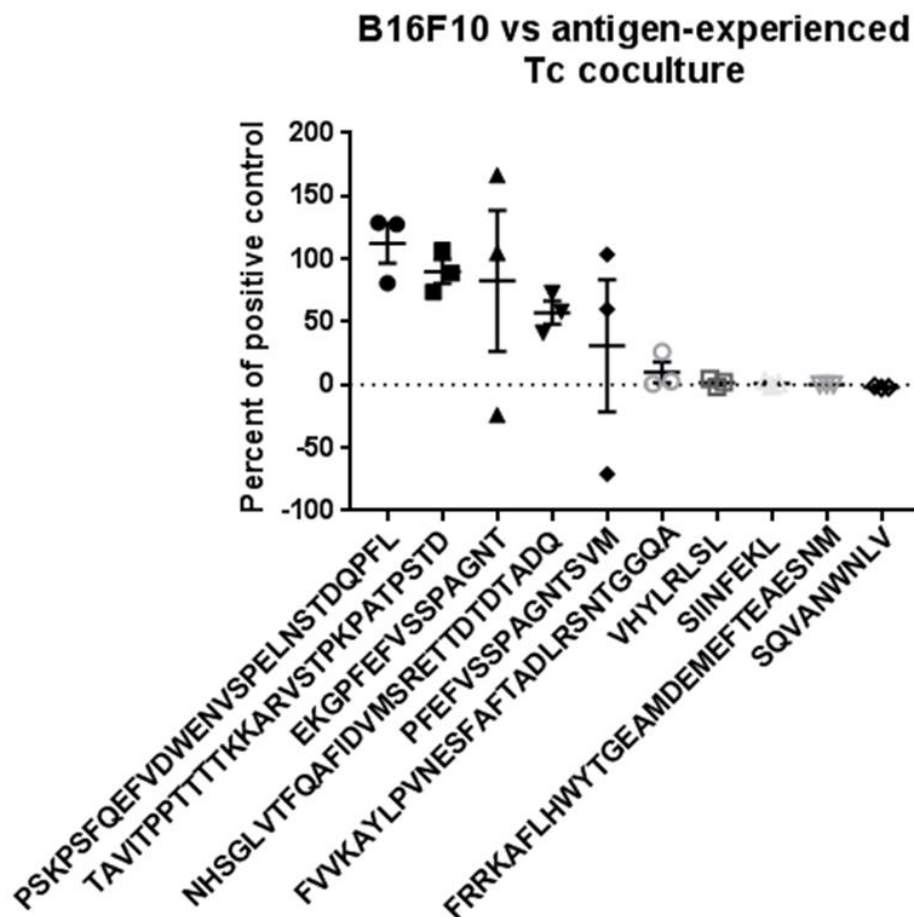


Figure 4.6: IFN- γ ELISpot in a co-culture assay of neoantigen-experiences T cells and B16F10 tumor cell.

For the delivery platform, PLGA-PEG-NH₂ was selected for the NP matrix, with a redox-sensitive succinimidyl 3-(2-pyridyldithio)propionate (SPDP) linker conjugated to the polymer amine group. Subsequently, c-terminus modified neoantigens containing a cysteamide functional group was attached to the SPDP moiety of the polymer, resulting in an oxidation-sensitive neoantigen peptide release mechanism. This ndNP chemistry was designed such that neoantigen epitopes would be released upon cellular uptake in the endosome of an antigen-presenting cell.

Therapeutic vaccine treatment studies

We next conducted a treatment study to demonstrate the feasibility of our proposed neoantigen-delivery nanoparticle (ndNP) platform (**Figure 4.7**). Treatments in B16F10-bearing mice began on day 4 after tumor injections (7.5×10^4 cells, s.c.), when tumors were just palpable, with vaccination and anti-PD-1 therapy given according to **Figure 4.8** timeline. ndNPs were loaded with the STING agonist DMXAA as adjuvant. Mice were given either ndNP containing our eight validated neoantigens (NP-mix peptide; n = 10), ndNPs containing the previously published B16-M30 reference neoantigen peptide⁷⁰ (NP-ref peptide; n = 5), free DMXAA with either free neoantigen peptides (Free mix peptide; n = 10) or free reference neoantigen peptide (Free ref peptide; n = 10), DMXAA-only NP control (DMXAA-NP; n = 5), free DMXAA only control (n = 5), blank NP with no-peptide/no-DMXAA control (NP void, n = 5), anti-PD-1 only control (PD1 only; n = 5), or PBS only control (PBS; n = 5). Peptide and DMXAA adjuvant loading concentrations, as well as size, polydispersion index (PDI), and zeta potential characteristics of each NP group is shown in Table 4.1.

Formulation	Peptide (ug/dose)	DMXAA (ug/dose)	Size (nm)	PDI	Zeta
Void NP	0	0	78.1±0.8	0.097±0.014	-16.6±0.5
DMXAA NP	0	68.9	70.1±0.4	0.142±0.021	-21.3±0.4
Ref NP	105	131	96.5±0.8	0.320±0.014	-19.5±0.2
Mix NP	105 (15 for each peptide)	68.9	104.5±5.6	0.283±0.062	2.5±0.2

Table 4.1: Characterization of neoantigen-delivering nanoparticle formulations and controls.

Tumor growth was significantly delayed in ndNP treated animals, with ndNP containing our predicted neoantigens outperforming all other treatment groups and controls (Welch's t-test tumor volume $p < 0.05$ by day 20). Based upon Luminex studies taken from peripheral bleeds on day 10, we observed increases in pro-inflammatory cytokines in ndNP-mix peptide treated animals, which were significantly differentially clustered from all other groups by hierarchical clustering (**Figure 4.9**).

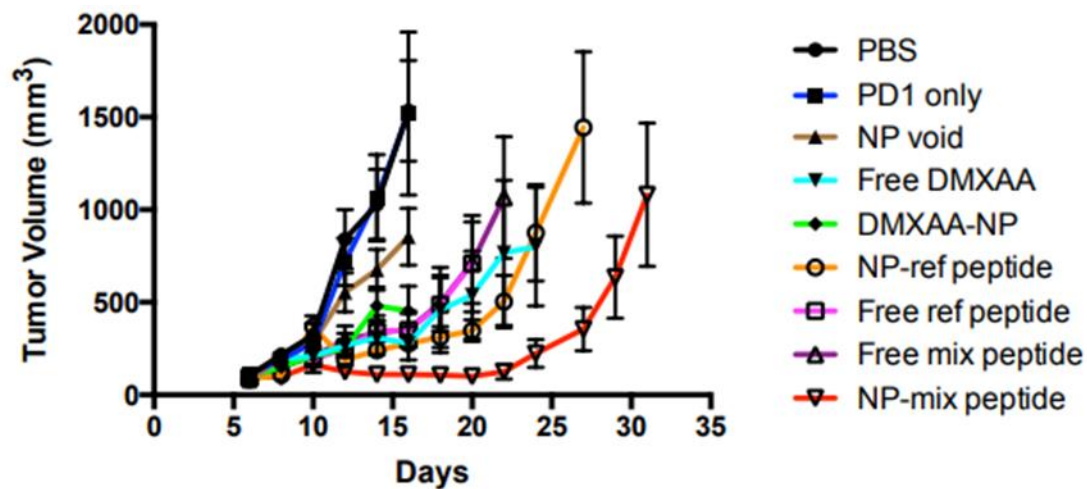


Figure 4.7: Tumor growth curves for B16F10 bearing mice treated with neoantigen delivering nanoparticles or free neoantigenic peptide. X-axis represents days post tumor injection, and y-axis represents tumor volume (mm^3).

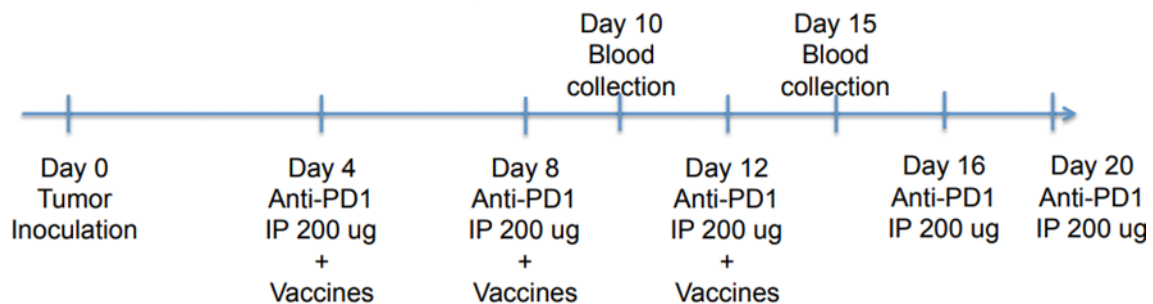


Figure 4.8: Experimental timeline for ndNP treatment study.

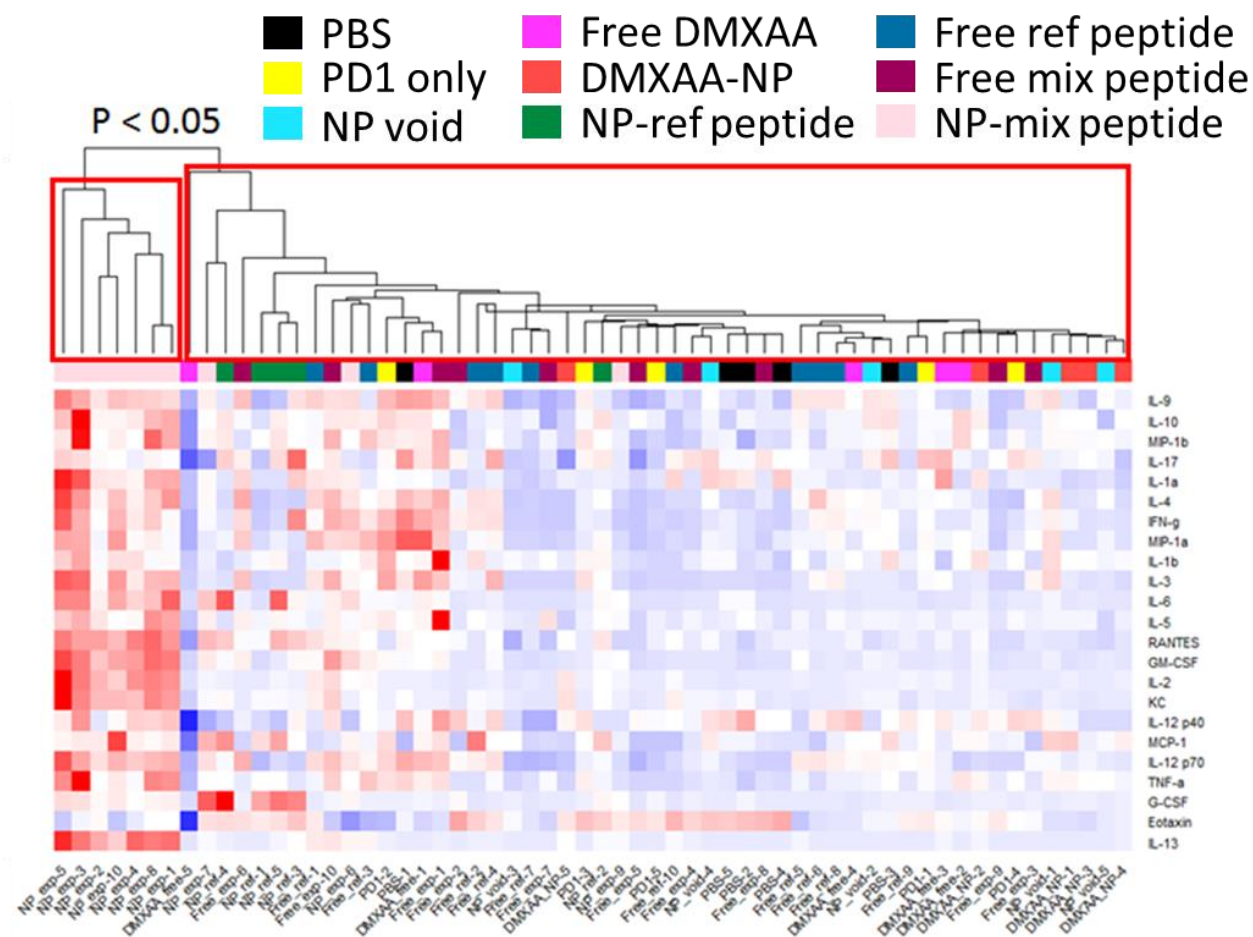


Figure 4.9: Heatmap of Luminex cytokine z-scores measured in day 10 plasma levels from animals in Fig. 2 treatment study. Samples (columns) are ordered by hierarchical clustering by z-score of cytokine levels (rows), with boxes around the dendrogram representing significance via the R package pvclust.

Overall, these studies provide proof-of-principle for the superiority of a NP-based neoantigen vaccine platform over current standard free-peptide vaccines, suggesting the ndNP platform may allow for the use of a greater range of neoantigens that otherwise may not be substantially immunogenic as free-peptides. This improved clinical efficacy is associated with increases in peripheral levels of pro-inflammatory cytokines and chemokines, suggesting the combination of multiple neoantigens, DMXAA adjuvant, and a NP delivery platform is capable of greater immune stimulation

than free-peptide/DMXAA vaccine. Currently, the mechanism behind the enhanced immunogenicity and efficacy of this ndNP platform remains unknown. Potential hypotheses include 1) enhanced DC uptake due to particle size and charge characteristics, 2) decreased peptide degradation, and 3) co-localization of peptide and DMXAA adjuvant. Future studies will be performed to elucidate the mechanism of enhanced efficacy, including experiments to analyze the necessary cell populations (e.g. cell depletion studies, *in vitro/ex vivo* phenotyping of cell populations, transcriptomics analysis of tumor and lymph node infiltrating populations) and NP characteristics (e.g. separation of peptide- and DMXAA-delivering NP, alteration of NP chemistry to modulate loading, size, and charge characteristics). Compared to published peptide (200µg per peptide¹⁹⁴) and DMXAA (500µg¹⁹⁵) treatment doses, current peptide and adjuvant dosing is relatively low in NP groups (**Table 4.1**), suggesting optimization of NP chemistry to improve loading efficiency and capacity may further increase the efficacy of ndNP treatment. In future studies, we will study methods to improve ndNP loading and comprehensively elucidate the immunological mechanism for improved ndNP efficacy.

4.2.3 Materials and methods

Neoantigen and mHA prediction and ELISpot immunogenicity studies

Neoantigen and mHA predictions were performed using protocol previously described in section 2.1.2: *Neoantigen prediction*. ELISpot immunogenicity studies were performed according to protocols previously described in Chapter 2.1.2:

Vaccine/ELISPOT assay for neoantigen immunogenicity and Neoantigen-enriched T-cell Coculture.

Luminex analysis

Peripheral blood was collected from cheek bleeds of tumor bearing animals on day 10 after tumor injection, allowing blood to clot. After clotting (>15 minutes), samples were spun at 13,000RPM for 15 minutes on a desktop centrifuge, collecting remaining serum. Serum samples were flash frozen on dry ice and stored at -80°C until use. Luminex studies were performed using the Bio-Plex Pro Mouse Cytokine 23-plex assay (Bio-rad, #m60009rdpd), according to manufacturer protocol. Subsequent analyses were performed using custom scripts, showing hierarchical clustered, z-score normalized cytokine concentration values for each serum sample.

ndNP synthesis and treatment studies

PLGA-PEG-NH₂ (m.w. 17kDa), succinimidyl 6-[3(2-pyridyldithio)propionamido]hexanoate (LC-SPDP), and N,N-Diisopropylethylamine (DIPEA) were combined at a 1:4:10 molar ratio, respectively, in DMF solvent. Reaction was left overnight at room temperature under normal atmosphere. Product was subsequently precipitated with a cold mixture of methanol and diethyl ether (1:1 volume) and dried under vacuum. The dried precipitant was mixed with c-terminus cysteamide modified neoantigen peptide at a 1:2 molar ratio, respectively, in DMF solvent. Reaction was left at room temperature for 48 hours under N₂ atmosphere. Conjugated polymer product was precipitated in a mixture of cold methanol and diethyl ether (0.5 – 0.8:1 by volume) and dried under vacuum. Peptide conjugation efficiency was confirmed using the Pierce Quantitative Fluorometric Peptide Assay, according to manufacturer protocol. Peptide conjugation chemistry was confirmed with H-NMR.

Nanoparticle formation was performed using nanoprecipitation. DMXAA was dissolved in acetone at 1 mg/mL, and peptide-polymer conjugate dissolved in DMF at 10 mg/mL. DMXAA and peptide-polymer solutions were combined at 1:100 by mass. This mixture was added dropwise into water (1:3 organic to water by volume) and stirred aggressively by magnetic stir plate. This solution was left for 4 hours at room temperature under ventilation to allow for evaporation of organic solvent. Subsequent formed particles are washed three-times in DI H₂O in an Amicon Ultra Centrifugal Filters (50 mL, 100,000 NMWL). Particle size and charge were confirmed using dynamic light scattering and zeta potentiometry, respectively. DMXAA loading was quantified using UV-Vis spectroscopy absorption at 345 nM. Washed NP was added to DPBS at 100 µL per dose before final injection.

For treatment studies, peptide dosage was normalized to 100 µg across all treatment groups (except peptide-free controls), and DMXAA dose was 130 µg in Ref NP group and 70 µg in all other treatment groups (except DMXAA-free controls). Total polymer mass ranged 7-13 mg per treatment. All vaccine treatments were given as intradermal injections in the skin directly adjacent to the tumor. Anti-PD-1 co-therapy was given as 200 µg intraperitoneal injections in 100 µL total volume PBS.

CHAPTER 5: Future Directions and Conclusion

The works presented here represent a multidisciplinary approach to study the role of the adaptive immune system in modulation of the tumor immune microenvironment. The focus of these studies is to 1) develop biologically relevant models and tools to elucidate the microenvironment of various cancer subtypes, 2) elucidate the mechanism of action for existing immunotherapies (i.e. anti-PD-1 therapy), 3) improve upon the efficacy of current anti-tumor vaccine targets (i.e. neoantigens and mHA), and 4) identify novel tumor specific antigen targets for biomarker and therapeutic vaccine development (i.e. hERV antigens). In addition to these studies, we are performing ongoing projects to follow up on the findings presented above.

To develop a deeper understanding of the biological features associated with the anti-PD-1 mixed response phenotype in BBN963, we are performing single cell transcriptomics and CyToF proteomics analyses on tumor infiltrating lymphocytes. For single cell RNA-seq (scRNA-seq) analysis of BBN963 tumors, tumor bearing animals were treated with anti-PD-1 therapy and monitored for response. Primary responders (n = 3) and non-responders (n = 3) to therapy were selected, with tumor infiltrating lymphocytes enriched from the tumor using gradient centrifugation. These cells were then run through a 10x Chromium Controller, with downstream library preparation performed according to the 10x 3' gene expression profiling kit. These samples are currently under analysis, with the aim of elucidating transcriptional differences associated with primary resistance to anti-PD-1 therapy. From preliminary studies using

bulk RNA-seq and Luminex studies on pre-treatment peripheral blood samples in BBN963 tumor bearing animals, we observed increases in gene signatures associated with five different toll-like receptor (TLR) pathways as well as increases in pro-inflammatory cytokines/chemokines (IL-1a, IL-1b, IL-2, MIP-1a, RANTES) and decreases in IL-5 in samples that subsequently respond to anti-PD-1 therapy. Altogether, this suggests response to anti-PD-1 therapy may be dictated by the presence or absence of pre-treatment systemic inflammation levels. Analysis of scRNA-seq data from post-treatment tumor samples will allow us to observe the subsequent immune differences in these tumors, painting a clearer picture of the connection between pre-treatment and post-treatment patterns of response to checkpoint inhibitor therapy.

In addition, we have been developing a murine CyToF mass cytometry panel in collaboration with the UNC Flow Cytometry core facility. This 35-40 marker panel will be used to identify and phenotype the various tumor infiltrating leukocytes in anti-PD-1 responsive and non-responsive tumors. From initial studies using a flow cytometric panel, we have observed that the time to which a tumor develops resistance to anti-PD-1 therapy is correlated with a decrease in total CD45+ immune infiltration, but an increase in the relative frequencies of exhaustion-associated cell phenotypes (Tregs, terminally differentiated CD4 and CD8 T cells, PD-1 expressing T cells, myelocytic and granulocytic MDSCs, dendritic cells, and macrophages) to stem-like cell phenotypes (naïve and central memory CD4 and CD8 T cells, B cells, and total CD4 and CD8 T cell frequencies). Altogether, this suggests that longitudinal development of resistance to anti-PD-1 therapy is potentially triggered through immune exclusion in the tumor, with

remaining infiltrating immune cells displaying a more exhausted phenotype. Future CyToF studies will allow us to comprehensively study this pattern, including analysis of various other checkpoint inhibitor (CTLA-4, LAG-3, TIM-3), costimulatory (OX-40, CD80/86), and innate M1/M2 (Arg-1, Ym-1) markers.

Our analysis on the role of hERVs in modulation of the tumor immune microenvironment primarily focused on ccRCC; however, several other tumor types displayed similar patterns of significant association between hERV expression versus patient outcomes and immune signatures. Apart from ccRCC (TCGA KIRC), low grade glioma (LGG) demonstrated the second greatest number of significantly prognostic hERVs. As such, we have begun correlative analyses in LGG to study the impact of hERV expression on the cancer disease process. Initial findings show differential hERV expression patterns among IDH1/2 mutant and wild-type LGG tumors – a key driver of oncogenesis in LGG – with IDH1/2 mutant tumors showing significantly lower overall hERV expression than IDH1/2 wild-type tumors.

Lastly, our analysis on the design and delivery of neoantigen-based cancer vaccines has demonstrated our capacity to use computational methods to improve neoantigen prediction, as well as using a nanoparticle delivery platform to improve vaccine immunogenicity and outcomes. Our computational analysis provided an initial *in silico* approach for selectively filtering out high-immunogenicity murine neoantigen epitopes, providing a promising strategy for application in human neoantigen selection. Future directions for this work include increasing the sample size available for model design, which would allow for further increases in predictive power. Furthermore, validation in a human neoantigen vaccine study is necessary, testing if this

computational approach can predict for clinical outcome similarly to what was observed in our pre-clinical validation experiments.

Our initial studies on a nanoparticle neoantigen vaccine approach demonstrated significantly better survival and tumor growth control than free-peptide controls. Paired with this efficacy, peripheral inflammatory cytokine and chemokine levels were preferentially upregulated in our ndNP treated group, suggesting a strong immune component to the ndNP's mechanism of action. In future studies, we plan to 1) improve the peptide and adjuvant loading efficiencies of the ndNP platform and 2) comprehensively elucidate the mechanism of action for ndNP's increased efficacy over free-peptide vaccines. The first of these goals is being actively pursued by members of the lab of Andrew Wang, looking at potentially novel synthesis techniques to both increase synthesis efficiency and absolute peptide/adjuvant loading capacity of ndNPs. Considering the current vaccination dose of our ndNPs is relatively low for both peptide (~100ug) and DMXAA adjuvant (~70ug) but still shows significant survival benefit, we expect an optimized strategy will further bolster our ability to cure tumor bearing animals. In order to elucidate the mechanism of action for ndNPs, we will rely upon flow cytometric and RNA-seq approaches to compare the immune infiltrate between free-peptide and ndNP treated animals. These well validated approaches will provide a jumping-off point for more detailed studies to confirm the role of various immune populations in response to ndNP therapy. We hypothesize to observe the importance of both innate and adaptive immune arms, with APC populations such as DCs being necessary for neoantigen uptake and presentation, pro-inflammatory innate populations such as M1 macrophages and activated DCs to be important to drive adaptive

immunity, and presence of antigen-specific T cells necessary to carry out anti-tumor effector function. Previous studies have suggested that the majority of anti-tumor T cells in neoantigen treated animals are derived against class II MHC epitopes, despite the fact that CD8⁺ CTLs have been historically thought to be the most important component in the anti-tumor immune response. It remains to be seen if ndNP therapy differentially modulates the CD4 and CD8 arms of the T cell response in a manner unique from free-peptide vaccination.

The ultimate goal for all of these studies is to apply the knowledge and techniques described here for treatment of human cancers. With the advent of universal immunotherapy treatment strategies such as checkpoint blockade therapy, immuno-oncology has become an integral portion of our management of various cancers. Our work in chapter 2 highlights the immune correlates of responsiveness to anti-PD-1 therapy in basal-like bladder cancer, and development of these biologically faithful cancer models provides an avenue to further understand the effects of checkpoint blockade inhibitors and tumor-antigen vaccine therapies. Current clinical studies in melanoma suggest that similar to checkpoint blockade therapy, not all patients respond to neoantigen vaccine therapy, with no clear explanation for resistance to therapy. Future directions for the field will include expanding tumor-specific antigen vaccine therapy to other cancer types. As such, elucidation of neoantigens in our BBN and UPPL models provides us with the capacity to better understand how to most effectively deliver these vaccines in bladder cancer, as well as how to overcome resistance that may develop subsequent to therapy in these models.

The future of immuno-oncology is largely focused on the use of tumor-specific antigen targets to drive anti-tumor adaptive immune responses. With conventional SNV neoantigens showing promise in pre-clinical and clinical trials, we are now striving to expand the targetable epitope landscape of cancers, increase the power of current targets, and understand how these adaptive immune therapies synergize with existing universal immunotherapies. Our work in chapter 3 provides a method for genomic identification of tumor-specific hERV antigenic targets, which may allow for a novel class of TSA targets for therapeutic leverage in ccRCC and other cancer types. Currently, our results suggest that a large proportion of ccRCC TILs may already be hERV-specific, suggesting that these tumor-specific T cells may be terminally exhausted and not able to carry out effector function. Future studies will include 1) understanding the mechanism of immune suppression for hERV-specific T cells within ccRCC tumors, and how we may reverse this exhaustion to re-awaken their effector function, and 2) leveraging tumor-specific hERV antigens for therapeutic purposes, including development of a robust hERV-related biomarker for immunotherapy responsiveness and application of hERV antigens for vaccine and cellular therapies. With evidence of enhanced vaccine efficacy through the use of a NP delivery platform presented in chapter 4, hERV and other TSA targets may additionally benefit from the use of a nano-delivery system alongside neoantigens. In summary, the studies presented in this dissertation were pursued with the goal to understand and improve anti-tumor immunotherapeutics, with the hope that they may one day improve our capacity to impact survival and quality-of-life for all cancer patients.

APPENDIX 1: RNA-seq Analysis of the Tumor Microenvironment

1. Introduction

Over the last several decades, we have observed a marked increase in the use of next-generation sequencing methods, including whole exome/genome sequencing and whole transcriptome profiling, allowing for characterization of a wide variety of sample types throughout a broad set of scientific disciplines. The field of immunogenomics grew from a convergence of genomics and data science approaches applied to immunological questions, largely driven by cancer biologists and immunologists seeking to understand the tumor immune microenvironment from large next generation sequencing datasets such as those of The Cancer Genome Atlas (TCGA). Immunogenomics is largely focused on the immune response in the context of malignancy, within which the complex tumor-immune microenvironment can be dissected with the use of transcriptomic analysis of tumor and tumor-infiltrating lymphocytes.

The initial evaluation of the tumor microenvironment was performed using cDNA microarray technology. However, microarray technology is limited by 1) transcript-specific probes that do not allow novel transcripts to be queried, 2) limited range for the detection of low abundant transcripts, and 3) inability to alter the process to improve this detection. The use of microarray technologies has largely been replaced by whole transcriptome RNA-seq methods, which circumvent the issues associated with microarray analysis. Using RNA-seq, investigators are able to identify tens of thousands of genes within a single tumor-derived sample. The use of RNA-seq to characterize tumors has allowed investigators to reconstruct the cellular heterogeneity

of the tumor microenvironment from archival tissues^{196,197}. Additionally, RNA-seq can be used in combination with or lieu of pathological approaches to subtype cancers¹⁹⁸. Among immunogenomic advancements aided through the use of RNA-seq include correlative analyses of responders versus non-responders to immunotherapy¹⁸², design of biomarkers for predicting patient prognosis and response to therapies^{199,200}, and characterization of the antigen spectrum of a tumor and subsequent targeting of these antigens (neoantigens^{71,201}, cancer testes antigens¹⁹⁰, tumor associated antigens²⁰², etc.). These analyses have allowed for a greater understanding of the tumor-immune microenvironment, with recent advancement in of single-cell sequencing technologies providing even further granularity in deconstructing the complicated cellular immune microenvironment.

Evaluation of the tumor-immune microenvironment with RNA-seq can frequently provide data orders of magnitude larger than conventional immunological techniques such as flow cytometry (which require fresh sample processing) or other assays that are not accessible from FFPE material. As a result, consistency and automation of the RNA-seq workflow is necessary. In this chapter, we will provide a summary of our RNA-seq workflow, which is broken down into the following steps: 1) tissue collection and isolation of RNA, 2) library preparation and sequencing, 3) data processing and quality control, 4) alignment and quantitation, and 5) analysis of data. Lastly, it should be noted that the field of RNA-seq analysis is rapidly progressing, with more accurate methods constantly in development. While we have provided examples and recommendations for analysis software in the chapter, the fluid nature of this field may mean that some of these methods may be replaced in the near future by newer

technologies. As such, the reader should examine recent developments in the field and make adaptations as these newer technologies are made available.

2. Materials

2.1. Tissue collection, RNA isolation, and QC

- PCR Workstation
- Life Technologies RNaseZap RNase Decontamination Wipes
- Sigma-Aldrich RNaseZap spray
- Absolute Ethanol, molecular biology grade
- Roche High Pure RNA Paraffin Kit
- Qiagen QIAshredder
- Qiagen RNEasy Mini Kit
- Qiagen RNEasy Micro Kit
- 2-Mercaptoethanol
- Qiagen TissueRuptor II
- Qiagen TissueRuptor Disposable Probes
- 15mL polypropylene (PP) centrifuge tubes
- Qiagen DNase RNase-Free DNase Set
- Molecular Biology Grade Water
- DNA low-bind tubes
- Qubit BR RNA assay kit
- Qubit HS RNA assay kit
- ThermoFisher Qubit 4.0 Fluorometer
- Agilent 2200 TapeStation Instrument

- Agilent RNA ScreenTape
- Agilent RNA ScreenTape Sample Buffer
- Agilent RNA ScreenTape Ladder
- ThermoFisher NanoDrop One^C Microvolume UV-Vis Spectrophotometer

2.2. Library preparation and sequencing

2.2.1. Library preparation kits:

- mRNA:
 - KAPA Stranded mRNA-Seq Kit
 - Illumina Truseq Stranded mRNA
 - Nugen Universal Plus mRNA-seq
 - Takara Smart-Seq v4 Ultra Low Input RNA Kit for Sequencing
- Total RNA:
 - Illumina Truseq Stranded Total RNA
 - KAPA Stranded RNA-Seq Kit with RiboErase
 - Nugen Ovation Universal RNA-Seq with Any Deplete
 - Nugen Ovation Solo RNA-Seq System with Any Deplete
 - Takara SMARTer Stranded Total RNA-Seq Kit v2 - Pico Input Mammalian
- FFPE:
 - Illumina Truseq Stranded Total RNA
 - Kapa Stranded RNAseq with RiboErase
 - Nugen Ovation RNA-Seq FFPE System with AnyDeplete
 - Takara SMARTer Universal Low Input RNA Kit

- Illumina Truseq RNA Exome

2.2.2. Quantification

- KAPA library quantification kit

2.2.3. Nucleotide Concentration

- Qiagen RNeasy MinElute Cleanup Kit
- KAPA Pure Beads
- Beckman Coulter Agencourt RNAClean XP

2.2.4. Depletion Kit

- Nugen AnyDeplete

2.3. Data processing and quality control, alignment and quantification, and analysis of data

2.3.1. Computer: Our analyses are performed on a computing cluster

comprised of many interconnected, individual machines. If your analyses are limited to a small number of samples (tens), a high-powered computer running a Unix-based operating system (>8 cores, >32 Gb RAM) may be able to run most analyses mentioned below. However, if greater computational power is required and a computing cluster is not available, we recommend the use of Google Compute Engine (which we have historically used for certain high-requirement jobs).

2.3.2. Workspace: If running analyses on multiple computing clusters or outside computing engines, we recommend consultation with a data scientist and use of a containerization method such as Docker (<https://www.docker.com>) for convenience and stability. Putting analysis pipelines into Docker allows

for greater ease, as all parametrization and dependences are packaged together within the Docker environment.

2.3.3. Software: The following programs are recommended for analyses mentioned within this chapter (See **Table A1.1** for a software summary table):

- BCL2fastq
- FastQC
- BMap
- STAR aligner
- Picard tools
- Salmon quantifier
- Samtools
- Differential gene expression software (DESeq2, limma+voom, NOISeq, edgeR)
- Gene set analysis software (GSEA, ssGSEA, GSVA)
- TCR/BCR inference tool (MiXCR, V'DJer)
- MHC inference tool (PHLAT, HLAProfiler)
- MHC binding affinity predictor (NetMHCPan4.0, NetMHCIIPan)
- Viral/ERV quantification software (Virdetect, hervQuant)

3. Methods

3.1. Isolation of total RNA and QC

3.1.1. General considerations

RNA isolation is critical to the success of RNA-sequencing and as a result maximizing yield and purity of RNA is crucial. The time needed for tissue collection needs to be minimized to prevent RNA degradation. The collection of tissue in this protocol is optimized for a specific amount of RNA; the addition of a greater amount of tissue may paradoxically reduce the yield of RNA. Please remember to perform all isolations with an extraction agent in a fume hood with gloves and eye protection. RNA may be extracted from fresh or flash frozen samples or FFPE material. A number of extraction methods exist and an isolation strategy should be chosen based on the starting material and RNA subpopulation of choice^{203,204}. Beta-mercaptoethanol (2-ME) is commonly added to guanidium-based lysis buffers to improve RNA isolation from whole tissues samples abundant in RNases²⁰⁵, and should be added in the manufacturer's recommended amount when using commercially available kits (e.g. Qiagen RNEasy micro/mini). When freezing RNA or material for subsequent RNA extraction, nuclease free, tight-closure tubes such as Eppendorf DNA LoBind tubes are recommended to prevent contamination from RNases. The volume of lysis buffer needed per sample should be determined empirically based on cell type and number or tissue type and mass, using the manufacturer's recommendations as a general guideline. For total RNA isolation, we routinely use the Qiagen Rneasy Mini kit when processing tissue or when starting with larger cell numbers and the Rneasy Micro Kit when starting with fewer than 500,000 cells.

Given that RNA is easily degradable and potentially prone to contamination, certain workspace precautions should be taken²⁰⁶:

- Optimally, an RNA-only workspace with a molecular biology hood (to prevent contamination from debris in the air) should be used during extraction and reverse transcription, with a separate workspace for DNA-related molecular biology. Additionally, having a separate space for different species may prevent cross-contamination between different experiments.
- To further prevent cross-contamination, reagents used for handling RNA should remain in the RNA-only workspace and used exclusively for handling RNA. Ensure all reagents are RNase free and/or molecular biology grade.
- Use disposable, sterile RNase-free plasticware that does not require pre-treatment and barrier pipette tips.
- The workspace should be cleaned with an RNase removing material, such as Sigma RNaseZap RNase decontamination solution.
- RNase-free gloves and gowns should be worn to prevent contamination from skin cells during handling of RNA.
- As a general rule, RNA and DNA should be kept on ice while handling (unless otherwise stated by a protocol), working as quickly as possible. Keep UV-light sources away from nucleic acids to prevent degradation.

For FFPE slides, it is recommended to have a pathologist score the slides to ensure the material taken for RNA extraction is the tissue of choice (ex. tumor), and to control for estimated cellular heterogeneity when comparing experimental groups²⁰⁷. Numerous commercially available FFPE extraction kits have been compared^{208–210} or modified²¹¹ and should be chosen based on downstream applications. We routinely use

the Roche High Pure RNA Paraffin Kit for manual RNA extraction or the Maxwell 16 LEV RNA FFPE Purification Kit for automated extraction.

See note 1

3.1.2. Collection/Suspension/Lysis using Qiagen reagents

- i. When starting with fresh tissue, the material should be sectioned into small pieces (<20 mg). If starting with a single cell suspension, the cells should first be washed in PBS, pelleted, and the supernatant removed.
- ii. RLT lysis buffer (component of Qiagen RNEasy kits) supplemented with 1% (v/v) beta-mercaptoethanol is then added to each cell pellet or 20 mg piece of tissue and vortexed. The sample resuspended in RLT can then be flash frozen with either liquid nitrogen or an ice bath using dry ice and 70-100% ethanol. If no lysis buffer is available, the tissue or cell pellet can be frozen dry and lysis buffer added upon thawing.
- iii. Fresh tissue in RLT or thawed tissue in RLT can be homogenized with the tissue disrupter (e.g. Qiagen TissueRuptor II) according to the manufacturer's instructions. We typically homogenize tissue in a nuclease free 50 mL conical using the Qiagen TissueRuptor II at full speed for 30 seconds.
- iv. Homogenized tissue should then be transferred to a QIAshredder before proceeding to the Rneasy Mini Kit. If the starting material is a single cell suspension, the cells in RLT can be transferred directly to a QIAshredder for homogenization prior to using the RNeasy Mini Kit for large cell numbers or Rneasy Micro Kit for smaller cell numbers. When starting with fewer than 100,000 cells, we vortex the cells in lysis buffer at full speed for 1 minute to

homogenize in place of using a Qias shredder in order to minimize nucleic acid loss.

- v. The Qiagen Rneasy kits can be used as directed and variations are available that include an extra step utilizing a genomic DNA eliminator column (Rneasy Plus kits) or on-column DNA digestion with Dnase (Qiagen Rnase-Free Dnase Set).
- vi. Molecular biology grade water should be used for eluting RNA and should be pipetted directly onto the column filter. During this step, care should be taken not to touch the filter or the sides of the column with the pipette tip. The elution volume should be chosen carefully based on the amount of input material. If the eluent is too dilute, the RNA may need to be concentrated in order to perform QC.

RNA should be stored at -80° C and should always be aliquoted to avoid unnecessary freeze-thaw cycles.

3.1.3. QC

Three methods of quality control should be used for the most comprehensive measure of RNA quality:

- i. Qubit or similar method for high sensitivity fluorometric quantification
- ii. Spectrophotometer (Nanodrop or similar) for purity assessment
- iii. Fragment analyzer (Tapestation, LapChip, etc.) measuring electrophoretic mobility to determine RNA integrity

Ideally, 2 µL of sample should each be used for Qubit quantification and Nanodrop to improve accuracy of the readings. Also ensure the sample concentration

is within the working range of the instrument since many of the corresponding instrument kits have minimum and maximum cutoffs beyond which the reading is unreliable. Follow the temperature requirements of the reagents required to operate the QC instruments, as the readings are often temperature sensitive.

Some RNAseq library preparation methods will be more sensitive to contamination than others. Nanodrop measures contaminants and reports the ratio of absorbance of a sample at 260 and 280 nm and the ratio at 260 and 230 nm. A 260/280 ratio of 2.0 ± 0.02 is generally accepted as pure RNA while expected 260/230 values are typically in the range of 2.0-2.2^{206,212}. Many library prep methods recommend a 260/280 and 260/230 ratio of at least 1.7. A low 260/280 ratio indicates contamination, often with protein or extraction solutions such as phenol, while low 260/230 ratios indicate presence of compounds that absorb light at 230 nm such as EDTA, carbohydrates, and/or phenol. RNA integrity number (RIN; electropherogram-based quality metric), devised by Agilent^{213,214}, and the DV200 metric (the number of nucleic acid fragments greater than 200 nucleotides long), developed and recommended by Illumina²¹⁵, are two measures commonly reported by fragment analyzers to assess RNA degradation. Fully intact RNA has a RIN score of 10, while partially degraded RNA and strongly degraded RNA will have a RIN of 5 and 3, respectively.

3.2. Library preparation

Two factors largely determine which RNA-seq library preparation kit one should use: quality and quantity of the starting material. Some recommendations for kits can be seen below in Figure A1.1. Though there are many more library preparation kits than

those listed below, these are recommendations based on standard operating procedure at the University of North Carolina at Chapel Hill's High Throughput Sequencing Facility.

See notes 2-6.

3.3. Sequencing

We use an Illumina sequencing platform for the vast majority of our RNA-seq analyses, given the exceptional amount and quality of data provided. Below is a summary of current Illumina platforms (see **Table A1.2**) and when we would select each for sequencing:

- **HiSeq 4000:** Used for the majority of our whole transcriptome RNA-seq runs. Good cost/performance ratio, but relatively slow run-times compared to NextSeq and NovaSeq 6000 instruments. However, is known to have an increase in duplicates compared to the earlier HiSeq2500 due to the patterned flow cell.
- **HiSeq 2500:** A less optimal option, as it provides fewer reads without considerable decreases in cost. Typically, the HiSeq 4000 is favored in place of the HiSeq 2500, unless library preparation methods are only compatible with the HiSeq 2500.
- **Nextseq:** Occasionally used when sequencing a small sample set (<8 samples per run). Fast run-times and low instrument costs make this an ideal option for groups with relatively lower throughput sequencing experiments.
- **MiSeq:** Not used for whole transcriptome RNA-seq due to limited sequencing depth, but can be used for TCR/BCR amplicon studies.
- **Novaseq 6000:** Likely to replace the HiSeq 4000 as our primary whole transcriptome platform within the coming years. Relatively higher instrument

costs but substantially higher reads per run makes this an ideal option for groups with very high run throughputs.

For the majority of human and murine RNA-seq analyses, paired-end 2x50bp sequencing chemistry will provide adequate length for accurate alignment of reads to a reference genome. The exceptions to this are 1) if the focus of one's sequencing run is to identify novel splice variants or resolve genomic regions with many long repeated elements, or 2) the reference genome/transcriptome for the derivative organism is not well characterized, for which longer reads may be optimal. The length of sequencing can also be influenced by the type of RNA. It is easier to have longer reads on higher quality fresh frozen samples than in FFPE which are inherently fragmented to sizes around 130-150 bp.

3.4. Data processing and quality control

3.4.1. Read quality metrics

Before raw sequencing data is converted to downstream formats, several sequencing metrics should be considered:

- **Cluster density:** Metric for DNA density on sequencing flow cell. Lower cluster density maintains quality but sacrifices data output, while overloading can result in poor image resolution and base quality. Recommended cluster densities vary for each Illumina machine and optimal loading concentrations should be consulted prior to sequencing. Improper library quantification can result in inaccurate loading concentrations – we typically rely on Nanodrop and fragment analyzers to determine library quality but Qubit for concentration calculations.

We additionally use the KAPA library quantification kit (KK4824) to quantify

libraries with suspected low qualities or contaminations, as it can accurately quantify the concentration of libraries specifically, without quantification of non-library DNA content.

- **Quality score:** The quality score per sequencing cycle as well as a histogram of quality distribution are provided for each run. This Q30 (Phred) quality score represents the likelihood of error for each particular base call. Optimally, scores should reach 30 (99.9% accuracy) or greater across all cycles and base pair positions.

3.4.2. BCL to FASTQ conversion, demultiplexing

Conversion from Illumina sequencing instrument generated basecall files (BCL) to downstream FASTQ format is performed using the bcl2fastq software, which simultaneously demultiplexes samples based upon sequence index. To properly demultiplex samples, a sample sheet must be provided to the software, containing a row for each sample included within the run and the following columns (description given after colon):

- FCID: Flow cell ID
- Lane: Lane number as an integer 1-8
- SampleID: ID of the sample
- SampleRef: Reference used for alignment of the sample
- Index: Index used for generation of a particular library. If two indices were used, they should be separated by a hyphen (e.g. ACCAGTAA-GGACATGA). See *note 7*.
- Description: Description of the sample

- Control: “Y” indicates sample is a control; “N” indicates sample is not a control
- Recipe: What library preparation method was used for this sample
- Operator: Name/ID of the operator of this sample
- SampleProject: Name of project under which this sample belongs

For details of how to install and run bcl2fastq, please refer to the Illumina bcl2fastq conversion software support page (https://support.illumina.com/sequencing/sequencing_software/bcl2fastq-conversion-software.html).

See note 8

3.5. Pre-alignment QC

After conversion into FASTQ format, quality control is performed to identify potential issues arising from the sample preparation and sequencing process. Typically, we perform this using the FastQC software, which provides a simple and fast method to identify per base sequence quality, GC content, per base N content, sequence length distribution, sequence duplication levels, overrepresented sequences, and adapter content. Commonly used filters for excluding samples from downstream analysis in transcriptome profiling experiments include: 1) less than 30 million mapped reads in the sample, and 2) mean PHRED base quality ≤ 35 . Other filters are additionally applied after sample alignment, as described below.

See note 9

3.6. Alignment and quantification

3.6.1. Alignment methods

Many computational methods exist to map RNA-seq data to the reference genome, allowing for splice aware alignment of both mRNA and other RNA types (rRNA, intronic, and intergenic RNAs)²¹⁶. In recent years, our group has transitioned from exclusively using Mapsplice to STAR for RNA-seq alignment, which is primarily rooted in their equivalent ability to accurately align reads while dramatically improving alignment times^{99,176,217}. Apart from STAR, many other aligners have been compared in terms of speed and performance²¹⁶, demonstrating that the most reliable general-purpose aligners include STAR, CLC, Novoalign, and GSNAP. While accuracy of these other popular aligners are similar to STAR, runtimes for human-derived data are significantly faster by STAR than the other three aligners.

More recently, tools such as Sailfish, Salmon, and Kallisto allow for extremely fast but approximate quantification of genes directly from the FASTQ file, without alignment to a reference genome^{178,218,219}. Sailfish and Salmon make use of a quasi-mapping approach while Kallisto uses pseudo-alignment for estimated quantification of genes. Both of these methods mathematically similar, k-mer based algorithms, with the key difference that quasi-mapping uses suffix arrays while pseudo-alignment implements de Bruijn graphs. While these methods can provide very fast and fairly accurate estimates of gene expression, they do not perform as well from FFPE derived data, do not have the accuracy of genome aligners, and do not generate read-level data (BAM/SAM file). As such, we typically still rely on STAR for alignment of FASTQ files.

STAR requires a single-ended or pair-end FASTQ file(s) for alignment to the reference genome. Additionally, a reference genome must be supplied and further “built” by STAR for alignment, currently mm10 for murine and hg38 for human data. If a

STAR generated genome has not been previously built, reference genome sequences (in the form of FASTA files) and optionally an annotation file (in the form of a GTF file) need to be input into STAR for generating genome indexes. While the annotation file is not necessary to build the reference genome, it should be included to improve mapping accuracy. Limited STAR genomes are available from the creators of STAR (<http://labshare.cshl.edu/shares/gingeraslab/www-data/dobin/STAR/STARgenomes/>), but users are encouraged to generate their own genome indexes using the most up to date assemblies and annotations. The NCI's Genome Data Commons (GDC) also provides reference genomes that they use for their harmonization pipelines (<https://gdc.cancer.gov/about-data/data-harmonization-and-generation/gdc-reference-files>).

3.6.2. Post-alignment QC

After alignment, several quality control metrics are collected to ensure results can be interpreted without significant bias from technical outliers. Given that each sample set can vary dramatically, there are no strict cutoffs for any of these metrics. We try to determine the presence of technical outliers within the set and remove samples or are just aware of the sample quality when interpreting downstream analyses. The following metrics are commonly analyzed:

- Proportion aligned vs unaligned: Performed to ensure there are not an over-abundance of unaligned reads among all data.
- Percent of alignment by region: Comparison of percentage of total bases aligned to mRNA versus intergenic, intronic, or ribosomal RNA to ensure the transcriptome coverage is conserved between samples. These metrics are

measured using output from Picard Tools²²⁰. Typically, we want at least 10% of reads to map to mRNA, but the other metrics will vary by library and RNA type (See note 10).

- Number of non-zero genes: Performed to determine coverage among all genes and identify low diversity samples.
- Relative log expression: Analysis of total aligned reads per sample to ensure read distributions are similar across samples. This gives an intuitive view of the global variation in relative expression²²¹.
- Upper quartile comparison: Calculated as $\frac{\text{Median}(\text{all UQ values across cohort})}{\text{UQ for a given sample}}$, where UQ denotes the upper quartile (75th percentile) value among all read counts per sample. This metric provides a scaling factor for each sample representing the relative multiplier necessary for UQ read-normalization of that sample relative to all other samples in the set. Alternatively to the above method, DESeq2's `sizeFactor` function can also be utilized to calculate a scaling factor. Samples with particularly high scaling values generally have lower mRNA mapping and normalization of these samples will result in amplification of noise.
- Principle component analysis: Performed to identify potential technical outliers.

3.6.3. Quantification methods

Gene expression profiling experiments require generation of quantified gene expression values for all genes represented in the sequencing data. In recent years, the use of RSEM and Cufflinks as quantifiers have widely been replaced by newer, faster quantifiers such as Sailfish and Salmon^{178,218,222,223}. All of these tools are orders

of magnitude faster in run time compared to older quantifiers while maintaining similar or better accuracies²²⁴.

As mentioned earlier, Sailfish and Salmon can directly quantify FASTQ files without genome alignment; however, they can additionally be used downstream of an aligner strictly as a transcript quantifier. We typically pair Salmon quantifier (quant mode) downstream of STAR alignment. Salmon requires an unsorted BAM file as input, and we use the transcriptome-space BAM file as input, with an hg38 or mm10 reference transcriptome FASTA file as reference.

3.7. Select methods of analysis

- Prior to analysis, gene expression matrices are derived through combining the raw count data for each sample into a matrix.
- From this raw matrix, some threshold can be applied to drop lowly expressed genes, such as filtering by a minimum read count threshold or dropping all genes with zero expression for all samples (i.e. tissue specific genes). For tumor experiments, we typically have relied on dropping all genes which are not expressed in >70% of all samples, which provides a conservative cutoff to filter out lowly expressed genes but may in some instances introduce bias away from these rare genes.
- Next, this raw, filtered expression matrix is normalized. Common methods include upper quartile normalization (UQN), median normalization, normalizing RPKM (Reads Per Kilobase Million), FPKM (Fragments Per Kilobase Million), TPM (Transcripts Per Kilobase Million), or relying on a software package such as DESeq2 (varianceStabilizingTransformation; VST) or edgeR (Trimmed Mean of

M; TMM)^{168,225}. These software package normalization methods lead to a more stable normalization than the other methods²²⁶.

- If not using DESeq2 VST or edgeR TMM for normalization, the normalized matrix is $\log_2(x+1)$ transformed for a final expression matrix.

See note 11

3.7.1. Differential gene expression analysis

A wide variety of differential gene expression analysis tools exist, with popular tools including edgeR, DESeq2, limma and voom, NOISeq, SAMSeq (samr), EBSeq, bayseq, sleuth, among others. Direct comparison of these popular methods suggests NOISeq, DESeq2, and limma+voom have the best sensitivity/specificity performance metrics, with further suggestions that integration of multiple methods may further improve overall performance²²⁷. Another common tool for differential gene expression analysis is edgeR, which has been shown to have similar performance compared to DESeq2^{225,228}.

We perform differential gene expression analysis using DESeq2, using a gene expression matrix of raw count as input¹⁶⁸. This matrix is automatically normalized by DESeq2 prior to differential expression analysis. In the case of Salmon derived expression data, counts need to be converted to an integer DESeq2.

3.7.2. Immune gene signature analysis

Immune gene signatures are composed of a set of genes, typically specific to an immune cell or pathway of interest combined with a method to transform expression levels of signature genes into a single score for each sample. We calculate immune gene signatures using a normalized matrix and perform screening such that signatures

where >30% of respective genes demonstrate zero expression in a particular sample are not considered for downstream analyses. The IGS score is calculated as the mean of the expression of all genes within a particular signature²²⁹.

Alternatively, genes within each signature can instead be scaled across the cohort, taking the median value as the IGS score. This extra normalization step can help reduce biases incurred by highly or lowly expressed genes, but may also reduce sensitivity if those genes have a high degree of biological significance. The following list of citations contains gene signatures we regularly use in our analyses:

- Palmer C et al. BMC Genomics 2006; PMID:16704732¹⁵⁹
- Schmidt M et al Cancer Res 2008; PMID:18593943²³⁰
- Beck et al Clin Cancer Research 2009; PMID:19188147²³¹
- Rody A et al. Breast Cancer Res 2009; PMID:19272155²³²
- Chan et al PNAS 2009; PMID:19666525¹⁵⁷
- Prat A et al Breast Cancer Res 2010; PMID:20813035¹⁵⁸
- Fan C et al. BMC Med Genomics 2011; PMID:21214954²³³
- Rody A et al. Breast Cancer Res 2011; PMID:21978456²³⁴
- Bindea G et al. Immunity 2013; PMID:24138885¹⁰⁰
- Iglesia MD et al. Clinical Cancer Research 2014; PMID:24916698¹⁰¹
- Kardos J and Chai S et al. JCI insights 2016; PMID:27699256⁸³
- Charoentong P et al. Cell Reports 2017; PMID 28052254²³⁵
- Vestéinn et al Immunity 2018; PMID: 29628290⁵⁰
- MSigDB gene sets¹⁶⁰
- Gene Ontology terms 0050853 – GO:0050853; PMID:NA

- Gene Ontology terms 0050852 – GO:0050852; PMID:NA

3.7.3. Gene pathway analysis

Gene pathway analyses provide a measure for pathways which have genes expressed at levels higher than by chance. Among immunogenomic-related pathways, we typically use MSigDB gene sets for the bulk of our analysis¹⁶⁰. Of particular relevance includes the C7 immunologic gene sets, C2 curated gene sets, C5 gene ontology gene sets, and the hallmark gene sets. There are several methods for performing gene pathway analysis, among which include 1) standard GSEA analysis, 2) weighted analysis, and 3) network-based approaches. Below, we will provide a summary and examples for each approach.

Commonly used pathway analysis tools for standard GSEA analysis include GSEA, single sample GSEA (ssGSEA), and GSVA for gene pathway analysis^{236–238}. Standard GSEA analysis takes in a discrete and predefined gene set that typically represents a biological state, comparing whether RNA-seq or microarray expression data between two biological groups show phenotypic differences based upon those gene sets. Additionally, ssGSEA and GSVA are able to generate gene signature expression values for each individual sample, which GSEA is not. Thus, GSEA is only able to compare signature expression among pre-defined groups. While GSEA, ssGSEA, and GSVA are among the most popular gene set analysis tools, other gene pathway analysis software such as PLAGE, GLOBALTEST, and PADOG have demonstrated greater sensitivity and under certain conditions^{239–242}. As such, the accuracy of each analysis method may be dependent upon the biology of the sample

set, and thus the chosen method may require optimization and validation for the optimization of results.

Alternatively to standard GSEA, weighted approaches such as GSEAPrerank take into account a predefined list of rank-ordered genes to calculate the enrichment score²⁴³. The gene's ranks thus define the weight of its contribution to the enrichment score. This can be particularly useful when the ranking metrics provided by standard GSEA are not appropriate for the data, or if the expression data is derived from a non-standard approach (targeted methods, ChIP-seq, GWAS studies).

Another method for gene pathway calculation is a network-based approach, as exemplified by DawnRank, which ranks potential driver genes based on their impact on differential expression of downstream genes in a molecular interaction network²⁴⁴. DawnRank performs these analyses on a per-patient basis, allowing for identification of personalized driver genes without biases from the rest of the cohort. It should be noted that to call driver mutations, DawnRank additionally requires variant call files, which typically is derived using DNA data.

3.7.4. Deconvolution

The incredibly complex cellular composition of a tumor microenvironment underscores the difficult question of how to deconvolute the proportional signals from each cell type. Among cellular deconvolution tools currently available, CIBERSORT and TIMER are the most popular for characterization of the tumor microenvironment^{196,197}. CIBERSORT is designed to infer the relative proportion of individual immune populations among total leukocytes, while TIMER instead aims to infer immune population abundance amount the total tumor microenvironment. The

limitation of both tools is their reference is derived from peripherally collected leukocytes from healthy donors, with the assumption that these transcriptional patterns do not substantially differ from their tumor infiltrating counterparts. At this time, it is not clear which of these two methods provides more accurate estimates of tumor infiltrating immune populations from bulk RNA-seq data.

3.7.5. TCR/BCR inference tools

We have directly compared the performance of several TCR/BCR inference tools, including MiXCR, MiTCR, TRUST, and V'DJer^{162,245–247}. Based on these comparisons, our preferred inference method is MiXCR for TCR calling and MiXCR/V'DJer for BCR calling.

MiXCR-based TCR inference is performed according to recommended settings from the Mi lab for short-read RNA-seq data (<https://mixcr.readthedocs.io/en/master/rnaseq.html>; subheading “Typical analysis workflow”), which typically yields 10^0 to 10^2 total clones, depending upon sequencing depth and RNA quality. From the MiXCR export file output, we perform diversity and clonotypes sharing calculations through standard diversity calculation formulas (species evenness, and diversity indices such as Gini-Simpson or Shannon entropy). We have found that analyses from samples with very few identified clones (10^1 - 10^2) results in inaccurate diversity calculations, and thus a minimum clone cutoff should be optimized and implemented. We avoid the use of TRUST because of its identification of a large frequency of “non-canonical” CDR3-regions, which can be as short as a single amino-acid residue and are unlikely to be truly derived from TCR sequences.

BCR inference is performed using both MiXCR and V'DJer. Unlike MiXCR, V'DJer uses an assembly-based inference method for calling full length BCR calls from fresh-frozen derived RNA. As a result, V'DJer is able to provide full length BCR sequences into the constant region for isoform calling, which allows for single base resolution of the BCR. In a comparison of these two tools, MiXCR was demonstrated to have greater sensitivity and less computational intensity compared to V'DJer²⁴⁸, and therefore may be more relevant in situations where population-levels statistics are of primary interest rather than identification of full length BCR-sequences.

See note 12

3.7.6. HLA inference

HLA typing has historically been performed through the use of PCR, Sanger sequencing, or flow cytometric approaches, with next generation sequencing recently emerging as a potentially higher throughput and more cost effective approach²⁴⁹. The majority of these approaches rely upon the use of HLA region targeted DNA sequencing, preventing the identification of biologically meaningful data outside of HLA typing. Additionally, targeted sequencing requires the use of capture probes, which may result in loss of capture for polymorphisms within the MHC genes. Whole exome/genome approaches suffer from their requirement of very high read depth, with nearly half a billion sequencing reads necessary for accurate calling^{250,251}.

As a result of these limitation, RNA-seq derived MHC calling methods have been recently developed, which allows for accurate calling of alleles without limiting data for uses beyond this purpose. One example of such a tool is PHLAT, which can use both DNA and RNA as input for HLA calling⁴⁵. Another recent tools is HLAProfiling, which

takes a k-mer approach to allow for identification of both common and rare alleles from RNA-seq data⁴⁷.

3.7.7. Neoantigen prediction

Several published neoantigen prediction pipelines exist, although they almost all require additional tumor-derived whole-exome sequencing data in order to accurately call mutations. As such, we will discuss several neoantigen prediction tools currently available, without enumerating on the exact DNA inputs necessary for running the software. A more recent approach comes from Neopepsee, which attempts to increase calling accuracy through incorporation of amino acid level immunogenicity information derived via a machine learning algorithm trained on a dataset of reported class I MHC epitopes known to exhibit a positive T-cell effect²⁵². Another tool is pVACtools, which also integrates DNA and RNA data to call class I and II neoantigens, importantly with the inclusion of point mutations, indels, gene fusions, and frameshift mutations derived epitopes²⁵³. Lastly, another tool is INTEGRATE-neo, which is a neoantigen prediction pipeline with a focus on gene fusion derived epitopes²⁵⁴.

Most neoantigen calling pipelines work through a similar process, which we have simplified below:

- i. **Variant calling:** Mutations are identified using a variant calling program, with DNA-seq and RNA-seq inputs. DNA sequences corresponding to peptides are retrieved and translated in silico into protein sequences.
- ii. **Analysis of variant expression:** RNA-seq data is used to quantify read coverage of all called mutations. The expression levels of each peptide generated are determined by the lowest mutation RNA-sequencing read

- coverage. Peptides which do not meet a minimum read coverage are filtered out.
- iii. **HLA typing:** For human samples with unknown HLA type, HLA typing software is applied as described in the above section.
 - iv. **Enumeration of possible variant peptides:** Generally, 8-11mers are considered for class I epitopes while 15mers are considered for class II epitopes. Several groups rely upon the use of long peptides (closer to 30 amino acid residues in length), with the idea that these longer peptides will allow for better antigen-presenting cell processing and presentation.
 - v. **MHC binding prediction:** Binding affinity to MHC molecules expressed by the tumor for all possible peptides generated from mutations is predicted. Perhaps the most widely used MHC binding affinity prediction software is NetMHCpan (version 4.0) and NetMHCIIpan (version 3.2) for class I and II epitopes, respectively ^{39,181}. Peptides are filtered by their binding affinities (IC₅₀ nM) to each allele in the tumor sample's HLA type. Peptides with an IC₅₀ value of less than 500 nM for at least one allele are typically considered predicted neoantigens.

3.7.8. Viral quantification

Expression of viral and human endogenous retroviral (hERV) RNA can drive immunological phenotypes in cancer^{52,200}. We have developed tools for quantification of vertebrate viral and human endogenous retroviral (hERV) transcripts from RNA-seq data. The first of these tools is *VirDetect*, which specifically detects viruses from RNA-sequencing⁵². Reads are aligned to the human genome and reads that don't align to

the human genome are then aligned to the masked viral genomes. The novelty of *VirDetect* is the masking of the viral genome for areas of human homology and areas of low complexity. The masking allows for higher specificity and limits the need for manual curation.

The commands can be found here:

<https://github.com/dmarron/virdetect/blob/master/VirdetectManual.pdf>

The second tool is *hervQuant*, which allows for quantification of nearly 4,000 full-length, intact hERVs from short read RNA-seq data²⁰⁰. *hervQuant* has currently been optimized and validated for 2x50bp fresh-frozen RNA-seq data, making it relevant for the majority of TCGA RNA-seq samples. Information for running *hervQuant* can be found at:

<https://unclineberger.org/vincent/resources>.

4. Notes

- 4.1.** For RNA extraction from FFPE, we prefer the use of blocks rather than slides, as the greater surface area exposure to the outside environment on slides is associated with more degradation. We have greatest success from using freshly cut blocks, discarding the first scroll and collecting toward the center of the block. Typically, we take 4-6 slides of 10 μ m for RNA extraction.
- 4.2.** We and others have contributed to the NCI's Biorepositories and Biospecimen Research Branch best practices for assessing nucleic acid quality from FFPE tissues²⁵⁵. In many degraded RNA samples, the average fragment size of the RNA is around 130-150 bp. However, we have still been able to generate successful total RNA-seq libraries even with low DV200s. For mRNA based

library strategies, it is best to start with RINs >7 for best quality, though RINs 5-6 are occasionally successful but not as consistent. RIN cutoffs of 7 have been used in projects like TCGA. For more degraded RNAs, it is better to use total RNA or capture based protocols that do not have a strong requirement on intact RNA and can be used with samples of low RIN or DV200. We typically are successful with 80-90% of FFPE libraries, particularly with doubling the max starting amount of RNA (ex 200ng for RNA exome, or 500-1000ng for Total RNA). When a protocol calls for fragmentation, this is based on the suspected quality of the RNA and the desired length of sequencing. In general, we typically do not fragment samples with RINs less than 5.

- 4.3.** For kits that require the starting RNA to be concentrated into a small volume, there are a number of concentration methods including column methods, like Qiagen's Rneasy MinElute Cleanup kit, bead purifications, like KAPA's Pure Beads or Beckman Coulter's RNAClean XP, or ethanol precipitation.
- 4.4.** Some samples, including RNA from blood, might produce more desirable results following the depletion of unwanted transcripts, such as ribosomal RNA or Globin RNA. Using a depletion kit, like one from Nugen's AnyDeplete line, will selectively deplete unwanted transcripts, enriching for sequencing reads of choice. Total RNA input may need to be increased if using a depletion kit.
- 4.5.** If multiple kits from Figure A1.1 would work for a given quality and quantity of starting RNA, other factors such as price, kit availability, and laboratory familiarity should be considered in selecting the right kit as well as desired RNA

analysis – coding vs noncoding transcriptome, alternative transcripts, or structural alterations.

4.6. It is not recommended to compare sequencing analysis across different library preparation kits for the same project, as each kit will have its own biases.

Comparing data across multiple library preparation methods may result in preferential up-/down-regulation of certain genes between different kits.

4.7. The use of dual indexes is preferred, as it reduces the prevalence of index hopping/library switching.

4.8. FASTQ format is a text-based format for storing read data, and is comprised of four lines per sequenced read:

- Sequence identifier, preceded by a “@” character. Often lists the coordinates on the sequencing chip. (E.g.: @UNC20:291:000000000-AKVVA:1:1101:16893:1549 2:N:0:AGGCANACTCTCTA)
- Nucleotide sequence letters (E.g.: AGCGTTGGG)
- A “+” character, followed optionally by the same sequence identifier in line 1. Often left blank. (E.g.: +)
- Quality scores for each base value from line 2. For current Illumina derived FASTQ files, a PHRED score between 0 and 40 are given, which provides the error probability for each respective base. (E.g. >>3>>ADFB)

4.9. Of QC metrics provided by FastQC, we focus most closely on the per-base sequencing quality (typically given as a PHRED score), overrepresented sequences, and adapter content. Sequencing quality should ideally remain high across the full length of the read; however, we have noticed that amplicon

sequencing methods frequently demonstrate a dramatic drop in quality in the last 25-50% of the read length, without significant issues with downstream processing. Particularly in peripheral blood, ribosomal RNA and globin-related genes can often appear as overrepresented genes. Overrepresented sequences can be input into NCBI nucleotide BLAST to identify the source, correcting for future preparations if necessary. Lastly, high adapter content can result from non-ideal PCR conditions or RNA fragments shorter than the sequencing length. If high adapter content is present, a trimming software to remove adaptor contamination should be considered (we most frequently use `bbduk` from the BBMap suite²⁵⁶).

4.10. Depending on the library and the quality of the RNA, different amounts of reads will map to mRNA²⁵⁷. In mRNA or exon capture based methods, typically 60-80% of reads will map to mRNA. However, in total RNA-seq, this number is much lower and varies by RNA quality. Total RNA-seq can range from ~10-30% of reads mapping to mRNA in FFPE and ~30-50% in fresh frozen, with corresponding increases in intron and intergenic regions compared to mRNA-seq. At minimum, to reach an equivalent amount RNA expression data as in microarrays, it is important to aim for at least 15-30 million reads mapping to mRNA and to aim even higher for all the additional benefits one gets from a sequencing vs array based approach.

4.11. It is important to note that certain analysis packages (such as DESeq2) require an unfiltered, untransformed input matrix for analysis, so it is imperative that the input format is identified prior to analysis.

4.12. V'DJer can be run in normal and sensitive modes. We typically rely on normal mode unless greater sensitivity is necessary – in limited testing, sensitive mode had a 50-1200% increase in runtimes and 0-1000% increase in RAM.

Figures and Tables

Analysis type	Software name	Source	Manuscript citation
BCL to FASTQ conversion	bcl2fastq	https://support.illumina.com/sequencing/sequencing_software/bcl2fastq-conversion-software.html	258
Pre-alignment QC	Fastqc	https://www.bioinformatics.babraham.ac.uk/projects/fastqc/	259
Read trimming	BBMap: bbduk	https://sourceforge.net/projects/bbmap/	256
Aligner	STAR	https://github.com/alexdobin/STAR	176
	CLC	https://www.qiagenbioinformatics.com/products/clc-main-workbench/	260
	Novoalign	http://www.novocraft.com/products/novoalign/	261
	GSNAP	https://github.com/juliangehring/GMAP-GSNAP	262
Quantifier	Salmon	https://combine-lab.github.io/salmon/	178
	Sailfish	http://www.cs.cmu.edu/~ckingsf/software/sailfish/	218
	Kallisto	https://pachterlab.github.io/kallisto/	219
General utilities	Samtools	http://samtools.sourceforge.net/	177
	Picard tools	https://broadinstitute.github.io/picard/	220
Differential gene expression	DESeq2	https://bioconductor.org/packages/release/bioc/html/DESeq2.html	168
	limma/voom	https://bioconductor.org/packages/release/bioc/html/limma.html	263,264
	NOISeq	https://bioconductor.org/packages/release/bioc/html/NOISeq.html	265
	edgeR	https://bioconductor.org/packages/release/bioc/html/edgeR.html	225
Gene set analysis software	GSEA	http://software.broadinstitute.org/gsea/index.jsp	236,243
	ssGSEA		237
	GSVA	https://bioconductor.org/packages/release/bioc/html/GSVA.html	238
	GSEAPreranked	http://software.broadinstitute.org/cancer/software/genepattern/modules/docs/GSEA-Preranked/1	243
	Dawnrank	https://github.com/MartinFXP/DawnRank	244

TCR/BCR inference	MiXCR	https://github.com/milaboratory/mixcr	162
	V'DJer	https://github.com/mozack/vdjer	247
MHC inference	PHLAT	https://sites.google.com/site/phlatfortype/	45
	HLAProfiler	https://github.com/ExpressionAnalysis/HLAProfiler	47
MHC binding affinity	NetMHCPan4.0	http://www.cbs.dtu.dk/services/NetMHCPan/	39
	NetMHCII Pan 3.2	http://www.cbs.dtu.dk/services/NetMHCIIpan/	181
Neoantigen calling	Neopepsee	https://sourceforge.net/p/neopepsee/wiki/Home/	252
	pVACtools	https://github.com/griffithlab/pVACtools	253
	INTEGRATE-neo	https://github.com/ChrisMaherLab/INTEGRATE-Neo	254
Viral/ERV quantification	Virdetect	https://github.com/dmarron/virdetect/blob/master/VirdetectManual.pdf	52
	hervQuant	https://unclineberger.org/vincent/resources	200

Table A1.1: Summary of recommended software.

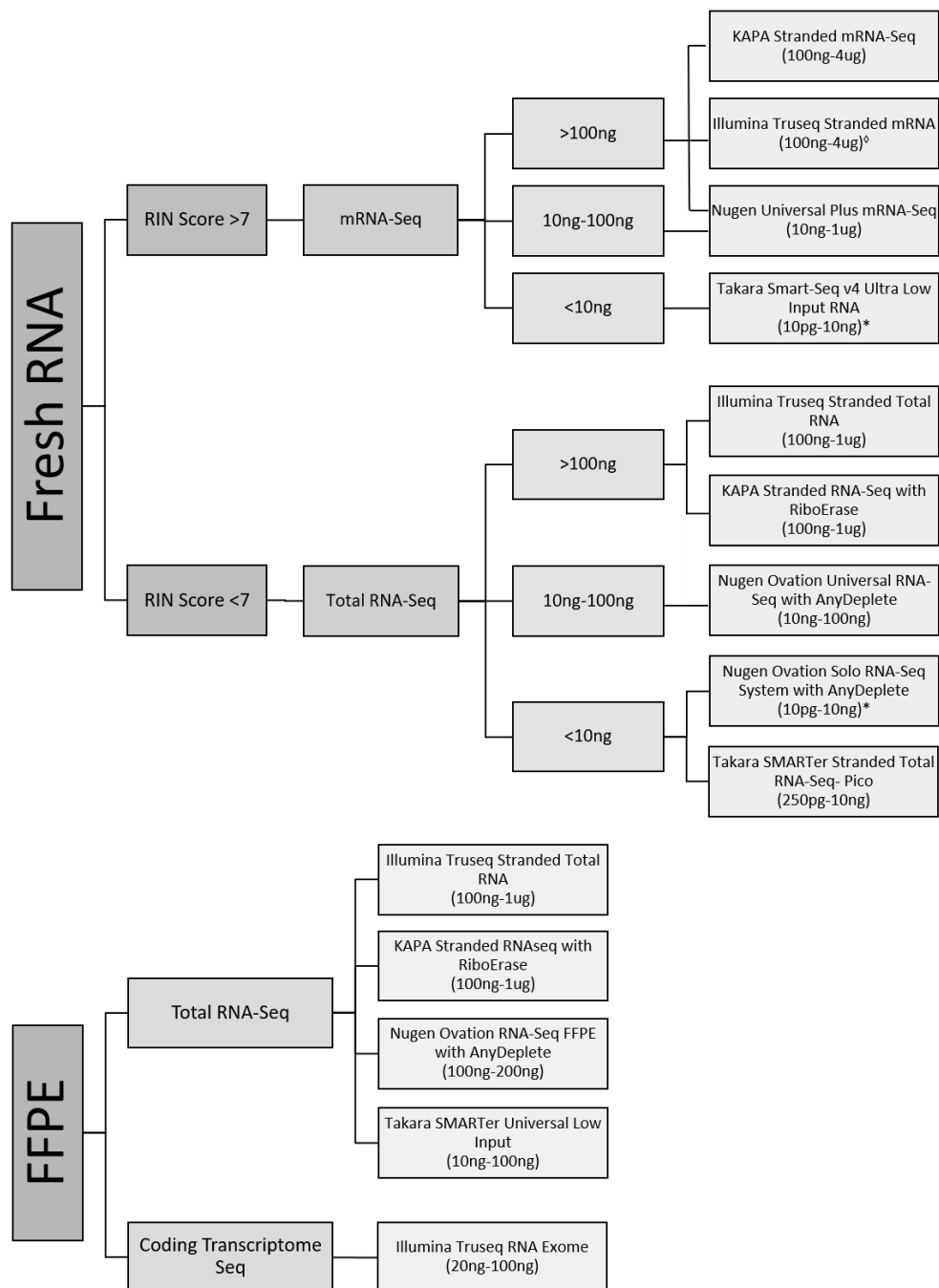


Figure A1.1. RNA-seq Library Preparation Kit Decision Tree. All quantities listed are the total RNA inputs, as recommended by manufacturer protocols. Several kits also have an mRNA input option (◇) or a whole cell input option (*).

	NextSeq	HiSeq 4000	NovaSeq 6000
Output range	20–120 Gb	125–1500 Gb	134–6000 Gb
Run time	11–29 hr	< 1–3.5 days	13–44 hr
Reads per run	130–400 million	2.5–5 billion	Up to 20 billion
Maximum read length	2 × 150 bp	2 × 150 bp	2 × 150 bp
Samples per run	2–8	50–100	26–400
Relative price per sample	Higher Cost	Mid cost	Lower cost
Relative instrument price	Lower Cost	Mid cost	Higher cost

Table A1.2: Illumina sequencing platforms recommended for whole transcriptome sequencing by the manufacturer. Specs and table adapted from <https://www.illumina.com/systems/sequencing-platforms/comparison-tool.html>.

**APPENDIX 2: The Cancer Genome Atlas comprehensive molecular
characterization of renal cell carcinoma**

Please refer to <https://doi.org/10.1016/j.celrep.2018.03.075> for full text

APPENDIX 3: Molecular and clinical characterization of a claudin-low subtype of gastric cancer.

Please refer to DOI: 10.1200/PO.17.00047 for full text.

**APPENDIX 4: Endogenous retrovirus expression is associated with response to
immune checkpoint blockade in clear cell renal cell carcinoma.**

Please refer to DOI: [10.1172/jci.insight.121522](https://doi.org/10.1172/jci.insight.121522) for full text.

APPENDIX 5: Dual immunotherapy nanoparticle improves T-cell activation and cancer immunotherapy.

Please refer to DOI: [10.1002/adma.201706098](https://doi.org/10.1002/adma.201706098) for full text.

**APPENDIX 6: CD30-Redirected Chimeric Antigen Receptor T Cells Target CD30+
and CD30- Embryonal Carcinoma via Antigen-dependent and Fas/FasL
Interactions.**

Please refer to DOI: 10.1172/jci.insight.121522 for full text.

ENDNOTES

Author lists (* contributed equally to this work):

- **Chapter 2.1:** Ryoichi Saito*, Christof C. Smith*, Takanobu Utsumi, Lisa M. Bixby, Jordan Kardos, Sara E. Wobker, Kyle G. Stewart, Shengjie Chai, Ujjawal Manocha, Kevin M. Byrd, Jeffrey S. Damrauer, Scott E. Williams, Benjamin G. Vincent* and William Y. Kim*
- **Chapter 2.2:** Denis R. Beckford Vera*, Christof C. Smith*, Lisa M. Bixby, Dylan M. Glatt, Stuart S. Dunn, Ryoichi Saito, William Y. Kim, Jonathan S. Serody, Benjamin G. Vincent *, Matthew C. Parrott*
- **Chapter 3:** Christof C. Smith, Kathryn E. Beckermann, Dante S. Bortone, Aguirre A. De Cubas, Lisa M. Bixby, Samuel J. Lee, Anshuman Panda, Shridar Ganesan, Gyan Bhanot, Eric M. Wallen, Matthew I. Milowsky, William Y. Kim, W. Kimryn Rathmell, Ronald Swannstrom, Joel S. Parker, Jonathan S. Serody*, Sara R. Selitsky*, and Benjamin G. Vincent*
- **Chapter 4.1:** Christof C. Smith, Shengjie Chai, Amber Washington, and Benjamin G. Vincent
- **Chapter 4.2:** Christof C. Smith*, Yu Mi*, Shengjie Chai, Andrew Z. Wang*, Benjamin G. Vincent*
- **Appendix I:** Christof C. Smith, Lisa M. Bixby, Kelsey L. Miller, Sara R. Selitsky, Dante S. Bortone, Katherine A. Hoadley, Benjamin G. Vincent, and Jonathan S. Serody
- **Appendix II:** TCGA Pan-Kidney working group

- **Appendix III:** Tomohiro F. Nishijima, Jordan Kardos, Shengjie Chai, Christof C. Smith, Dante S. Bortone, Sara R. Selitsky, Joel S. Parker, Hanna K. Sanoff, Michael S. Lee, and Benjamin G. Vincent
- **Appendix IV:** Anshuman Panda, Aguirre A. de Cubas, Mark Stein, Gregory Riedlinger, Joshua Kra, Tina Mayer, Christof C. Smith, Benjamin G. Vincent, Jonathan S. Serody, Kathryn E. Beckermann, Shridar Ganesan, Gyan Bhanot, and W. Kimryn Rathmell
- **Appendix V:** Yu Mi, Christof C. Smith, Feifei Yang, Yanfei Qi, Kyle C. Roche, Jonathan S. Serody, Benjamin G. Vincent, and Andrew Z. Wang
- **Appendix VI:** Lee K. Hong, Yuhui Chen, Christof C. Smith, Stephanie A. Montgomery, Benjamin G. Vincent, Gianpietro Dotti and Barbara Savoldo

Personal contributions to all sections

- **Chapter 2.1:** Immunological analyses represented in Figures 4-7 of final manuscript¹⁸². Writing and editing of manuscript.
- **Chapter 2.2:** Immunological analyses represented in Figures 4-6 and Tables 3,4 of final manuscript²⁶⁶. Writing and editing of manuscript.
- **Chapter 3:** Analyses and writing for all sections of the manuscript.
- **Chapter 4.1:** Analyses and writing for all sections of the manuscript.
- **Chapter 4.2:** Analyses and writing for all sections of the manuscript.
- **Appendix I:** Writing and editing for all sections of the manuscript.
- **Appendix II:** Immunogenomic analysis represented in Figure 6 of final manuscript²⁶⁷.

- **Appendix III:** Assistance with immunogenomic analysis and interpretation of results.
- **Appendix IV:** Assistance with immunogenomic analysis and interpretation of results.
- **Appendix V:** Immunological analyses represented in Figures 2,4 of final manuscript¹⁹³. Writing and editing of manuscript.
- **Appendix VI:** Assistance with immunogenomic analysis and interpretation of results.

REFERENCES

1. Binnewies, M. *et al.* Understanding the tumor immune microenvironment (TIME) for effective therapy. *Nat. Med.* **24**, 541–550 (2018).
2. Wherry, E. J. T cell exhaustion. *Nature Immunology* **12**, 492–499 (2011).
3. Gong, J., Chehrazi-Raffle, A., Reddi, S. & Salgia, R. Development of PD-1 and PD-L1 inhibitors as a form of cancer immunotherapy: A comprehensive review of registration trials and future considerations. *Journal for ImmunoTherapy of Cancer* **6**, (2018).
4. Perou, C. M. *et al.* Molecular portraits of human breast tumours. *Nature* **406**, 747–752 (2000).
5. Choi, W. *et al.* Identification of Distinct Basal and Luminal Subtypes of Muscle-Invasive Bladder Cancer with Different Sensitivities to Frontline Chemotherapy. *Cancer Cell* **25**, 152–165 (2014).
6. Weinstein, J. N. *et al.* Comprehensive molecular characterization of urothelial bladder carcinoma. *Nature* **507**, 315–322 (2014).
7. Damrauer, J. S. *et al.* Intrinsic subtypes of high-grade bladder cancer reflect the hallmarks of breast cancer biology. *Proc. Natl. Acad. Sci.* **111**, 3110–3115 (2014).
8. Hugo, W. *et al.* Genomic and Transcriptomic Features of Response to Anti-PD-1 Therapy in Metastatic Melanoma. *Cell* **165**, 35–44 (2016).
9. Riaz, N. *et al.* Tumor and Microenvironment Evolution during Immunotherapy with Nivolumab. *Cell* **171**, 934–949.e15 (2017).
10. Auslander, N. *et al.* Robust prediction of response to immune checkpoint blockade therapy in metastatic melanoma. *Nature Medicine* (2018). doi:10.1038/s41591-018-0157-9
11. Smith, C. C. *et al.* Endogenous retroviral signatures predict immunotherapy response in clear cell renal cell carcinoma. *J. Clin. Invest.* (2018). doi:10.1172/JCI121476
12. Panda, A. *et al.* Endogenous retrovirus expression is associated with response to immune checkpoint pathway in clear cell renal cell carcinoma. *JCI Insight* **3**, (2018).
13. Yarchoan, M., Johnson, B. A., Lutz, E. R., Laheru, D. A. & Jaffee, E. M. Targeting neoantigens to augment antitumour immunity. *Nature Reviews Cancer* **17**, 209–222 (2017).
14. Sahin, U. *et al.* Personalized RNA mutanome vaccines mobilize poly-specific

- therapeutic immunity against cancer. *Nature* **547**, 222–226 (2017).
15. Ott, P. A. *et al.* An immunogenic personal neoantigen vaccine for patients with melanoma. *Nature* **547**, 217–221 (2017).
 16. Turajlic, S. *et al.* Insertion-and-deletion-derived tumour-specific neoantigens and the immunogenic phenotype: a pan-cancer analysis. *Lancet Oncol.* **18**, 1009–1021 (2017).
 17. Löwer, R., Löwer, J. & Kurth, R. The viruses in all of us: characteristics and biological significance of human endogenous retrovirus sequences. *Proc. Natl. Acad. Sci.* **93**, 5177–5184 (1996).
 18. Boller, K. *et al.* Human endogenous retrovirus HERV-K113 is capable of producing intact viral particles. *J. Gen. Virol.* **89**, 567–572 (2008).
 19. Faff, O. *et al.* Retrovirus-like particles from the human T47D cell line are related to mouse mammary tumour virus and are of human endogenous origin. *J. Gen. Virol.* **73**, 1087–1097 (1992).
 20. Wang-Johanning, F. *et al.* Expression of multiple human endogenous retrovirus surface envelope proteins in ovarian cancer. *Int. J. Cancer* **120**, 81–90 (2007).
 21. Büscher, K. *et al.* Expression of human endogenous retrovirus K in melanomas and melanoma cell lines. *Cancer Res.* **65**, 4172–4180 (2005).
 22. Wang-Johanning, F. *et al.* Expression of human endogenous retrovirus K envelope transcripts in human breast cancer. *Clin. Cancer Res.* **7**, 1553–1560 (2001).
 23. Contreras-Galindo, R. *et al.* Human Endogenous Retrovirus K (HML-2) Elements in the Plasma of People with Lymphoma and Breast Cancer. *J. Virol.* **82**, 9329–9336 (2008).
 24. Wang-Johanning, F. *et al.* Detecting the expression of human endogenous retrovirus E envelope transcripts in human prostate adenocarcinoma. *Cancer* **98**, 187–197 (2003).
 25. Yoshida, M., Miyoshi, I. & Hinuma, Y. Isolation and characterization of retrovirus from cell lines of human adult T-cell leukemia and its implication in the disease. *Proc. Natl. Acad. Sci.* **79**, 2031–2035 (1982).
 26. Kalyanaraman, V. S. *et al.* A new subtype of human T-cell leukemia virus (HTLV-II) associated with a T-cell variant of hairy cell leukemia. *Science (80-)*. **218**, 571–573 (1982).
 27. Florl, A. R., Löwer, R., Schmitz-Dräger, B. J. & Schulz, W. A. DNA methylation and expression of LINE-1 and HERV-K provirus sequences in urothelial and renal

- cell carcinomas. *Br. J. Cancer* **80**, 1312–1321 (1999).
28. Chiappinelli, K. B. *et al.* Inhibiting DNA Methylation Causes an Interferon Response in Cancer via dsRNA Including Endogenous Retroviruses. *Cell* **162**, 974–986 (2015).
 29. Goel, S. *et al.* CDK4/6 inhibition triggers anti-tumour immunity. *Nature* (2017). doi:10.1038/nature23465
 30. Sauter, M. *et al.* Human endogenous retrovirus K10: expression of Gag protein and detection of antibodies in patients with seminomas. *J. Virol.* **69**, 414–21 (1995).
 31. Cherkasova, E. *et al.* Detection of an immunogenic HERV-E envelope with selective expression in clear cell kidney cancer. *Cancer Res.* **76**, 2177–2185 (2016).
 32. Takahashi, Y. *et al.* Regression of human kidney cancer following allogeneic stem cell transplantation is associated with recognition of an HERV-E antigen by T cells. *J. Clin. Invest.* **118**, 1099–109 (2008).
 33. Shen, H. *et al.* Integrated Molecular Characterization of Testicular Germ Cell Tumors. *Cell Rep.* **23**, 3392–3406 (2018).
 34. Smit, A., Hubley, R. & Green, P. RepeatMasker Open-4.0. 2013-2015 . <http://www.repeatmasker.org> (2013).
 35. Paces, J. HERVd: the Human Endogenous RetroViruses Database: update. *Nucleic Acids Res.* **32**, 50D–50 (2004).
 36. Kim, T. H., Jeon, Y. J., Kim, W. Y. & Kim, H. S. HESAS: HERVs expression and structure analysis system. *Bioinformatics* **21**, 1699–1700 (2005).
 37. Tongyoo, P. *et al.* EnHERV: Enrichment analysis of specific human endogenous retrovirus patterns and their neighboring genes. *PLoS One* **12**, (2017).
 38. Vargiu, L. *et al.* Classification and characterization of human endogenous retroviruses; mosaic forms are common. *Retrovirology* **13**, 7 (2016).
 39. Jurtz, V. *et al.* NetMHCpan-4.0: Improved Peptide–MHC Class I Interaction Predictions Integrating Eluted Ligand and Peptide Binding Affinity Data. *J. Immunol.* j1700893 (2017). doi:10.4049/jimmunol.1700893
 40. Mayer, J., Blomberg, J. & Seal, R. L. A revised nomenclature for transcribed human endogenous retroviral loci. *Mob. DNA* **2**, (2011).
 41. Rooney, M. S., Shukla, S. A., Wu, C. J., Getz, G. & Hacohen, N. Molecular and genetic properties of tumors associated with local immune cytolytic activity. *Cell*

- 160**, 48–61 (2015).
42. Cherkasova, E. *et al.* Inactivation of the von Hippel-Lindau tumor suppressor leads to selective expression of a human endogenous retrovirus in kidney cancer. *Oncogene* **30**, 4697–4706 (2011).
 43. Shukla, S. A. *et al.* Comprehensive analysis of cancer-associated somatic mutations in class I HLA genes. *Nat. Biotechnol.* **33**, 1152–1158 (2015).
 44. Szolek, A. *et al.* OptiType: Precision HLA typing from next-generation sequencing data. *Bioinformatics* **30**, 3310–3316 (2014).
 45. Bai, Y., Wang, D. & Fury, W. PHLAT: Inference of high-resolution HLA types from RNA and whole exome sequencing. in *Methods in Molecular Biology* **1802**, 193–201 (2018).
 46. Ka, S. *et al.* HLAScan: Genotyping of the HLA region using next-generation sequencing data. *BMC Bioinformatics* **18**, (2017).
 47. Buchkovich, M. L. *et al.* HLAProfiler utilizes k-mer profiles to improve HLA calling accuracy for rare and common alleles in RNA-seq data. *Genome Med.* **9**, (2017).
 48. Hoof, I. *et al.* NetMHCpan, a method for MHC class I binding prediction beyond humans. *Immunogenetics* **61**, 1–13 (2009).
 49. Rajasagi, M. *et al.* Systematic identification of personal tumor-specific neoantigens in chronic lymphocytic leukemia. *Blood* **124**, 453–462 (2014).
 50. Thorsson, V. *et al.* The Immune Landscape of Cancer. *Immunity* **48**, 812–830.e14 (2018).
 51. Jayasinghe, R. G. *et al.* Systematic Analysis of Splice-Site-Creating Mutations in Cancer. *Cell Rep.* **23**, 270–281.e3 (2018).
 52. Selitsky, S. R., Marron, D., Mose, L., Parker, J. S. & Dittmer, D. P. Epstein-Barr Virus-Positive Cancers Show Altered B-Cell Clonality. *mSystems* (2018).
 53. Gao, Q. *et al.* Driver Fusions and Their Implications in the Development and Treatment of Human Cancers. *Cell Rep.* **23**, 227–238.e3 (2018).
 54. Trimble, C. L. *et al.* Safety, efficacy, and immunogenicity of VGX-3100, a therapeutic synthetic DNA vaccine targeting human papillomavirus 16 and 18 E6 and E7 proteins for cervical intraepithelial neoplasia 2/3: a randomised, double-blind, placebo-controlled phase 2b trial. *Lancet (London, England)* **386**, 2078–2088 (2015).
 55. Taylor, G. S. *et al.* A recombinant modified vaccinia ankara vaccine encoding Epstein-Barr Virus (EBV) target antigens: A phase I trial in UK patients with EBV-

- positive cancer. *Clin. Cancer Res.* **20**, 5009–5022 (2014).
56. Kim, W. S. *et al.* Autologous EBV-Specific T Cells (CMD-003): Early Results from a Multicenter, Multinational Phase 2 Trial for Treatment of EBV-Associated NK/T-Cell Lymphoma. *Blood* **130**, 4073 LP-4073 (2017).
 57. De Smedt, L. *et al.* Microsatellite instable vs stable colon carcinomas: Analysis of tumour heterogeneity, inflammation and angiogenesis. *Br. J. Cancer* **113**, 500–509 (2015).
 58. Linnebacher, M. *et al.* Frameshift peptide-derived T-cell epitopes: A source of novel tumor-specific antigens. *Int. J. Cancer* **93**, 6–11 (2001).
 59. Lyu, X. *et al.* Detection of 22 common leukemic fusion genes using a single-step multiplex qRT-PCR-based assay. *Diagn. Pathol.* (2017). doi:10.1186/s13000-017-0634-3
 60. Ley, T. J., Ding, L., Raphael, B. J., Mungall, A. J. & *et al.* Genomic and Epigenomic Landscapes of Adult De Novo Acute Myeloid Leukemia The Cancer Genome Atlas Research Network. *N. Engl. J. Med.* (2013). doi:10.1056/NEJMoa1301689
 61. Adamia, S. *et al.* A Genome-wide aberrant RNA Splicing in patients with acute myeloid leukemia identifies novel potential disease markers and therapeutic targets. *Clin. Cancer Res.* (2014). doi:10.1158/1078-0432.CCR-13-0956
 62. Wang, L. *et al.* *SF3B1* and Other Novel Cancer Genes in Chronic Lymphocytic Leukemia. *N. Engl. J. Med.* (2011). doi:10.1056/NEJMoa1109016
 63. Yoshida, K. *et al.* Frequent pathway mutations of splicing machinery in myelodysplasia. *Nature* (2011). doi:10.1038/nature10496
 64. Kar, S. A. *et al.* Spliceosomal gene mutations are frequent events in the diverse mutational spectrum of chronic myelomonocytic leukemia but largely absent in juvenile myelomonocytic leukemia. *Haematologica* (2013). doi:10.3324/haematol.2012.064048
 65. Visconte, V., Makishima, H., Maclejewski, J. P. & Tiu, R. V. Emerging roles of the spliceosomal machinery in myelodysplastic syndromes and other hematological disorders. *Leukemia* **26**, 2447–2454 (2012).
 66. Quesada, V. *et al.* Exome sequencing identifies recurrent mutations of the splicing factor *SF3B1* gene in chronic lymphocytic leukemia. *Nat. Genet.* **44**, 47–52 (2012).
 67. Lee, S. C. W. *et al.* Modulation of splicing catalysis for therapeutic targeting of leukemia with mutations in genes encoding spliceosomal proteins. *Nat. Med.* **22**, 672–678 (2016).

68. Irvine, D. J., Hanson, M. C., Rakhra, K. & Tokatlian, T. Synthetic Nanoparticles for Vaccines and Immunotherapy. *Chemical Reviews* **115**, 11109–11146 (2015).
69. Gregory, A. E., Titball, R. & Williamson, D. Vaccine delivery using nanoparticles. *Front. Cell. Infect. Microbiol.* **3**, (2013).
70. Kreiter, S. *et al.* Mutant MHC class II epitopes drive therapeutic immune responses to cancer. *Nature* **520**, 692–696 (2015).
71. Castle, J. C. *et al.* Exploiting the mutanome for tumor vaccination. *Cancer Res.* **72**, 1081–1091 (2012).
72. Kranz, L. M. *et al.* Systemic RNA delivery to dendritic cells exploits antiviral defence for cancer immunotherapy. *Nature* **534**, 396–401 (2016).
73. Kuai, R., Ochyl, L. J., Bahjat, K. S., Schwendeman, A. & Moon, J. J. Designer vaccine nanodiscs for personalized cancer immunotherapy. *Nature Materials* (2016). doi:10.1038/nmat4822
74. Kuai, R. *et al.* Subcutaneous Nanodisc Vaccination with Neoantigens for Combination Cancer Immunotherapy. *Bioconjug. Chem.* **29**, 771–775 (2018).
75. Min, Y. *et al.* Antigen-capturing nanoparticles improve the abscopal effect and cancer immunotherapy. *Nat. Nanotechnol.* **12**, 877–882 (2017).
76. Siegel RL, Miller KD, J. A. Cancer Statistics , 2017. *CA Cancer J Clin* **67**, 7–30 (2017).
77. Sjö Dahl, G. *et al.* A molecular taxonomy for urothelial carcinoma. *Clin. Cancer Res.* **18**, 3377–3386 (2012).
78. Volkmer, J.-P. *et al.* Three differentiation states risk-stratify bladder cancer into distinct subtypes. *Proc. Natl. Acad. Sci.* **109**, 2078–2083 (2012).
79. Rebouissou, S. *et al.* EGFR as a potential therapeutic target for a subset of muscle-invasive bladder cancers presenting a basal-like phenotype. *Sci. Transl. Med.* **6**, (2014).
80. Dyrskjø t, L. *et al.* Identifying distinct classes of bladder carcinoma using microarrays. *Nat. Genet.* **33**, 90–96 (2003).
81. Hedegaard, J. *et al.* Comprehensive Transcriptional Analysis of Early-Stage Urothelial Carcinoma. *Cancer Cell* **30**, 27–42 (2016).
82. Robertson, A. G. *et al.* Comprehensive Molecular Characterization of Muscle-Invasive Bladder Cancer. *Cell* **171**, 540–556.e25 (2017).
83. Kardos, J. *et al.* Claudin-low bladder tumors are immune infiltrated and actively

immune suppressed. *JCI Insight* **1**, (2016).

84. Powles, T. *et al.* MPDL3280A (anti-PD-L1) treatment leads to clinical activity in metastatic bladder cancer. *Nature* **515**, 558–562 (2014).
85. Rosenberg, J. E. *et al.* Atezolizumab in patients with locally advanced and metastatic urothelial carcinoma who have progressed following treatment with platinum-based chemotherapy: A single-arm, multicentre, phase 2 trial. *Lancet* **387**, 1909–1920 (2016).
86. Sharma, P. *et al.* Nivolumab monotherapy in recurrent metastatic urothelial carcinoma (CheckMate 032): a multicentre, open-label, two-stage, multi-arm, phase 1/2 trial. *Lancet Oncol.* **17**, 1590–1598 (2016).
87. Massard, C. *et al.* Safety and efficacy of durvalumab (MEDI4736), an anti-programmed cell death ligand-1 immune checkpoint inhibitor, in patients with advanced urothelial bladder cancer. *J. Clin. Oncol.* **34**, 3119–3125 (2016).
88. Bellmunt, J. *et al.* Pembrolizumab as Second-Line Therapy for Advanced Urothelial Carcinoma. *N. Engl. J. Med.* **376**, 1015–1026 (2017).
89. Apolo, A. B. *et al.* Avelumab, an anti-programmed death-ligand 1 antibody, in patients with refractory metastatic urothelial carcinoma: Results from a multicenter, Phase Ib study. *J. Clin. Oncol.* **35**, 2117–2124 (2017).
90. Summerhayes, I. C. & Franks, L. M. Effects of donor age on neoplastic transformation of adult mouse bladder epithelium in vitro. *J. Natl. Cancer Inst.* **62**, 1017–1032 (1979).
91. Vasconcelos-Nóbrega, C., Colaço, A., Lopes, C. & Oliveira, P. A. BBN as an urothelial carcinogen. *In Vivo* **26**, 727–739 (2012).
92. Kobayashi, T., Owczarek, T. B., McKiernan, J. M. & Abate-Shen, C. Modelling bladder cancer in mice: Opportunities and challenges. *Nature Reviews Cancer* **15**, 42–54 (2015).
93. Zhang, Z. T., Pak, J., Shapiro, E., Sun, T. T. & Wu, X. R. Urothelium-specific expression of an oncogene in transgenic mice induced the formation of carcinoma in situ and invasive transitional cell carcinoma. *Cancer Res.* **59**, 3512–3517 (1999).
94. Grippo, P. J. & Sandgren, E. P. Highly invasive transitional cell carcinoma of the bladder in a simian virus 40 T-antigen transgenic mouse model. *Am. J. Pathol.* **157**, 805–813 (2000).
95. Rampias, T. *et al.* A new tumor suppressor role for the Notch pathway in bladder cancer. *Nat. Med.* **20**, 1199–1205 (2014).

96. Puzio-Kuter, A. M. *et al.* Inactivation of p53 and Pten promotes invasive bladder cancer. *Genes Dev.* **23**, 675–680 (2009).
97. Trotman, L. C. *et al.* Pten dose dictates cancer progression in the prostate. *PLoS Biol.* **1**, (2003).
98. Liu, X. *et al.* ROCK inhibitor and feeder cells induce the conditional reprogramming of epithelial cells. *Am. J. Pathol.* **180**, 599–607 (2012).
99. Wang, K. *et al.* MapSplice: Accurate mapping of RNA-seq reads for splice junction discovery. *Nucleic Acids Res.* **38**, (2010).
100. Bindea, G. *et al.* Spatiotemporal dynamics of intratumoral immune cells reveal the immune landscape in human cancer. *Immunity* **39**, 782–795 (2013).
101. Iglesia, M. D. *et al.* Prognostic B-cell signatures using mRNA-seq in patients with subtype-specific breast and ovarian cancer. *Clin. Cancer Res.* **20**, 3818–3829 (2014).
102. Suzuki, R. & Shimodaira, H. Pvcust: An R package for assessing the uncertainty in hierarchical clustering. *Bioinformatics* **22**, 1540–1542 (2006).
103. Wölfl, M. & Greenberg, P. D. Antigen-specific activation and cytokine-facilitated expansion of naive, human CD8+T cells. *Nat. Protoc.* **9**, 950–966 (2014).
104. Rock, J. R. *et al.* Basal cells as stem cells of the mouse trachea and human airway epithelium. *Proc. Natl. Acad. Sci.* **106**, 12771–12775 (2009).
105. Iglesia, M. D. *et al.* Genomic analysis of immune cell infiltrates across 11 tumor types. *J. Natl. Cancer Inst.* **108**, (2016).
106. Fantini, D. *et al.* A Carcinogen-induced mouse model recapitulates the molecular alterations of human muscle invasive bladder cancer. *Oncogene* **37**, 1911–1925 (2018).
107. Li, S. *et al.* The tumor suppressor PTEN has a critical role in antiviral innate immunity. *Nat. Immunol.* **17**, 241–249 (2016).
108. Peng, W. *et al.* Loss of PTEN promotes resistance to T cell-mediated immunotherapy. *Cancer Discov.* **6**, 202–216 (2016).
109. Brien, S. M. O. *et al.* Improved Survival with Ipilimumab in Patients with Metastatic Melanoma. *N. Engl. J. Med.* 1467–1476 (2012). doi:10.1056/NEJMoa1409312
110. Hamid, O. *et al.* Safety and Tumor Responses with Lambrolizumab (Anti-PD-1) in Melanoma. *N. Engl. J. Med.* **369**, 134–144 (2013).
111. Wolchok, J. D. *et al.* Nivolumab plus Ipilimumab in Advanced Melanoma. *N. Engl.*

- J. Med.* **369**, 122–133 (2013).
112. Weinstock, M. & McDermott, D. Targeting PD-1/PD-L1 in the treatment of metastatic renal cell carcinoma. *Therapeutic Advances in Urology* **7**, 365–377 (2015).
 113. Gettinger, S. N. *et al.* Overall survival and long-term safety of nivolumab (anti-programmed death 1 antibody, BMS-936558, ONO-4538) in patients with previously treated advanced non-small-cell lung cancer. *J. Clin. Oncol.* **33**, 2004–2012 (2015).
 114. Borghaei, H. *et al.* Nivolumab versus Docetaxel in Advanced Nonsquamous Non-Small-Cell Lung Cancer. *N. Engl. J. Med.* **373**, 1627–39 (2015).
 115. Tumei, P., Harview, C., Yearley, J. & Al, E. PD-1 blockade induces responses by inhibiting adaptive immune resistance. *Nature* **515**, 568–571 (2014).
 116. Ahmadzadeh, M. *et al.* Tumor antigen – specific CD8 T cells infiltrating the tumor express high levels of PD-1 and are functionally impaired Tumor antigen – specific CD8 T cells infiltrating the tumor express high levels of PD-1 and are functionally impaired. *Blood* **114**, 1537–1544 (2009).
 117. McCracken, M. N., Tavaré, R., Witte, O. N. & Wu, A. M. Advances in PET Detection of the Antitumor T Cell Response. 187–231 (2016). doi:10.1016/bs.ai.2016.02.004
 118. Kochenderfer, J. N. & Rosenberg, S. A. Treating B-cell cancer with T cells expressing anti-CD19 chimeric antigen receptors. *Nature Reviews Clinical Oncology* **10**, 267–276 (2013).
 119. Rashidian, M., Keliher, E. J., Bilate, A. M., Duarte, J. N. & Wojtkiewicz, G. R. Noninvasive imaging of immune responses. **112**, 1–6 (2015).
 120. Kircher, M. F., Gambhir, S. S. & Grimm, J. Noninvasive cell-tracking methods. *Nat. Rev. Clin. Oncol.* **8**, 677–688 (2011).
 121. Tavaré, R. *et al.* Immuno-PET of Murine T Cell Reconstitution Postadoptive Stem Cell Transplantation Using Anti-CD4 and Anti-CD8 Cys-Diabodies. **56**, 1258–1264 (2015).
 122. Fischer, G., Seibold, U., Schirmacher, R., Wängler, B. & Wängler, C. ⁸⁹Zr, a radiometal nuclide with high potential for molecular imaging with pet: Chemistry, applications and remaining challenges. *Molecules* **18**, 6469–6490 (2013).
 123. Kasbollah, A., Eu, P., Cowell, S. & Deb, P. Review on production of ⁸⁹Zr in a medical cyclotron for PET radiopharmaceuticals. *J. Nucl. Med. Technol.* **41**, 35–41 (2013).

124. Mendler, C. T., Gehring, T., Wester, H.-J., Schwaiger, M. & Skerra, A. ⁸⁹Zr-Labeled Versus ¹²⁴I-Labeled αHER2 Fab with Optimized Plasma Half-Life for High-Contrast Tumor Imaging In Vivo. *J. Nucl. Med.* **56**, 1112–8 (2015).
125. Tavaré, R. *et al.* Engineered antibody fragments for immuno-PET imaging of endogenous CD8⁺ T cells in vivo. *Proc. Natl. Acad. Sci.* **111**, 1108–1113 (2014).
126. Tavaré, R. *et al.* Enhanced immunoPET of ALCAM-positive colorectal carcinoma using site-specific ⁶⁴Cu-DOTA conjugation. *Protein Eng. Des. Sel.* **27**, 317–324 (2014).
127. Kaminski, N., Roberts, J. & Guthrie, F. Target ricin by coupling to an anti-macrophage monoclonal antibody. *J Immunopharmacol* **8**, 15–37 (1986).
128. Countouriotis, A., Moore, T. B. & Sakamoto, K. M. Cell Surface Antigen and Molecular Targeting in the Treatment of Hematologic Malignancies. *Stem Cells* **20**, 215–229 (2002).
129. Loubaki, L., Tremblay, T. & Bazin, R. In vivo depletion of leukocytes and platelets following injection of T cell-specific antibodies into mice. *J. Immunol. Methods* **393**, 38–44 (2013).
130. Ledbetter, J. A. & Herzenberg, L. A. Xenogeneic monoclonal antibodies to mouse lymphoid differentiation antigens. *Immunol. Rev.* **47**, 63–90 (1979).
131. Howard, M. *et al.* Identification of a T cell-derived b cell growth factor distinct from interleukin 2. *J. Exp. Med.* **155**, 914–23 (1982).
132. Cobbold, S. P., Jayasuriya, A., Nash, A., Prospero, T. D. & Waldmann, H. Therapy with monoclonal antibodies by elimination of T-cell subsets in vivo. *Nature* **312**, 548–551 (1984).
133. Larimer, B. M., Wehrenberg-Klee, E., Caraballo, A. & Mahmood, U. Quantitative CD3 PET Imaging Predicts Tumor Growth Response to Anti-CTLA-4 Therapy. *J. Nucl. Med.* **57**, 1607–1611 (2016).
134. Broere, F., Apasov, S. G., Sitkovsky, M. V & Eden, W. Van. Principles of Immunopharmacology. *Princ. Immunopharmacol.* 15–28 (2011). doi:10.1007/978-3-0346-0136-8
135. Gattinoni, L., Powell, D. J., Rosenberg, S. A. & Restifo, N. P. Adoptive immunotherapy for cancer: Building on success. *Nature Reviews Immunology* **6**, 383–393 (2006).
136. Liu, S. Bifunctional coupling agents for radiolabeling of biomolecules and target-specific delivery of metallic radionuclides ☆. *Adv. Drug Deliv. Rev.* **60**, 1347–1370 (2008).

137. Price, E. W. & Orvig, C. Matching chelators to radiometals for radiopharmaceuticals. *Chem. Soc. Rev.* **43**, 260–90 (2014).
138. Vosjan, M. J. W. D. *et al.* Conjugation and radiolabeling of monoclonal antibodies with zirconium-89 for PET imaging using the bifunctional chelate p-isothiocyanatobenzyl-desferrioxamine. *Nat. Protoc.* **5**, 739–743 (2010).
139. Zeglis, B. M. & Lewis, J. S. The Bioconjugation and Radiosynthesis of ^{89}Zr -DFO-labeled Antibodies. *J. Vis. Exp.* (2015). doi:10.3791/52521
140. Chang, A. J., De Silva, R. A. & Lapi, S. E. Development and characterization of ^{89}Zr -labeled panitumumab for immuno-positron emission tomographic imaging of the epidermal growth factor receptor. *Mol. Imaging* **12**, 1–11 (2013).
141. Piersma, S. J. *et al.* High number of intraepithelial CD8+tumor-infiltrating lymphocytes is associated with the absence of lymph node metastases in patients with large early-stage cervical cancer. *Cancer Res.* **67**, 354–361 (2007).
142. Diederichsen, A. C. P., Hjelmberg, J. V. B., Christensen, P. B., Zeuthen, J. & Fenge, C. Prognostic value of the CD4+/CD8+ratio of tumour infiltrating lymphocytes in colorectal cancer and HLA-DR expression on tumour cells. *Cancer Immunol. Immunother.* **52**, 423–428 (2003).
143. Chin, Y. *et al.* Phenotypic analysis of tumor-infiltrating lymphocytes from human breast cancer. *Anticancer Res.* **12**, 1463–1466 (1992).
144. Nagao, M. *et al.* Mutagenicity of N-Butyl-N-(4-hydroxybutyl) nitrosamine, a Bladder Carcinogen, and Related Compounds Mutagenicity of N-Butyl-N-(4-hydroxybutyl) nitrosamine, a Bladder Carcinogen, and Related Compounds1. 399–407 (1977).
145. Bryan, G. T. The Pathogenesis of Experimental Bladder Cancer1. *Cancer Res.* **37**, 2813–2816 (1977).
146. Bannert, N. & Kurth, R. The Evolutionary Dynamics of Human Endogenous Retroviral Families. *Annu. Rev. Genomics Hum. Genet.* **7**, 149–173 (2006).
147. Katzourakis, A., Rambaut, A. & Pybus, O. G. The evolutionary dynamics of endogenous retroviruses. *Trends in Microbiology* **13**, 463–468 (2005).
148. Kalyanaraman, V. S. *et al.* A New Subtype of Human T-Cell Leukemia Virus (HTLV-II) Associated with a T-Cell Variant of Hairy Cell Leukemia. *Source Sci. New Ser.* **218**, 571–573 (1982).
149. Haase, K., Mösch, A. & Frishman, D. Differential expression analysis of human endogenous retroviruses based on ENCODE RNA-seq data. *BMC Med. Genomics* **8**, 71 (2015).

150. Paces, J., Pavlíček, A. & Paces, V. HERVd: database of human endogenous retroviruses. *Nucleic Acids Res.* **30**, 205–206 (2002).
151. Levy, A., Sela, N. & Ast, G. TranspoGene and microTranspoGene: Transposed elements influence on the transcriptome of seven vertebrates and invertebrates. *Nucleic Acids Res.* **36**, (2008).
152. Loayza-Puch, F. *et al.* Tumour-specific proline vulnerability uncovered by differential ribosome codon reading. *Nature* **530**, 490–494 (2016).
153. Lavie, L., Kitova, M., Maldener, E., Meese, E. & Mayer, J. CpG methylation directly regulates transcriptional activity of the human endogenous retrovirus family HERV-K (HML-2). *J. Virol.* **79**, 876 (2005).
154. Okada, M. *et al.* Role of DNA methylation in transcription of human endogenous retrovirus in the pathogenesis of systemic lupus erythematosus. *J Rheumatol* **29**, 1678–1682 (2002).
155. Stengel, S., Fiebig, U., Kurth, R. & Denner, J. Regulation of human endogenous retrovirus-K expression in melanomas by CpG methylation. *Genes Chromosom. Cancer* **49**, 401–411 (2010).
156. Goel, S. *et al.* CDK4/6 inhibition triggers anti-tumour immunity. *Nature* (2017). doi:10.1038/nature23465
157. Chan, K. S. *et al.* Identification, molecular characterization, clinical prognosis, and therapeutic targeting of human bladder tumor-initiating cells. *Proc. Natl. Acad. Sci. U. S. A.* **106**, 14016–14021 (2009).
158. Prat, A. *et al.* Phenotypic and molecular characterization of the claudin-low intrinsic subtype of breast cancer. *Breast Cancer Res.* **12**, R68 (2010).
159. Palmer, C., Diehn, M., Alizadeh, A. A. & Brown, P. O. Cell-type specific gene expression profiles of leukocytes in human peripheral blood. *BMC Genomics* **7**, (2006).
160. Liberzon, A. *et al.* Molecular signatures database (MSigDB) 3.0. *Bioinformatics* **27**, 1739–1740 (2011).
161. Şenbabaoglu, Y. *et al.* Erratum to: Tumor immune microenvironment characterization in clear cell renal cell carcinoma identifies prognostic and immunotherapeutically relevant messenger RNA signatures [Genome Biology. 17, (2016) (231)] DOI: 10.1186/s13059-016-1092-z. *Genome Biology* **18**, (2017).
162. Bolotin, D. A. *et al.* MiXCR: Software for comprehensive adaptive immunity profiling. *Nature Methods* **12**, 380–381 (2015).
163. Hancock, D. C. & O'Reilly, N. J. Synthetic Peptides as Antigens for Antibody

- Production. in *Immunochemical Protocols* 13–25 (2005). doi:10.1385/1-59259-873-0:013
164. Ljungberg, B. *et al.* EAU guidelines on renal cell carcinoma: 2014 update. *European Urology* **67**, 913–924 (2015).
 165. Liu, J. *et al.* An Integrated TCGA Pan-Cancer Clinical Data Resource to Drive High-Quality Survival Outcome Analytics. *Cell* **173**, 400–416.e11 (2018).
 166. Schumacher, T. N. & Schreiber, R. D. Neoantigens in cancer immunotherapy. *Science* (80-.). **348**, 69–74 (2015).
 167. Wang, R.-F. & Wang, H. Y. Immune targets and neoantigens for cancer immunotherapy and precision medicine. *Cell Res.* **27**, 11–37 (2017).
 168. Love, M. I., Huber, W. & Anders, S. Moderated estimation of fold change and dispersion for RNA-seq data with DESeq2. *Genome Biol.* **15**, 550 (2014).
 169. Michel, A. M. *et al.* GWIPS-viz: Development of a ribo-seq genome browser. *Nucleic Acids Res.* **42**, (2014).
 170. Altman, J. D. *et al.* Phenotypic analysis of antigen-specific T lymphocytes. *Science* **274**, 94–6 (1996).
 171. Rodenko, B. *et al.* Generation of peptide-MHC class I complexes through UV-mediated ligand exchange. *Nat. Protoc.* **1**, 1120–1132 (2006).
 172. Toebe, M. *et al.* Design and use of conditional MHC class I ligands. *Nat. Med.* **12**, 246–251 (2006).
 173. Bakker, A. H. *et al.* Conditional MHC class I ligands and peptide exchange technology for the human MHC gene products HLA-A1, -A3, -A11, and -B7. *Proc. Natl. Acad. Sci. U. S. A.* **105**, 3825–30 (2008).
 174. Protocol for fluorescent Flex-T™ generation and antigen specific CD8+ T cell staining.
 175. Protocol for HLA class I ELISA to evaluate peptide exchange.
 176. Dobin, A. *et al.* STAR: Ultrafast universal RNA-seq aligner. *Bioinformatics* **29**, 15–21 (2013).
 177. Li, H. *et al.* The Sequence Alignment/Map format and SAMtools. *Bioinformatics* **25**, 2078–2079 (2009).
 178. Patro, R., Duggal, G., Love, M. I., Irizarry, R. A. & Kingsford, C. Salmon provides fast and bias-aware quantification of transcript expression. *Nat. Methods* **14**, 417–419 (2017).

179. Dolton, G. *et al.* More tricks with tetramers: A practical guide to staining T cells with peptide-MHC multimers. *Immunology* **146**, 11–22 (2015).
180. Bodenhofer, U., Bonatesta, E., Horejš-Kainrath, C. & Hochreiter, S. msa: an R package for multiple sequence alignment. *Bioinformatics* **31**, 3997–9 (2015).
181. Andreatta, M. *et al.* Accurate pan-specific prediction of peptide-MHC class II binding affinity with improved binding core identification. *Immunogenetics* **67**, 641–650 (2015).
182. Saito, R. *et al.* Molecular subtype-specific immunocompetent models of high-grade urothelial carcinoma reveal differential neoantigen expression and response to immunotherapy. *Cancer Res.* **78**, 3954–3968 (2018).
183. Wilkerson, M. D. *et al.* Integrated RNA and DNA sequencing improves mutation detection in low purity tumors. *Nucleic Acids Res.* **42**, (2014).
184. Nielsen, M. & Andreatta, M. NetMHCpan-3.0; improved prediction of binding to MHC class I molecules integrating information from multiple receptor and peptide length datasets. *Genome Med.* **8**, (2016).
185. Ene, C. I. & Fine, H. A. Many Tumors in one: A daunting therapeutic prospect. *Cancer Cell* **20**, 695–697 (2011).
186. Longo, D. L. Tumor heterogeneity and personalized medicine. *N. Engl. J. Med.* **366**, 956–7 (2012).
187. Greaves, M. & Maley, C. C. Clonal evolution in cancer. *Nature* **481**, 306–313 (2012).
188. Coulie, P. G. *et al.* A mutated intron sequence codes for an antigenic peptide recognized by cytolytic T lymphocytes on a human melanoma. *Proc. Natl. Acad. Sci.* **92**, 7976–7980 (1995).
189. Gubin, M. M., Artyomov, M. N., Mardis, E. R. & Schreiber, R. D. Tumor neoantigens: Building a framework for personalized cancer immunotherapy. *Journal of Clinical Investigation* **125**, 3413–3421 (2015).
190. Simpson, A. J. G., Caballero, O. L., Jungbluth, A., Chen, Y. T. & Old, L. J. Cancer/testis antigens, gametogenesis and cancer. *Nature Reviews Cancer* **5**, 615–625 (2005).
191. Vigneron, N., Stroobant, V., van den Eynde, B. J. & van der Bruggen, P. Database of T cell-defined human tumor antigens: The 2013 update. *Cancer Immunity* **13**, (2013).
192. Heemskerk, B., Kvistborg, P. & Schumacher, T. N. M. The cancer antigenome. *EMBO Journal* **32**, 194–203 (2013).

193. Mi, Y. *et al.* A Dual Immunotherapy Nanoparticle Improves T-Cell Activation and Cancer Immunotherapy. *Adv. Mater.* **30**, (2018).
194. Kreiter, S. *et al.* Mutant MHC class II epitopes drive therapeutic immune responses to cancer. *Nature* **520**, 692–696 (2015).
195. Corrales, L. *et al.* Direct Activation of STING in the Tumor Microenvironment Leads to Potent and Systemic Tumor Regression and Immunity. *Cell Rep.* **11**, 1018–1030 (2015).
196. Newman, A. M. *et al.* Robust enumeration of cell subsets from tissue expression profiles. *Nat. Methods* **12**, 453–457 (2015).
197. Li, B. *et al.* Comprehensive analyses of tumor immunity: Implications for cancer immunotherapy. *Genome Biol.* **17**, (2016).
198. Cancer Genome Atlas Research Network. Comprehensive Molecular Portraits of Invasive Lobular Breast Cancer. *Cell* **163**, 506–519 (2015).
199. Hellmann, M. D. *et al.* Tumor Mutational Burden and Efficacy of Nivolumab Monotherapy and in Combination with Ipilimumab in Small-Cell Lung Cancer. *Cancer Cell* **33**, 853–861.e4 (2018).
200. Smith, C. C. *et al.* Endogenous retroviral signatures predict immunotherapy response in clear cell renal cell carcinoma. *J. Clin. Invest.* (2018).
201. Matsushita, H. *et al.* Cancer exome analysis reveals a T-cell-dependent mechanism of cancer immunoediting. *Nature* **482**, 400–404 (2012).
202. Coulie, P. G., Van Den Eynde, B. J., Van Der Bruggen, P. & Boon, T. Tumour antigens recognized by T lymphocytes: At the core of cancer immunotherapy. *Nature Reviews Cancer* **14**, 135–146 (2014).
203. Ali, N., Rampazzo, R. D. C. P., Costa, A. Di. T. & Krieger, M. A. Current Nucleic Acid Extraction Methods and Their Implications to Point-of-Care Diagnostics. *BioMed Research International* **2017**, (2017).
204. Escobar, M. D. & Hunt, J. L. A cost-effective RNA extraction technique from animal cells and tissue using silica columns. *J. Biol. Methods* **4**, 72 (2017).
205. Chirgwin, J. M., Przybyla, A. E., MacDonald, R. J. & Rutter, W. J. Isolation of Biologically Active Ribonucleic Acid from Sources Enriched in Ribonuclease. *Biochemistry* **18**, 5294–5299 (1979).
206. Farrell, R. E. *RNA Methodologies: Laboratory Guide for Isolation and Characterization.* Elsevier/Academic Press (2010). doi:10.1016/B978-0-12-374727-3.00025-5

207. Amini, P. *et al.* An optimised protocol for isolation of RNA from small sections of laser-capture microdissected FFPE tissue amenable for next-generation sequencing. *BMC Mol. Biol.* **18**, (2017).
208. Kresse, S. H. *et al.* Evaluation of commercial DNA and RNA extraction methods for high-throughput sequencing of FFPE samples. *PLoS One* **13**, e0197456 (2018).
209. Bonin, S. *et al.* Multicentre validation study of nucleic acids extraction from FFPE tissues. *Virchows Arch.* **457**, 309–317 (2010).
210. Patel, P. G. *et al.* Reliability and performance of commercial RNA and DNA extraction kits for FFPE tissue cores. *PLoS One* **12**, (2017).
211. Patel, P. G. *et al.* Preparation of Formalin-fixed Paraffin-embedded Tissue Cores for both RNA and DNA Extraction. *J. Vis. Exp.* 1–10 (2016). doi:10.3791/54299
212. Nielsen, H. *RNA Methods and Protocols. Methods in Molecular Biology* **703**, (2011).
213. Schroeder, A. *et al.* The RIN: An RNA integrity number for assigning integrity values to RNA measurements. *BMC Mol. Biol.* **7**, (2006).
214. Mueller, O. & Schroeder, A. RNA Integrity Number (RIN) – Standardization of RNA Quality Control Application. *Nano* 1–8 (2004). doi:10.1101/gr.189621.115.7
215. Illumina. *Evaluating RNA Quality from FFPE Samples.* (2016).
216. Baruzzo, G. *et al.* Simulation-based comprehensive benchmarking of RNA-seq aligners. *Nat. Methods* **14**, 135–139 (2017).
217. Engström, P. G. *et al.* Systematic evaluation of spliced alignment programs for RNA-seq data. *Nat. Methods* **10**, 1185–1191 (2013).
218. Patro, R., Mount, S. M. & Kingsford, C. Sailfish enables alignment-free isoform quantification from RNA-seq reads using lightweight algorithms. *Nat. Biotechnol.* **32**, 462–464 (2014).
219. Bray, N. L., Pimentel, H., Melsted, P. & Pachter, L. Near-optimal probabilistic RNA-seq quantification. *Nat. Biotechnol.* **34**, 525–527 (2016).
220. Broad Institute. Picard tools. <https://broadinstitute.github.io/picard/> (2016). Available at: <https://broadinstitute.github.io/picard/%5Cnhttp://broadinstitute.github.io/picard/>.
221. McCall, M. N., Murakami, P. N., Lukk, M., Huber, W. & Irizarry, R. A. Assessing affymetrix GeneChip microarray quality. *BMC Bioinformatics* **12**, (2011).

222. Li, B. & Dewey, C. N. RSEM: Accurate transcript quantification from RNA-Seq data with or without a reference genome. *BMC Bioinformatics* **12**, (2011).
223. Trapnell, C. *et al.* Differential gene and transcript expression analysis of RNA-seq experiments with TopHat and Cufflinks. *Nat. Protoc. Protoc.* **7**, 562–578 (2012).
224. Zhang, C., Zhang, B., Lin, L. L. & Zhao, S. Evaluation and comparison of computational tools for RNA-seq isoform quantification. *BMC Genomics* **18**, (2017).
225. Robinson, M. D., McCarthy, D. J. & Smyth, G. K. edgeR: A Bioconductor package for differential expression analysis of digital gene expression data. *Bioinformatics* **26**, 139–140 (2009).
226. Li, X. *et al.* A comparison of per sample global scaling and per gene normalization methods for differential expression analysis of RNA-seq data. *PLoS One* **12**, e0176185 (2017).
227. Costa-Silva Juliana AND Domingues, D. A. N. D. L. F. M. RNA-Seq differential expression analysis: An extended review and a software tool. *PLoS One* **12**, 1–18 (2017).
228. Schurch, N. J. *et al.* How many biological replicates are needed in an RNA-seq experiment and which differential expression tool should you use? *RNA* **22**, 839–851 (2016).
229. Fan, C. *et al.* Concordance among Gene-Expression– Based Predictors for Breast Cancer. *N Engl J Med* **355**, 560–569 (2006).
230. Schmidt, M. *et al.* The humoral immune system has a key prognostic impact in node-negative breast cancer. *Cancer Res.* **68**, 5405–5413 (2008).
231. Beck, A. H. *et al.* The macrophage colony-stimulating factor 1 response signature in breast carcinoma. *Clin. Cancer Res.* **15**, 778–787 (2009).
232. Rody, A. *et al.* T-cell metagene predicts a favorable prognosis in estrogen receptor-negative and HER2-positive breast cancers. *Breast Cancer Res.* **11**, (2009).
233. Fan, C. *et al.* Building prognostic models for breast cancer patients using clinical variables and hundreds of gene expression signatures. *BMC Med. Genomics* **4**, (2011).
234. Rody, A. *et al.* A clinically relevant gene signature in triple negative and basal-like breast cancer. *Breast Cancer Res.* **13**, R97 (2011).
235. Charoentong, P. *et al.* Pan-cancer Immunogenomic Analyses Reveal Genotype-Immunophenotype Relationships and Predictors of Response to Checkpoint

- Blockade. *Cell Rep.* **18**, 248–262 (2017).
236. Mootha, V. K. *et al.* PGC-1 α -responsive genes involved in oxidative phosphorylation are coordinately downregulated in human diabetes. *Nat. Genet.* **34**, 267–273 (2003).
 237. Barbie, D. A. *et al.* Systematic RNA interference reveals that oncogenic KRAS-driven cancers require TBK1. *Nature* **462**, 108–112 (2009).
 238. Hänzelmann, S., Castelo, R. & Guinney, J. GSEA: Gene set variation analysis for microarray and RNA-Seq data. *BMC Bioinformatics* **14**, (2013).
 239. Tomfohr, J., Lu, J. & Kepler, T. B. Pathway level analysis of gene expression using singular value decomposition. *BMC Bioinformatics* **6**, (2005).
 240. Hulsege, I., Kommadath, A. & Smits, M. A. Globaltest and GOEAST: two different approaches for Gene Ontology analysis. *BMC Proc.* **3**, S10 (2009).
 241. Tarca, A. L., Draghici, S., Bhatti, G. & Romero, R. Down-weighting overlapping genes improves gene set analysis. *BMC Bioinformatics* **13**, 136 (2012).
 242. Tarca, A. L., Bhatti, G. & Romero, R. A comparison of gene set analysis methods in terms of sensitivity, prioritization and specificity. *PLoS One* **8**, (2013).
 243. Subramanian P; Mootha, VK; Mukherjee, S; Ebert, BL; Gillette, MA; Paulovich, A; Pomeroy, SL; Golub, TR; Lander, ES; Mesirov, JP., A. T. Gene set enrichment analysis: a knowledge-based approach for interpreting genome-wide expression profiles. *Proc Natl Acad Sci U S A.* **102**, 15545–15550 (2005).
 244. Hou, J. P. & Ma, J. DawnRank: Discovering personalized driver genes in cancer. *Genome Med.* **6**, (2014).
 245. Bolotin, D. A. *et al.* MiTCR: Software for T-cell receptor sequencing data analysis. *Nature Methods* **10**, 813–814 (2013).
 246. Li, B. *et al.* Ultrasensitive detection of TCR hypervariable-region sequences in solid-tissue RNA-seq data. *Nature Genetics* **49**, 483–484 (2017).
 247. Mose, L. E. *et al.* Assembly-based inference of B-cell receptor repertoires from short read RNA sequencing data with V'DJer. *Bioinformatics* **32**, 3729–3734 (2016).
 248. Bolotin, D. A. *et al.* Antigen receptor repertoire profiling from RNA-seq data. *Nat. Biotechnol.* **35**, 908–911 (2017).
 249. Weimer, E. T., Montgomery, M., Petraroia, R., Crawford, J. & Schmitz, J. L. Performance Characteristics and Validation of Next-Generation Sequencing for Human Leucocyte Antigen Typing. *J. Mol. Diagnostics* **18**, (2016).

250. Nariai, N. *et al.* HLA-VBSeq: Accurate HLA typing at full resolution from whole-genome sequencing data. *BMC Genomics* **16**, (2015).
251. Major, E., Rigó, K., Hague, T., Bérces, A. & Juhos, S. HLA typing from 1000 Genomes whole genome and whole exome illumina data. *PLoS One* **8**, (2013).
252. Kim, S. *et al.* Neopepsee: Accurate genome-level prediction of neoantigens by harnessing sequence and amino acid immunogenicity information. *Ann. Oncol.* **29**, 1030–1036 (2018).
253. Hundal, J. *et al.* Abstract 3995: pVAC-Seq: A genome-guided *in silico* approach to identify tumor neoantigens for personalized immunotherapy. *Cancer Res.* **76**, 3995–3995 (2016).
254. Zhang, J., Mardis, E. R. & Maher, C. A. INTEGRATE-neo: A pipeline for personalized gene fusion neoantigen discovery. *Bioinformatics* **33**, 555–557 (2017).
255. Greytak, SR; Engel, KB; Zmuda, E; Casas-Silva, E; Guan, P; Hoadley, KA; Mungall, AJ; Wheeler, DA; Doddapaneni, HV; Moore, H. National Cancer Institute Biospecimen Evidence-Based Practices: Harmonizing Procedures for Nucleic Acid Extraction from Formalin-Fixed, Paraffin-Embedded Tissue. *Biopreserv Biobank.* **16**, 247–250 (2018).
256. Bushnell & Brian. BBMap: A Fast, Accurate, Splice-Aware Aligner. *Conference: 9th Annual Genomics of Energy & Environment Meeting* (2014). doi:10.1186/1471-2105-13-238
257. Zhao, W. *et al.* Comparison of RNA-Seq by poly (A) capture, ribosomal RNA depletion, and DNA microarray for expression profiling. *BMC Genomics* **15**, (2014).
258. Illumina. *bcl2fastq2 Software v2.19.1 Release Notes.* (2017).
259. Andrews, S. FastQC: A quality control tool for high throughput sequence data. Available at: www.bioinformatics.babraham.ac.uk/projects/fastqc/. *FastQC: A quality control tool for high throughput sequence data.* Available at: www.bioinformatics.babraham.ac.uk/projects/fastqc/ (2010).
260. Qiagen. *CLC Assembly Cell USER MANUAL.* (2018).
261. Hercus, C., Albertyn, Z. Novoalign. *Novocr. Technol.* (2012).
262. Wu, T. D., Reeder, J., Lawrence, M., Becker, G. & Brauer, M. J. GMAP and GSNAP for genomic sequence alignment: Enhancements to speed, accuracy, and functionality. in *Methods in Molecular Biology* **1418**, 283–334 (2016).
263. Smyth, G. K. Limma: linear models fro microarray data. in *Bioinformatics and*

Computational Biology Solutions using R and Bioconductor 397–420 (2005).
doi:10.1007/0-387-29362-0_23

264. Law, C. W., Chen, Y., Shi, W. & Smyth, G. K. Voom: Precision weights unlock linear model analysis tools for RNA-seq read counts. *Genome Biol.* **15**, (2014).
265. Tarazona, S. *et al.* Data quality aware analysis of differential expression in RNA-seq with NOISeq R/Bioc package. *Nucleic Acids Res.* **43**, (2015).
266. Beckford Vera, D. R. *et al.* Immuno-PET imaging of tumor-infiltrating lymphocytes using zirconium-89 radiolabeled anti-CD3 antibody in immune-competent mice bearing syngeneic tumors. *PLoS One* **13**, (2018).
267. The Cancer Genome Atlas Network. Comprehensive molecular characterization of clear cell renal cell carcinoma. *Nature* **499**, 43–9 (2013).